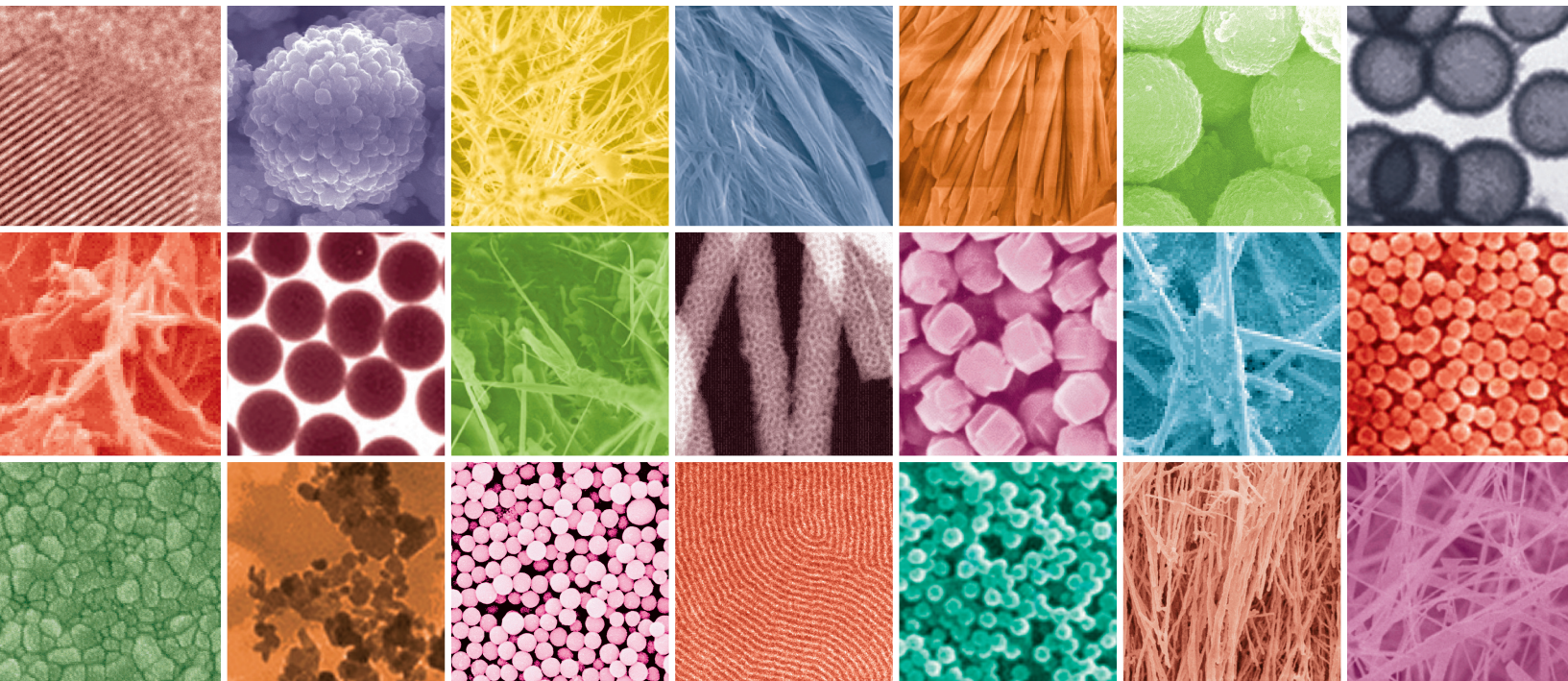


The Potential of Nanomaterials for Drug Delivery, Cell Tracking, and Regenerative Medicine 2013

Guest Editors: Krasimir Vasilev, Haifeng Chen, and Patricia Murray





**The Potential of Nanomaterials for
Drug Delivery, Cell Tracking,
and Regenerative Medicine 2013**

Journal of Nanomaterials

**The Potential of Nanomaterials for
Drug Delivery, Cell Tracking,
and Regenerative Medicine 2013**

Guest Editors: Krasimir Vasilev, Haifeng Chen,
and Patricia Murray



Copyright © 2014 Hindawi Publishing Corporation. All rights reserved.

This is a special issue published in "Journal of Nanomaterials." All articles are open access articles distributed under the Creative Commons Attribution License, which permits unrestricted use, distribution, and reproduction in any medium, provided the original work is properly cited.

Editorial Board

Katerina E. Aifantis, USA
Nageh K. Allam, USA
Margarida Amaral, Portugal
Xuedong Bai, China
Lavinia Balan, France
Enrico Bergamaschi, Italy
Theodorian Borca-Tasciuc, USA
C. Jeffrey Brinker, USA
Christian Brosseau, France
Xuebo Cao, China
Shafiq Chowdhury, USA
Kwang-Leong Choy, UK
Cui ChunXiang, China
Miguel A. Correa-Duarte, Spain
Shadi A. Dayeh, USA
Ali Eftekhari, USA
Claude Estournès, France
Alan Fuchs, USA
Lian Gao, China
Russell E. Gorga, USA
Hongchen Chen Gu, China
Mustafa O. Guler, Turkey
John Z. Guo, USA
Smrati Gupta, Germany
Michael Harris, USA
Zhongkui Hong, China
Michael Z. Hu, USA
David Hui, USA
Y.-K. Jeong, Republic of Korea
Sheng-Rui Jian, Taiwan
Wanqin Jin, China
Rakesh K. Joshi, UK
Zhenhui Kang, China
F. Karimzadeh, Iran
Alireza Khataee, Iran

Do K. Kim, Korea
Alan K. T. Lau, Hong Kong
Burtrand Lee, USA
Jun Li, Singapore
Benxia Li, China
Xing-Jie Liang, China
Shijun Liao, China
Gong-Ru Lin, Taiwan
Tianxi Liu, China
Jun Liu, USA
Songwei Lu, USA
Daniel Lu, China
Jue Lu, USA
Ed Ma, USA
Gaurav Mago, USA
Santanu K. Maiti, India
Sanjay R. Mathur, Germany
V. Mittal, UAE
Weihai Ni, Germany
Sherine Obare, USA
Atsuto Okamoto, Japan
Abdelwahab Omri, Canada
Edward A. Payzant, USA
Kui-Qing Peng, China
Anukorn Phuruangrat, Thailand
Mahendra Rai, India
Suprakas Sinha Ray, South Africa
Ugur Serincan, Turkey
Huaiyu Shao, Japan
Donglu Shi, USA
V. Sivakov, Germany
M. Striccoli, Italy
Bohua Sun, South Africa
Saikat Talapatra, USA
Nairong Tao, China

T. Thongtem, Thailand
S. Thongtem, Thailand
Alexander Tolmachev, Ukraine
Valeri P. Tolstoy, Russia
Tsung-Yen Tsai, Taiwan
Takuya Tsuzuki, Australia
Raquel Verdejo, Spain
Mat U. Wahit, Malaysia
Zhenbo Wang, China
Ruiping Wang, Canada
Shiren Wang, USA
Cheng Wang, China
Yong Wang, USA
Jinquan Wei, China
Ching-Ping Wong, Hong Kong
Xingcai Wu, China
Guodong Xia, Hong Kong
Ping Xiao, UK
Zhi Li Xiao, USA
Yangchuan Xing, USA
Shuangxi Xing, China
Nanping Xu, China
Doron Yadlovker, Israel
Yingkui Yang, China
Khaled Youssef, USA
Kui Yu, Canada
William W. Yu, USA
Haibo Zeng, China
Tianyou Zhai, China
Renyun Zhang, Sweden
Bin Zhang, China
Yanbao Zhao, China
Lianxi Zheng, Singapore
Chunyi Zhi, Hong Kong

Contents

The Potential of Nanomaterials for Drug Delivery, Cell Tracking, and Regenerative Medicine 2013, Krasimir Vasilev, Haifeng Chen, and Patricia Murray
Volume 2014, Article ID 872681, 2 pages

Nanocomposites of Polyacrylic Acid Nanogels and Biodegradable Polyhydroxybutyrate for Bone Regeneration and Drug Delivery, Mikael Larsson, Anna Bergstrand, Lilyan Mesiah, Celine Van Vooren, and Anette Larsson
Volume 2014, Article ID 371307, 9 pages

Nanotechnological Advances in Cutaneous Medicine, Jessica E. Jackson, Zlatko Kopecki, and Allison J. Cowin
Volume 2013, Article ID 808234, 8 pages

Emerging Stem Cell Controls: Nanomaterials and Plasma Effects, F. F. Borghi, A. E. Rider, S. Kumar, Z. J. Han, D. Haylock, and K. Ostrikov
Volume 2013, Article ID 329139, 15 pages

Release Kinetics and Antibacterial Efficacy of Microporous β -TCP Coatings, Michael Seidenstuecker, Yahya Mrestani, Reinhard H. H. Neubert, Anke Bernstein, and Hermann O. Mayr
Volume 2013, Article ID 842951, 8 pages

Nanoparticle-Based Drug Delivery for Therapy of Lung Cancer: Progress and Challenges, Anish Babu, Amanda K. Templeton, Anupama Munshi, and Rajagopal Ramesh
Volume 2013, Article ID 863951, 11 pages

Magnetic and Structural Studies of CoFe_2O_4 Nanoparticles Suspended in an Organic Liquid, Branka Babić-Stojić, Vukoman Jokanović, Dušan Milivojević, Zvonko Jagličić, Darko Makovec, Nataša Jović, and Milena Marinović-Cincović
Volume 2013, Article ID 741036, 9 pages

pH Responsive Self-Assembly of Cucurbit[7]urils and Polystyrene-Block-Polyvinylpyridine Micelles for Hydrophobic Drug Delivery, Basem A. Moosa, Afnan Mashat, Wengang Li, Karim Fhayli, and Niveen M. Khashab
Volume 2013, Article ID 719168, 6 pages

Development of Lecithin Nanoemulsion Based Organogels for Permeation Enhancement of Metoprolol through Rat Skin, J. Varshosaz, S. Andalib, M. Tabbakhian, and N. Ebrahimzadeh
Volume 2013, Article ID 139437, 10 pages

***In Vivo* Study of Ligament-Bone Healing after Anterior Cruciate Ligament Reconstruction Using Autologous Tendons with Mesenchymal Stem Cells Affinity Peptide Conjugated Electrospun Nanofibrous Scaffold**, Jingxian Zhu, Xin Zhang, Zhenxing Shao, Linghui Dai, La Li, Xiaoqing Hu, Xiaokun Wang, Chunyan Zhou, and Yingfang Ao
Volume 2013, Article ID 831873, 11 pages

Enhanced Ca²⁺ Entry and Tyrosine Phosphorylation Mediate Nanostructure-Induced Endothelial Proliferation, Michaela Schernthaner, Gerd Leitinger, Heimo Wolinski, Sepp D. Kohlwein, Bettina Reisinger, Ruxandra-A. Barb, Wolfgang F. Graier, Johannes Heitz, and Klaus Groschner
Volume 2013, Article ID 251063, 10 pages

Novel Caffeic Acid Nanocarrier: Production, Characterization, and Release Modeling, Milad Fathi, Maryam Mirlohi, Jaleh Varshosaz, and Golnoosh Madani
Volume 2013, Article ID 434632, 9 pages

Restoration of Critical-Sized Defects in the Rabbit Mandible Using Autologous Bone Marrow Stromal Cells Hybridized with Nano- β -tricalcium Phosphate/Collagen Scaffolds, Xuehui Zhang, Mingming Xu, Xinggang Liu, Feng Zhang, Yan Wei, Song Meng, Xiaohan Dai, Aizhu Duan, and Xuliang Deng
Volume 2013, Article ID 913438, 8 pages

Polymeric Nanosuspensions for Enhanced Dissolution of Water Insoluble Drugs, Roya Yadollahi, Krasimir Vasilev, Clive A. Prestidge, and Spomenka Simovic
Volume 2013, Article ID 170201, 10 pages

Fabrication of Conductive Polypyrrole Nanofibers by Electrospinning, Yiqun Cong, Shize Liu, and Haifeng Chen
Volume 2013, Article ID 148347, 6 pages

Microfluidic Device for Controllable Chemical Release via Field-Actuated Membrane Incorporating Nanoparticles, Xiang Wang, Shunbo Li, Limu Wang, Xin Yi, Yu Sanna Hui, Jianhua Qin, and Weijia Wen
Volume 2013, Article ID 864584, 6 pages

***In Vitro* Evaluation of Cytotoxicity of Colloidal Amorphous Silica Nanoparticles Designed for Drug Delivery on Human Cell Lines**, Venugopal Balakrishnan, Hajarul Azwana Ab Wab, Khairunisak Abdul Razak, and Shaharum Shamsuddin
Volume 2013, Article ID 729306, 8 pages

Effects of Polymeric Additives on the Crystallization and Release Behavior of Amorphous Ibuprofen, Su Yang Lee, Guiduk Yu, and Il Won Kim
Volume 2013, Article ID 503069, 7 pages

Editorial

The Potential of Nanomaterials for Drug Delivery, Cell Tracking, and Regenerative Medicine 2013

Krasimir Vasilev,^{1,2} Haifeng Chen,³ and Patricia Murray⁴

¹ Mawson Institute, University of South Australia, Mawson Lakes, SA 5095, Australia

² School of Advanced Manufacturing, University of South Australia, Mawson Lakes, SA 5095, Australia

³ Department of Biomedical Engineering, College of Engineering, Peking University, Beijing 100871, China

⁴ Institute of Translational Medicine, The University of Liverpool, Liverpool L69 3GE, UK

Correspondence should be addressed to Krasimir Vasilev; krasimir.vasilev@unisa.edu.au

Received 3 February 2014; Accepted 3 February 2014; Published 9 March 2014

Copyright © 2014 Krasimir Vasilev et al. This is an open access article distributed under the Creative Commons Attribution License, which permits unrestricted use, distribution, and reproduction in any medium, provided the original work is properly cited.

Nanomaterials are already revolutionizing medical treatments and diagnostics and could have the potential to diagnose and treat various life-threatening diseases. Well advanced technologies that have become possible, thanks to the properties of materials at the nanoscale, are the application of magnetic and gadolinium oxide nanoparticles in MRI imaging, magnetic immunoassays, magnetic hyperthermia, the use of drug nanosuspensions to improve drug dissolution and bioavailability, and many others. Various nanoscale carriers have been developed and are currently being explored for targeted delivery of therapeutics in order to increase the efficacy of the drugs and eliminate problems such as systemic toxicity. Nanoengineered scaffolds produced by various traditional and innovative techniques may give the opportunity to regenerate tissues and organs. The potential of nanoscale systems to bring healthcare treatments to a new dimension has galvanized research in this field and new applications are being reported almost every week. The aim of this special issue is to present some of the exciting new developments in the field, highlight current challenges, and point towards future directions.

This special issue contains a collection of excellent contributions from established laboratories around the world. It contains instructive reviews and original research articles dealing with the diverse areas that are the subject of this special issue.

Three excellent reviews were published in this special issue. These reviews present comprehensive summaries of the

recent developments in the particular field, critical assessment of published literature, and the authors' prospective of the future directions. A review from the group of K. Ostrikov deals with the challenges associated with controlling the behavior of stem cells. The review focuses on using plasma-based techniques for the manufacturing and modification of tailored nanostructured surfaces for stem cell control. The review also provides the authors' views on the links between plasma physics, materials science, nanoscience, and stem cell biology. Another excellent review by J. E. Jackson et al. focuses on the use of nanoparticles as novel drug carriers in wound repair and regeneration. The authors' motivation for writing this review is the growing number of antibiotic-resistant bacteria, in conjunction with an increase in population age and clinical obesity that urgently requires novel, more efficient methods for wound care. The review critically discusses the advantages and limitations of nanotechnology for the treatment of wounds and other cutaneous disorders. Another review published in the special issue focuses on nanoparticle-based drug delivery for treating lung cancer. This review summarizes current progress in nanoparticle-based drug delivery systems that target lung cancer treatment. The review further outlines the challenges in the areas of pharmacology, toxicology, immunology, large-scale manufacturing, and regulatory issues that hinder the transition of these new therapies from the bench to the bedside.

Fourteen quality research articles were selected for publication in this special issue. Several of these articles tackle

problems related to drug delivery and offer innovative solutions. M. Fathi et al. present novel caffeic acid nanocarriers. The problems with improving the solubility of poorly soluble drugs through nanosuspensions are addressed by R. Yadollahi et al. In another article, X. Wang and coworkers report a novel magnetic-membrane-based microfluidic platform for controllable release. pH responsive polymeric micelles for delivery of hydrophobic drug are described by B. A. Moosa et al. Infections are an important problem with medical treatments. An article by M. Seidenstuecker et al. is focused on the release kinetics and antibacterial efficacy of microporous β TCP coatings. B. M. Sahoo et al. report on the microwave enhanced drug synthesis as an enabling technology to synthesize potential antimicrobial agents. The special issue also contains articles presenting novel opportunities for regenerative medicine. An *in vivo* study on the use of electrospun nanofibrous scaffolds for ligament-bone healing is provided by J. Zhu et al. The group of Y. Cong from Peking University reports on the fabrication of conductive polypyrrole nanofibers by electrospinning. M. Larsson et al. report on novel “*Nanocomposites of polyacrylic acid nanogels and biodegradable polyhydroxybutyrate for bone regeneration and drug delivery.*” The special issue also contains an interesting article entitled “*Magnetic and structural studies of CoFe_2O_4 nanoparticles suspended in an organic liquid.*” The authors suggest that these nanoparticles can be of interest for medical imaging. Surface properties have been recognized as important mediators of cellular behavior. The role of substrate topography in endothelial cell proliferation is elucidated in an article entitled “*Enhanced Ca^{2+} entry and tyrosine phosphorylation mediate nanostructure-induced endothelial proliferation.*” The issues of potential hazards associated with the use of nanomaterials in medicine are also embedded in the special issue via an article by V. Balakrishnan et al. entitled “*In vitro evaluation of cytotoxicity of colloidal amorphous silica nanoparticles designed for drug delivery on human cell lines.*”

Acknowledgments

The editorial team would like to thank all authors for their excellent contributions. This special issue would not have been of such quality without the constructive criticism of the reviewers. We gratefully acknowledge all colleagues who contributed to the peer review process. We also acknowledge the great support and assistance of the publishing team of the Journal of Nanomaterials. Krasimir Vasilev would also like to thank the Australian Research Council for fellowship FT100100292 which allowed him the time to edit this special issue. Haifeng Chen thanks the support from the Ministry of Science and Technology of China (Grants 2012CB933903). Patricia Murray acknowledges support from the UK Engineering and Physical Sciences Research Council (EP/H046143/1).

*Krasimir Vasilev
Haifeng Chen
Patricia Murray*

Research Article

Nanocomposites of Polyacrylic Acid Nanogels and Biodegradable Polyhydroxybutyrate for Bone Regeneration and Drug Delivery

Mikael Larsson,^{1,2,3} Anna Bergstrand,^{1,3} Lilyan Mesiah,¹
Celine Van Vooren,¹ and Anette Larsson^{1,3}

¹ Department of Chemical and Biological Engineering, Chalmers University of Technology, 41296 Gothenburg, Sweden

² Ian Wark Research Institute, University of South Australia, Mawson Lakes Campus, Mawson Lakes, SA 5095, Australia

³ SuMo BIOMATERIALS, VINN Excellence Center at Chalmers University of Technology, 41296 Gothenburg, Sweden

Correspondence should be addressed to Mikael Larsson; larsson.mikael@gmail.com

Received 26 July 2013; Accepted 22 October 2013; Published 16 January 2014

Academic Editor: Haifeng Chen

Copyright © 2014 Mikael Larsson et al. This is an open access article distributed under the Creative Commons Attribution License, which permits unrestricted use, distribution, and reproduction in any medium, provided the original work is properly cited.

Biodegradable cell scaffolds and local drug delivery to stimulate cell response are currently receiving much scientific attention. Here we present a nanocomposite that combines biodegradation with controlled release of lithium, which is known to enhance bone growth. Nanogels of lithium neutralized polyacrylic acid were synthesized by microemulsion-templated polymerization and were incorporated into a biodegradable polyhydroxybutyrate (PHB) matrix. Nanogel size was characterized using dynamic light scattering, and the nanocomposites were characterized with regard to structure using scanning electron microscopy, mechanical properties using tensile testing, permeability using tritiated water, and lithium release in PBS using a lithium specific electrode. The nanogels were well dispersed in the composites and the mechanical properties were good, with a decrease in elastic modulus being compensated by increased tolerance to strain in the wet state. Approximately half of the lithium was released over about three hours, with the remaining fraction being trapped in the PHB for subsequent slow release during biodegradation. The prepared nanocomposites seem promising for use as dual functional scaffolds for bone regeneration. Here lithium ions were chosen as model drug, but the nanogels could potentially act as carriers for larger and more complex drugs, possibly while still carrying lithium.

1. Introduction

To introduce additional functionality in a biodegradable polyhydroxybutyrate (PHB) matrix, polyacrylic acid (PAA) nanogels were incorporated to form a hybrid solid-gel nanocomposite. This highly designed material structure approach is in line with recent developments in the biomaterials field.

Biodegradable materials have long been investigated for use in tissue engineering and drug delivery, as seen from literature [1–3], but attention has turned towards structured and/or multifunctional materials [3, 4]. One material class that has been widely investigated for use in biomedical applications is polyhydroxyalkanoates (PHA), as it incorporates a range of naturally occurring biocompatible aliphatic

polyesters, including PHB [5]. The characteristics and material properties of different PHA vary greatly, for example, mechanical properties and degradation rates can be tailored by the monomer composition [2, 3, 5]. When it comes to PHB it has a strong tendency for crystallization [5] and has a slow biodegradation rate compared to most biodegradable polyesters [6]. With regard to mechanical properties it is hard and brittle, where the brittleness is a disadvantage [5], and copolymers/composites may be better suited for biomedical applications [2, 5]. Nonetheless, PHB is generally nontoxic [5], likely because the polymer and its final degradation products are naturally occurring in humans [7, 8], and has been investigated for use in bone tissue engineering [2, 5, 9–11] and nerve scaffolding [12–14], among other applications. Recently there have been reports on creating nano-microporous PHB

matrixes using an aqueous emulsion as template for the voids in the material [6, 15].

PAA is an anionic polyelectrolyte that is easily polymerized and crosslinked into macroscopic hydrogels that can swell hundreds of times their dry weight, especially when the acid protons are neutralized with sodium [16]. PAA is a pharmaceutically used excipient also known under the name Carbopol [17]. There have been numerous studies on the use of PAA as a component in materials for biomedical applications, both because of its high swelling capability and because the polyanionic charge allows for easy loading of cationic molecules. In the last decade, there have been some reports on the preparation of PAA nanogels [18–20], and such nanogels have been investigated as drug carriers [18, 19]. Based on available literature on PHB, PAA nanogels, and other materials where nanodrug carriers have been incorporated in a macroscopic matrix [21–23], we recognized that if PAA nanogels could be synthesized and incorporated into PHB matrixes, then they could provide additional functionality to the materials by acting as drug carriers and possibly also altering the mechanical properties for beneficial effects. However, rather than incorporating conventional drugs into the PAA nanogels, as already proven possible, the very small monovalent cation lithium was chosen as a model substance. Lithium has been shown to activate the Wnt-signaling pathway [24, 25], leading to accumulation of β -catenin protein [25], a protein that in turn positively regulates osteoblasts [26], which clearly is of interest for bone-tissue engineering. In fact, lithium has been shown to increase bone mass and improve fracture healing in mice/rats [24, 26, 27]. Given the interest in PHB for bone-tissue regeneration lithium is a relevant choice as model drug; in addition, if controlled release is possible for lithium it will surely be possible for larger cationic drugs, especially if polyvalent.

In this study, we report on the successful preparation of drug loaded PHB-PAA nanogel composite films with designed structure, controlled release of lithium, and improved mechanical properties.

2. Materials and Methods

2.1. Materials. Acetone, acrylic acid anhydrous, chloroform puriss p.a, lithium hydroxide, N,N'-methylenebisacrylamid (MBA), poly-[(R)-3-hydroxybutyric acid] (PHB), polysorbate 80, poly[(R)-3-hydroxybutyric acid], potassium persulfate, Span 80, and N,N,N',N'-Tetramethylethylenediamine (TEMED) were purchased from Sigma Aldrich. Hexane was purchased from Fischer scientific. Milli-Q (Millipore) water was used throughout the experiments.

2.2. Preparation of Lithium Loaded PAA Nanogels by Reverse Microemulsion Polymerization. Adapted from work by others [18, 19], the following method was used for PAA nanogel preparation. In a vial 3.43 g Span 80 and 2.62 g Tween 80 were added, followed by 100 mL hexane (oil phase). The flask was capped and the content mixed with a magnetic stirrer so that tween and span were fully dissolved. The aqueous phase was prepared as follows: 1.5 mL of 10% (w/w) LiOH in H₂O

was added to 500 μ L acrylic acid. Subsequently, using H₂O as solvent, 214 μ L of 5% (w/v) MBA suspension, 500 μ L 2% (w/v) potassium persulfate, and 40 μ L of 20% (w/v) TEMED were added.

The microemulsion was formed by dropwise addition of the aqueous phase into the oil phase while a homogenizer (IKA, Taquara) was running at 14000 rpm. After the addition, the speed of the homogenizer was increased to 24000 rpm for 3 min, followed by 14000 rpm until all foam had disappeared (about 45 sec). The emulsion was transferred to a 60°C water bath and was stirred at 400 rpm using a magnetic stirrer. For the first 10 minutes the emulsion was covered with aluminum foil and bubbled with N₂, after which the vial was capped and the reaction was allowed to proceed for 6 h, after which the vial was vented, resealed, and left under stirring at room temperature overnight. For washing, product and solvent were transferred to 50 mL falcon tubes, and centrifuged at 5100 rpm for 6 h at 4°C using a Sigma 4kl5 centrifuge (Labex). The supernatants were decanted and the pellets were resuspended in acetone for a total volume of 20 mL and were centrifuged again at 5100 rpm for 10 min at 4°C, repeated three times. Finally, the pellets were re-suspended in acetone (final volume 5 mL) and mixed with magnetic stirrer overnight. The opaque dispersions were centrifuged down, the acetone was discarded, and the pellets were dispersed in 1 mL chloroform, pooled, and stored until further use and analysis.

2.3. Nanogel Size Characterization. Prior to washing samples were taken out and dispersed in H₂O. The dispersion was centrifuged, and the supernatant was diluted 100 times and filtered with a 0.20 μ m filter before analysis by dynamic light scattering (DLS) using a N4 plus submicron particle size analyzer (Beckman Coulter). The program was set to run at room temperature and measured all angles (5.7°, 11.1°, 23.0°, 30.2°, 62.6°, and 90.0°) for 6 min.

2.4. Film Preparation. Pure PHB films were prepared as follows: 560 mg PHB was dissolved in 8 mL chloroform under magnetic stirring in a 58°C water bath for 1 h. The solution was left to cool down to room temperature after which the PHB solution was poured in a glass petri dish. Film casting was performed by allowing the chloroform to evaporate without lid for 2 min before loosely covering the dish with a lid until the next day, at which point the evaporation was complete. To ensure an even evaporation, the glass petri dish had double layered tape on two edges.

PHB films containing PAA nanogels were prepared as above, with the following differences: PHB was dissolved in 6 mL chloroform, and the desired mass of PAA nanogels were mixed with 2 mL chloroform. The nanogel dispersion was then mixed with the PHB solution using a homogenizer (DII8, IKA) for 15 s, and casting was performed as for pure PHB films.

2.5. Film Structure Characterization. Dry films and freeze-dried (LABCONCO, FreeZone 6) swollen films were cut into sections to display the interior regions of the films. Before

the SEM analysis, all samples were sputter coated with gold in argon atmosphere for about 1 min using a S150B Sputter Coater (Edwards). SEM analysis was conducted using a LEO Ultra 55 SEM equipped with a field emission gun (LEO Electron Microscopy Group).

2.6. Swelling Analysis. Films were cut in 1.5×2 cm pieces. Dry weight and thickness of the pieces were recorded. The pieces were swollen in Milli-Q water or PBS buffer (pH 7.4). At pre-determined time times, excess water was removed by blotting the films on a paper and the weight and thickness of the samples were noted. The film pieces were then resubmerged. The swelling was calculated as

$$\text{Swelling degree (Q)} = \frac{W_s - W_d}{W_d}, \quad (1)$$

where W_s is the weight of the swollen sample and W_d is the dry weight.

2.7. Tensile Testing. Each film was cut into three rectangular strips using an 8.5 mm thick parallel cutter. The average thickness of each stripe was determined from three different sites. The films were mounted into the tensile tester (Instron) and were pulled until breakage while the force displacement was recorded.

2.8. Water Permeability. Film pieces were cut out, and the thickness was measured in triplicates and placed between the donor and acceptor compartment in diffusion cells. Subsequently, 50 mL of Milli-Q water was simultaneously added to the donor and acceptor compartments and $10 \mu\text{L}$ of tritiated water (400 kBq) was added to the donor compartments. During the experiment, the cells were placed on a rotating table for mixing at ambient temperature. At specified times $500 \mu\text{L}$ was extracted from the acceptor compartment and replaced with Milli-Q water. To determine the diffusive flow across the films, the tritium activity in the acceptor compartment was compared to the initial activity in the donor compartment using a liquid scintillation analyser (Tri-carb 2810 TR, Perkin Elmer). The permeability (P) of the films was calculated using the following equation:

$$\frac{2PS}{V}t = -\ln\left(\frac{C_{d,0} - 2C_a}{C_{d,0}}\right), \quad (2)$$

where S is the area through which diffusion occurs, V is the volume of the individual donor and acceptor compartments, t is the time, $C_{d,0}$ is the concentration in donor compartment at time zero, and C_a is the concentration in the acceptor compartment at time t . From a plot of $-\ln[(C_{d,0} - 2C_a)/C_{d,0}]$ versus time, P was calculated from the slope [28]. To eliminate contributions from film thickness (h), P was normalized by multiplication with h at time zero.

2.9. Lithium Release. PHB films containing 15 and 25% PAA were cut into 1.8×2 cm pieces that were subsequently immersed in 30 mL PBS buffer under stirring. At pre-determined times a calibrated ion specific electrode (ISE) for

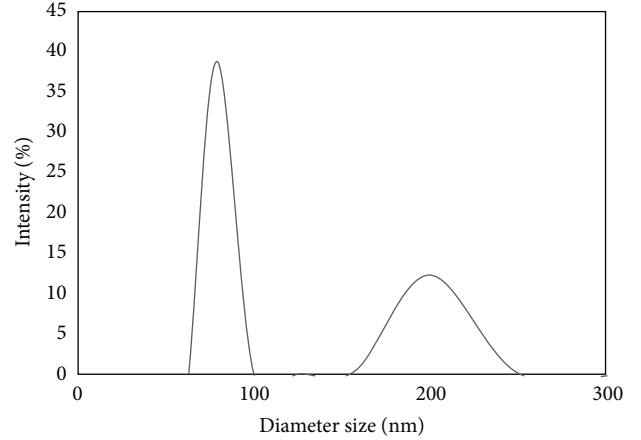


FIGURE 1: Exemplifying plot of intensity-size distribution for the nanogels in water.

TABLE 1: Average sizes and relative mass fraction, determined from DLS using the angle of 90° .

Diameter (nm)	Std. dev. (nm)	Relative mass fraction
79	5.4	3.3
200	13.7	1

lithium ions was used to measure the concentration of released lithium ions.

3. Results and Discussion

3.1. PAA Nanogel Synthesis and Characterization. Nanogels of PAA were prepared by reverse phase microemulsion polymerization. The model drug lithium was incorporated into the gels by neutralizing the carboxylic acid of the acrylic acid monomers prior to the polymerizations reaction. The condition of electroneutrality as well as the low chemical potential of lithium ions in the hydrophilic nanogels, compared to in the hydrophobic solvents used for washing, would lead to lithium remaining in the gels.

Analysis of the nanogels using DLS revealed two populations with different size, as shown in Figure 1. The average size of the two populations was about 80 nm and 200 nm, respectively. Similar results were obtained for all angles, indicating a spherical geometry of the nanogels.

From the intensity distribution the mass ratio between the two populations was calculated, recognizing that larger particles are given more weight in intensity distribution obtained from DLS. The calculations revealed that the mass fraction of nanogels in the population with smaller size was about three times the mass fraction in the population with larger size (see Table 1).

3.2. Casting of PHB-Nanogel Composite Films. Films of PHB with or without nanogels were prepared by solvent evaporation. All prepared films had thicknesses in the range of $95 \mu\text{m}$ – $150 \mu\text{m}$ and displayed a smooth surface. Pure PHB films were slightly opaque, and with increasing nanogel

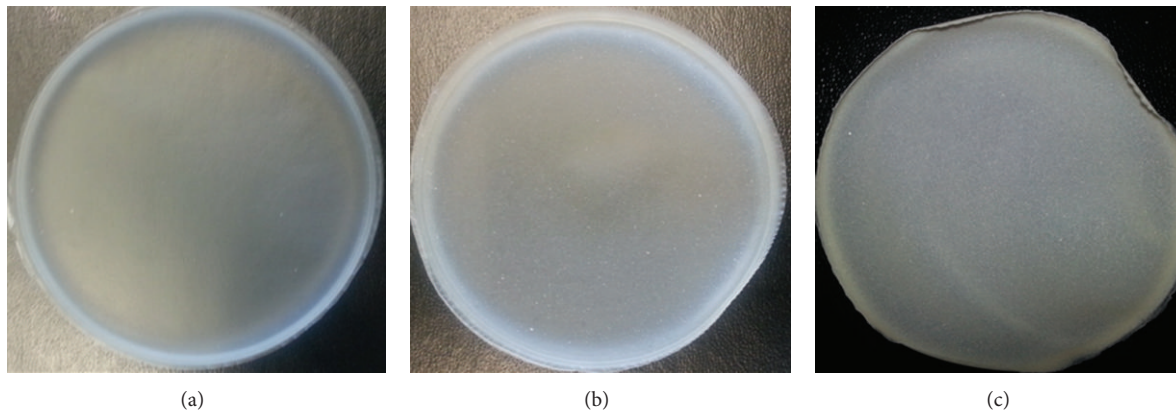


FIGURE 2: Photos of, (a) a PHB film, (b) PHB films containing 5% (w/w) PAA, and (c) PHB films containing 25% (w/w) PAA.

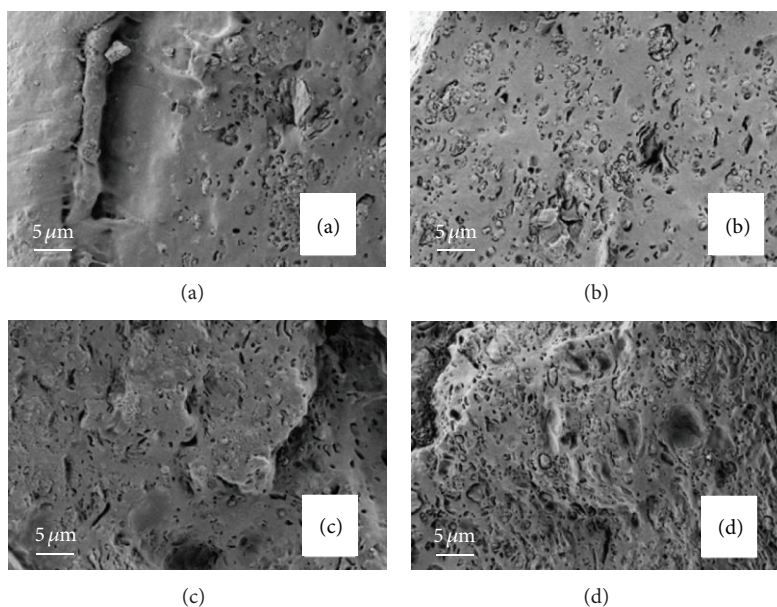


FIGURE 3: SEM micrographs showing the cross-sections of dry PHB films with different amounts of PAA nanogels: (a) PHB + 5% (w/w) PAA; (b) PHB + 10% (w/w) PAA; (c) PHB + 15% (w/w) PAA, and (d) PHB + 25% (w/w) PAA.

content the opaqueness increased, so that the films with 25% nanogels appeared close to white (Figure 2).

3.3. Morphology of the PHB-Nanogel Composite Films. To characterize the morphology of the formed nanocomposite films they were analysed using SEM. Analyses were performed both on dry films and on films swollen and subsequently freeze-dried. The dry films revealed an increasing porosity with increasing nanogel content (Figure 3).

For swollen and freeze-dried films, the trend of increasing porosity with increasing nanogel content was even more pronounced (Figure 4), not surprising given that the PAA nanogels should swell in water and delocalize the surrounding PHB to some extent. Upon freeze drying the changed structure should remain to large parts. In summary, the nanogels were well dispersed throughout the nano-composite, induced

a more porous structure, and swelled in water to further increase the porosity of the PHB matrix.

3.4. Swelling and Water Permeability of the PHB-Nanogel Composite Films. Swelling and permeability are both of relevance for biomedical applications. The swelling influences mechanical properties and mass transfer in the material, while permeability is a measurement of how easy molecules can be transported through the material.

In PBS pure PHB films displayed little swelling, but the swelling increased with increasing nanogel content. A large increase in swelling (per mass nanogel) was seen for the samples with the lowest nanogel content (5%), followed by smaller increase with additional nanogel addition (Figure 5(a)). The trend was similar for swelling in Milli-Q water but with some notable differences. The swelling of pure PHB

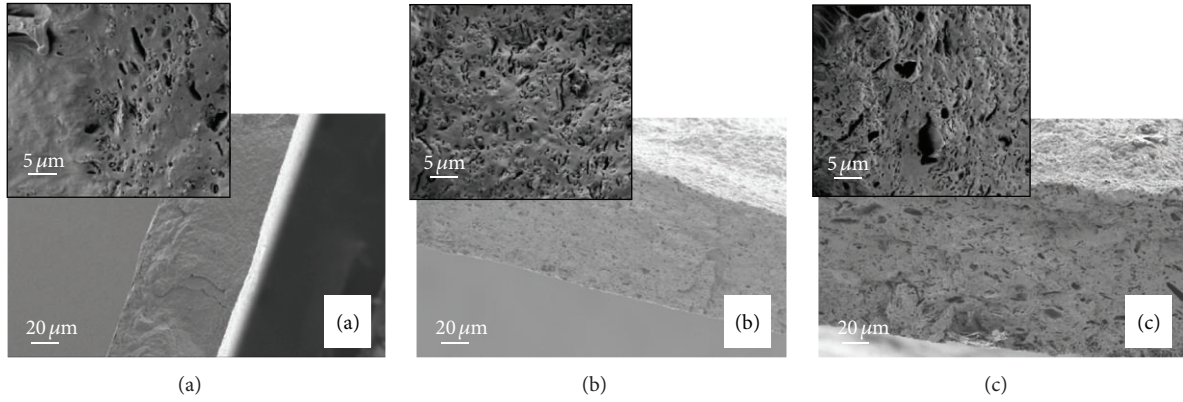


FIGURE 4: SEM micrographs showing the cross-sections of swollen and subsequently freeze-dried PHB films with different PAA nanogel content: (a) PHB; (b) PHB + 15% (w/w) PAA; (c) PHB + 25% (w/w) PAA.

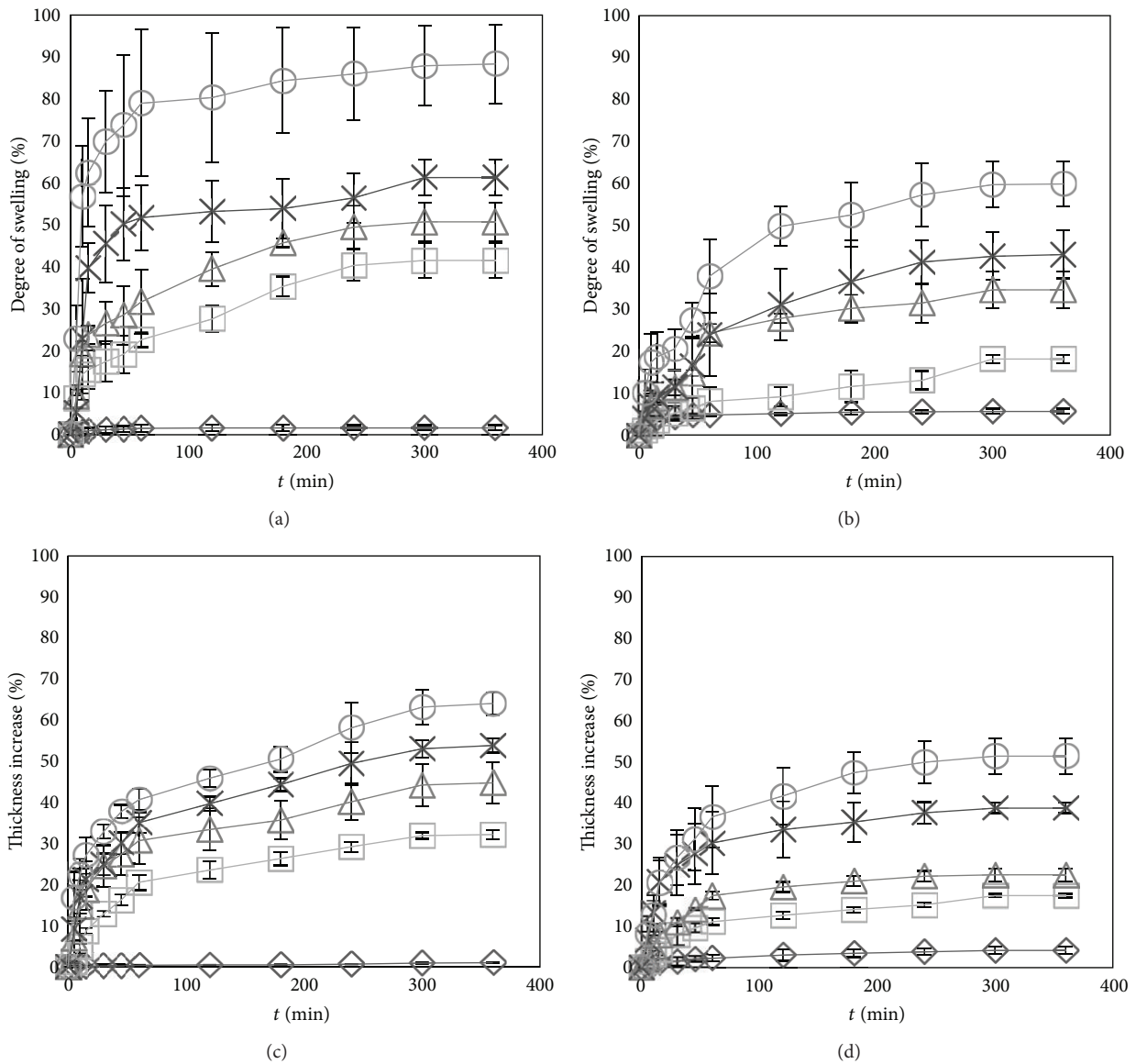


FIGURE 5: Swelling behavior of PHB films with different PAA nanogel content. (a) % mass increase in PBS buffer, (b) % mass increase in Milli-Q water, (c) % thickness increase in PBS buffer, and (d) % thickness increase in Milli-Q water. \diamond = PHB, \square = PHB + 5% PAA, Δ = PHB + 10% PAA, \times = PHB + 15% PAA, \circ = PHB + 25% PAA. Error bars indicate one standard deviation ($n = 3$).

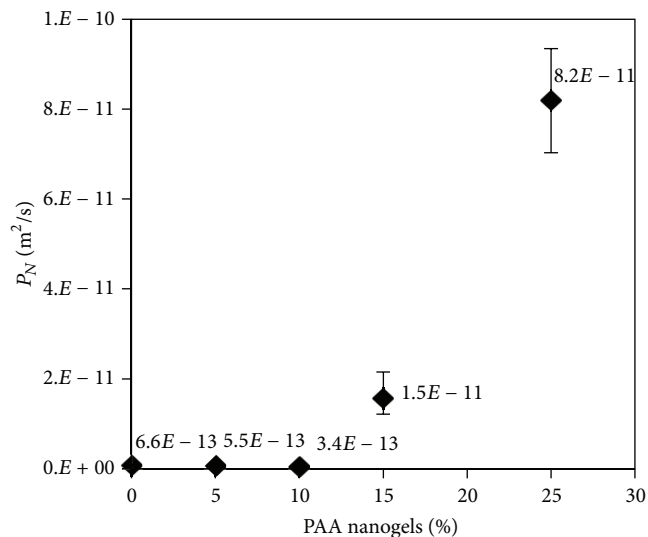


FIGURE 6: Water permeability normalized for initial film thickness for PHB films with different PAA nanogel content. Error bars indicate min/max ($n = 2-5$).

was somewhat increased in Milli-Q water, while the swelling of the composites was reduced for all nanogel contents (Figure 5(b)). To elucidate the dimensional changes upon swelling the thickness of swollen samples was measured in addition to weight. It was found that most of the swelling occurred by increasing the thickness of the samples (Figures 5(c) and 5(d)). The exact mechanisms behind the observed swelling, behaviours may be complex and merit further investigation before conclusions are drawn. However, what can be stated is that the nanogels increased the swelling of the composite and that they should exist in a swollen gel state inside submerged composites. Furthermore, since the thickness of PHB increased upon submersion in PBS the PHB did indeed swell; that is, the increase in mass was not only due to water becoming trapped in cracks and pores.

It is well known that for polymer materials the diffusion coefficient quickly increases with swelling of the material [29] and that in a composite combining regions with small and large diffusion coefficients the spatial distribution of those will influence the permeability [30]. Therefore, permeability analysis was conducted on pure PHB films and the composites. Very low permeability was observed for pure PHB films and composites with 5% and 10% nanogels, while for films with higher (15% and 25%) nanogel content the permeability increased rapidly (Figure 6). The results are explained as follows: the diffusion is slow in PHB, while it is fast in the swollen nanogels. Below a critical nanogel content there is no connectivity between them and the permeability is limited by diffusion through PHB. However, at higher nanogel concentrations they form a coherent network that percolates through the films, effectively creating channels with large diffusion coefficient, with increased permeability as a consequence. The results are in agreement with those from the SEM analysis and are highly relevant for predicting drug release behaviour of the PHB-nanogel composites. For

composites with $\leq 10\%$ nanogels drug release would likely be controlled by degradation of the PHB, while for higher nanogel content at least a fraction of the loaded drug would be released faster through diffusion.

3.5. Release of Lithium from the PHB-Nanogel Composite Films. Having established the structure and permeability of the PHB-nanogel composites, the release of lithium was investigated for nanogel contents of 15% and 25%. Composites with lower nanogel content were excluded as the permeability analysis had revealed them to only allow for very limited diffusion through them. Worth mentioning is that *in vivo* the composites with very low permeability should release nanogels and loaded drugs as the PHB degrade.

Both the composites with 15% and 25% nanogels displayed a close to linear release of lithium during the first 1.5 h, after which the drug release levelled off. At the final measuring time of 7 h the percent of lithium released from the gels was 41% and 58% for nanogel contents of 15% and 25%, respectively (Figure 7). The fact that the drug release is far from 100% indicates that a fraction of the nanogels are not part of the percolating network; thus, the release of lithium from this fraction is extremely slow, so that only the release of lithium in the percolating nanogel fraction is detected. The observation that a higher percent of lithium was released from the composites with higher nanogel content is coherent with that the fraction of nanogels belonging to the percolating network increases with nanogel content, as expected. The lithium release profiles indicate that the prepared PHB-nanogel composites can be loaded with drug for controlled diffusive release of active agents, if the nanogel content is high enough. At lower nanogel content the release will instead be determined by PHB degradation. If desired it should be possible to achieve a combination of fast diffusion controlled release and slow degradation controlled release by choosing suitable nanogel content.

3.6. Mechanical Properties of the PHB-Nanogel Composite Films. Even if PHB has been investigated with promising results for bone-tissue regeneration, it has been stated that its brittleness may limit the use of pure PHB in therapeutic applications [2, 5]. Recognizing the importance of mechanical properties in biomedical applications the PHB-nanogel composite films were analysed using tensile testing in the dry and equilibrium swollen state. With increasing nanogel content the elastic modulus (E) decreased from 1.4 GPa to 0.7 GPa and from 1 GPa to 0.5 GPa for dry and equilibrium swollen samples, respectively (Figure 8(a)). The decrease in E with nanogel addition was expected, especially in the wet state where E of the nanogel phase is very low. With regard to tolerance to extension (the percent extension at which breakage occurred) there was no conclusive effect of nanogel content for the dry samples. However, for equilibrium swollen samples tolerance to extension surprisingly increased (Figure 8(b)). This improvement in extension properties suggests that the wet nanogels interact with the PHB on a molecular level, causing plasticizing of the material.

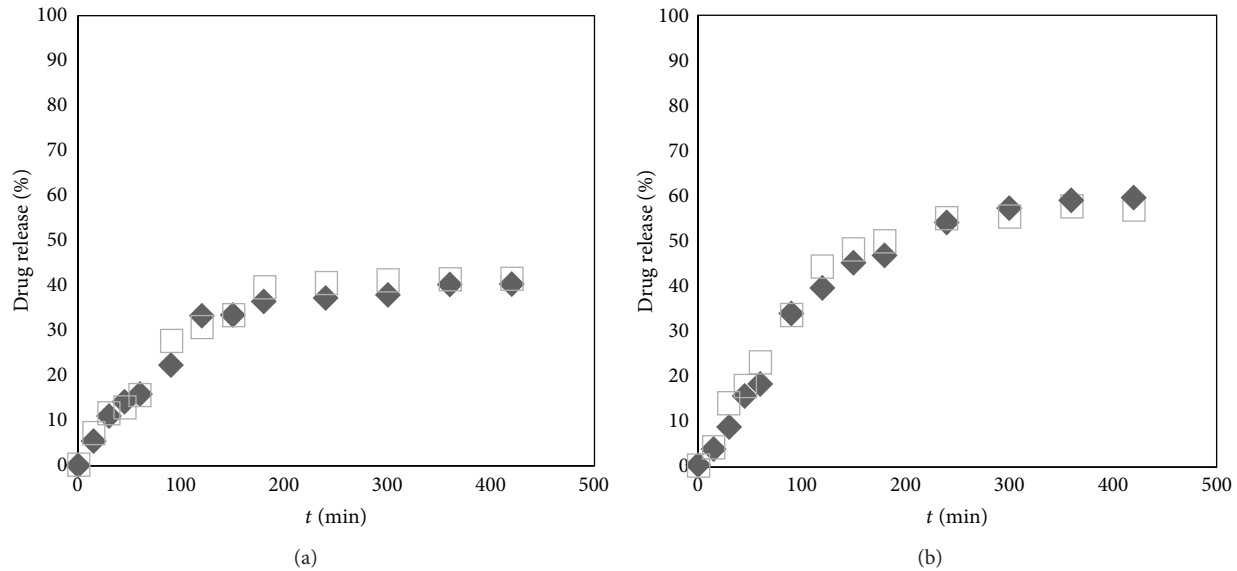


FIGURE 7: Release of lithium ions from PHB-nanogel composite films in PBS. (a) 15% (w/w) nanogels, (b) 25% (w/w) nanogels. The different markers indicate two independent experiments.

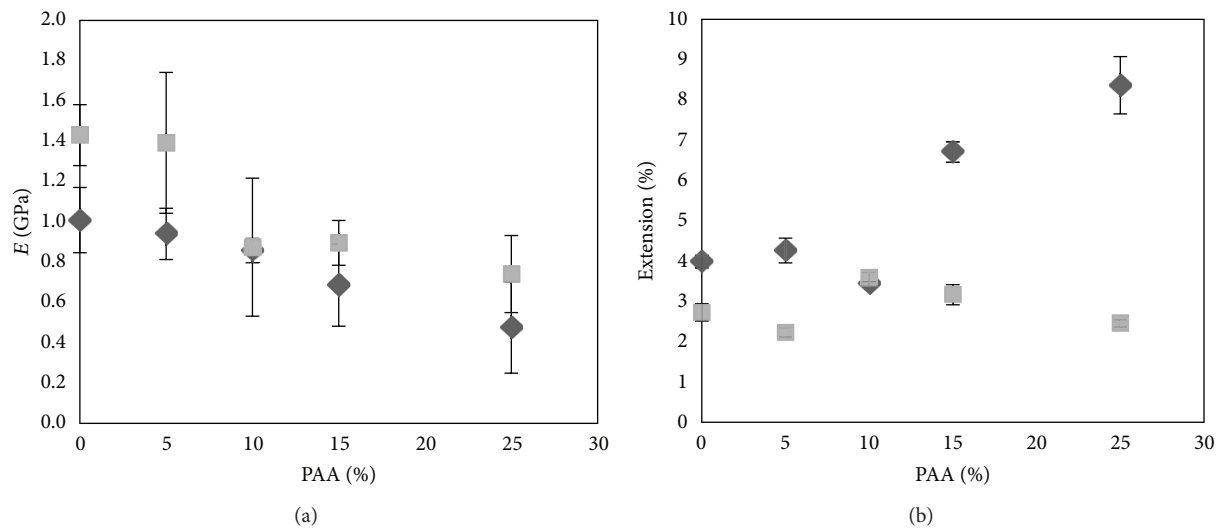


FIGURE 8: (a) Elastic modulus and (b) extension at breakage for dry (\square) and swollen (\diamond) PHB films with different PAA nanogel content. Error bars indicate one standard deviation ($n = 3$).

The results from the tensile testing revealed that the PHB-nanogel composites retained a high elastic modulus, even if decreased to about half. More importantly the composites seem to overcome the limitation of the inherent brittleness of PHB, making the composites highly interesting for therapeutic uses.

4. Conclusion

Composite films composed of PHB and PAA nanogels were prepared and characterized. The results indicate that the composites may be well suitable for biomedical uses as a biodegradable material where nanostructural design may be

used to tune drug release mechanism, from diffusion controlled to degradation controlled. Furthermore, controlled release was demonstrated for the small lithium ion which together with improved tolerance to deformation suggest the nanocomposites to be suitable for bone-tissue engineering. Lithium is a relevant therapeutic substance in itself, but even more, the fact that controlled release is achieved for the small monovalent lithium ion clearly indicates potential for delivery of more complex substances. Further investigations involving the material would involve both fundamental investigations of the mechanisms behind swelling behaviour and mechanical properties, as well as applied *in vivo* studies using lithium and other therapeutic substances.

Conflict of Interests

The authors declare that there is no conflict of interests regarding the publication of this paper.

Acknowledgments

This project was part of the VINN Excellence Centre SuMo Biomaterials (Supermolecular Biomaterials-Structure dynamics and properties). The financial support from the centre is gratefully acknowledged. Further financial support was acquired from the Swedish Research Council and from the Chalmers Bioscience Program, Chalmers University of Technology. Many thanks are due to Anders Mårtensson and Dr. Romain Bordes (Chalmers University of Technology) for assistance with SEM and DLS analyses.

References

- [1] M. Chasin and R. Langer, Eds., *Biodegradable Polymers as Drug Delivery Systems*, Marcel Dekker, New York, NY, USA, 1990.
- [2] M. I. Sabir, X. Xu, and L. Li, "A review on biodegradable polymeric materials for bone tissue engineering applications," *Journal of Materials Science*, vol. 44, no. 21, pp. 5713–5724, 2009.
- [3] Y. Yang and A. J. El Haj, "Biodegradable scaffolds—delivery systems for cell therapies," *Expert Opinion on Biological Therapy*, vol. 6, no. 5, pp. 485–498, 2006.
- [4] M. Larsson, W. C. Huang, M. H. Hsiao et al., "Biomedical applications and colloidal properties of amphiphilically modified chitosan hybrids," *Progress in Polymer Science*, vol. 38, no. 9, pp. 1307–1328, 2013.
- [5] S. K. Misra, S. P. Valappil, I. Roy, and A. R. Boccaccini, "Polyhydroxyalkanoate (PHA)/inorganic phase composites for tissue engineering applications," *Biomacromolecules*, vol. 7, no. 8, pp. 2249–2258, 2006.
- [6] A. Bergstrand, H. Andersson, J. Cramby, K. Sott, and A. Larsson, "Preparation of porous poly(3-Hydroxybutyrate) films by water-droplet templating," *Journal of Biomaterials and Nanobiotechnology*, vol. 3, no. 4, pp. 431–439, 2012.
- [7] R. N. Reusch, A. W. Sparrow, and J. Gardiner, "Transport of poly- β -hydroxybutyrate in human plasma," *Biochimica et Biophysica Acta*, vol. 1123, no. 1, pp. 33–40, 1992.
- [8] T. Saito, K. Tomita, K. Juni, and K. Ooba, "In vivo and in vitro degradation of poly(3-hydroxybutyrate) in rat," *Biomaterials*, vol. 12, no. 3, pp. 309–312, 1991.
- [9] C. Doyle, E. T. Tanner, and W. Bonfield, "In vitro and in vivo evaluation of polyhydroxybutyrate and of polyhydroxybutyrate reinforced with hydroxyapatite," *Biomaterials*, vol. 12, no. 9, pp. 841–847, 1991.
- [10] A. Zonari, S. Novikoff, N. R. P. Electo et al., "Endothelial differentiation of human stem cells seeded onto electrospun polyhydroxybutyrate/polyhydroxybutyrate-co-hydroxyvalerate fiber mesh," *PLoS ONE*, vol. 7, no. 4, Article ID e35422, 2012.
- [11] E. C. Carlo, A. P. B. Borges, R. J. Del Carlo et al., "Comparison of in vivo properties of hydroxyapatite-polyhydroxybutyrate composites assessed for bone substitution," *Journal of Craniofacial Surgery*, vol. 20, no. 3, pp. 853–859, 2009.
- [12] P.-N. Mohanna, R. C. Young, M. Wiberg, and G. Terenghi, "A composite pol-hydroxybutyrate-glia growth factor conduit for long nerve gap repairs," *Journal of Anatomy*, vol. 203, no. 6, pp. 553–565, 2003.
- [13] M. Åberg, C. Ljungberg, E. Edin et al., "Clinical evaluation of a resorbable wrap-around implant as an alternative to nerve repair: a prospective, assessor-blinded, randomised clinical study of sensory, motor and functional recovery after peripheral nerve repair," *Journal of Plastic, Reconstructive and Aesthetic Surgery*, vol. 62, no. 11, pp. 1503–1509, 2009.
- [14] M. T. Khorasani, S. A. Mirmohammadi, and S. Irani, "Polyhydroxybutyrate (PHB) scaffolds as a model for nerve tissue engineering application: fabrication and in vitro assay," *International Journal of Polymeric Materials*, vol. 60, no. 8, pp. 562–575, 2011.
- [15] C. Zhijiang, "Biocompatibility and biodegradation of novel PHB porous substrates with controlled multi-pore size by emulsion templates method," *Journal of Materials Science*, vol. 17, no. 12, pp. 1297–1303, 2006.
- [16] M. Larsson, S. Gustafsson, E. Olsson, and A. Larsson, "Effect of calcium neutralization on elastic and swelling properties of crosslinked poly(acrylic acid)—correlation to inhomogeneities and phase behaviour," *e-Polymers*, vol. 9, no. 1, pp. 1683–1696, 2013.
- [17] R. C. Rowe, P. J. Sheskey, and M. E. Quinn, Eds., *Handbook of Pharmaceutical Excipients*, Pharmaceutical Press and American Pharmacist Association, Chicago, Ill, USA, 6th edition, 2009.
- [18] T. K. De and A. S. Hoffman, "An ophthalmic formulation of a beta-adrenoceptor antagonist, levobetaxolol, using poly(acrylic acid) nanoparticles as carrier: loading and release studies," *Journal of Bioactive and Compatible Polymers*, vol. 16, no. 1, pp. 20–31, 2001.
- [19] T. K. De and A. S. Hoffman, "A reverse microemulsion polymerization method for preparation of bioadhesive polyacrylic acid nanoparticles for mucosal drug delivery: loading and release of timolol maleate," *Artificial Cells, Blood Substitutes, and Immobilization Biotechnology*, vol. 29, no. 1, pp. 31–46, 2001.
- [20] R. Melinda Molnar, M. Bodnar, J. F. Hartmann, and J. Borbely, "Preparation and characterization of poly(acrylic acid)-based nanoparticles," *Colloid and Polymer Science*, vol. 287, no. 6, pp. 739–744, 2009.
- [21] M. H. Hsiao, M. Larsson, A. Larsson et al., "Design and characterization of a novel amphiphilic chitosan nanocapsule-based thermo-gelling biogel with sustained in vivo release of the hydrophilic anti-epilepsy drug ethosuximide," *Journal of Controlled Release*, vol. 161, no. 3, pp. 942–948, 2012.
- [22] L.-J. Lin, M. Larsson, and D.-M. Liu, "A novel dual-structure, self-healable, polysaccharide based hybrid nanogel for biomedical uses," *Soft Matter*, vol. 7, no. 12, pp. 5816–5825, 2011.
- [23] L. Zhao, L. Zhu, F. Liu et al., "pH triggered injectable amphiphilic hydrogel containing doxorubicin and paclitaxel," *International Journal of Pharmaceutics*, vol. 410, no. 1–2, pp. 83–91, 2011.
- [24] P. Clément-Lacroix, M. Ai, F. Morvan et al., "Lrp5-independent activation of Wnt signaling by lithium chloride increases bone formation and bone mass in mice," *Proceedings of the National Academy of Sciences of the United States of America*, vol. 102, no. 48, pp. 17406–17411, 2005.
- [25] C. M. Hedgepeth, L. J. Conrad, J. Zhang, H.-C. Huang, V. M. Y. Lee, and P. S. Klein, "Activation of the Wnt signaling pathway: a molecular mechanism for lithium action," *Developmental Biology*, vol. 185, no. 1, pp. 82–91, 1997.
- [26] Y. Chen, H. C. Whetstone, A. C. Lin et al., "Beta-catenin signaling plays a disparate role in different phases of fracture repair: implications for therapy to improve bone healing," *PLoS Medicine*, vol. 4, no. 7, article e249, 2007.

- [27] F. Kugimiya, H. Kawaguchi, S. Ohba et al., "GSK-3 β controls osteogenesis through regulating Runx2 activity," *PLoS ONE*, vol. 2, no. 9, article e837, 2007.
- [28] G. Van den Mooter, C. Samyn, and R. Kinget, "Characterization of colon-specific azo polymers: a study of the swelling properties and the permeability of isolated polymer films," *International Journal of Pharmaceutics*, vol. 111, no. 2, pp. 127–136, 1994.
- [29] L. Masaro and X. X. Zhu, "Physical models of diffusion for polymer solutions, gels and solids," *Progress in Polymer Science*, vol. 24, no. 5, pp. 731–775, 1999.
- [30] M. Larsson, J. Hjártstam, and A. Larsson, "Novel nanostructured microfibrillated cellulose-hydroxypropyl methylcellulose films with large one-dimensional swelling and tunable permeability," *Carbohydrate Polymers*, vol. 88, no. 2, pp. 763–771, 2012.

Review Article

Nanotechnological Advances in Cutaneous Medicine

Jessica E. Jackson, Zlatko Kopecki, and Allison J. Cowin

Centre for Regenerative Medicine, Mawson Institute, Division of ITEE, University of South Australia, Mawson Lakes, Adelaide SA5095, Australia

Correspondence should be addressed to Allison J. Cowin; allison.cowin@unisa.edu.au

Received 4 September 2013; Accepted 27 October 2013

Academic Editor: Krasimir Vasilev

Copyright © 2013 Jessica E. Jackson et al. This is an open access article distributed under the Creative Commons Attribution License, which permits unrestricted use, distribution, and reproduction in any medium, provided the original work is properly cited.

Wound healing is an area of unmet clinical need. Current treatments include occlusive dressings, hydrogels, and antimicrobials to control infection. However with the growing number of antibiotic-resistant bacteria and the increase in population age and clinical obesity, it is becoming proportionally harder to treat wounds with the drugs that have worked in the past. There is an urgent requirement for efficient mechanism-based treatments and more efficacious drug delivery systems. The potential of using nanoparticles as a drug delivery system has been identified and investigated. Nanoparticles have the ability to protect and carry drugs to specific targets in the body, enabling slower degradation, enhancing drug penetration, improving treatment efficacy with lower systemic absorption, and reducing unwanted side effects. Here we discuss the advantages and limitations of nanotechnology for the treatment of wounds and other cutaneous disorders.

1. Introduction

The skin is the largest organ in the body and is the first line of defence against invading pathogens. The primary function of the skin is to act as a protective barrier against the environment as any large insult or loss of skin integrity can lead to disability or death [1, 2]. Adult cutaneous wound healing is a complicated process involving a cascade of events and interactions between numerous cells and cell mediators [3, 4]. This process aims to restore the complete skin barrier function quickly, often at the expense of correct anatomical repair [5]. There are several dressings and devices currently available on the medical wound care market impregnated with a range of compounds which aim to optimise the wound healing environment, providing faster, more efficient wound healing [6]. There are, however, many limitations with using these dressings in clinical practice including poor skin penetration, low stability, and localised side effects. Consequently, there is a need for the development of novel and more efficient drug-delivery systems [7]. The advent of nanotechnologies has the potential to fulfil this and the design and implementation of target-selective, time-controlled drug delivery systems for cutaneous healing and regenerative medicine now exists [8, 9].

While naturally occurring nanoporous minerals have been used on an industrial scale as effective catalysts for decades, today there are a number of different substances used for the production of nanoporous materials including carbon, silicon, silicates, ceramics, metals, various polymers, metallic minerals, and compounds of organic materials [10]. The use of micro- and nanotechnology is becoming more frequent in biomedical science, both in the development of diagnostics and in clinical therapies. Development of novel therapies in cutaneous healing has been greatly facilitated by the discovery of novel nanomaterials including nanoparticles, nanotubes, nanoengineered scaffolds, and nanoscale surface modifications [11]. The use of this technology has the potential to increase drug efficacy and decrease adverse effects by delivering specific quantities of drugs to specific target sites over a determined period of time. Nanomaterials are currently being investigated for their applications in cutaneous wound healing and their potential uses include molecule delivery, nanofibres for tissue scaffolds and surface modification for implantable materials [12]. Nanotherapy is manipulation of matter, at an atomic or molecular scale, used for delivery of therapeutic agents to tissues *in vivo* [13]. The main examples of nanotherapy being developed for use in cutaneous medicine include solid lipid nanoparticles, which are

nanoparticles made of lipids and lipid blends, and nanostructured lipid carriers, a second generation of smarter drug carrier systems made up of physiological, biodegradable, and biocompatible lipid materials and surfactants. These are both currently accepted as applicable routes for the delivery of drugs *in vivo* [14, 15]. The aim of this paper is to review the potential of nanomaterials for the improvement of cutaneous healing, while comparing current clinical therapies to developing ones and assessing the strengths and limitations of both.

2. Transcutaneous Delivery of Nanoparticles

Penetration of nanoparticles through intact skin is a controversial topic and has been a major focus of research in both the pharmaceutical and cosmetic industry examining the transcutaneous delivery of both nonbiodegradable and biodegradable nanomaterials [16]. Titanium dioxide (TiO₂) and zinc oxide (ZnO) are two of the most widely characterized nonbiodegradable nanoparticles studied in this regard due to their wide use in both sunscreens and cosmetics. There are, however, conflicting studies reporting on the epidermal penetration of titanium dioxide and its accumulation in several major organs. This has raised safety and toxicity concerns due to oxidative stress induced by deposited nanoparticles after prolonged dermal exposure [13, 17]. In recent years, however, developments in nanotechnology have highlighted the potential use of biodegradable nanoparticles including liposomes, niosomes, nanosized emulsions, and solid lipid nanoparticles as the carrier systems for drug delivery through the protective stratum corneum [18]. Solid lipid nanoparticles (SLN) are a new generation of nanoparticulate active-substance vehicles with advantages of controlled release, low irritation, and protection of active compounds [19]. Their small particle size ensures close contact with the stratum corneum and improved penetration of the encapsulated agent through the skin layers [20]. The complete biodegradation of lipid nanoparticles and their biocompatible chemical nature has highlighted lipid nanoparticles as “nanosafe carriers” for topical drug delivery with studies examining their use for delivery of glucocorticoids (prednicarbate, betamethasone, and prednisolone) and nonsteroidal anti-inflammatory drugs (indomethacin, celecoxib, ketoprofen, ketorolac, flurbiprofen) for potential treatment of acne, skin mycoses, atopic dermatitis, and psoriasis [21].

The efficacy of topically applied drugs used in clinical dermatology is determined by their mechanism of action and their ability to pass through the protective skin barrier. Drug permeation through the skin occurs via the passive diffusion of drugs through the transepidermal or transappendageal route [13]. In contrast, transcutaneous delivery of nanoparticles is dependent on a number of factors including desquamation rate of stratum corneum, permeation pathway, and the size of nanoparticles [22]. The majority of studies to date suggest that nanoparticles only permeate the superficial layers of the skin *in vivo* and remain in the stratum corneum, while only a few studies suggest full epidermal penetration and dermal absorption. It is generally accepted that nanoparticles

do not diffuse across the basement membrane and their deposition in the skin occurs through follicular penetration (Figure 1(a)) [18]. In the context of clinical dermatology, controlled drug delivery and release via the hair follicles using nanoparticles offer an exciting opportunity for therapy development as hair follicles are surrounded by capillaries and antigen presenting cells, are associated with the sebaceous glands, and are the host of stem cells in the bulge region of the hair follicle [23]. Consequently delivery of drugs, proteins, or antibodies to the epidermis through follicular penetration offers novel avenues of therapy development for number of dermatological conditions where patients still have intact skin eg eczema, psoriasis, mycoses and atopic dermatitis (further discussed in Section 4 and Table 1).

One area of current research focus is the potential use of nanoparticles for noninvasive transcutaneous immunisation. Compared to microparticles which cannot penetrate the skin to the extent that would allow the application of the required dose of antigen nanoparticles, delivery through the follicular pathway has been shown to penetrate deeper into the hair follicle than molecules in solution, help stabilize the protein based antigens, and can improve and modulate immune response [40]. This particular route of drug/vaccine delivery is particularly important for immunocompromised patients including the elderly, patients with poor wound healing, and young children [41]. Studies by Mittal et al. demonstrate an effective needle-free application of vaccines across the skin by delivery of polymeric nanoparticles using ovalbumin antigen and a double emulsion nanotechnology method using pharmaceutically biocompatible and biodegradable polymers poly(lactide-co-glycolide) (PLGA) or chitosan-coated PLGA (Chit-PLGA) demonstrating increased protection from cleavage and functional biological activity of the antigen [41]. In addition, epidermal permeation of nanoparticles has also been reported following mechanical stress including the use of harsh vehicles or skin damage following needle puncture or wounding [13].

Transcutaneous delivery of nanoparticles and dermal absorption of drugs, proteins, or antibodies to patients suffering from chronic inflamed wounds or nonhealing ulcers are not hindered by the protective skin barrier as those patients have large open wounds. For patients with open wounds, treatments can be delivered using nanotechnology by incorporating drug carrying nanoparticles into dressings or hydrogels allowing controlled sustained release of nanoparticles to the dermis (Figure 1(b)). Preliminary *in vitro* and *in vivo* studies have shown that both solid lipid nanoparticle and nanostructured lipid carrier hydrogels can be used to successfully deliver flurbiprofen to skin with sustainable and controlled drug delivery over 24 hrs with functional anti-inflammatory effects on the tissue [30]. Current research developments are focused on designing biodegradable dressings and dermal scaffolds incorporating nanoparticle delivery systems for the controlled release of drugs, proteins, and antibodies to open wounds *in vivo*.

The use of antibody based therapy for treatment of cutaneous diseases has been demonstrated previously with Infliximab (trade name Remicade), a monoclonal antibody against tumour necrosis factor alpha (TNF- α) used to treat

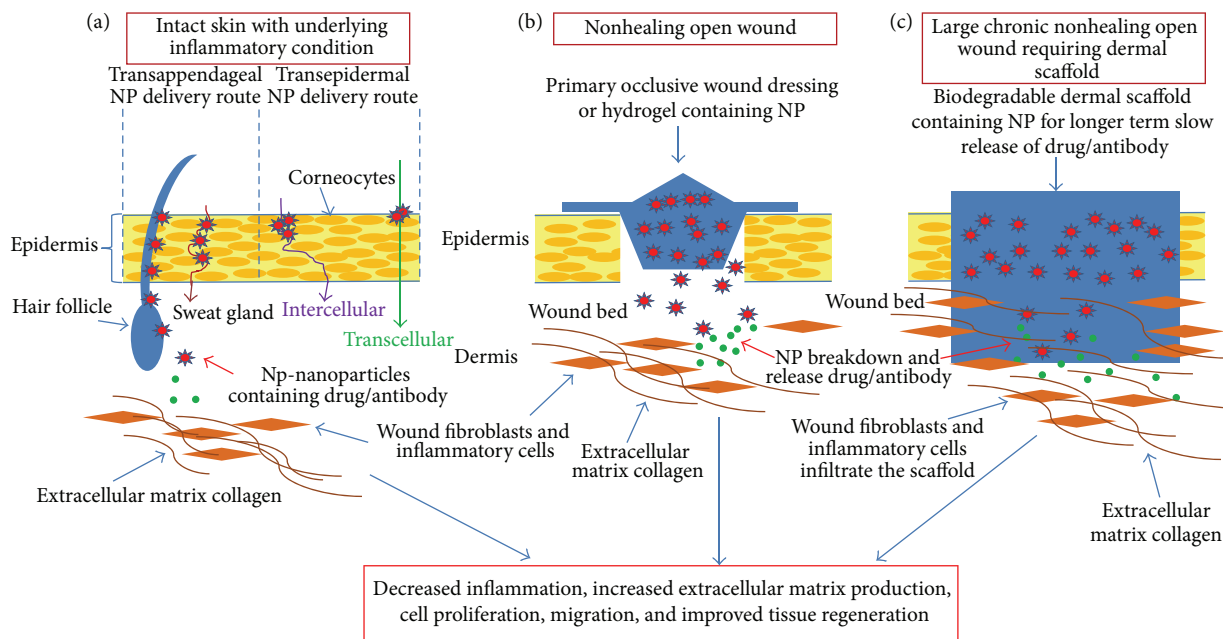


FIGURE 1: Nanoparticle technology for transcutaneous delivery of drug agents to intact or wounded skin leading to improved wound outcomes. (a) Transepithelial delivery of nanoparticles is limited by the poor penetration through the protective stratum corneum. Transappendageal nanoparticle delivery through hair follicle offers potential for treatment of conditions where skin is intact. ((b)-(c)) Incorporation of drug carrying nanoparticles into dressings and scaffolds allows controlled sustained release of biologically active agents into open wounds intradermally hence resulting in improved healing and reduced scarring.

TABLE 1: The use of nanoparticle technology for delivery of drugs transcutaneously targeting the most common cutaneous pathologies.

Nanoparticle type	Drug	Skin type	Study	Delivery type and penetration	Targeted cutaneous disease pathology	Literature studies
Solid lipid nanoparticle	Glucocorticoids, corticosteroids	Human	In vitro and in vivo	Transepidermal delivery, no penetration to the dermis	Inflammatory skin diseases, dermatitis, rheumatic disease	Sivaramakrishnan et al., 2004 [24]; Jensen et al., 2010 [25]; Zhang and Smith, 2011 [26]; Schlupp et al., 2011 [27]; Puglia et al., 2006 [28]
Solid lipid nanoparticle	Nonsteroidal anti-inflammatory drugs	Human	In vitro and in vivo	Delivery via NP enriched hydrogels with sustained continued drug release to the dermis	Musculoskeletal disorders	Jain et al., 2005 [29]; Bhaskar et al., 2009 [30]
Solid lipid nanoparticle	Antiandrogens, retinoids	Human	In vitro and in vivo	Transappendageal NP delivery to hair follicle and upper papillary dermis	Skin acne	Munster et al., 2005 [31]; Štecová et al., 2007 [32]; Castro et al., 2007 [33]
Solid lipid nanoparticle	Antifungal agents	Human	Ex vivo and in vivo	Topical gel delivery of NP with penetration to upper papillary dermis	Skin mycoses	Bhalekar et al., 2009 [34]; Sanna et al., 2007 [35]
Solid lipid nanoparticle	Retinoids, furocoumarins	Mouse and human	In vivo	Topical gel delivery to the epidermis	Psoriasis	Fang et al., 2008 [19]; Agrawal et al., 2010 [15]; Lin et al., 2010 [36]
Solid lipid nanoparticle	Tacrolimus	Porcine	In vitro and in vivo	Topical gel delivery with dermal penetration	Atopic dermatitis	Pople and Singh, 2010 [37]
Nanostructured lipid carriers	Antihypersensitive drugs and anaesthetics	Mouse and human	In vitro and in vivo	Topical gel delivery to the epidermis	Hair loss treatment and pain relief after surgery	Silva et al., 2009 [38]; Puglia et al., 2011 [39]

autoimmune diseases including psoriasis [42]. While the use of nanotechnology for the delivery of antibodies to wounds using scaffolds in vivo is yet to be demonstrated, nanotechnology has been used in numerous studies exploring the delivery of antibodies to tissue in vivo using experimental animals models of breast [43] and colon [44] cancer and osteoarthritis [45]. In addition, recent studies using nanomedicine to deliver therapeutic antibody in the experimental model of myeloma have shown that a combination therapy of anti-ABCG2mAb and paclitaxel loaded iron oxide magnetic nanoparticles has a significant effect on reduction of tumour growth in vivo compared to paclitaxel, iron oxide nanoparticles, or anti-ABCG2mAb treatment alone hence demonstrating the synergetic effect of combinational therapy in nanomedicine [46].

3. Nanotechnology and Cutaneous Infection

With the evolution of new antibiotic resistant strains of bacteria, wound infection rates are increasing and more aggressive wound management is required [47]. Infection in wounds, particularly in chronic, nonhealing, and burn wounds is a leading cause of morbidity and mortality. Good clinical practice involves using systemic and topical antimicrobial prophylaxis to reduce the microbial load in the wound as infected wounds have slower healing outcomes [48]. One of the current strategies for combating these infections is the use of noble metals as antimicrobial agents. The leader in this field is silver which has been used for its antimicrobial properties for centuries [49]. Silver based compounds are highly toxic to microorganisms showing strong effects on 16 bacterial species including *E. coli* [50]. It is now regularly used as an antimicrobial prophylaxis treatment for burns, open wounds, and chronic ulcers [51]. Silver in its metallic state is inert but upon reaction with wound fluid and moisture from skin it becomes ionized and highly reactive [52]. It binds to tissue proteins, blocks bacterial respiratory enzyme pathways, and causes structural changes of the bacterial cell wall and nuclear membrane hence leading to cell death [53–55]. Nanosilver particles are commonly used in many forms in the treatment of wounds. Silver nitrate is a common antimicrobial used in the treatment of chronic wounds; however, it can be irritating to tissues and also causes semipermanent staining of tissues and surfaces to which it contacts [56]. Silver sulfadiazine (SSD) was introduced as a topical chronic and burn wound treatment in the 1960s to overcome the shortcomings of silver nitrate, but both are limited due to a short therapeutic window, silver inactivation by wound fluid, and the formation of a pseudochar [57]. Using new nanotechnology to create sustained release of silver nanoparticles increases the therapeutic window of each dressing. One of these nanosilver impregnated dressings is Acticoat, which is an absorbent rayon-polyester core sandwiched between two layers of silver-coated, high-density polyethylene [57]. The outer layer works to provide antimicrobial effects whilst the inner core maintains a moist wound environment [58].

The use of silver dressings for the management of burns and chronic wounds is now a globally accepted therapy, with

Acticoat leading the way for the worldwide management of burns. The efficacy of Acticoat and silver sulfadiazine against several strains of bacteria including MRSA showed 100% clearance for both dressings by the end of the study. Acticoat; however, showed a significantly higher clearance at days 6 and 12 [59]. The effectiveness of Acticoat to chlorhexidine acetate and fusidic acid also showed no significant difference in effectiveness against resistant bacteria, however Acticoat was suggested as the best choice of treatment due to its sustained release properties [60].

New advances in polymer technology are allowing many dressings, previously used only to provide an optimal healing environment, to be impregnated with silver nanoparticles to add to their effectiveness. Bacterial cellulose hydrogels produced by *Acetobacter xylinum* have long been used to provide an effective, moist healing environment but without any antimicrobial activity, and the risk of infection was high. Impregnation of these dressings with silver nanoparticles by immersion in silver nitrate has significantly improved the efficiency of these hydrogels [61]. Although the powerful antimicrobial effects of silver compounds are well documented, there is evidence to suggest that it may have a negative effect on wound healing. Studies have shown that silver compounds can delay wound healing by extending the inflammation phase [62]. They have also been shown to be highly toxic to keratinocytes and fibroblasts [51]. A large oral intake of silver causes a condition known as “argyria” which is characterised by silver granule deposition into the skin leading to a permanent blue/gray discoloration [63]. In patients affected by argyria, silver granules can be found in all organs of the body and recent case studies have suggested that argyria can be an effect of topical delivery of silver in dressings such as Acticoat [64–66]. Treatment of burn wounds with Acticoat has caused raised liver enzymes and argyria like symptoms in some patients [67]. This has resulted in changes in clinical guidelines with current recommendation of using these dressings for shorter period of time and intermittently hence highlighting the need for improved design of dressings with antibacterial activity and functional wound promoting ability.

4. Dermatological Advances

Skin diseases are one of the most widespread complaints with over 80% of the population suffering from a condition at some point in their lives [68]. Although some are merely a cosmetic issue, others are more serious, causing pain, severe scarring, and morbidity. Due to the lower risk of systemic side effects and the ability to apply directly to the problem area, topical treatments of skin disease are preferred [69]. Current treatments are effective but many carry severe side effects so there remains a need for more advanced technology and nanotechnology is fast becoming a leader in this field.

Acne is a common skin disease with a high rate of prevalence in adolescents. It is characterised by increased sebum production, ductal cornification, bacterial colonization of the pilosebaceous ducts, and inflammation [70]. Acne can be severe and often results in permanent scarring and disfigurement. The most common treatment for mild to moderate

acne is the use of oral retinoids. This is a highly effective treatment option; however, it does cause a high incidence of side effects including sensitivity to sunlight, irritation, and erythema, resulting in low patient compliance. The encapsulation of retinoids into solid lipid nanoparticles (SLN) for use as a topical treatment has increased drug penetration, improved efficacy, and reduced side effects [61]. The current treatment for moderate to severe and prolonged acne involves the use of oral antiandrogens, such as combined cyproterone acetate/ethinyl estradiol to reduce sebum secretion and acne lesions. However, these drugs have severe side effects including feminisation of the male fetus in females, and use in males can lead to loss of libido, gynecomastia, and loss of bone mineral density [71]. To avoid these systemic effects and to reduce the side effects, research has led to the discovery of liposomes and solid lipid nanoparticles (SLN) loaded with steroidal and antisteroidal antiandrogens (drospirenone and cyproterone). The use of these nanoparticles increases drug penetration fourfold, increases the efficacy, and reduces the side effects when compared to oral drug options [72].

Psoriasis is a chronic skin inflammatory disorder that drastically impairs quality of life. The most common forms of treatment currently are topical; however, with limited information on their mechanism of action and evidence of accumulation in adipose tissue [73], their use in clinical practice is limited. The advent of new lipid nanoparticle drug delivery systems has the possibility to improve the efficacy and safety of these topical compounds [68]. One of the most common treatments for mild psoriasis is topical application of Tretinoin, a metabolite of vitamin A. Although effective against psoriasis, this treatment has severe side effects including erythema, burning, and increased sensitivity to light [74]. To overcome this, tretinoin has been incorporated into SLN, which not only improved permeation and efficacy, but also significantly decreased the incidence of erythema and sun sensitivity [75]. More severe psoriasis can be treated with Acitretin, an oral retinoid which although effective also has severe side effects including alopecia, skin peeling, and cheilitis [76]. Once incorporated into SLN, a higher deposit of Acitretin at the plaque site as well as significantly improved therapeutic response and a significant reduction in local side effects has been observed [68]. In addition, a recent clinical trial using Acitretin delivered via nanostructured lipid carriers demonstrated significantly improved clinical effects on patients with psoriasis [15].

Fungal skin infections are one of the most widespread diseases known to man with topical therapy the preferred method of treatment due to high patient compliance, self-administration, and low risk of systemic side effects [77]. Current treatments although effective are relatively slow-acting and so SLN are being investigated to improve efficacy. There are several antifungal agents used for the treatment of human mycoses which are currently undergoing investigation of their efficacy when incorporated with SLN including miconazole nitrate [78], clotrimazole [79], ketoconazole [80] and econazole nitrate [35].

The results from these studies show that when the drugs were incorporated into an SLN there was an increased rate and level of skin penetration, higher efficacy, and less local

side effects. Selected examples of current research developments using nanoparticle technologies for the delivery of drugs transcutaneously are presented in Table 1.

5. Development of Nanoengineered Dermal Scaffolds for Improved Healing and Reduced Scar Formation

The impact of scarring, both mentally and physically, immensely affects a large number of patients and their families which is often witnessed following burn injuries to large area of the body. Currently, there is a lack of effective scaffold treatments available for treatments of nonhealing wounds, with no approved scaffold treatments that have been shown to reduce scar formation during wound healing [81]. In the case of major burns where injury damages the deep dermis and no sources of cells for regeneration remain, there is a requirement to provide a dermal scaffold to fill in the deep wound [82]. Current commercial products address some of the immediate demands of wound care including protective covering or lost epidermal/dermal material; however, these are far from optimal, often addressing only one aspect of injury. Current scaffolds are made from xenobiotic animal derived materials and have short shelf life, nontrivial application, and high production costs [81, 83]. While there is a wide range of biologic and polymeric materials currently available on the market their efficacy is far from optimal highlighting the need for the development of next generation scaffolds which actively promote healing, and decrease scarring [81].

In the past five years there has been a significant increase in the *in vivo* use of both synthetic and natural biodegradable polymers and materials. Through the process of electrospinning, nanofibres can be processed to create nanofibrous scaffolds with open and interconnected porosity. Poly-(ϵ -caprolactone) (PCL)/gelatin nanofibrous scaffolds have been shown to have improved biocompatibility and improved mechanical, physical, and chemical properties, allowing improved wound healing and dermal reconstitution [82]. In addition, nanofibrous scaffolds facilitate the impregnation of allogeneic keratinocytes, xenogenic fibroblasts, and antibacterial agents for improved wound healing and decreased infection rates [14, 84, 85].

The use of nanotechnology now provides a novel platform for the design of functionalized, treatment specific scaffolds which, in addition to providing a matrix for cell proliferation and differentiation, can also carry drug containing nanoparticles. Enzymes, present in the wound environment, can dynamically degrade the nanoparticles allowing the optimal dose of biologically active drug to be released intradermally over a sustained period. This may promote rapid cellular migration under the dressing and onto and into the scaffold, resulting in regenerative wound healing and reduced scar formation (Figure 1(c)). While the use of nanotechnology for drug delivery using dermal scaffold is still being developed, further research in nanomedicine offers hope for improved treatment options in cutaneous medicine.

6. Conclusion

Nanotechnology presents an exciting new opportunity for the development of a safer and more efficient drug strategy for many dermatological conditions. While there are a number of examples of nanoparticle cosmetic products currently on the market, commercially available nanoparticle products for drug delivery through healthy or wounded skin are still under development [21, 22]. With the advent of new nano-based drug delivery systems which can be specifically formulated to target specific cells and fit a desired release profile and penetration depth, the face of medical research is truly evolving. There is, however, much research still to be performed to understand the chronic effects and to continue to improve patient tolerance and drug efficacy in vivo.

Conflict of Interests

The authors declare that there is no conflict of interests regarding the publication of this paper.

Authors' Contribution

Jessica E. Jackson and Zlatko Kopecki contributed equally to this paper.

Acknowledgments

Allison J. Cowin is supported by the NHMRC Senior Research Fellowship (no. 1002009). Zlatko Kopecki is supported by the NHMRC Early Career Fellowship (no. 1036509).

References

- [1] A. J. Singer and R. A. F. Clark, "Cutaneous wound healing," *The New England Journal of Medicine*, vol. 341, no. 10, pp. 738–746, 1999.
- [2] P. Silacci, L. Mazzolai, C. Gauci, N. Stergiopoulos, H. L. Yin, and D. Hayoz, "Gelsolin superfamily proteins: key regulators of cellular functions," *Cellular and Molecular Life Sciences*, vol. 61, no. 19–20, pp. 2614–2623, 2004.
- [3] S. Werner and R. Grose, "Regulation of wound healing by growth factors and cytokines," *Physiological Reviews*, vol. 83, no. 3, pp. 835–870, 2003.
- [4] G. Broughton II, J. E. Janis, and C. E. Attinger, "The basic science of wound healing," *Plastic and Reconstructive Surgery*, vol. 117, no. 7, 2006.
- [5] J. E. Jackson, Z. Kopecki, D. H. Adams, and A. J. Cowin, "Flii neutralizing antibodies improve wound healing in porcine pre-clinical studies," *Wound Repair and Regeneration*, vol. 20, no. 4, pp. 523–536, 2012.
- [6] J. S. Boateng, K. H. Matthews, H. N. E. Stevens, and G. M. Eccleston, "Wound healing dressings and drug delivery systems: a review," *Journal of Pharmaceutical Sciences*, vol. 97, no. 8, pp. 2892–2923, 2008.
- [7] G. Jeon, S. Y. Yang, and J. K. Kim, "Functional nanoporous membranes for drug delivery," *Journal of Materials Chemistry*, vol. 22, no. 30, pp. 14814–14834, 2012.
- [8] L. Vaccari, D. Canton, N. Zaffaroni, R. Villa, M. Tormen, and E. di Fabrizio, "Porous silicon as drug carrier for controlled delivery of doxorubicin anticancer agent," *Microelectronic Engineering*, vol. 83, no. 4–9, pp. 1598–1601, 2006.
- [9] A. Solanki, J. D. Kim, and K.-B. Lee, "Nanotechnology for regenerative medicine: nanomaterials for stem cell imaging," *Nanomedicine*, vol. 3, no. 4, pp. 567–578, 2008.
- [10] S. Polarz and B. Smarsly, "Nanoporous Materials," *Journal of Nanoscience and Nanotechnology*, vol. 2, no. 6, pp. 581–612, 2002.
- [11] E. Gultepe, D. Nagesha, S. Sridhar, and M. Amiji, "Nanoporous inorganic membranes or coatings for sustained drug delivery in implantable devices," *Advanced Drug Delivery Reviews*, vol. 62, no. 3, pp. 305–315, 2010.
- [12] E. Engel, A. Michiardi, M. Navarro, D. Lacroix, and J. A. Planell, "Nanotechnology in regenerative medicine: the materials side," *Trends in Biotechnology*, vol. 26, no. 1, pp. 39–47, 2008.
- [13] M. E. Lane, "Nanoparticles and the skin applications and limitations," *Journal of Microencapsulation*, vol. 28, no. 8, pp. 709–716, 2011.
- [14] S. P. Zhong, Y. Z. Zhang, and C. T. Lim, "Tissue scaffolds for skin wound healing and dermal reconstruction," *Wiley Interdisciplinary Reviews*, vol. 2, no. 5, pp. 510–525, 2010.
- [15] Y. Agrawal, K. C. Petkar, and K. K. Sawant, "Development, evaluation and clinical studies of Acitretin loaded nanostructured lipid carriers for topical treatment of psoriasis," *International Journal of Pharmaceutics*, vol. 401, no. 1–2, pp. 93–102, 2010.
- [16] E. Kimura, Y. Kawano, H. Todo, Y. Ikarashi, and K. Sugibayashi, "Measurement of skin permeation/penetration of nanoparticles for their safety evaluation," *Biological & pharmaceutical bulletin*, vol. 35, no. 9, pp. 1476–1486, 2012.
- [17] J. Wu, W. Liu, C. Xue et al., "Toxicity and penetration of TiO₂ nanoparticles in hairless mice and porcine skin after subchronic dermal exposure," *Toxicology Letters*, vol. 191, no. 1, pp. 1–8, 2009.
- [18] A. C. Watkinson, A. Bunge, Hadgraft, and M. Lane, "Nanoparticles do not penetrate human skin—a theoretical perspective," *Pharmaceutical Research*, vol. 30, no. 8, pp. 1943–1946, 2013.
- [19] J.-Y. Fang, C.-L. Fang, C.-H. Liu, and Y.-H. Su, "Lipid nanoparticles as vehicles for topical psoralen delivery: solid lipid nanoparticles (SLN) versus nanostructured lipid carriers (NLC)," *European Journal of Pharmaceutics and Biopharmaceutics*, vol. 70, no. 2, pp. 633–640, 2008.
- [20] Z. Mei, H. Chen, T. Weng, Y. Yang, and X. Yang, "Solid lipid nanoparticle and microemulsion for topical delivery of triptolide," *European Journal of Pharmaceutics and Biopharmaceutics*, vol. 56, no. 2, pp. 189–196, 2003.
- [21] C. Puglia and F. Bonina, "Lipid nanoparticles as novel delivery systems for cosmetics and dermal pharmaceuticals," *Expert Opinion on Drug Delivery*, vol. 9, no. 4, pp. 429–441, 2012.
- [22] J. Lademann, H. Richter, M. C. Meinke et al., "Drug delivery with topically applied nanoparticles: science fiction or reality," *Skin Pharmacology and Physiology*, vol. 36, no. 4–6, pp. 227–233, 2013.
- [23] A. Patzelt and J. Lademann, "Drug delivery to hair follicles," *Expert Opin Drug Deliv*, vol. 10, no. 6, pp. 787–797, 2013.
- [24] R. Sivaramkrishnan, C. Nakamura, W. Mehnert, H. C. Korting, K. D. Kramer, and M. Schäfer-Korting, "Glucocorticoid entrapment into lipid carriers—characterisation by paretic spectroscopy and influence on dermal uptake," *Journal of Controlled Release*, vol. 97, no. 3, pp. 493–502, 2004.
- [25] L. B. Jensen, L. B. Jensen, E. Magnusson et al., "Corticosteroid solubility and lipid polarity control release from solid lipid nanoparticles," *International Journal of Pharmaceutics*, vol. 390, no. 1, pp. 53–60, 2010.

- [26] J. Zhang and E. Smith, "Percutaneous permeation of betamethasone 17-valerate incorporated in lipid nanoparticles," *Journal of Pharmaceutical Sciences*, vol. 100, no. 3, pp. 896–903, 2011.
- [27] P. Schlupp, P. Schlupp, T. Blaschke et al., "Drug release and skin penetration from solid lipid nanoparticles and a base cream: a systematic approach from a comparison of three glucocorticoids," *Skin Pharmacology and Physiology*, vol. 24, no. 4, pp. 199–209, 2011.
- [28] C. Puglia, R. Filosa, A. Peduto et al., "Evaluation of alternative strategies to optimize ketorolac transdermal delivery," *Aaps Pharmscitech*, vol. 7, no. 3, pp. E61–E69, 2006.
- [29] S. Jain, W. T. Yap, and D. J. Irvine, "Synthesis of protein-loaded hydrogel particles in an aqueous two-phase system for coincident antigen and CpG oligonucleotide delivery to antigen-presenting cells," *Biomacromolecules*, vol. 6, no. 5, pp. 2590–2600, 2005.
- [30] K. Bhaskar, J. Anbu, V. Ravichandiran, V. Venkateswarlu, and Y. M. Rao, "Lipid nanoparticles for transdermal delivery of flurbiprofen: formulation, in vitro, ex vivo and in vivo studies," *Lipids in Health and Disease*, vol. 8, article 6, 2009.
- [31] U. Munster, C. Nakamura, A. Haberland et al., "RU, 58841-myristate prodrug development for topical treatment of acne and androgenetic alopecia," *Die Pharmazie*, vol. 60, no. 1, pp. 8–12, 2005.
- [32] Štecová, J. W. Mehnert, T. Blaschke et al., "Cyproterone acetate loading to lipid nanoparticles for topical acne treatment: particle characterisation and skin uptake," *Pharmaceutical Research*, vol. 24, no. 5, pp. 991–1000, 2007.
- [33] G. A. Castro, R. L. Oréfice, J. M. Vilela, M. S. Andrade, and L. A. Ferreira, "Development of a new solid lipid nanoparticle formulation containing retinoic acid for topical treatment of acne," *Journal of Microencapsulation*, vol. 24, no. 5, pp. 395–407, 2007.
- [34] M. R. Bhalekar, V. Pokharkar, A. Madgulkar, N. Patil, and N. Patil, "Preparation and evaluation of miconazole nitrate-loaded solid lipid nanoparticles for topical delivery," *AAPS PharmSciTech*, vol. 10, no. 1, pp. 289–296, 2009.
- [35] V. Sanna, E. Gavini, M. Cossu, G. Rassu, and P. Giunchedi, "Solid lipid nanoparticles (SLN) as carriers for the topical delivery of econazole nitrate: in-vitro characterization, ex-vivo and in-vivo studies," *Journal of Pharmacy and Pharmacology*, vol. 59, no. 8, pp. 1057–1064, 2007.
- [36] S. C. Lin, P. Dollé, L. Ryckebusch et al., "Endogenous retinoic acid regulates cardiac progenitor differentiation," *Proceedings of the National Academy of Sciences*, vol. 107, no. 20, pp. 9234–9239, 2010.
- [37] P. V. Pople and K. K. Singh, "Targeting tacrolimus to deeper layers of skin with improved safety for treatment of atopic dermatitis," *International Journal of Pharmaceutics*, vol. 398, no. 1, pp. 165–178, 2010.
- [38] A. Silva, D. Santos, D. C. Ferreira, and E. B. Souto, "Minoxidil-loaded nanostructured lipid carriers (NLC): characterization and rheological behaviour of topical formulations," *Die Pharmazie*, vol. 64, no. 3, pp. 177–182, 2009.
- [39] C. Puglia, M. G. Sarpietro, F. Bonina, F. Castelli, M. Zammataro, and S. Chiechio, "Development, characterization, and in vitro and in vivo evaluation of benzocaine- and lidocaine-loaded nanostructured lipid carriers," *Journal of Pharmaceutical Sciences*, vol. 100, no. 5, pp. 1892–1899, 2011.
- [40] A. Mittal, A. S. Raber, and S. Hansen, "Particle based vaccine formulations for transcutaneous immunization," *Hum Vaccin Immunother*, vol. 9, no. 9, 2013.
- [41] A. Mittal et al., "Non-invasive delivery of nanoparticles to hair follicles: a perspective for transcutaneous immunization," *Vaccine*, vol. 31, no. 34, pp. 3442–3451, 2013.
- [42] J. S. Gall and R. E. Kalb, "Infliximab for the treatment of plaque psoriasis," *Biologics*, vol. 2, no. 1, pp. 115–124, 2008.
- [43] H. Chen, L. Wang, Q. Yu et al., "Anti-HER2 antibody and ScFvEGFR-conjugated antifouling magnetic iron oxide nanoparticles for targeting and magnetic resonance imaging of breast cancer," *International Journal of Nanomedicine*, vol. 8, no. 1, pp. 3781–3794, 2013.
- [44] A. H. Abouzeid, N. R. Patel, I. M. Rachman, S. Senn, and V. P. Torchilin, "Anti-cancer activity of anti-GLUT1 antibody-targeted polymeric micelles co-loaded with curcumin and doxorubicin," *Journal of Drug Targeting*, vol. 21, no. 10, pp. 994–1000, 2013.
- [45] H. Cho, R. Magid, D. C. Danila, T. Hunsaker, E. Pinkhassik, and K. A. Hasty, "Theranostic Immunoliposomes for Osteoarthritis," *Nanomedicine*, 2013.
- [46] Y. Zhao, D. Y. Alakhova, and A. V. Kabanov, "Can Nanomedicines Kill Cancer Stem Cells?" *Advanced Drug Delivery Reviews*. In press.
- [47] J. B. Wright, K. Lam, and R. E. Burrell, "Wound management in an era of increasing bacterial antibiotic resistance: a role for topical silver treatment," *American Journal of Infection Control*, vol. 26, no. 6, pp. 572–577, 1998.
- [48] M. C. Robson, "Wound infection: a failure of wound healing caused by an imbalance of bacteria," *Surgical Clinics of North America*, vol. 77, no. 3, pp. 637–650, 1997.
- [49] J. W. Alexander, "History of the medical use of silver," *Surgical Infections*, vol. 10, no. 3, pp. 289–292, 2009.
- [50] I. Sondi and B. Salopek-Sondi, "Silver nanoparticles as antimicrobial agent: a case study on *E. coli* as a model for Gram-negative bacteria," *Journal of Colloid and Interface Science*, vol. 275, no. 1, pp. 177–182, 2004.
- [51] B. S. Atiyeh, M. Costagliola, S. N. Hayek, and S. A. Dibo, "Effect of silver on burn wound infection control and healing: review of the literature," *Burns*, vol. 33, no. 2, pp. 139–148, 2007.
- [52] M. Rai, A. Yadav, and A. Gade, "Silver nanoparticles as a new generation of antimicrobials," *Biotechnology Advances*, vol. 27, no. 1, pp. 76–83, 2009.
- [53] J. Tian, K. K. Y. Wong, C.-M. Ho et al., "Topical delivery of silver nanoparticles promotes wound healing," *ChemMedChem*, vol. 2, no. 1, pp. 129–136, 2007.
- [54] A. B. Lansdown, "Silver. I: its antibacterial properties and mechanism of action," *Journal of wound care*, vol. 11, no. 4, pp. 125–130, 2002.
- [55] S. Arora, J. Jain, J. M. Rajwade, and K. M. Paknikar, "Cellular responses induced by silver nanoparticles: in vitro studies," *Toxicology Letters*, vol. 179, no. 2, pp. 93–100, 2008.
- [56] J. B. Wright, K. Lam, D. Hansen, and R. E. Burrell, "Efficacy of topical silver against fungal burn wound pathogens," *American Journal of Infection Control*, vol. 27, no. 4, pp. 344–350, 1999.
- [57] K. Dunn and V. Edwards-Jones, "The role of Acticoat with nanocrystalline silver in the management of burns," *Burns*, vol. 30, no. 1, pp. S1–S9, 2004.
- [58] R. Khundkar, C. Malic, and T. Burge, "Use of Acticoat dressings in burns: what is the evidence?" *Burns*, vol. 36, no. 6, pp. 751–758, 2010.
- [59] Y. Huang, X. Li, Z. Liao et al., "A randomized comparative trial between Acticoat and SD-Ag in the treatment of residual burn wounds, including safety analysis," *Burns*, vol. 33, no. 2, pp. 161–166, 2007.

- [60] E. Ülkür, O. Oncul, H. Karagoz, E. Yeniz, and B. Çeliköz, "Comparison of silver-coated dressing (Acticoat), chlorhexidine acetate 0.5% (Bactigrass), and fusidic acid 2% (Fucidin) for topical antibacterial effect in methicillin-resistant Staphylococci-contaminated, full-skin thickness rat burn wounds," *Burns*, vol. 31, no. 7, pp. 874–877, 2005.
- [61] T. Maneerung, S. Tokura, and R. Rujiravanit, "Impregnation of silver nanoparticles into bacterial cellulose for antimicrobial wound dressing," *Carbohydrate Polymers*, vol. 72, no. 1, pp. 43–51, 2008.
- [62] A.-R. C. Lee, H. Leem, J. Lee, and K. C. Park, "Reversal of silver sulfadiazine-impaired wound healing by epidermal growth factor," *Biomaterials*, vol. 26, no. 22, pp. 4670–4676, 2005.
- [63] R. H. Demling and L. Desanti, "The role of silver in wound healing. Part I: effects of silver on wound management," *Wounds*, vol. 13, no. 1, pp. 4–15, 2001.
- [64] J. P. Marshall II and R. P. Schneider, "Systemic argyria secondary to topical silver nitrate," *Archives of Dermatology*, vol. 113, no. 8, pp. 1077–1079, 1977.
- [65] N. Myerson Fisher, E. Marsh, and R. Lazova, "Scar-localized argyria secondary to silver sulfadiazine cream," *Journal of the American Academy of Dermatology*, vol. 49, no. 4, pp. 730–732, 2003.
- [66] G. Chaby, V. Viseux, J. F. Poulain, B. De Cagny, J. P. Denooux, and C. Lok, "Topical silver sulfadiazine-induced acute renal failure," *Annales de Dermatologie et de Vénérologie*, vol. 132, no. 11, part 1, pp. 891–893, 2005.
- [67] M. Trop, M. Novak, S. Rodl, B. Hellbom, W. Kroell, and W. Goessler, "Silver-coated dressing acticoat caused raised liver enzymes and argyria-like symptoms in burn patient," *The Journal of Trauma*, vol. 60, no. 3, pp. 648–652, 2006.
- [68] C. Puglia and F. Bonina, "Lipid nanoparticles as novel delivery systems for cosmetics and dermal pharmaceuticals," *Expert Opinion on Drug Delivery*, vol. 9, no. 4, pp. 429–441, 2012.
- [69] M. Schäfer-Korting, W. Mehnert, and H.-C. Korting, "Lipid nanoparticles for improved topical application of drugs for skin diseases," *Advanced Drug Delivery Reviews*, vol. 59, no. 6, pp. 427–443, 2007.
- [70] A.O. Acne, "Pathological mechanisms of acne with special emphasis on Propionibacterium acnes and related therapy," *Acta Dermato-Venereologica*, vol. 83, no. 4, pp. 241–248, 2003.
- [71] W. A. van Vloten, C. W. van Haselen, E. J. van Zuuren, C. Gerlinger, and R. Heithacker, "The effect of 2 combined oral Contraceptives containing either drospirenone or cyproterone acetate on acne and seborrhea," *Cutis*, vol. 69, no. 4, pp. 2–15, 2002.
- [72] J. Štecová, W. Mehnert, T. Blaschke et al., "Cyproterone acetate loading to lipid nanoparticles for topical acne treatment: particle characterisation and skin uptake," *Pharmaceutical Research*, vol. 24, no. 5, pp. 991–1000, 2007.
- [73] J.-H. Saurat, "Retinoids and psoriasis: novel issues in retinoid pharmacology and implications for psoriasis treatment," *Journal of the American Academy of Dermatology*, vol. 41, no. 3, pp. S2–S6, 1999.
- [74] J. Pardeike, A. Hommoss, and R. H. Müller, "Lipid nanoparticles (SLN, NLC) in cosmetic and pharmaceutical dermal products," *International Journal of Pharmaceutics*, vol. 366, no. 1–2, pp. 170–184, 2009.
- [75] K. A. Shah, A. A. Date, M. D. Joshi, and V. B. Patravale, "Solid lipid nanoparticles (SLN) of tretinoin: potential in topical delivery," *International Journal of Pharmaceutics*, vol. 345, no. 1–2, pp. 163–171, 2007.
- [76] A. K. Gupta, M. T. Goldfarb, C. N. Ellis, and J. V. Voorhees, "Side-effect profile of acitretin therapy in psoriasis," *Journal of the American Academy of Dermatology*, vol. 20, no. 6, pp. 1088–1093, 1989.
- [77] I. P. Kaur and S. Kakkar, "Topical delivery of antifungal agents," *Expert Opinion on Drug Delivery*, vol. 7, no. 11, pp. 1303–1327, 2010.
- [78] S. Jain, S. Jain, P. Khare, A. Gulbake, D. Bansal, and S. K. Jain, "Design and development of solid lipid nanoparticles for topical delivery of an anti-fungal agent," *Drug Delivery*, vol. 17, no. 6, pp. 443–451, 2010.
- [79] P. Dandagi, S. Kumar MM Sanghvi, V. S. Mastiholimath, and A. P. Gadad, "Design and characterization of clotrimazole nanoparticles: an-approach to controlled drug delivery," *Inventi Impact*, vol. 2011, 2011.
- [80] E. B. Souto and R. H. Müller, "SLN and NLC for topical delivery of ketoconazole," *Journal of Microencapsulation*, vol. 22, no. 5, pp. 501–510, 2005.
- [81] R. V. Shevchenko, S. L. James, and S. E. James, "A review of tissue-engineered skin bioconstructs available for skin reconstruction," *Journal of the Royal Society Interface*, vol. 7, no. 43, pp. 229–258, 2010.
- [82] E. J. Chong, T. T. Phan, I. J. Lim et al., "Evaluation of electrospun PCL/gelatin nanofibrous scaffold for wound healing and layered dermal reconstitution," *Acta Biomaterialia*, vol. 3, no. 3, pp. 321–330, 2007.
- [83] H. Carsin, P. Ainaud, H. Bevera et al., "Cultured epithelial autografts in extensive burn coverage of severely traumatized patients: a five year single-center experience with 30 patients," *Burns*, vol. 26, no. 4, pp. 379–387, 2000.
- [84] M. Cai, Z. Li, F. Fan, Q. Huang, X. Shao, and G. Song, "Design and Synthesis of Novel Insecticides Based on the Serotonergic Ligand 1-[(4-Aminophenyl)ethyl]-4-[3-(trifluoromethyl)phenyl]piperazine(PAPP)," *Journal of Agricultural and Food Chemistry*, vol. 58, no. 5, pp. 2624–2629, 2010.
- [85] P. T. S. Kumar, S. Abhilash, K. Manzoor, S. V. Nair, H. Tamura, and R. Jayakumar, "Preparation and characterization of novel β -chitin/nanosilver composite scaffolds for wound dressing applications," *Carbohydrate Polymers*, vol. 80, no. 3, pp. 761–767, 2010.

Review Article

Emerging Stem Cell Controls: Nanomaterials and Plasma Effects

F. F. Borghi,^{1,2} A. E. Rider,^{1,2} S. Kumar,¹ Z. J. Han,¹ D. Haylock,^{3,4} and K. Ostrikov^{1,2}

¹ CSIRO Materials Science and Engineering, P.O. Box 218, Lindfield, NSW 2070, Australia

² Complex Systems, School of Physics, The University of Sydney, NSW 2006, Australia

³ CSIRO Materials Science and Engineering, Private Bag 33, Clayton, VIC 3169, Australia

⁴ The Australian Regenerative Medicine Institute, Monash University, VIC 3168, Australia

Correspondence should be addressed to A. E. Rider; amanda.rider@csiro.au and K. Ostrikov; kostya.ostrikov@csiro.au

Received 9 September 2013; Accepted 9 October 2013

Academic Editor: Krasimir Vasilev

Copyright © 2013 F. F. Borghi et al. This is an open access article distributed under the Creative Commons Attribution License, which permits unrestricted use, distribution, and reproduction in any medium, provided the original work is properly cited.

Stem cells (SC) are among the most promising cell sources for tissue engineering due to their ability to self-renew and differentiate, properties that underpin their clinical application in tissue regeneration. As such, control of SC fate is one of the most crucial issues that needs to be fully understood to realise their tremendous potential in regenerative biology. The use of functionalized nanostructured materials (NM) to control the microscale regulation of SC has offered a number of new features and opportunities for regulating SC. However, fabricating and modifying such NM to induce specific SC response still represent a significant scientific and technological challenge. Due to their versatility, plasmas are particularly attractive for the manufacturing and modification of tailored nanostructured surfaces for stem cell control. In this review, we briefly describe the biological role of SC and the mechanisms by which they are controlled and then highlight the benefits of using a range of nanomaterials to control the fate of SC. We then discuss how plasma nanoscience research can help produce/functionalise these NMs for more effective and specific interaction with SCs. The review concludes with a perspective on the advantages and challenges of research at the intersection between plasma physics, materials science, nanoscience, and SC biology.

1. Introduction

Controlling the fate of stem cells (SC) is one of the most crucial issues in regenerative biology and medicine. This versatile type of cell, with promising applications due to their ability to renew their own population and become other types of cells (Figure 1(c)), constitutes the fundamental element of cell therapy. The approach depends upon isolation of SC cells from a tissue as is the case for adult or somatic SC or undifferentiated SC from a culture of pluripotent SC then culture *in vitro* to generate differentiated mature functional cells for use in regeneration of aged, injured, and diseased tissues. However, cell therapy presents challenges that goes beyond the usual tissue engineering—which combine high-performance materials and signaling factors with living cells to restore tissue functions. It involves cells which, when stimulated by specific growth/differentiation factors (e.g., soluble proteins, insoluble attached proteins, and extracellular matrix (ECM) molecules), give rise to a range of heterogeneous cell types (Figure 1(c)). The success of this approach relies

on knowing which of these factors affects SC fate and how this interaction occurs. This is a very difficult task and also depends on how and when the factors are delivered, that is, affected by the growth factor presentation (conformation) and time dependent. Studies also show that it is not only the chemical factors but also the physical interaction between the biomaterials and SC that influence the behavior of cells in culture [1, 2] since it directs the forces exerted by cells on the ECM and are believed to trigger gene activation and suppression [3–6].

This suggests the important role of controlling the environmental material properties (density, stiffness, and architecture) as well as regarding how exactly the growth/differentiation factors are presented and delivered (Figure 2). For this task, biomaterials are being developed to contain and deliver combinations of factors in a controllable way. Gels that mimic the ECM, functionalized polymers, inert metals/alloys, calcium phosphates, nanoparticles, nanostructured surfaces, and several others are just some examples

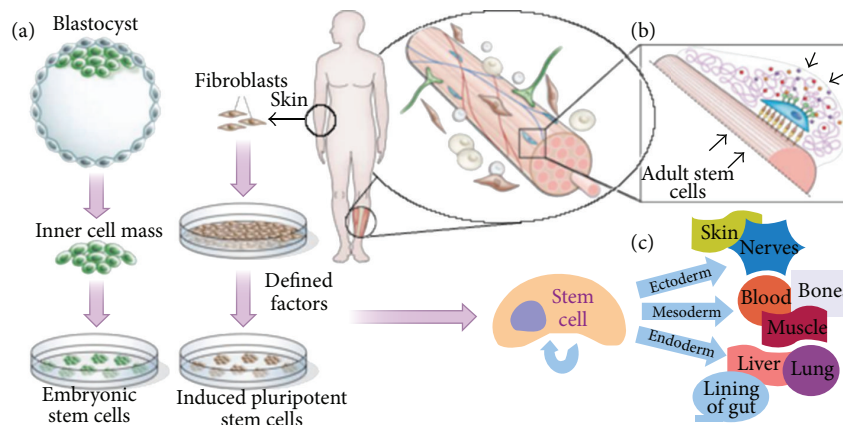


FIGURE 1: (a) The two sources of pluripotent stem cells. (b) Adult tissue as source of adult (multipotent) stem cell. (c) Differentiation path to each cell lineage. ((a) and (b) adapted from [7], reprinted with permission from Macmillan Publishers Ltd.: Nature, Copyright (2009).)

of functional materials that are currently used to study and control SC fate [1, 7–13]. Although there has been a considerable advance in the area of gels and scaffolds, here we focus on nanomaterials (nanoparticles, nanofibers, and nanostructured surfaces) that can influence selection, proliferation, and differentiation of SC.

To achieve a greater degree of control, reproducibility, scalability, and synthetic materials have gained a significant advantage over naturally occurring materials [1]. In order to precisely design nanomaterials' architecture, its mechanical properties and binding sites for the proper presentation of ligands, techniques to produce and functionalize these materials are required. As an attractive alternative to widely used lithography and chemistry processes, we discuss some of the new advances in self-assembled plasma-made nanomaterials [14]. Furthermore, the plasma environment can be used to produce building blocks for nanoscale assembly and reactive free radicals for surface modification and in addition can be used for controlled synthesis and processing of self-organized nanomaterials [15].

This review will briefly describe in Section 2 the biological role of SC and some of the known mechanisms by which they can be controlled. Section 3 will then highlight the benefits of using a range of nanomaterials to control the fate of SCs. Within Section 4, we discuss how plasma nanoscience has the potential to produce or functionalize these NMs to improve their interaction with SCs. The review will conclude with a perspective on the advantages and challenges of research at the intersection between cell biology, plasma science, materials science, nanoscience, and engineering.

2. The Biological Role of Stem Cells

2.1. Basic Information. Stem cells (SC) are present in mammals from the beginning of their life until their death. They form the first cell aggregates, during embryogenesis, and are able to self-renew their own population and, in order to form an adult animal, can differentiate into virtually any cell type; moreover, within the adult mammal tissue, specific adult SC

are also responsible for regenerating mature injured tissues [1, 7–9]. Due to these two defining properties, namely, self-renewability and specific differentiation, SC play a pivotal role in cell therapy for treating/restoring damaged tissues by direct replacement of diseased cells [1, 8, 9, 17].

Stem cells can be divided into two broad categories: pluripotent (embryonic SC (ESC) or induced SC (iPSC)) and adult SC. Each of these different SC types is derived or obtained in different ways [7, 9] (Figures 1(a) and 1(b)). For example, ESC are derived from cells that are removed from the inner cell mass of the blastocyst (or embryoblast); iPSC are a reprogrammed adult cell (from any tissue cell back to pluripotent stem cells) [21, 22]; and the adult SC are found in adult tissues within specific anatomical locations and niches. Adult SCs are found in many tissues and organs such as the bone marrow, gastrointestinal tract, skin, and within the central nervous system where their physiological role is to provide an ongoing supply of mature cells or to facilitate tissue repair [1, 7–9, 23] (Figure 1(b)). Although adult SCs' ability to proliferate and differentiate decreases with the age of the donor and also with time spent in cell culture [24, 25], the use of this approach in cell therapy still remains of great importance as for some tissues it is relatively easy to isolate and manipulate their resident SCs. For example, hematopoietic stem cells are readily isolated from bone marrow or blood and are routinely used for transplantation [26].

Since 1981, when mouse ESC (mESC) were first isolated by Evans and Kaufman [27], the use of these cells in regenerative medicine has been the subject of great interest [8], especially in tissue engineering because of the major limitations of artificial implants [9]. The use of ESC as a cellular model also helps us to understand early developmental events at the molecular and cellular level and potentially models of disease progression and epigenetic regulation of cellular fate [28, 29]. This review will focus on, but is not limited to, SC fate control by use of synthetic nanomaterials, combined or not with the defined growth factors (rather than isolating SC or growth factors themselves). For a discussion of the isolation of SC from different adult tissues [30–32] and the generation of

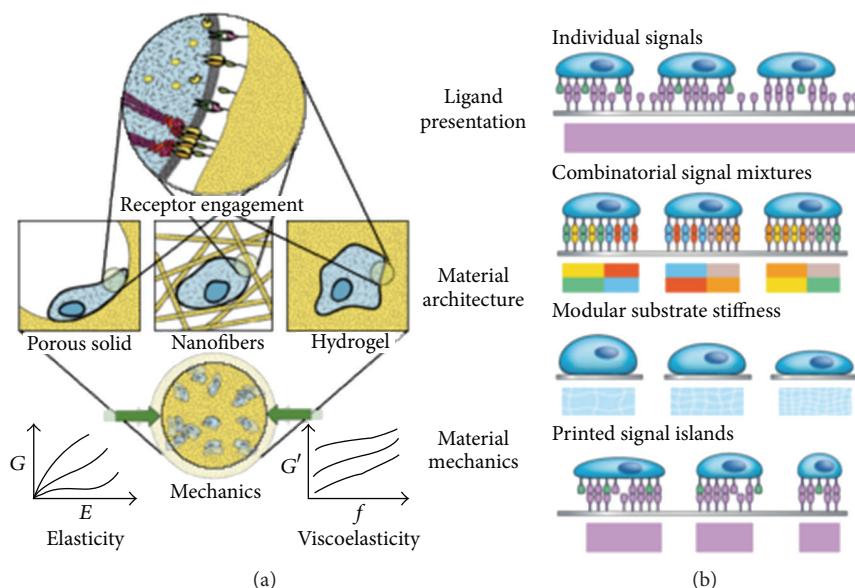


FIGURE 2: (a) Factors that control stem cell fate in 3D materials, namely, ligand presentation, material structure, and mechanical properties. (b) Four strategies to be used with 2D materials for controlling stem cells. ((a) is reprinted from [1] Copyright (2009), with permission from Elsevier. (b) is reprinted from [7] by permission from Macmillan Publishers Ltd.: Nature Copyright (2009).)

pluripotent cells from multipotent ones through reprogramming, we refer the interested reader to a number of other reviews [21, 22, 33, 34].

2.2. Controlling the Fate of Stem Cells. Growth factors, which for the remainder of this paper will include hormones, proteins, and cytokines, have been shown in numerous works to improve the control over either adult or pluripotent SC. The appropriate use of biochemical signals directly added into the culture medium can maintain or differentiate SC [35–38]. Retinoic acid (RA), activin-A, TGF- β , and insulin-like growth factor 1 (IGF-1) are seen as being responsible for promoting differentiation of murine ESC (mESC) into lung epithelial progenitor cells and pancreatic endocrine cells (alpha, beta, gamma, and delta) [39, 40]. In addition to the great importance to choose which growth factor to use for SC control, the cellular niche—the specific tissue site responsible for regulation of SC fate in the body [9, 41, 42] (Figure 1(b))—helps us to understand the role of the growth factor availability and presentation time as well as the need for a material support for insoluble transmembrane receptor ligands, as well as its specific presentation to the cells. The material selection can be based on the desire to maintain an undifferentiated SC in a culture for a long time or to directly control cell differentiation [1, 9].

For proper application in tissue engineering or adult SC-based therapy, it is desirable to choose/manufacture a biomaterial that closely mimics the “robust spatial and temporal microenvironment of biophysical and biochemical signals” (such as chemokines, cytokines, and growth factors, membrane ligands, and ECM molecules) [7, 26]. Ideally, this microenvironment is an artificial version of the stem cell

niche, promoting SC self-renewal or specific differentiation without loss of the key SC attributes [7, 41–45]. Therefore, to control SC behavior and achieve homogeneous and efficient cell differentiation, it is crucial to understand the effects of the identity, presentation, and density of the differentiation factors (e.g., ligands and signals), as well as the material micro- and nanoarchitecture and mechanical properties, which will be described in the next section [3, 9, 11].

The hydrogel is a well-established culture media that has been used for decades to mimic the microenvironment of stem cells in the human body [2, 8, 46–48]. This is due to its high water content, elasticity, biocompatibility, and the ability of nutrients and growth factors to diffuse through it [46–49]. Hydrogels, either natural or synthetic, closely resemble the consistency of the native body tissue by adjusting the hydrogels’ crosslinks [8, 50]. Thus they provide efficient adhesion sites for cells and biological signals and also guidance for cell orientation and proliferation [3].

These materials can be used instead of feeder-cell layers for supporting hESC culture and maintenance and were first reported by Xu et al. [51–53] using natural hydrogels, with proven ability to differentiate hESCs [54]. Collagen is an example of a natural hydrogel which is capable of cell encapsulation [55], support of ESC-derived endothelial cells, [56] and, in high concentrations, inhibit the embryonic body (EB) apoptosis and enhance its differentiation [54]. Moreover, collagen in association with fibronectin or laminin was able to differentiate SC into endothelial and cardiomyocyte cells, respectively [54]. Furthermore, denaturated collagen becomes porous gelatin, and is also biocompatible and extensively used [57, 58]. Other important natural materials hyaluronic acid and alginate, are both able to encapsulate SC

and keep them undifferentiated [59] and also differentiate SC into cardiac [60] and hepatic lineage [61] (Figure 1(c)). Likewise, the commercial Matrigel, comprising multiple natural ECM components, has the ability to direct SC into endothelial cells [62] and enhanced neovascular formation [63].

2.3. Present-Day Challenges. The use of natural materials, however, presents some limitations, like batch-to-batch variations, weak mechanical properties, and manufacturing difficulties [64]. Synthetic hydrogels, however, are not usually subject to these limitations and instead offer relatively easy control over biochemical properties and represent risk-free media [7–9, 65, 66]. The most commonly used synthetic biomaterials include polyethylene glycol (PEG), polyvinyl alcohol (PVA), polylactic acid (PLA), and poly(L)lactic acid (PLLA), and polylactic-co-glycolic acid (PLGA), which are microfabricated to be active, degradable, porous, and/or stiff enough to induce SC differentiation both *in vitro* and *in vivo* [1, 8, 9]. The first biomaterial listed, PEG, is a polymer composed of nanofibers and is capable of cell encapsulation and differentiation in numerous tissues (e.g., bone tissue [67, 68]). Also being able to maintain a neural SC culture, PLA can be produced with aligned fibers and induce aligned neural cells [20]. The PLGA usually helps differentiating neural SC into neural cells [69]. Moreover, when mixed with PLLA, it also promotes differentiation of ESCs into numerous cell lineages [70–72].

All these results highlight some important factors about the medium architecture and applied forces, present in the natural cell niche, that mechanically control SC fate [2, 73]. Some limitations for the use of hydrogels in the mechanical control of SC fate, however, include an inability to be synthesized at a stiffness that mimics higher mechanical strength tissues such as bone, cartilage, and ligaments [8]. Moreover, although other studies show that hydrogels provide a 3D structure to support cells, this is not always in the right spatial dimension (e.g., nanoscale), as that conferred by nanofibrillar proteins secreted by cells (e.g., collagen) present in cellular niche [9, 69, 74].

Although the successful application of synthetic hydrogels modified with numerous growth factors (GF) to mimic the SC niche and control the SC fate has been demonstrated, the strict control of its chemical functionalization, degradation rates, ligand presentation, and mechanical properties still remain challenging. The strategies adopted nowadays involve the use of nanomaterials [75, 76]. For example, some growth factors can be adsorbed on nanoparticle surfaces and then controllably released in the culture medium. Nanomaterials can also be added to hydrogels in order to control stiffness. Micro- and nanoscale patterning is now capable of building materials with specific topographies in order to control the cell focal interaction in different scales and shapes as well as providing spots for the attachment of localized ligands and preventing diffusion [77]. New technologies also provide better control over the surface chemistry of biomaterials. For example, functionalization with chemical radicals allows the attachment of biological factors or may lead to hydrophilic properties depending on the specific applications.

3. Materials Science Approaches for Stem Cell Control

3.1. Brief Overview and Critical Factors. Substantial research efforts in micro- and nanoscale science and technology are aimed at controlling material topography, surface biochemistry, and mechanical properties, in order to mimic and understand the natural cellular environment. In this way, many techniques (e.g., chemical vapor deposition, lithography, and sputtering) have achieved high fabrication resolutions which made it possible to study the effects of material properties on cell-material interactions [78–81]. These techniques may be used to fabricate nanomaterials, such as nanoparticles, nanodots, nanostructured surfaces, and nanoarchitected scaffolds composed of nanofibers which can directly affect the cells' focal attachment and apply forces that change the cell shape and alignment—important factors in controlled cell differentiation [2, 73]. Furthermore, some of these techniques are used to chemically modify the surface with reactive radicals [82, 83], control degradation rates, hydrophilicity [84], and ensure proper presentation of the growth factors, either soluble or attached, thereby directly influencing SC behavior [7–9, 85].

As extensively reported, the ECM plays a significant role in controlling cellular behavior by different factors (forces, topography, growth factors, and ligands) at different levels—from macro- to nanoscales [1, 7, 9–11, 86]. Here we emphasize that materials science approaches hold a major potential for the recreation of diverse cellular environments, which can control these factors in order to better mimic and understand the natural physicochemical ECM features, any relevant spatial, and temporal scales [7, 8, 10]. The most advanced approach is to reduce the complex *in vivo* system to a controllable simplified system where the desirable factors (e.g., density, porosity, surface energy, topography, chemical radicals, surface ligands, and soluble factors) are combined with the custom designed nanostructures, surfaces, or scaffolds [15]. This approach is very promising to increase our understanding of the most relevant factors for SC control [7].

In the following, we will discuss engineered biomaterials with nanofeatures, either functionalized or functionalized with the specific growth factors. This approach helps to maintain SCs “stemness,” which is essential for stem cell therapy or, alternatively, to differentiate the SCs, which is crucial for tissue engineering. Nanomaterials will be discussed in order of increasing dimensionality (from 0D to 3D).

3.2. Zero- and One-Dimensional Nanomaterials. Having at least two dimensions in the nanoscale, 0D and 1D materials have huge surface/volume ratios which enable properties that are different compared to film/bulk materials. These properties are mainly guided by the materials' composition, size, and shape, crystallinity, and how they emerge as a surface property [76, 87–89]. Depending on the media, some characteristics, such as the surface charge, hydrophobicity, particle aggregation, and dissolution, are of great importance for biological applications. Moreover, these properties regulate the interaction of nanomaterials with proteins dispersed

in the media [75, 76, 90, 91] and with cells (e.g., binding receptors, blocking pores, and membrane rupture) [92–94].

Nanoparticles, nanodots, nanowires, carbon nanotubes (CNT), graphene flakes, and many other zero- and one-dimensional materials have found numerous applications in biomedicine. For example, quantum dots and CNTs have been used for *in vivo* imaging [95, 96], and nanofibers and nanoparticles have been used for gene/drug delivery [97, 98]. Moreover, magnetic nanoparticles were also used to induce hyperthermal tumor reduction [89]; Ag and Au nanoparticles [99] have bactericidal properties (Ag, Au [99]) whereas TiO₂, ZnO, and organic [100] nanoparticles have been shown to have high UV absorbance. Recently, other versatile materials have been designed for high-precision sensing [101, 102].

Despite many biomedical-related applications of this class of nanomaterials, only a few applications on direct SC differentiation and maintenance have been reported in the literature. Meanwhile, these small building blocks can dramatically change the media properties, like hydrogels' stiffness and polymers' conductivity. Recently, it was reported that a hybrid hydrogel-CNTs reinforced scaffold induced a rapid hMSC proliferation [103]. Their effect was due to the suitable mechanical properties of the scaffold. These properties could be achieved by controlling the CNT quantity, for the formation of specific tissues (e.g., cardiac [104]). The CNT were also incorporated in polymer matrices to fabricate electrically conductive scaffolds, aiming at differentiation and interaction with neural and cardiac cells via electric signals [103, 105, 106].

It is well known that nanomaterials in a biological fluid bind with proteins differently from plain substrates [75, 76, 90], forming an organized and complex (e.g., time-dependent) structure called the “protein corona.” Some common proteins, like albumin, immunoglobulin, and fibrinogen, are found to bind strongly to CNTs, iron oxide, and polymeric particles. The properties listed above (e.g., surface composition, hydrophobicity, and charge) influence the protein adsorption and mediate cell-NP interaction (e.g., binding, uptake). Therefore, the understanding of the formation of the protein corona is seen as one of the important objectives in bio-nanoscience [76, 90–93].

Ranging from microseconds to days [91], the duration of protein-nanoparticle interaction can be used for controllable protein delivery through to SC control. It can be directly introduced into nondegradable (or with difficult degradation rate control) scaffolds [10, 103] or *in vivo* [3], as was done before with other biochemical factors loaded into microspheres [107, 108]. Nanoparticle-protein interaction also represents a promising application of protein presentation in diversified conformations [1, 7, 76, 86, 109], which is an important issue in the SC fate selection.

Using nanomaterials, it is also possible to produce unique thin films. For example, TiO₂ nanoparticles increase MSC attachment by altering surface roughness [110]. In another study, the use of TiN nanoparticles also promotes hMSCs attachment. More than merely cell attachment, applications of these nanomaterial films can be extended, targeting protein binding and presentation as well as controllable hydrophobicity.

3.3. Two-Dimensional Nanomaterials. Biomaterial designed surfaces are the simplest, more controllable- and well-explored model for probing factors for controlling the cell fate (different ligand presentation strategy can be found in Figure 2(b)). The development of building and patterning techniques has made it easier to improve the understanding of cell biology over the smallest scale of the interaction between the cells and their natural niches. Furthermore, this development made it possible to mimic such niches by appropriate material patterns—from hydrogels using soft embossing technique to hard ceramics by electron beam lithography (EBL). The EBL technique—just one example among many useful techniques—can provide virtually any topographical nanoarchitecture desired (e.g., cones, tubes, pitches, and domes) in order to mimic the cell niche.

Cells have the ability to sense and adapt to these environmental nanofeatures, using their filopodia [17, 111–113]. Although this has been known, at least since 1952 [114], the improvement of fabrication techniques over the last decade has allowed the study of interactions at markedly smaller scales. Topography combined with material composition and hardness was shown to exert spatially resolved forces over the cells' cytoskeleton [2, 16–18, 115–117], thereby modifying the cell shape and possibly controlling their fate. Chen et al. showed that smaller ECM islands change cell morphology (leading to a more rounded shape), profoundly altering the actin cytoskeleton and the organization of focal contacts [115, 116] (Figures 3(a) and 3(b)).

More examples of the options for nanoscale control over different cell types can be found elsewhere related to the dimensions and type of the nanostructure (e.g., grooves, pits, and pores) [16, 18, 112, 113, 118]. For example, an increase in the apoptotic response of endothelial cells was related to a decrease in the diameter of the cell's culture size [16]. Cell fate is therefore controlled by complex intracellular mechanisms affected not only by the size and type of nanostructure but also by symmetry. Highly ordered square nanoarrays produced by EBL induced low fibroblasts adhesion (Figure 4) [113]. Moreover, normalised array data show broad downregulation of genes in fibroblasts cultured on hexagonal pattern, indicating that mechanical forces lead to changes in gene regulation [117]. However, the same hexagonal symmetry of gold nanodots binding with integrin receptors has shown that separation between dots is an important factor to control cell adhesion and proliferation [119].

These and many other mechanisms can be used to direct SC growth and differentiation [120]. The same mechanisms to control the cell shape, alignment, and adhesion using mimic-designed biomaterials were studied in order to control stem cell proliferation and differentiation [17]. A similar effect of low adhesion induced by highly ordered nanotopographies was reported by Dalby et al., where they demonstrated significantly increased hMSC osteogenic differentiation [18]. Mesenchymal stem cells also show clear alignment and elongation when cultured on a surface with nanogrooves [121, 122]. Yim et al. also reported that the upregulation of neuronal markers (SOX2, MAP2, neurofilament light peptide, and tyrosine hydroxylase) was observed and enhanced if the surface was coated with retinoic acid [121].

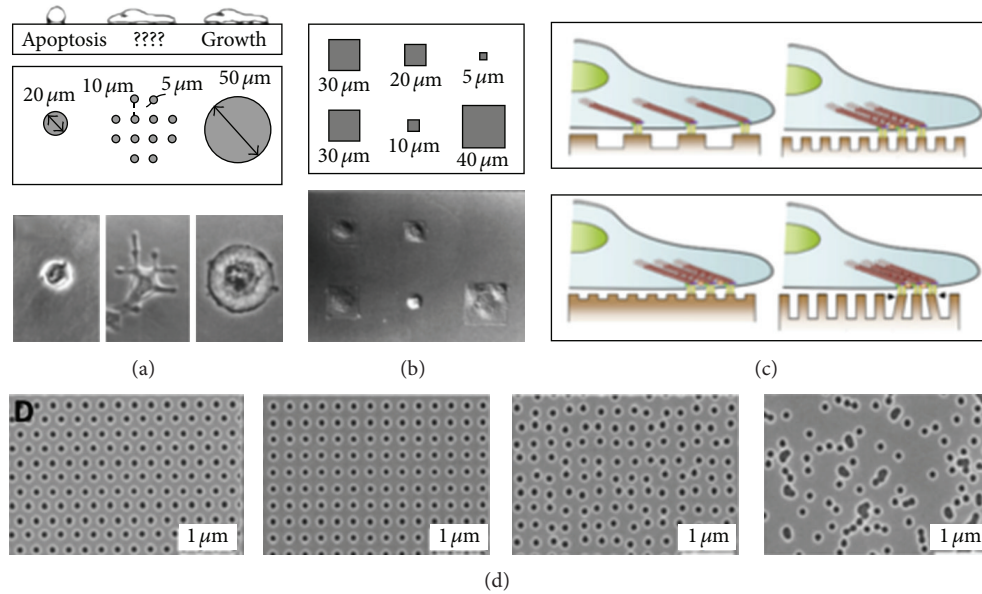


FIGURE 3: (a) Substrate controlling the cell shape and fate. (b) The signal islands strategy being applied to control stem cells. (c) Different nanostructured surface exerts different forces over the cytoskeleton of the cell. (d) Example of nanostructured organization (hexagonal, square, dislocated square, and disordered). ((a) and (b) reprinted from [16] with permission from AAAS. (c) reprinted from [17], Copyright (2009), with permission from Elsevier. (d) reprinted by permission from Macmillan Publishers Ltd.: Nature Materials [18], Copyright (2007).)

The above studies suggest that nanotopological cues may be used to direct hMSC and hESC into specific cell lineages. Acting as a component of the ECM, they change the cell shape—that is, modify the cytoskeleton structure—by controlling the number and density of focal adhesion sites in response to nanostructures shape, size, and symmetry (Figure 3(c) and 3(d)). A direct consequence is the change in the cell's cytoskeleton's structure which in turn activates specific genes via mechanotransduction mechanisms (Figure 3(c)), which are presently not fully understood. Moreover, nanotopography can be used as a spatially well-defined platform to exert proper presentation of immobilized biochemical factors (e.g., proteins, ligands, and radical groups) in order to control cell adhesion, migration, and differentiation [66, 123]. Furthermore, surface nanoarchitecturing can dramatically change the surface properties, for example, hydrophilicity [18] and biocompatibility [101].

Graphene is another 2D material being actively studied for SC support. Although it is a relatively new material, its surface properties were shown to promote growth and proliferation of hMSC on a range of graphene-coated substrates [124] and to enhance the differentiation of human neural stem cells (hNSC) [125]. Moreover, graphene and graphene oxide were shown to stimulate hMSC differentiation toward the osteogenic lineage [126–128]. These materials were also studied as a platform for induced pluripotent SC and induced differentiation of these cells into an endodermal type [129].

3.4. Three-Dimensional Nanomaterials. The natural niche for tissue-specific adult SCs is not a plane surface. In contrast, it is three-dimensional and presents biological cues at different

scales and directions (Figure 1(b)) [1, 7–9, 130]. Moreover, cells are not static and can “feel” the presence of tension and electrical signals in media. A 3D fibrous scaffold is a viable model to use as a mimic of body tissue when studying the proliferation and differentiation of SCs [131–133]. Whilst 2D materials represent a simple model for isolating the control factors for SCs in fundamental research, 3D materials possess a more complex architecture which can be tailored more precisely for real tissue engineering. The combination of these scaffolds and adult cells (e.g., fibroblasts and osteoblasts) for the regeneration of connective tissues is well documented [9, 134–138].

Commonly made of biopolymers, nanofibrous scaffolds (NFS) are used to support SC growth (attachment, proliferation, and organization) and differentiation [8, 10, 11, 70]. Recent studies reported that NFS can promote the differentiation of hMSCs even without intentional addition of growth factors [139]. However, similar to other nanoarchitected surfaces, nanofibers can also be designed for molecule/ligand presentation and delivery [140–142]. In addition to surface composition and mechanical properties, diffusion of GFs and migration of cells should be taken into account.

Nevertheless, the results previously discussed for 2D materials, such as cell alignment to substrate and controlling cell size and shape, also hold for 3D materials. For example, using the electrospinning technique, Li et al. produced and used polymer NFS to induce differentiation of hMSC into the chondrocyte lineage in order to substitute for the micromass cell pellet culture [143]. The same group reported the differentiation of hMSCs from a single patient into adipogenic, chondrogenic, and osteogenic lineages utilizing

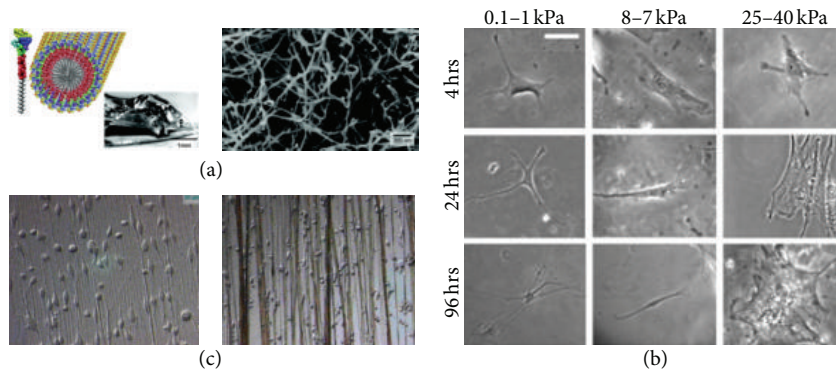


FIGURE 4: (a) Self-assembled peptide, micro- and SEM view of the produced scaffold. (b) Matrix elasticity controlling the stem cell fate. (c) Cells growing on nano- and microfibers scaffolds with visible evidences of cell alignment with fibers produced via electrospinning. ((a) reprinted from [19] with permission from AAAS., (b) reprinted from [2], Copyright (2006), with permission from Elsevier., (c) reprinted from [20], Copyright (2005), with permission from Elsevier).

the same NF matrix [144]. The same technique was also used to produce aligned nano- and micro-FS [20]. Neural SCs cultured on that media grew such that they were aligned with the fibers, independently of their diameter (Figure 4(c)). However, the differentiation rates were higher (as evidenced by a strong protein expression) on the nanofibrous rather than on the microfibrinous scaffolds [20]. Importantly, not only differentiation but SC proliferation was reported using synthetic polyamide NF matrix [133].

A notable advantage of these materials is the reasonably high level of control over elasticity, an important characteristic due to the strong influence over the SC fate [2, 145]. This property is hard to control when using 2D materials and can be set closer to the elasticity of biological tissues using nanofibers [7]. Moreover, introduction of carbon nanotubes/fibers into polymeric matrices can lead to an increase in mechanical properties, electrical conductivity, and reactivity of the biomaterials [146, 147]. Recently, Subramony et al. [134] showed the time control of mechanical stimulation during MSC growth and its effects on cell differentiation. Mechanical tension combined with the matrix alignment led to the development of fibroblasts *in vitro* without any significant chemical influence.

Instead of polymers, another two classes of materials that are used for NF 3D scaffolds deserve specific attention, namely, carbon nanotubes/fibers and self-assembled peptide nanofibers (Figure 4(a)). Carbon nanomaterials have already been discussed in this review. Nevertheless, nanofibers of this abundant and nontoxic material have been effective in differentiating neural stem cells as well as offering good electrical conductivity, high reactivity [146], and increased absorption of laminin [148]. On the other hand, some peptide sequences known to direct SC differentiation can self-assemble in order to form a high-density NF scaffold [19]. Some useful characteristics of these peptide scaffolds are the high water content and the diffusion of nutrients, bioactive factors, and oxygen sufficient for the survival of large numbers of cells for extended periods of time [19].

4. Potential Use of Plasmas for Materials for Stem Cell Control

4.1. Plasma-Based Process Overview. Plasma-based synthesis and processing of nanomaterials are an interdisciplinary research field [14, 15, 149]. A wide range of applications resulted from the control over the properties involved in plasma-based systems such as source power, frequency, and chemistry. A range of species such as ions, electrons, atoms, and radicals are present in a plasma discharge. The principal property of plasma processes is the capability to deliver these species at a desired substrate with controllable energy, thus enabling nanoscale self-assembly [150–155] and deterministic fabrication of nanomaterials [14, 15, 152, 156–164]. Some examples of plasma-produced nanomaterials are presented in Figure 5. Interestingly, these carbon-based nanostructures—vertically aligned graphene and carbon nanotubes—can only be obtained via plasma-based processes [165].

The focus on direct medical applications of plasmas—where the related substrate can be a living tissue—is also increasing [166, 167]. For example, low-temperature plasmas have been used for treating diseases in animal models [88, 168, 169]. Reactive species produced in low-temperature plasma (e.g., free radicals as well as reactive oxygen and nitrogen species (ROS/RNS) such as O, OH, H₂O₂, O₃, NO, and NO₂) [169, 170]) have a fundamental role in chemical reactions, as they can be used to regulate the level of ROS and RNS in intracellular space in order to control cell fate [88, 167]. The role of ROS and RNS in cell control is widely studied; amongst other things they have been shown to influence cell “stemness” [171] and proliferation [172, 173].

Recently, atmospheric-pressure plasma jets showed a special selectivity, killing cancer cells without affecting normal cells [174]. These and similar (e.g., dielectric barrier discharges) devices were also used under different doses to inactivate pathogens and microorganisms such as bacteria, fungi, and viruses [168, 169, 175]. This type of plasma has found numerous applications in medicine and several others such as sterilization of surgical instruments, skin,

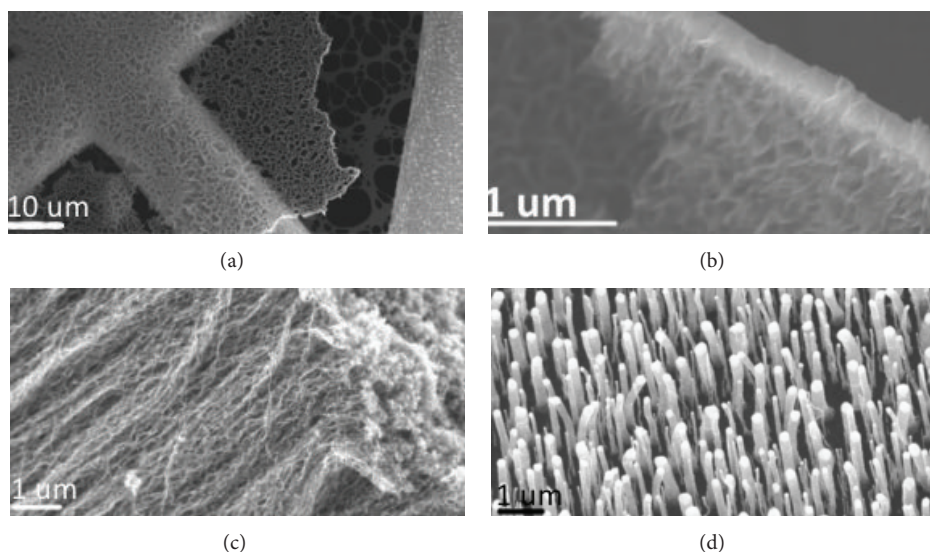


FIGURE 5: SEM of plasma-produced carbon nanostructures. (a) Vertical aligned graphene (VAG) on a TEM grid. (b) Detail of VAG. (c) Side view of high-density vertical aligned carbon nanotubes (VACN). (d) Top view of low-density VACN tips. Original research results from the Plasma Nanoscience Laboratories at CSIRO.

and wound disinfection/healing [88, 176–180]. Atmospheric pressure plasmas have also been demonstrated to support “plasma bullets” [181, 182]; such exotic structures are likely to lead to a range of promising medical applications and should be the subject of further investigation.

Control over SC fate mediated by plasmas is also possible; for example [183], atmospheric-pressure room-temperature plasmas can effectively induce *in vitro* differentiation of neural stem cells (NSCs) predominantly into neuronal lineage. After plasma treatment, the murine NSC exhibited rapid proliferation and differentiation into neurons with high efficiency.

There are, however, potential disadvantages associated with the use of plasmas for direct medical application; these are largely related to the presence of plasma-generated energetic ROS/RNS and UV radiation [184]. Studies have shown that, depending on the specific conditions (i.e., plasma dose/irradiation and cell type), plasmas may affect cell properties (i.e., adhesion, membrane permeability, migration, and apoptosis/necrosis) and possibly damage DNA and modify proteins [184]. Further study and clinical trials are required before practical use of plasmas as direct medical tools.

Plasmas may also be used to fabricate micro- and nanostructures (see Figure 5) as well as appropriately functionalized surfaces, suitable for SC control. The aim of the rest of this section is to track where plasma technologies have an implication over materials production and modification for stem cell control and highlight where it could have potential uses.

4.2. Plasma-Based Nanofabrication. The existence of energetic species in plasmas makes it suitable for dry etching applications and many other materials synthesis and processing [152, 157, 159, 163, 185]. These techniques can produce patterns in hard materials at micro- and nanoscales. These

patterns in turn can be used to control the alignment and shape of SCs. The material removed from a target using plasmas can also be used for functional thin film deposition, with almost no restriction over the target composition or substrate shape—which is an advantage for coating 3D materials [14, 15, 149, 186]. Moreover, the properties of these thin films can be precisely tailored, for example, to enable degradation after use [159, 187]. Other considerations for biological applications are the production time and cost [16], which can be reduced in plasma processes [151, 153, 188].

The applications, namely, etching, deposition and, surface modification, are the most common in literature, although plasma-based processes are capable of producing a variety of nanomaterials [151, 189], namely, nanoparticles [190, 191], nanodots [155, 192], and various allotropes of carbon (e.g., nanodiamond [15], nanotubes [158, 189], nanocones [193], nanowalls, and graphene [102, 160, 161, 194]). Plasma techniques also provide the control over the properties of these nanomaterials (e.g., size, shape, and surface reactivity) [99, 152, 157, 162, 163, 195]. As discussed above, these properties are essential to bind proteins and cells, as well as for the delivery of specific (e.g., differentiation) factors in order to control the SC fate. Moreover, due to the unique ability to dissociate molecules (e.g., hydrogen), the control over some properties is not achievable by other techniques such as neutral gas-based CVD or by wet chemistry routes [165].

The control over the nanostructural properties is related to the plasma ability to generate and concentrate building units (BU) of nanoscale matter [15, 99]. Moreover, these BU can be directly delivered to a substrate and build a wide range of complex architectures discussed previously to mimic the SC natural niche and control cell fate. The plasma environments have specific features and control self-assembly of nanostructures into patterns and arrays (often termed “mask-less”). Plasma processes have also been reported to

lead to a sustainable energy saving and reduction of greenhouse emissions. Interestingly, carbon nanotubes and other one-dimensional nanostructures show pronounced vertical alignment which is not common to thermal CVD [165].

For the same reason, plasma-based technologies have long been reported as an effective route for surface treatment [15]. The importance of this fact is, for example, the ability to chemically improve the biocompatibility of the surface by increasing its hydrophilicity, which in turn increases the cell proliferation [8, 158, 163]. Moreover, several limitations (e.g., control over chemical properties and difficulties in sterilization) could be overcome by plasma-based techniques. Furthermore, plasma-based techniques were used to functionalize important nanomaterials such as CNTs leading to better substrates for the enhancement of cell growth and proliferation [196].

Regarding the control of SC fate, it is well known that the proliferation (without differentiation) or the differentiation to desired lineages requires both growth factors and, for some specific SC, mechanical stimulation. Several strategies can be followed to reach this goal, for example, production of specific tailored nanostructures with or without bound/immobilised growth factors that directly promote SC expansion or controlled differentiation. These nanostructures can be added to hydrogels/nanoscaffolds in order to temporally control the delivery of GFs and migration of cells. Surfaces can also be plasma-tailored with desired nanostructures to mechanically guide the SC via focal contact or be used as binding point to ligands/chemical radicals or both, leading to SC proliferation/differentiation according to the input stimulus.

An example involving a plasma-treated nanostructure coated with a specific GF was reported by Arnold et al. [119]. In order to understand the role of a precise molecular arrangement on cell response, a substrate was patterned with Au nanodots (<8 nm), highly ordered with controllable distances, via self-assembly of diblock copolymer micelles. After the assembly of the nanodots, the polymer was completely removed by the plasma treatment and the dot-patterned substrate was functionalized with a specific peptide (c(RGDfK)), which has a high affinity to the $\alpha v \beta$ -integrin. Due to the small surface area of the nanodot, only one integrin can attach to each dot and the effect of the arranged binding sites could be studied. Such an approach is powerful as it enables control over the presentation of mass amounts of specific signals/ligands at precise spatial locations and size scales and therefore an ability to dissect how cells respond to variations in ligand density. There is great potential to exploit this approach to critically examine the presentation of defined amounts of combinations of biological signals to stem cells. We predict that sophisticated nanoengineering based on plasma generated biomaterials will underpin a new era in cell culture.

5. Conclusions and Challenges for Future Research

In this review, we have discussed sources and applications of SCs and the mechanisms by which they can be controlled and

subsequently, the use of nanomaterials to control SCs. We have pointed out the properties that make low-temperature plasmas a suitable tool to use in the production and functionalization of these NMs for more effective and specific interaction with SCs, both through direct treatment and as a versatile nanofabrication tool [15].

Due to the many unique characteristics of low-temperature plasmas, we believe that the direct use of plasmas, especially atmospheric plasmas, should be considered as a viable strategy to direct SC differentiation. Plasmas as a nanofabrication tool should be focused on developing “lab on a chip” devices as suitable platforms for the differentiation of SCs into any cell lineage through mechanical and/or electrical stimulus.

Tissue engineering and SC biology can benefit greatly from advances in plasma nanoscience [15]. Nanomaterial design is leading to a greater degree of control over cell attachment and migration in order to grow multilevel tissues (or organs, e.g., skin). This control also contributes to basic studies on mimicking ECM properties and ligands quantity and presentation as well as elucidating the role of time in growth factors delivery.

Acknowledgments

F. F. Borghi acknowledges the support from the Science Without Borders Program of the Brazilian Government, A. E. Rider and Z. J. Han acknowledge the support from the CSIRO Sensors and Sensor Network TCP, and A. E. Rider and S. Kumar acknowledge the support from the CSIRO OCE Postdoctoral Fellowship schemes. This work is partially supported by the Australian Research Council (ARC) and CSIRO's OCE Science Leadership Program.

References

- [1] K. Saha, J. F. Pollock, D. V. Schaffer, and K. E. Healy, “Designing synthetic materials to control stem cell phenotype,” *Current Opinion in Chemical Biology*, vol. 11, no. 4, pp. 381–387, 2007.
- [2] A. J. Engler, S. Sen, H. L. Sweeney, and D. E. Discher, “Matrix elasticity directs stem cell lineage specification,” *Cell*, vol. 126, no. 4, pp. 677–689, 2006.
- [3] J. A. Burdick and G. Vunjak-Novakovic, “Engineered microenvironments for controlled stem cell differentiation,” *Tissue Engineering A*, vol. 15, no. 2, pp. 205–219, 2009.
- [4] G. H. Altman, R. L. Horan, I. Martin et al., “Cell differentiation by mechanical stress,” *The FASEB Journal*, vol. 16, no. 2, pp. 270–272, 2002.
- [5] D. L. Butler, N. Juncosa-Melvin, G. P. Boivin et al., “Functional tissue engineering for tendon repair: a multidisciplinary strategy using mesenchymal stem cells, bioscaffolds, and mechanical stimulation,” *Journal of Orthopaedic Research*, vol. 26, no. 1, pp. 1–9, 2008.
- [6] V. Terraciano, N. Hwang, L. Moroni et al., “Differential response of adult and embryonic mesenchymal progenitor cells to mechanical compression in hydrogels,” *Stem Cells*, vol. 25, no. 11, pp. 2730–2738, 2007.
- [7] M. P. Lutolf, P. M. Gilbert, and H. M. Blau, “Designing materials to direct stem-cell fate,” *Nature*, vol. 462, no. 7272, pp. 433–441, 2009.

- [8] E. Dawson, G. Mapili, K. Erickson, S. Taqvi, and K. Roy, "Biomaterials for stem cell differentiation," *Advanced Drug Delivery Reviews*, vol. 60, no. 2, pp. 215–228, 2008.
- [9] N. S. Hwang, S. Varghese, and J. Elisseeff, "Controlled differentiation of stem cells," *Advanced Drug Delivery Reviews*, vol. 60, no. 2, pp. 199–214, 2008.
- [10] C. Chai and K. W. Leong, "Biomaterials approach to expand and direct differentiation of stem cells," *Molecular Therapy*, vol. 15, no. 3, pp. 467–480, 2007.
- [11] C. Cha, W. B. Liechty, A. Khademhosseini, and N. A. Peppas, "Designing biomaterials to direct stem cell fate," *ACS Nano*, vol. 6, no. 11, pp. 9353–9358, 2012.
- [12] T. M. A. Henderson, K. Ladewig, D. N. Haylock, K. M. Mclean, and A. J. O. Connor, "Cryogels for biomedical applications," *Journal of Materials Chemistry B*, vol. 1, pp. 2682–2695, 2013.
- [13] J. Nigro, J. F. White, J. A. M. Ramshaw, D. N. Haylock, S. K. Nilsson, and J. A. Werkmeister, "The effect of bovine endosteum-derived particles on the proliferation of human mesenchymal stem cells," *Biomaterials*, vol. 31, no. 21, pp. 5689–5699, 2010.
- [14] K. Ostrikov, U. Cvelbar, and A. B. Murphy, "Plasma nanoscience: setting directions, tackling grand challenges," *Journal of Physics D*, vol. 44, no. 17, Article ID 174001, 2011.
- [15] K. Ostrikov, E. C. Neyts, and M. Meyyappan, "Plasma nanoscience: from nano-solids in plasmas to nano-plasmas in solids," *Advances in Physics*, vol. 62, no. 2, pp. 113–224, 2013.
- [16] C. S. Chen, M. Mrksich, S. Huang, G. M. Whitesides, and D. E. Ingber, "Geometric control of cell life and death," *Science*, vol. 276, no. 5317, pp. 1425–1428, 1997.
- [17] F. Guilak, D. M. Cohen, B. T. Estes, J. M. Gimble, W. Liedtke, and C. S. Chen, "Control of stem cell fate by physical interactions with the extracellular matrix," *Cell Stem Cell*, vol. 5, no. 1, pp. 17–26, 2009.
- [18] M. J. Dalby, N. Gadegaard, R. Tare et al., "The control of human mesenchymal cell differentiation using nanoscale symmetry and disorder," *Nature Materials*, vol. 6, no. 12, pp. 997–1003, 2007.
- [19] G. A. Silva, C. Czeisler, K. L. Niece et al., "Selective differentiation of neural progenitor cells by high-epitope density nanofibers," *Science*, vol. 303, no. 5662, pp. 1352–1355, 2004.
- [20] F. Yang, R. Murugan, S. Wang, and S. Ramakrishna, "Electrospinning of nano/micro scale poly(l-lactic acid) aligned fibers and their potential in neural tissue engineering," *Biomaterials*, vol. 26, no. 15, pp. 2603–2610, 2005.
- [21] K. Okita, T. Ichisaka, and S. Yamanaka, "Generation of germline-competent induced pluripotent stem cells," *Nature*, vol. 448, no. 7151, pp. 313–317, 2007.
- [22] M. Wernig, A. Meissner, R. Foreman et al., "In vitro reprogramming of fibroblasts into a pluripotent ES-cell-like state," *Nature*, vol. 448, no. 7151, pp. 318–324, 2007.
- [23] M. Mimeault and S. K. Batra, "Concise review: recent advances on the significance of stem cells in tissue regeneration and cancer therapies," *Stem Cells*, vol. 24, no. 11, pp. 2319–2345, 2006.
- [24] C. Fehrer and G. Lepperdinger, "Mesenchymal stem cell aging," *Experimental Gerontology*, vol. 40, no. 12, pp. 926–930, 2005.
- [25] A. Stolzing and A. Scutt, "Age-related impairment of mesenchymal progenitor cell function," *Aging Cell*, vol. 5, no. 3, pp. 213–224, 2006.
- [26] L. B. To, D. N. Haylock, P. J. Simmons, and C. A. Juttner, "The biology and clinical uses of blood stem cells," *Blood*, vol. 89, no. 7, pp. 2233–2258, 1997.
- [27] M. J. Evans and M. H. Kaufman, "Establishment in culture of pluripotent cells from mouse embryos," *Nature*, vol. 292, no. 5819, pp. 154–156, 1981.
- [28] L. Jakobsson, J. Kreuger, and L. Claesson-Welsh, "Building blood vessels—stem cell models in vascular biology," *The Journal of Cell Biology*, vol. 177, no. 5, pp. 751–755, 2007.
- [29] S.-I. Nishikawa, L. M. Jakt, and T. Era, "Embryonic stem-cell culture as a tool for developmental cell biology," *Nature Reviews Molecular Cell Biology*, vol. 8, no. 6, pp. 502–507, 2007.
- [30] D. J. Prockop, "Marrow stromal cells as stem cells for non-hematopoietic tissues," *Science*, vol. 276, no. 5309, pp. 71–74, 1997.
- [31] M. F. Pittenger, "Multilineage potential of adult human mesenchymal stem cells," *Science*, vol. 284, no. 5411, pp. 143–147, 1999.
- [32] J. A. Thomson, J. Itskovitz-Eldor, S. S. Shapiro et al., "Embryonic stem cell lines derived from human blastocysts," *Science*, vol. 282, no. 5391, pp. 1145–1147, 1998.
- [33] K. Takahashi and S. Yamanaka, "Induction of pluripotent stem cells from mouse embryonic and adult fibroblast cultures by defined factors," *Cell*, vol. 126, no. 4, pp. 663–676, 2006.
- [34] M. Tada, Y. Takahama, K. Abe, N. Nakatsuji, and T. Tada, "Nuclear reprogramming of somatic cells by in vitro hybridization with ES cells," *Current Biology*, vol. 11, no. 19, pp. 1553–1558, 2001.
- [35] G. Bianchi, A. Banfi, M. Mastrogiacomo et al., "Ex vivo enrichment of mesenchymal cell progenitors by fibroblast growth factor 2," *Experimental Cell Research*, vol. 287, no. 1, pp. 98–105, 2003.
- [36] I. Martin, A. Muraglia, G. Campanile, R. Cancedda, and R. Quarto, "Fibroblast growth factor-2 supports ex vivo expansion and maintenance of osteogenic precursors from human bone marrow," *Endocrinology*, vol. 138, no. 10, pp. 4456–4462, 1997.
- [37] L. A. Solchaga, K. Penick, J. D. Porter, V. M. Goldberg, A. I. Caplan, and J. F. Welter, "FGF-2 enhances the mitotic and chondrogenic potentials of human adult bone marrow-derived mesenchymal stem cells," *Journal of Cellular Physiology*, vol. 203, no. 2, pp. 398–409, 2005.
- [38] S. Tsutsumi, A. Shimazu, K. Miyazaki et al., "Retention of multilineage differentiation potential of mesenchymal cells during proliferation in response to FGF," *Biochemical and Biophysical Research Communications*, vol. 288, no. 2, pp. 413–419, 2001.
- [39] H. J. Rippon, J. M. Polak, M. Qin, and A. E. Bishop, "Derivation of distal lung epithelial progenitors from murine embryonic stem cells using a novel three-step differentiation protocol," *Stem Cells*, vol. 24, no. 5, pp. 1389–1398, 2006.
- [40] M. Nakanishi, T. S. Hamazaki, S. Komazaki, H. Okochi, and M. Asashima, "Pancreatic tissue formation from murine embryonic stem cells in vitro," *Differentiation*, vol. 75, no. 1, pp. 1–11, 2007.
- [41] D. T. Scadden, "The stem-cell niche as an entity of action," *Nature*, vol. 441, no. 7097, pp. 1075–1079, 2006.
- [42] S. J. Morrison and A. C. Spradling, "Stem cells and niches: mechanisms that promote stem cell maintenance throughout life," *Cell*, vol. 132, no. 4, pp. 598–611, 2008.
- [43] R. Peerani and P. W. Zandstra, "Enabling stem cell therapies through synthetic stem cell-niche engineering," *The Journal of Clinical Investigation*, vol. 120, no. 1, pp. 60–70, 2010.
- [44] P. M. Gilbert and H. M. Blau, "Engineering a stem cell house into a home," *Stem Cell Research & Therapy*, vol. 2, no. 1, article 3, 2011.

- [45] D. N. Haylock and P. J. Simmons, "Approaches to hematopoietic stem cell separation and expansion," in *Handbook on Adult Stem Cell Biology*, p. 615, Elsevier/Academic Press, San Diego, Calif, USA, 2004.
- [46] A. S. Hoffman, "Hydrogels for biomedical applications," *Advanced Drug Delivery Reviews*, vol. 54, no. 1, pp. 3–12, 2002.
- [47] J. L. Drury and D. J. Mooney, "Hydrogels for tissue engineering: scaffold design variables and applications," *Biomaterials*, vol. 24, no. 24, pp. 4337–4351, 2003.
- [48] J. Kopeček and J. Yang, "Hydrogels as smart biomaterials," *Polymer International*, vol. 56, no. 9, pp. 1078–1098, 2007.
- [49] J. A. Hubbell, "Biomaterials in tissue engineering," *Biotechnology*, vol. 13, no. 6, pp. 565–576, 1995.
- [50] W. E. Hennink and C. F. van Nostrum, "Novel crosslinking methods to design hydrogels," *Advanced Drug Delivery Reviews*, vol. 54, no. 1, pp. 13–36, 2002.
- [51] C. Xu, M. S. Inokuma, J. Denham et al., "Feeder-free growth of undifferentiated human embryonic stem cells," *Nature Biotechnology*, vol. 19, no. 10, pp. 971–974, 2001.
- [52] M. Amit, C. Shariki, V. Margulets, and J. Itskovitz-Eldor, "Feeder layer- and serum-free culture of human embryonic stem cells," *Biology of Reproduction*, vol. 70, no. 3, pp. 837–845, 2004.
- [53] G. M. Beattie, A. D. Lopez, N. Bucay et al., "Activin A maintains pluripotency of human embryonic stem cells in the absence of feeder layers," *Stem Cells*, vol. 23, no. 4, pp. 489–495, 2005.
- [54] S. Battista, D. Guarnieri, C. Borselli et al., "The effect of matrix composition of 3D constructs on embryonic stem cell differentiation," *Biomaterials*, vol. 26, no. 31, pp. 6194–6207, 2005.
- [55] C.-F. Chang, M.-W. Lee, P.-Y. Kuo, Y.-J. Wang, Y.-H. Tu, and S.-C. Hung, "Three-dimensional collagen fiber remodeling by mesenchymal stem cells requires the integrin-matrix interaction," *Journal of Biomedical Materials Research A*, vol. 80, no. 2, pp. 466–474, 2007.
- [56] K. E. McCloskey, M. E. Gilroy, and R. M. Nerem, "Use of embryonic stem cell-derived endothelial cells as a cell source to generate vessel structures in vitro," *Tissue Engineering*, vol. 11, no. 3–4, pp. 497–505, 2005.
- [57] M. S. Ponticciello, R. M. Schinagl, S. Kadiyala, and F. P. Barry, "Gelatin-based resorbable sponge as a carrier matrix for human mesenchymal stem cells in cartilage regeneration therapy," *Journal of Biomedical Materials Research*, vol. 52, no. 2, pp. 246–255, 2000.
- [58] S. Tielens, H. Declercq, T. Gorski, E. Lippens, E. Schacht, and M. Cornelissen, "Gelatin-based microcarriers as embryonic stem cell delivery system in bone tissue engineering: an in-vitro study," *Biomacromolecules*, vol. 8, no. 3, pp. 825–832, 2007.
- [59] S. Gerecht, J. A. Burdick, L. S. Ferreira, S. A. Townsend, R. Langer, and G. Vunjak-Novakovic, "Hyaluronic acid hydrogel for controlled self-renewal and differentiation of human embryonic stem cells," *Proceedings of the National Academy of Sciences of the United States of America*, vol. 104, no. 27, pp. 11298–11303, 2007.
- [60] C. Ventura, M. Maioli, Y. Asara et al., "Butyric and retinoic mixed ester of hyaluronan: a novel differentiating glycoconjugate affording a high throughput of cardiogenesis in embryonic stem cells," *The Journal of Biological Chemistry*, vol. 279, no. 22, pp. 23574–23579, 2004.
- [61] T. Maguire, A. E. Davidovich, E. J. Wallenstein et al., "Control of hepatic differentiation via cellular aggregation in an alginate microenvironment," *Biotechnology and Bioengineering*, vol. 98, no. 3, pp. 631–644, 2007.
- [62] M. Ruhnke, H. Ungefroren, G. Zehle, M. Bader, B. Kremer, and F. Fändrich, "Long-term culture and differentiation of rat embryonic stem cell-like cells into neuronal, glial, endothelial, and hepatic lineages," *Stem Cells*, vol. 21, no. 4, pp. 428–436, 2003.
- [63] V. Planat-Benard, J.-S. Silvestre, B. Cousin et al., "Plasticity of human adipose lineage cells toward endothelial cells: physiological and therapeutic perspectives," *Circulation*, vol. 109, no. 5, pp. 656–663, 2004.
- [64] C. Xu, J.-Q. He, T. J. Kamp et al., "Human embryonic stem cell-derived cardiomyocytes can be maintained in defined medium without serum," *Stem Cells and Development*, vol. 15, no. 6, pp. 931–941, 2006.
- [65] H. J. Lee, J.-S. Lee, T. Chansakul, C. Yu, J. H. Elisseeff, and S. M. Yu, "Collagen mimetic peptide-conjugated photopolymerizable PEG hydrogel," *Biomaterials*, vol. 27, no. 30, pp. 5268–5276, 2006.
- [66] R. McBeath, D. M. Pirone, C. M. Nelson, K. Bhadriraju, and C. S. Chen, "Cell shape, cytoskeletal tension, and RhoA regulate stem cell lineage commitment," *Developmental Cell*, vol. 6, no. 4, pp. 483–495, 2004.
- [67] F. Yang, C. G. Williams, D.-A. Wang, H. Lee, P. N. Manson, and J. Elisseeff, "The effect of incorporating RGD adhesive peptide in polyethylene glycol diacrylate hydrogel on osteogenesis of bone marrow stromal cells," *Biomaterials*, vol. 26, no. 30, pp. 5991–5998, 2005.
- [68] C. R. Nuttelman, M. C. Tripodi, and K. S. Anseth, "In vitro osteogenic differentiation of human mesenchymal stem cells photoencapsulated in PEG hydrogels," *Journal of Biomedical Materials Research A*, vol. 68, no. 4, pp. 773–782, 2004.
- [69] Y. D. Teng, E. B. Lavik, X. Qu et al., "Functional recovery following traumatic spinal cord injury mediated by a unique polymer scaffold seeded with neural stem cells," *Proceedings of the National Academy of Sciences of the United States of America*, vol. 99, no. 5, pp. 3024–3029, 2002.
- [70] S. Levenberg, N. F. Huang, E. Lavik, A. B. Rogers, J. Itskovitz-Eldor, and R. Langer, "Differentiation of human embryonic stem cells on three-dimensional polymer scaffolds," *Proceedings of the National Academy of Sciences of the United States of America*, vol. 100, no. 22, pp. 12741–12746, 2003.
- [71] M. J. Mondrinos, S. Koutzaki, E. Jiwanmall et al., "Engineering three-dimensional pulmonary tissue constructs," *Tissue Engineering*, vol. 12, no. 4, pp. 717–728, 2006.
- [72] C. S. Young, H. Abukawa, R. Asrican et al., "Tissue-engineered hybrid tooth and bone," *Tissue Engineering*, vol. 11, no. 9–10, pp. 1599–1610, 2005.
- [73] D. E. Discher, P. Janmey, and Y.-L. Wang, "Tissue cells feel and respond to the stiffness of their substrate," *Science*, vol. 310, no. 5751, pp. 1139–1143, 2005.
- [74] E. K. F. Yim and K. W. Leong, "Significance of synthetic nanostructures in dictating cellular response," *Nanomedicine: Nanotechnology, Biology, and Medicine*, vol. 1, no. 1, pp. 10–21, 2005.
- [75] T. Cedervall, I. Lynch, S. Lindman et al., "Understanding the nanoparticle-protein corona using methods to quantify exchange rates and affinities of proteins for nanoparticles," *Proceedings of the National Academy of Sciences of the United States of America*, vol. 104, no. 7, pp. 2050–2055, 2007.
- [76] M. Lundqvist, J. Stigler, G. Elia, I. Lynch, T. Cedervall, and K. A. Dawson, "Nanoparticle size and surface properties determine

- the protein corona with possible implications for biological impacts,” *Proceedings of the National Academy of Sciences of the United States of America*, vol. 105, no. 38, pp. 14265–14270, 2008.
- [77] H. V. Unadkat, M. Hulsman, K. Cornelissen et al., “An algorithm-based topographical biomaterials library to instruct cell fate,” *Proceedings of the National Academy of Sciences of the United States of America*, vol. 108, no. 40, pp. 16565–16570, 2011.
- [78] G. M. Whitesides, E. Ostuni, S. Takayama, X. Jiang, and D. E. Ingber, “Soft lithography in biology and biochemistry,” *Annual Review of Biomedical Engineering*, vol. 3, pp. 335–373, 2001.
- [79] J. J. Norman and T. A. Desai, “Methods for fabrication of nanoscale topography for tissue engineering scaffolds,” *Annals of Biomedical Engineering*, vol. 34, no. 1, pp. 89–101, 2006.
- [80] A. Khademhosseini, R. Langer, J. Borenstein, and J. P. Vacanti, “Microscale technologies for tissue engineering and biology,” *Proceedings of the National Academy of Sciences of the United States of America*, vol. 103, no. 8, pp. 2480–2487, 2006.
- [81] D. Falconnet, G. Csucs, H. M. Grandin, and M. Textor, “Surface engineering approaches to micropattern surfaces for cell-based assays,” *Biomaterials*, vol. 27, no. 16, pp. 3044–3063, 2006.
- [82] B. G. Keselowsky, D. M. Collard, and A. J. García, “Integrin binding specificity regulates biomaterial surface chemistry effects on cell differentiation,” *Proceedings of the National Academy of Sciences of the United States of America*, vol. 102, no. 17, pp. 5953–5957, 2005.
- [83] A. J. García, M. D. Vega, and D. Boettiger, “Modulation of cell proliferation and differentiation through substrate-dependent changes in fibronectin conformation,” *Molecular Biology of the Cell*, vol. 10, no. 3, pp. 785–798, 1999.
- [84] W. G. Brodbeck, J. Patel, G. Voskerician et al., “Biomaterial adherent macrophage apoptosis is increased by hydrophilic and anionic substrates in vivo,” *Proceedings of the National Academy of Sciences of the United States of America*, vol. 99, no. 16, pp. 10287–10292, 2002.
- [85] P. X. Ma, “Biomimetic materials for tissue engineering,” *Advanced Drug Delivery Reviews*, vol. 60, no. 2, pp. 184–198, 2008.
- [86] D. Walczyk, F. B. Bombelli, M. P. Monopoli, I. Lynch, and K. A. Dawson, “What the cell ‘sees’ in bionanoscience,” *Journal of the American Chemical Society*, vol. 132, no. 16, pp. 5761–5768, 2010.
- [87] M.-E. Aubin-Tam and K. Hamad-Schifferli, “Structure and function of nanoparticle-protein conjugates,” *Biomedical Materials*, vol. 3, no. 3, Article ID 034001, 2008.
- [88] M. G. Kong, M. Keidar, and K. Ostrikov, “Plasmas meet nanoparticles—where synergies can advance the frontier of medicine,” *Journal of Physics D*, vol. 44, no. 17, Article ID 174018, 2011.
- [89] Q. A. Pankhurst, J. Connolly, S. K. Jones, and J. Dobson, “Applications of magnetic nanoparticles in biomedicine,” *Journal of Physics D*, vol. 36, no. 13, pp. R167–R181, 2003.
- [90] T. Cedervall, I. Lynch, M. Foy et al., “Detailed identification of plasma proteins adsorbed on copolymer nanoparticles,” *Angewandte Chemie—International Edition*, vol. 46, no. 30, pp. 5754–5756, 2007.
- [91] A. E. Nel, L. Mädler, D. Velegol et al., “Understanding biophysicochemical interactions at the nano-bio interface,” *Nature Materials*, vol. 8, no. 7, pp. 543–557, 2009.
- [92] P. Decuzzi and M. Ferrari, “The role of specific and non-specific interactions in receptor-mediated endocytosis of nanoparticles,” *Biomaterials*, vol. 28, no. 18, pp. 2915–2922, 2007.
- [93] H. Gao, W. Shi, and L. B. Freund, “Mechanics of receptor-mediated endocytosis,” *Proceedings of the National Academy of Sciences of the United States of America*, vol. 102, no. 27, pp. 9469–9474, 2005.
- [94] C. C. Fleck and R. R. Netz, “Electrostatic colloid-membrane binding,” *Europhysics Letters*, vol. 67, no. 2, pp. 314–320, 2004.
- [95] P. W. Barone, H. Yoon, R. Ortiz-García et al., “Modulation of single-walled carbon nanotube photoluminescence by hydrogel swelling,” *ACS Nano*, vol. 3, no. 12, pp. 3869–3877, 2009.
- [96] C. Zavaleta, A. de la Zerda, Z. Liu et al., “Noninvasive Raman spectroscopy in living mice for evaluation of tumor targeting with carbon nanotubes,” *Nano Letters*, vol. 8, no. 9, pp. 2800–2805, 2008.
- [97] H. Valo, L. Peltonen, S. Vehviläinen et al., “Electrospray encapsulation of hydrophilic and hydrophobic drugs in poly(L-lactic acid) nanoparticles,” *Small*, vol. 5, no. 15, pp. 1791–1798, 2009.
- [98] T. E. McKnight, A. V. Melechko, D. K. Hensley, D. G. J. Mann, G. D. Griffin, and M. L. Simpson, “Tracking gene expression after DNA delivery using spatially indexed nanofiber arrays,” *Nano Letters*, vol. 4, no. 7, pp. 1213–1219, 2004.
- [99] Z. J. Han, I. Levchenko, S. Kumar et al., “Plasma nanofabrication and nanomaterials safety,” *Journal of Physics D*, vol. 44, no. 17, Article ID 174019, 2011.
- [100] F. J. Aparicio, M. Holgado, A. Borrás et al., “Transparent nanometric organic luminescent films as UV-active components in photonic structures,” *Advanced Materials*, vol. 23, no. 6, pp. 761–765, 2011.
- [101] Y. Zhang, T. R. Nayak, H. Hong, and W. Cai, “Graphene: a versatile nanoplatform for biomedical applications,” *Nanoscale*, vol. 4, no. 13, pp. 3833–3842, 2012.
- [102] A. E. Rider, S. Kumar, S. A. Furman, and K. Ostrikov, “Self-organized Au nanoarrays on vertical graphenes: an advanced three-dimensional sensing platform,” *Chemical Communications*, vol. 48, no. 21, pp. 2659–2661, 2012.
- [103] S. R. Shin, H. Bae, J. M. Cha et al., “Carbon nanotube reinforced hybrid microgels as scaffold materials for cell encapsulation,” *ACS Nano*, vol. 6, no. 1, pp. 362–372, 2012.
- [104] S. R. Shin, S. M. Jung, M. Zalabany et al., “Carbon-nanotube-embedded hydrogel sheets for engineering cardiac constructs and bioactuators,” *ACS Nano*, vol. 7, no. 3, pp. 2369–2380, 2013.
- [105] C. Lau, M. J. Cooney, and P. Atanassov, “Conductive macroporous composite chitosan-carbon nanotube scaffolds,” *Langmuir*, vol. 24, no. 13, pp. 7004–7010, 2008.
- [106] N. W. S. Kam, E. Jan, and N. A. Kotov, “Electrical stimulation of neural stem cells mediated by humanized carbon nanotube composite made with extracellular matrix protein,” *Nano Letters*, vol. 9, no. 1, pp. 273–278, 2009.
- [107] M. Yamamoto and Y. Tabata, “Tissue engineering by modulated gene delivery,” *Advanced Drug Delivery Reviews*, vol. 58, no. 4, pp. 535–554, 2006.
- [108] M. C. Wake, P. D. Gerecht, L. Lu, and A. G. Mikos, “Effects of biodegradable polymer particles on rat marrow-derived stromal osteoblasts in vitro,” *Biomaterials*, vol. 19, no. 14, pp. 1255–1268, 1998.
- [109] F. Meder, J. Wehling, A. Fink et al., “The role of surface functionalization of colloidal alumina particles on their controlled interactions with viruses,” *Biomaterials*, vol. 34, no. 17, pp. 4203–4213, 2013.
- [110] D. S. Kommireddy, S. M. Sriram, Y. M. Lvov, and D. K. Mills, “Stem cell attachment to layer-by-layer assembled TiO₂ nanoparticle thin films,” *Biomaterials*, vol. 27, no. 24, pp. 4296–4303, 2006.

- [111] R. G. Flemming, C. J. Murphy, G. A. Abrams, S. L. Goodman, and P. F. Nealey, "Effects of synthetic micro- and nanostructured surfaces on cell behavior," *Biomaterials*, vol. 20, no. 6, pp. 573–588, 1999.
- [112] A. S. G. Curtis, N. Gadegaard, M. J. Dalby, M. O. Riehle, C. D. W. Wilkinson, and G. Aitchison, "Cells react to nanoscale order and symmetry in their surroundings," *IEEE Transactions on Nanobioscience*, vol. 3, no. 1, pp. 61–65, 2004.
- [113] M. J. Dalby, N. Gadegaard, M. O. Riehle, C. D. W. Wilkinson, and A. S. G. Curtis, "Investigating filopodia sensing using arrays of defined nano-pits down to 35 nm diameter in size," *The International Journal of Biochemistry & Cell Biology*, vol. 36, no. 10, pp. 2005–2015, 2004.
- [114] P. Weiss and B. Garber, "Shape and movement of mesenchyme cells as functions of the physical structure of the medium. Contributions to a quantitative morphology," *Proceedings of the National Academy of Sciences of the United States of America*, vol. 38, pp. 264–280, 1952.
- [115] C. S. Chen, J. L. Alonso, E. Ostuni, G. M. Whitesides, and D. E. Ingber, "Cell shape provides global control of focal adhesion assembly," *Biochemical and Biophysical Research Communications*, vol. 307, no. 2, pp. 355–361, 2003.
- [116] C. S. Chen, M. Mrksich, S. Huang, G. M. Whitesides, and D. E. Ingber, "Micropatterned surfaces for control of cell shape, position, and function," *Biotechnology Progress*, vol. 14, no. 3, pp. 356–363, 1998.
- [117] M. J. Dalby, M. J. P. Biggs, N. Gadegaard, G. Kalna, C. D. W. Wilkinson, and A. S. G. Curtis, "Nanotopographical stimulation of mechanotransduction and changes in interphase centromere positioning," *Journal of Cellular Biochemistry*, vol. 100, no. 2, pp. 326–338, 2007.
- [118] N. Gadegaard, S. Thoms, D. S. Macintyre et al., "Arrays of nanodots for cellular engineering," *Microelectronic Engineering*, vol. 67–68, pp. 162–168, 2003.
- [119] M. Arnold, E. A. Cavalcanti-Adam, R. Glass et al., "Activation of integrin function by nanopatterned adhesive interfaces," *ChemPhysChem*, vol. 5, no. 3, pp. 383–388, 2004.
- [120] P. J. Simmons, D. N. Haylock, and J. P. Lévesque, "Influence of cytokines and adhesion molecules on hematopoietic stem cell development," in *Ex Vivo Cell Therapy*, pp. 51–83, Elsevier, San Diego, Calif, USA, 1999.
- [121] E. K. F. Yim, S. W. Pang, and K. W. Leong, "Synthetic nanostructures inducing differentiation of human mesenchymal stem cells into neuronal lineage," *Experimental Cell Research*, vol. 313, no. 9, pp. 1820–1829, 2007.
- [122] S. Gerecht, C. J. Bettinger, Z. Zhang, J. T. Borenstein, G. Vunjak-Novakovic, and R. Langer, "The effect of actin disrupting agents on contact guidance of human embryonic stem cells," *Biomaterials*, vol. 28, no. 28, pp. 4068–4077, 2007.
- [123] J. M. Curran, R. Chen, and J. A. Hunt, "The guidance of human mesenchymal stem cell differentiation in vitro by controlled modifications to the cell substrate," *Biomaterials*, vol. 27, no. 27, pp. 4783–4793, 2006.
- [124] T. R. Nayak, H. Andersen, V. S. Makam et al., "Graphene for controlled and accelerated osteogenic differentiation of human mesenchymal stem cells," *ACS Nano*, vol. 5, no. 6, pp. 4670–4678, 2011.
- [125] S. Y. Park, J. Park, S. H. Sim et al., "Enhanced differentiation of human neural stem cells into neurons on graphene," *Advanced Materials*, vol. 23, no. 36, pp. H263–H267, 2011.
- [126] W. C. Lee, C. H. Y. X. Lim, H. Shi et al., "Origin of enhanced stem cell growth and differentiation on graphene and graphene oxide," *ACS Nano*, vol. 5, no. 9, pp. 7334–7341, 2011.
- [127] S. W. Crowder, D. Prasai, R. Rath et al., "Three-dimensional graphene foams promote osteogenic differentiation of human mesenchymal stem cells," *Nanoscale*, vol. 5, no. 10, pp. 4171–4176, 2013.
- [128] O. Akhavan, E. Ghaderi, and M. Shahsavari, "Graphene nanogrids for selective and fast osteogenic differentiation of human mesenchymal stem cells," *Carbon*, vol. 59, pp. 200–211, 2013.
- [129] G.-Y. Chen, D. W.-P. Pang, S.-M. Hwang, H.-Y. Tuan, and Y.-C. Hu, "A graphene-based platform for induced pluripotent stem cells culture and differentiation," *Biomaterials*, vol. 33, no. 2, pp. 418–427, 2012.
- [130] D. N. Haylock and S. K. Nilsson, "Stem cell regulation by the hematopoietic stem cell niche," *Cell Cycle*, vol. 4, no. 10, pp. 1353–1355, 2005.
- [131] Z. J. Han, A. E. Rider, M. Ishaq et al., "Carbon nanostructures for hard tissue engineering," *RSC Advances*, vol. 3, no. 28, pp. 11058–11072, 2013.
- [132] S. Zhang, "Fabrication of novel biomaterials through molecular self-assembly," *Nature Biotechnology*, vol. 21, no. 10, pp. 1171–1178, 2003.
- [133] A. Nur-E-Kamal, I. Ahmed, J. Kamal, M. Schindler, and S. Meiners, "Three-dimensional nanofibrillar surfaces promote self-renewal in mouse embryonic stem cells," *Stem Cells*, vol. 24, no. 2, pp. 426–433, 2006.
- [134] S. Subramony, B. Dargis, and M. Castillo, "The guidance of stem cell differentiation by substrate alignment and mechanical stimulation," *Biomaterials*, vol. 34, no. 8, pp. 1942–1953, 2012.
- [135] H. Liu and K. Roy, "Biomimetic three-dimensional cultures significantly increase hematopoietic differentiation efficacy of embryonic stem cells," *Tissue Engineering*, vol. 11, no. 1–2, pp. 319–330, 2005.
- [136] H. Tanaka, C. L. Murphy, C. Murphy, M. Kimura, S. Kawai, and J. M. Polak, "Chondrogenic differentiation of murine embryonic stem cells: effects of culture conditions and dexamethasone," *Journal of Cellular Biochemistry*, vol. 93, no. 3, pp. 454–462, 2004.
- [137] E. Hadjipanayi, V. Mudera, and R. A. Brown, "Close dependence of fibroblast proliferation on collagen scaffold matrix stiffness," *Journal of Tissue Engineering and Regenerative Medicine*, vol. 3, no. 2, pp. 77–84, 2009.
- [138] E. Cukierman, R. Pankov, and K. M. Yamada, "Cell interactions with three-dimensional matrices," *Current Opinion in Cell Biology*, vol. 14, no. 5, pp. 633–639, 2002.
- [139] M. D. Schofer, U. Boudriot, C. Wack et al., "Influence of nanofibers on the growth and osteogenic differentiation of stem cells: a comparison of biological collagen nanofibers and synthetic PLLA fibers," *Journal of Materials Science: Materials in Medicine*, vol. 20, no. 3, pp. 767–774, 2009.
- [140] Y. Soen, A. Mori, T. D. Palmer, and P. O. Brown, "Exploring the regulation of human neural precursor cell differentiation using arrays of signaling microenvironments," *Molecular Systems Biology*, vol. 2, article 37, 2006.
- [141] E. Garreta, E. Genovés, S. Borrós, and C. E. Semino, "Osteogenic differentiation of mouse embryonic stem cells and mouse embryonic fibroblasts in a three-dimensional self-assembling peptide scaffold," *Tissue Engineering*, vol. 12, no. 8, pp. 2215–2227, 2006.

- [142] I. Ahmed, A. S. Ponery, A. Nur-E-Kamal et al., "Morphology, cytoskeletal organization, and myosin dynamics of mouse embryonic fibroblasts cultured on nanofibrillar surfaces," *Molecular and Cellular Biochemistry*, vol. 301, no. 1-2, pp. 241-249, 2007.
- [143] W.-J. Li, R. Tuli, C. Okafor et al., "A three-dimensional nanofibrous scaffold for cartilage tissue engineering using human mesenchymal stem cells," *Biomaterials*, vol. 26, no. 6, pp. 599-609, 2005.
- [144] W.-J. Li, R. Tuli, X. Huang, P. Laquerriere, and R. S. Tuan, "Multilineage differentiation of human mesenchymal stem cells in a three-dimensional nanofibrous scaffold," *Biomaterials*, vol. 26, no. 25, pp. 5158-5166, 2005.
- [145] J. Holst, S. Watson, M. S. Lord et al., "Substrate elasticity provides mechanical signals for the expansion of hemopoietic stem and progenitor cells," *Nature Biotechnology*, vol. 28, no. 10, pp. 1123-1128, 2010.
- [146] G. Wei and P. X. Ma, "Partially nanofibrous architecture of 3D tissue engineering scaffolds," *Biomaterials*, vol. 30, no. 32, pp. 6426-6434, 2009.
- [147] S.-F. Wang, L. Shen, W.-D. Zhang, and Y.-J. Tong, "Preparation and mechanical properties of chitosan/carbon nanotubes composites," *Biomacromolecules*, vol. 6, no. 6, pp. 3067-3072, 2005.
- [148] D. A. Stout and T. J. Webster, "Carbon nanotubes for stem cell control," *Materials Today*, vol. 15, no. 7-8, pp. 312-318, 2012.
- [149] S. Samukawa, M. Hori, S. Rauf et al., "The 2012 plasma roadmap," *Journal of Physics D*, vol. 45, no. 25, Article ID 253001, 2012.
- [150] D. Mariotti, V. Švrček, and D. G. Kim, "Self-organized nanostructures on atmospheric microplasma exposed surfaces," *Applied Physics Letters*, vol. 91, no. 18, Article ID 183111, 2007.
- [151] I. Levchenko, K. Ostrikov, K. Diwan, K. Winkler, and D. Mariotti, "Plasma-driven self-organization of Ni nanodot arrays on Si(100)," *Applied Physics Letters*, vol. 93, no. 18, Article ID 183102, 2008.
- [152] S. Xu, I. Levchenko, S. Y. Huang, and K. Ostrikov, "Self-organized vertically aligned single-crystal silicon nanostructures with controlled shape and aspect ratio by reactive plasma etching," *Applied Physics Letters*, vol. 95, no. 11, Article ID 111505, 2009.
- [153] K. Ostrikov, I. Levchenko, and S. Xu, "Self-organized nanoarrays: plasma-related controls," *Pure and Applied Chemistry*, vol. 80, no. 9, pp. 1909-1918, 2008.
- [154] K. Ostrikov, I. Levchenko, U. Cvelbar, M. Sunkara, and M. Mozetic, "From nucleation to nanowires: a single-step process in reactive plasmas," *Nanoscale*, vol. 2, no. 10, pp. 2012-2027, 2010.
- [155] G. Arnoult, T. Belmonte, and G. Henrion, "Self-organization of SiO₂ nanodots deposited by chemical vapor deposition using an atmospheric pressure remote microplasma," *Applied Physics Letters*, vol. 96, no. 10, Article ID 101505, 2010.
- [156] K. Ostrikov, "Colloquium: reactive plasmas as a versatile nanofabrication tool," *Reviews of Modern Physics*, vol. 77, no. 2, pp. 489-511, 2005.
- [157] U. Cvelbar, K. Ostrikov, and M. Mozetic, "Reactive oxygen plasma-enabled synthesis of nanostructured CdO: tailoring nanostructures through plasma-surface interactions," *Nanotechnology*, vol. 19, no. 40, Article ID 405605, 2008.
- [158] Z. Han, B. Tay, C. Tan, M. Shakerzadeh, and K. Ostrikov, "Electrowetting control of Cassie-to-Wenzel transitions in superhydrophobic carbon nanotube-based nanocomposites," *ACS Nano*, vol. 3, no. 10, pp. 3031-3036, 2009.
- [159] A. Michelmore, P. M. Bryant, D. A. Steele, K. Vasilev, J. W. Bradley, and R. D. Short, "Role of positive ions in determining the deposition rate and film chemistry of continuous wave hexamethyl disiloxane plasmas," *Langmuir*, vol. 27, no. 19, pp. 11943-11950, 2011.
- [160] S. W. Lee, C. Mattevi, M. Chhowalla, and R. M. Sankaran, "Plasma-assisted reduction of graphene oxide at low temperature and atmospheric pressure for flexible conductor applications," *The Journal of Physical Chemistry Letters*, vol. 3, no. 6, pp. 772-777, 2012.
- [161] T. Kato and R. Hatakeyama, "Site- and alignment-controlled growth of graphene nanoribbons from nickel nanobars," *Nature Nanotechnology*, vol. 7, no. 10, pp. 651-656, 2012.
- [162] H. G. Yang, C. H. Sun, S. Z. Qiao et al., "Anatase TiO₂ single crystals with a large percentage of reactive facets," *Nature*, vol. 453, no. 7195, pp. 638-641, 2008.
- [163] H. Watanabe, H. Kondo, M. Hiramatsu et al., "Surface chemical modification of carbon nanowalls for wide-range control of surface wettability," *Plasma Processes and Polymers*, vol. 10, no. 7, pp. 582-592, 2013.
- [164] K. Tai, T. J. Houlahan, J. G. Eden, and S. J. Dillon, "Integration of microplasma with transmission electron microscopy: real-time observation of gold sputtering and island formation," *Scientific Reports*, vol. 3, article 1325, 2013.
- [165] M. Meyyappan, "A review of plasma enhanced chemical vapour deposition of carbon nanotubes," *Journal of Physics D*, vol. 42, no. 21, Article ID 213001, 2009.
- [166] M. Keidar, R. Walk, A. Shashurin et al., "Cold plasma selectivity and the possibility of a paradigm shift in cancer therapy," *British Journal of Cancer*, vol. 105, no. 9, pp. 1295-1301, 2011.
- [167] X. Yan, Z. Xiong, F. Zou et al., "Plasma-induced death of HepG2 cancer cells: intracellular effects of reactive species," *Plasma Processes and Polymers*, vol. 9, no. 1, pp. 59-66, 2012.
- [168] G. Fridman, G. Friedman, A. Gutsol, A. B. Shekhter, V. N. Vasilets, and A. Fridman, "Applied plasma medicine," *Plasma Processes and Polymers*, vol. 5, no. 6, pp. 503-533, 2008.
- [169] M. G. Kong, G. Kroesen, G. Morfill et al., "Plasma medicine: an introductory review," *New Journal of Physics*, vol. 11, no. 11, Article ID 115012, 2009.
- [170] J. Heinlin, G. Isbary, W. Stolz et al., "Plasma applications in medicine with a special focus on dermatology," *Journal of the European Academy of Dermatology and Venereology*, vol. 25, no. 1, pp. 1-11, 2011.
- [171] P. Chaudhari, Z. Ye, and Y. Y. Jang, "Roles of reactive oxygen species in the fate of stem cells," *Antioxidants & Redox Signaling*, 2012.
- [172] J. E. le Belle, N. M. Orozco, A. A. Paucar et al., "Proliferative neural stem cells have high endogenous ROS levels that regulate self-renewal and neurogenesis in a PI3K/Akt-dependant manner," *Cell Stem Cell*, vol. 8, no. 1, pp. 59-71, 2011.
- [173] P. M. Burch and N. H. Heintz, "Redox regulation of cell-cycle re-entry: cyclin D1 as a primary target for the mitogenic effects of reactive oxygen and nitrogen species," *Antioxidants and Redox Signaling*, vol. 7, no. 5-6, pp. 741-751, 2005.
- [174] M. Ishaq, M. M. Evans, and K. Ostrikov, "Effect of atmospheric gas plasmas on cancer cell signalling," *International Journal of Cancer*, 2013.
- [175] X. Pei, X. Lu, J. Liu et al., "Inactivation of a 25.5 μm Enterococcus faecalis biofilm by a room-temperature, battery-operated, handheld air plasma jet," *Journal of Physics D*, vol. 45, no. 16, Article ID 165205, 2012.

- [176] G. Fridman, M. Peddinghaus, M. Balasubramanian et al., "Blood coagulation and living tissue sterilization by floating-electrode dielectric barrier discharge in air," *Plasma Chemistry and Plasma Processing*, vol. 26, no. 4, pp. 425–442, 2006.
- [177] O. Lademann, H. Richter, A. Patzelt et al., "Application of a plasma-jet for skin antiseptics: analysis of the thermal action of the plasma by laser scanning microscopy," *Laser Physics Letters*, vol. 7, no. 6, pp. 458–462, 2010.
- [178] A. B. Shekhter, V. A. Serezhenkov, T. G. Rudenko, A. V. Pekshev, and A. F. Vanin, "Beneficial effect of gaseous nitric oxide on the healing of skin wounds," *Nitric Oxide—Biology and Chemistry*, vol. 12, no. 4, pp. 210–219, 2005.
- [179] M. Vleugels, G. Shama, X. T. Deng, E. Greenacre, T. Brocklehurst, and M. G. Kong, "Atmospheric plasma inactivation of biofilm-forming bacteria for food safety control," *IEEE Transactions on Plasma Science*, vol. 33, no. 2, pp. 824–828, 2005.
- [180] S. Deng, R. Ruan, C. K. Mok, G. Huang, X. Lin, and P. Chen, "Inactivation of *Escherichia coli* on almonds using nonthermal plasma," *Journal of Food Science*, vol. 72, no. 2, pp. M62–M66, 2007.
- [181] Y. Xian, X. Lu, J. Liu, S. Wu, D. Liu, and Y. Pan, "Multiple plasma bullet behavior of an atmospheric-pressure plasma plume driven by a pulsed dc voltage," *Plasma Sources Science and Technology*, vol. 21, no. 3, Article ID 034013, 2012.
- [182] X. Lu, M. Laroussi, and V. Puech, "On atmospheric-pressure non-equilibrium plasma jets and plasma bullets," *Plasma Sources Science and Technology*, vol. 21, no. 3, Article ID 034005, 2012.
- [183] Z. Xiong, S. Zhao, X. Mao et al., "Selective neuronal differentiation of neural stem cells induced by nanosecond microplasma agitation," *Stem Cell Research*, 2013.
- [184] P. Attri, B. Arora, and E. H. Choi, "Utility of plasma: a new road from physics to chemistry," *RSC Advances*, vol. 3, no. 31, pp. 12540–12567, 2013.
- [185] J. Zheng, R. Yang, L. Xie, J. Qu, Y. Liu, and X. Li, "Plasma-assisted approaches in inorganic nanostructure fabrication," *Advanced Materials*, vol. 22, no. 13, pp. 1451–1473, 2010.
- [186] M. J. Dalby, N. Gadegaard, and C. D. W. Wilkinson, "The response of fibroblasts to hexagonal nanotopography fabricated by electron beam lithography," *Journal of Biomedical Materials Research A*, vol. 84, no. 4, pp. 973–979, 2008.
- [187] S. Simovic, D. Losic, and K. Vasilev, "Controlled drug release from porous materials by plasma polymer deposition," *Chemical Communications*, vol. 46, no. 8, pp. 1317–1319, 2010.
- [188] R. J. Anthony, K. Y. Cheng, Z. C. Holman, R. J. Holmes, and U. R. Kortshagen, "An all-gas-phase approach for the fabrication of silicon nanocrystal light-emitting devices," *Nano Letters*, vol. 12, no. 6, pp. 2822–2825, 2012.
- [189] S. Kumar, I. Levchenko, K. Ostrikov, and J. A. McLaughlin, "Plasma-enabled, catalyst-free growth of carbon nanotubes on mechanically-written Si features with arbitrary shape," *Carbon*, vol. 50, no. 1, pp. 325–329, 2012.
- [190] X. Z. Huang, X. X. Zhong, Y. Lu et al., "Plasmonic Ag nanoparticles via environment-benign atmospheric microplasma electrochemistry," *Nanotechnology*, vol. 24, no. 9, Article ID 095604, 2013.
- [191] H. R. Maurer and H. Kersten, "On the heating of nano- and microparticles in process plasmas," *Journal of Physics D*, vol. 44, no. 17, Article ID 174029, 2011.
- [192] M. Shiratani, K. Koga, S. Ando et al., "Single step method to deposit Si quantum dot films using $H_2 + SiH_4$ VHF discharges and electron mobility in a Si quantum dot solar cell," *Surface and Coatings Technology*, vol. 201, no. 9–11, pp. 5468–5471, 2007.
- [193] S. Kumar, I. Levchenko, M. Keidar, and K. Ostrikov, "Plasma-enabled growth of separated, vertically aligned copper-capped carbon nanocones on silicon," *Applied Physics Letters*, vol. 97, no. 15, Article ID 151503, 2010.
- [194] S. Kumar and K. Ostrikov, "Unidirectional arrays of vertically standing graphenes in reactive plasmas," *Nanoscale*, vol. 3, no. 10, pp. 4296–4300, 2011.
- [195] S. Chattopadhyay, Y. F. Huang, Y. J. Jen, A. Ganguly, K. H. Chen, and L. C. Chen, "Anti-reflecting and photonic nanostructures," *Materials Science and Engineering R*, vol. 69, no. 1–3, pp. 1–35, 2010.
- [196] C. Cha, S. R. Shin, N. Annabi, M. R. Dokmeci, and A. Khademhosseini, "Carbon-based nanomaterials: multifunctional materials for biomedical engineering," *ACS Nano*, vol. 7, no. 4, pp. 2891–2897, 2013.

Research Article

Release Kinetics and Antibacterial Efficacy of Microporous β -TCP Coatings

Michael Seidenstuecker,¹ Yahya Mrestani,² Reinhard H. H. Neubert,²
Anke Bernstein,¹ and Hermann O. Mayr¹

¹ Department of Orthopedics and Trauma Surgery, University of Freiburg Medical Center, Hugstetter Str. 55, 79106 Freiburg, Germany

² Faculty of Natural Sciences I, Institute of Pharmacy, Martin-Luther-University, Wolf-Langenbeck-Str. 4, 06120 Halle/Saale, Germany

Correspondence should be addressed to Michael Seidenstuecker; michael.seidenstuecker@uniklinik-freiburg.de

Received 26 July 2013; Accepted 27 October 2013

Academic Editor: Krasimir Vasilev

Copyright © 2013 Michael Seidenstuecker et al. This is an open access article distributed under the Creative Commons Attribution License, which permits unrestricted use, distribution, and reproduction in any medium, provided the original work is properly cited.

Purpose. The aim of this study was to impregnate microporous β -TCP scaffolds with different antibiotic solutions and to determine their release behavior. **Materials and Methods.** We impregnated a β -TCP scaffold with antibiotics by using three methods: drop, dip, and stream coating with 120 mg/mL of antibiotic solution. After drying for 72 h at 37°C, 2 mL of distilled water was added to the antibiotic-coated plugs and incubated at 37°C. After defined time points (1, 2, 3, 6, 9, and 14 days), the liquid was completely replaced. The extracted liquid was analyzed by capillary zone electrophoresis and the Kirby Bauer disc diffusion test. For statistical analysis, we calculated a mean and standard deviation and carried out an analysis of variance using ANOVA. **Results.** The VAN and CLI release from the β -TCP scaffolds was rapid, occurring within 24 h with $89 \pm 0.8\%$ VAN and $90.4 \pm 1.5\%$ CLI regardless of the type of insulation. After six days, the VAN and CLI were completely released. All samples taken at later time points had a VAN or CLI concentration below the detection limit of 4 $\mu\text{g/mL}$. The released amounts of VAN and CLI within the first three days revealed antimicrobial activity.

1. Introduction

Osteoinductive calcium phosphate ceramics are suitable materials for delivery systems [1–5]. This applies in particular to the release of drugs to prevent bone infection. Local drug delivery is especially valuable in association with bone infection since it spares patients the adverse effects of systematically administered drugs, reduces the risks from resistant bacteria, and enables a high concentration of medication at the infection site [6]. A variety of materials have been used as carriers for the local delivery of antibiotics. These materials are classified as biodegradable or nondegradable. The most commonly used of the non-degradable material is PMMA, which is often impregnated with antibiotics such as gentamycin, clindamycin, or vancomycin. PMMA is not only used as a bone cement or with an antibiotic offset bone cement like PALACOS R+G, but also as antibiotic-impregnated PMMA beads such as SEPTOPAL chains which have been on the market for the last two decades. The major

drawback associated with PMMA beads is that they must be surgically removed after exposure to antibiotic release, which usually takes place four weeks after their implantation [7]. The use of biodegradable materials could therefore be advantageous to eliminate the need for a second operation. The most widely used biodegradable materials are polyglycolide and polylactide (PLGA/PLLA). PLGA and PLLA can be used as scaffolds [8], as biodegradable interference screws [9], as coating [5, 10], or as a composite material in combination with other biodegradable materials [11–13]. A disadvantage of polylactide-based materials is that they contain acidic degradation products [14].

Calcium phosphate ceramics (CPC) are suitable in this respect also, since they too are biodegradable [15]. Thus, various attempts have been made to combine CPC, mainly hydroxyapatite (HA) and beta tricalcium phosphate (β -TCP), with antibiotics. Due to its better solubility in water, β -TCP biodegrades faster [16]. HA and β -TCP have often

been used as granules [17] or powder [1, 18], combined with antibiotics. In most cases, the antibiotic was released within 24 to 72 hours [5, 18, 19]. The powders and granules are naturally very mechanically unstable. To produce TCP materials with sufficient mechanical properties, the pores must be small, and the porosity must be reduced to a value approaching 40%. Our group showed that a β -TCP ceramic with 5 μm interconnected micropores and with 40% porosity demonstrates good mechanical stability [20]. It is therefore suitable as a bone substitute material for fixation of cruciate ligaments [20–22] and as a scaffold for bone tissue engineering. Due to the interconnected microporosity, the ceramic is also suitable as a drug release system. Microporous β -TCP ceramics can serve both as a prevention measure and to treat surgical site infections (SSI), because it is mechanically more stable than macroporous β -TCP or granules. We thus loaded microporous ceramic materials with antibiotics for SSI-prevention purposes applying three different methods. We expected the TCP scaffold loaded with antibiotics (AB) to release antibiotics continuously over a period of weeks. We also anticipated that the loading procedure would not trigger a loss of antimicrobial activity. SSI lead to an alteration in the local pH level in the bone [23, 24]. Therefore, all experiments were conducted at a pH value of 5.0 and 7.4 to simulate realistic in vitro conditions

2. Materials and Methods

2.1. Preparation of β -TCP Ceramics. To produce β -TCP plugs, 80 g of α -tricalcium phosphate (α -TCP; $\text{Ca}_3(\text{PO}_4)_2$) and 20 g of tricalcium phosphate (Art no 102143, Merck, Switzerland; mixture of an apatite and some calcium hydrogen phosphate) were mixed with 60.0 ± 0.2 g of a solution containing 0.2 M Na_2HPO_4 and +1% polyacrylic acid (Art. No 81132, Fluka, Switzerland; Mw = 5.1 kDa). After 2.5 min of intensive stirring, the paste was poured into plastic syringes whose tip had been cut off ($\varnothing = 23$ mm). After 45 minutes, the hardened paste was covered with 10 mL of PBS 7.4 solution and incubated for 3 days at 60°C. The samples ($\varnothing = 23$ mm; $L \approx 70$ mm) were then dried at the same temperature and sintered at 1250°C for 4 h. Heating and cooling took place at 1°C/min. The cylinders were then machined to obtain plugs of 25 mm long and 10 mm in diameter. The last 2.5 mm of the plugs was given a spherical shape. The samples were then washed in ethanol to remove residual wear particles and calcined at 900°C to burn off all organic residues.

2.2. Characterization of β -TCP Ceramics. X-ray diffraction (XRD) was performed on a Bruker axs D8 Advance X-ray diffractometer (Billerica, USA) using CuK_α radiation at 40 kV and 40 mA. An XRD spectrum was obtained between 20° and 40° (2θ) in 0.01° steps. The XRD spectra of our samples were compared to the standard spectra of β -TCP from the Joint Committee on Powder Diffraction (JCPDS) database (β -TCP = JCPDS 9-169). Porosity was assessed on a POROTEC Pascal 440 (Hofheim, Germany) mercury porosimeter. To detect the morphology and for elementary analysis, we used a PHILIPS XL 30 ESEM FEG (Hamburg,

Germany) and an FEI QUANTA 250 FEG (Hillsboro, USA) with EDX unit. All images were taken with a backscattered electron detector. For the ESEM investigations, the β -TCP plugs were broken in the middle with a DUMONT (Montignez, Switzerland) cutting forceps and the breach area was investigated. Because of using ESEM, there was no special coating (carbon or gold) necessary on this breach area to achieve better contrast between ceramics and antibiotics.

2.3. Sample Preparation. Vancomycin- (VAN-) hydrochloride (Cell Pharm, Hannover, Germany) and Clindamycin (CLI) 2-phosphate (MP Biomedicals, Illkirch, France) solution with concentrations of 40, 80, and 120 mg/mL were prepared with deionized water. The β -TCP scaffolds were divided using a diamond band saw Exakt 310 (Exakt, Norderstedt, Germany) into segments of 3 mm \times \varnothing 10 mm. These segments were washed in pure ethanol (Carl Roth, Germany) to remove the sawdust and dried at 37°C for 24 h. Then they were weighed with a Scaltec SBA 32 scale (Goettingen, Germany) and stored in a compartment dryer at 37°C. Ten samples were used for each coating method. The loading experiments were carried out in triplicate.

Dip Coating. Dip coating was done in 24-well cell culture plates with 2 mL quantities of 40, 80, and 120 mg/mL VAN and CLI solutions. The scaffolds were incubated in the solutions for 24 h at room temperature (RT), transferred into other 24-well cell culture plates, and dried for 72 h at 37°C.

Drop Coating. Drop coating was done in 24-well cell culture plates. A drop of 125 μL of the 40, 80, and 120 mg/mL VAN or CLI solutions was placed on the front of the cylindrical scaffold. The 24-well plates were sealed with Parafilm M (Pechiney Plastic Packaging, Chicago, USA). After 2 h of incubation at RT, the scaffold was turned over and a further 125 μL drop of 40, 80 and 120 mg/mL or VAN CLI solution was placed on the other front. After 2 h of incubation at RT, the scaffolds were placed in a clean 24 well plate and dried for 72 h at 37°C.

Stream Coating. A third coating method was used to coat the TCP scaffolds with antibiotics. Because of its setup, we call this method “stream coating.” The scaffolds were put in a 5 mL syringe. The punch was pulled out and the ceramic scaffold was placed directly onto the syringe outlet. Then the scaffold was overlaid with 5 mL of antibiotic solution. Four mL of the solution was pressed through the scaffold, so that a constant supernatant of VAN solution remained beyond the scaffold. Pressures were increased by a 0.45 μm syringe filter. The scaffolds were then transferred to clean 24 well plates (TPP) and dried at 37°C for 72 h in a compartment dryer.

All samples were briefly swilled in deionized water after the drying procedure to remove the AB from the outer surface. The antibiotics' load amounts for each coating method were determined by weight in triplicate.

2.4. Drug Release. To assess the amount of antibiotic loaded, the drug-loaded scaffolds were weighed again and placed in 24-well plates. Two unloaded scaffolds were used as blanks.

Each 24-well plate was filled with 2 mL of deionized water, sealed with PARAFILM, and incubated at 37°C. All tests were conducted at pH values of 7.4 and 5.0. To setup a pH of 5.0, 0.1 M HCl was used. After 1, 2, 3, 6, 9, and 14 days, the scaffolds were removed and placed into new 24-well plates filled with 2 mL of deionized water. The solutions thus obtained were stored at -4°C for examination by capillary zone electrophoresis (CZE) and disc diffusion method (DDM).

2.5. Capillary Zone Electrophoresis. CZE experiments were performed on a Beckman Coulter P/ACE MDQ Molecular Characterization System (Brea, USA) with a 40.5 cm fused silica capillary (31 cm to detector) and 50 μm inner diameter. The analytic conditions were: field strength: 20 kV, temperature during measurement: 25°C, and injection pressure: 2 psi for 6 s. The detection wavelengths were 221 nm (VAN) and 200 nm (CLI). We prepared fresh running buffers, citric acid buffer, pH 3.2 to detect VAN and borate buffer, pH 9.2 to detect CLI [25]. The capillary was flushed for 6 min with 0.1 M NaOH, 6 min with deionized water, and 6 min with running buffer at a pressure of 20 psi before injecting each sample. All samples were measured in triplicate by UV.

2.6. Disc Diffusion Method. The released amounts of VAN and CLI were tested with a standard NCCLS disc diffusion test. DDM was performed on Mueller-Hinton agar (Carl Roth, Germany). A suspension of *Staphylococcus aureus* ATCC 25923 with a 0.5 McFarland standard was placed on the Mueller-Hinton agar. OXOID paper discs (Wesel, Germany) were moistened with 10 μL sample liquid and placed on Mueller Hinton agar. OXOID paper discs with 5 and 30 μg VAN and 2 and 10 μg CLI were used as standards. After 24 h incubation at 37°C, the zone diameters were measured in the usual manner.

2.7. Statistical Analysis. Origin 8.5.1 Professional (OriginLab Corporation, Northhampton, USA) was used for graphic presentations and statistical analysis. A probability of error (P) of less than 0.05 was defined as significant. All samples were measured in triplicate. Normal distribution was ascertained by means of the Shapiro-Wilk-Test. The Mann-Whitney Test was used to compare mean values.

3. Results

3.1. Characterization of β -TCP Ceramics. The EDX spectrum (Figure 1) shows that the chemical composition on the surface of the samples is made up of only Ca, P, and O atoms, as would be expected in calcium phosphate ceramics such as β -TCP. A quantification of the EDX spectra (only Ca and P without standards and with theoretical k-factors) results in 60 at% Ca and 40 at% P, that is, a Ca/P ratio of 1.5 and this is equal to TCP. Figure 2 shows an XRD pattern of our β -TCP sample in powder form (b) and the β -TCP standard from the JCPDS database (β -TCP = JCPDS 9-169) (a). The comparison of the two XRD spectra reveals a clear consensus with no signs of a further phase or a shift. Using mercury porosimetry we measured a mean pore radius of 2.44 ± 0.47 micron and

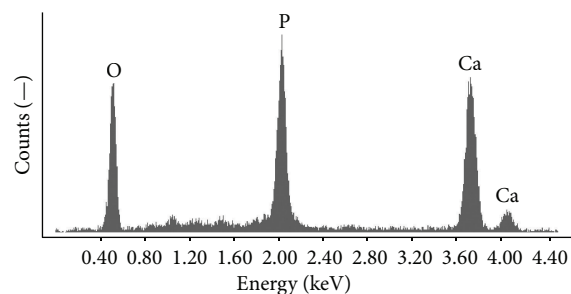


FIGURE 1: EDX spectrum of β -TCP sample; spectrum taken with Philips ESEM XL 30 FEG with 12 kV accelerator voltage and 100 sec lifetime counting period.

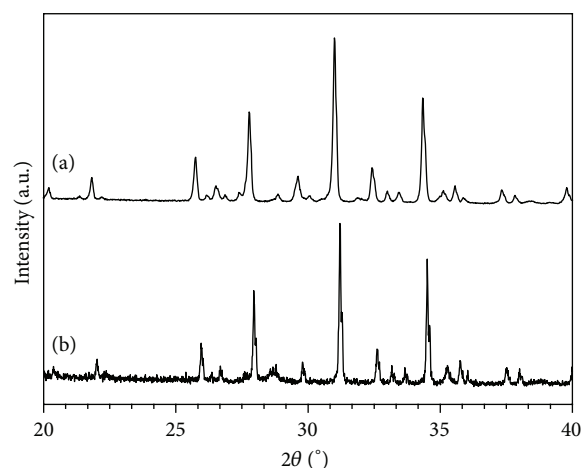


FIGURE 2: XRD patterns of the standard for β -TCP from JCPDS database (β -TCP = JCPDS 9-169) (a) and microporous β -TCP sample (b).

a total porosity of $46 \pm 1\%$. Figure 3 illustrates the pore size distribution. We also found a small amount of nanoporosity; the pore size distribution in Figure 3 shows a peak at 100 nm. Figure 4 contains an ESEM image of this nanoporosity.

3.2. Coating Experiments. The average weight of the β -TCP scaffolds before coating was $0.438 \text{ g} \pm 0.059 \text{ g}$ ($N = 90$). Table 1 summarizes our release-experiment results. The drop coating methods produced the maximum charge amount in all cases. The loading method we developed, in terms of load quantity, is in the second place. The dip coating method demonstrated the lowest load rate and took, compared to the other methods, the longest time to complete.

3.3. Coated AB Examination via ESEM/EDX. Studies using ESEM and EDX demonstrated that the antibiotic not only adheres to the outer surface of the test specimens, but also penetrates the core of the microporous ceramic. Figures 5 and 6 shows ESEM images that verify the diffusion of a substance into the porosities of the β -TCP scaffolds. The lighter structures are β -TCP and the darker areas represent VAN or CLI. Because we used a sensor for backscattered electrons, the brightness of the calcium phosphate ceramics in the image

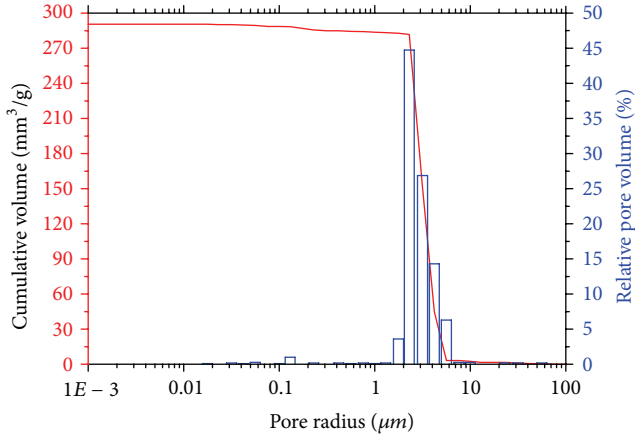


FIGURE 3: Pore size distribution of microporous β -TCP ceramics.

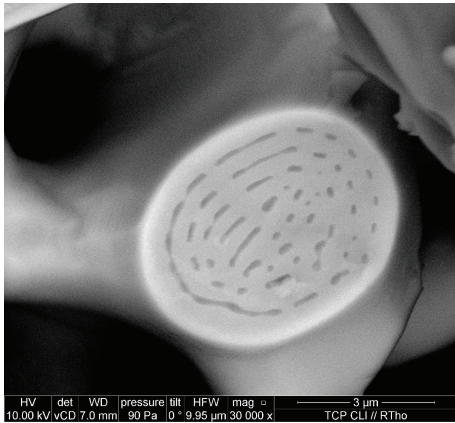


FIGURE 4: Nanoposity of β -TCP ceramics. Image taken with a backscattered electron detector, 10 kV accelerator voltage, pressure of 90 Pa, and magnification 30000x.

TABLE 1: Comparison of coating methods, quantities of antibiotics in the porous ceramics, and load duration ($N = 10$).

Coating	Load quantity of AB [26] achieved with AB solution of			Load duration
	40 mg/mL	80 mg/mL	120 mg/mL	
Drop coating	9.8 ± 2.3	14.7 ± 3.7	29.5 ± 2.5	4 h
Stream coating	6.7 ± 1.3	11 ± 2.7	20.6 ± 3.6	5 min
Dip coating	9.4 ± 0.79	9.4 ± 1.9	16.1 ± 2.7	1 d

is an indication of the higher atomic number of Ca. As the antibiotics mainly consist of carbon, they appear darker in the photograph. The white bars in Figure 6 reveal VAN's penetration depths into the porous ceramics in case of dip and drop coating. The penetration depth of drop-coated ceramics was on average $1000 \mu\text{m} \pm 127 \mu\text{m}$ and of dip-coated ceramics a mean $350 \mu\text{m} \pm 68 \mu\text{m}$. The EDX spectra in Figure 7 confirm this by virtue of the presence of carbon, chloride and

TABLE 2: Recovery rate of VAN using CZE ($N = 10$).

Coating method	Quantity of AB in scaffold (mg)	Quantity of AB recovered from scaffold by CZE (mg)	Recovery rate (%)
Drop coating pH 7.4 (VAN)	29.5 ± 2.5	27.2	92.2
Drop coating pH 5.0 (VAN)	29.5 ± 2.5	29.1	98.6
Dip coating pH 7.4 (VAN)	16.6 ± 1.3	16.04	96.6
Dip coating pH 5.0 (VAN)	16.1 ± 2.7	14.5	89.8
Stream coating pH 7.4 (VAN)	20.6 ± 3.6	19.5	94.5
Drop coating pH 7.4 (CLI)	22.2 ± 2.8	22.0	99.1
Dip coating pH 7.4 (CLI)	23.5 ± 2.9	23.4	99.6

sulfur, as VAN was available as VAN-HCl; we thus used the chloride as a marker element. Sulphur was employed as the elemental marker for CLI. Carbon is not found in the scaffold material in the quantities identified here, and chloride and sulphur never occur. In the EDX measurements we identified traces of carbon detected in the unloaded β -TCP samples. Those could be carbon residues from the microporous ceramics' manufacturing process. Further ESEM measurements were taken to ascertain how deeply VAN and CLI diffuse into the scaffold to rule out the possibility that the antibiotics were located exclusively on the scaffolds' perimeter.

3.4. Drug Release. These drug release experiments were conducted using 24-well cell culture plates with deionized water at pH 5.0, corresponding to the altered pH in the presence of inflammation, and pH 7.4. However, we detected no significant difference between the two pH values in the quantities of VAN released. The drip-coated scaffolds showed greater release of VAN during the first 24 h because of the higher quantity of VAN available: 29.5 ± 2.5 mg was transferred to the scaffolds and 26.3 ± 2.9 mg was released within 24 h. In contrast, the dip-coated scaffolds were loaded with 16.1 ± 2.7 mg VAN and released 14.3 ± 0.8 mg VAN within 24 h (Figure 8). The stream coating method achieved a load of 20.8 ± 3.6 mg VAN, and 16.9 ± 2.5 mg of VAN was released after 24 h.

VAN was released rapidly at both pH values: $88.25 \pm 3.6\%$ within 24 h. The release of CLI was also rapid: $90.4 \pm 1.5\%$ within 24 h. The VAN and CLI releases were complete after 6 days. All samples taken at later time points had a VAN concentration below the detection limit of $1 \mu\text{g/mL}$ or a CLI concentration below the detection limit of $2 \mu\text{g/mL}$. The proportion of released VAN recovered by means of CZE was $94.3 \pm 4.1\%$, and for CLI $99.4 \pm 0.4\%$.

A comparison of the coated and recovered quantities of VAN and CLI is shown in Table 2.

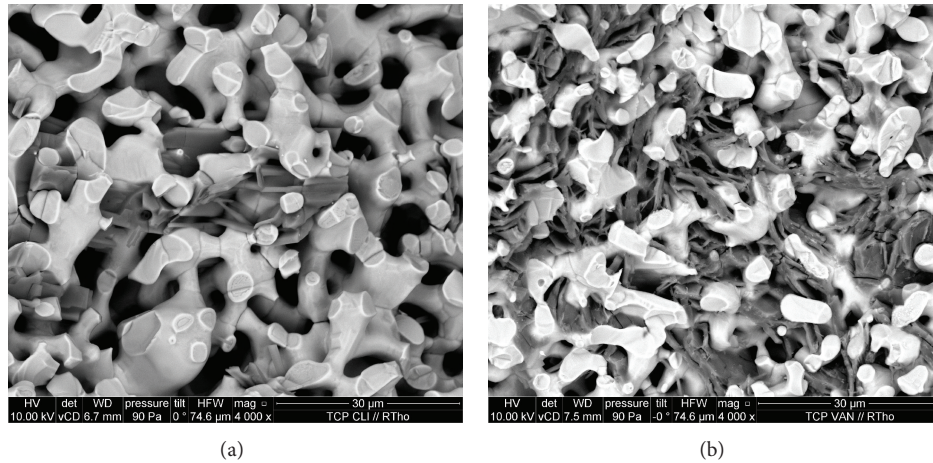


FIGURE 5: ESEM images of β -TCP impregnated (dip coating) with antibiotics. (a) CLI coating; (b) VAN coating. Images taken with a backscattered electron detector, 10 kV accelerator voltage, pressure of 90 Pa, and magnification 4000x; the calcium phosphate ceramic appears (due to Ca's higher atomic number) brighter than the antibiotics, which consist mainly of hydrocarbons. All images were taken from the breach area.

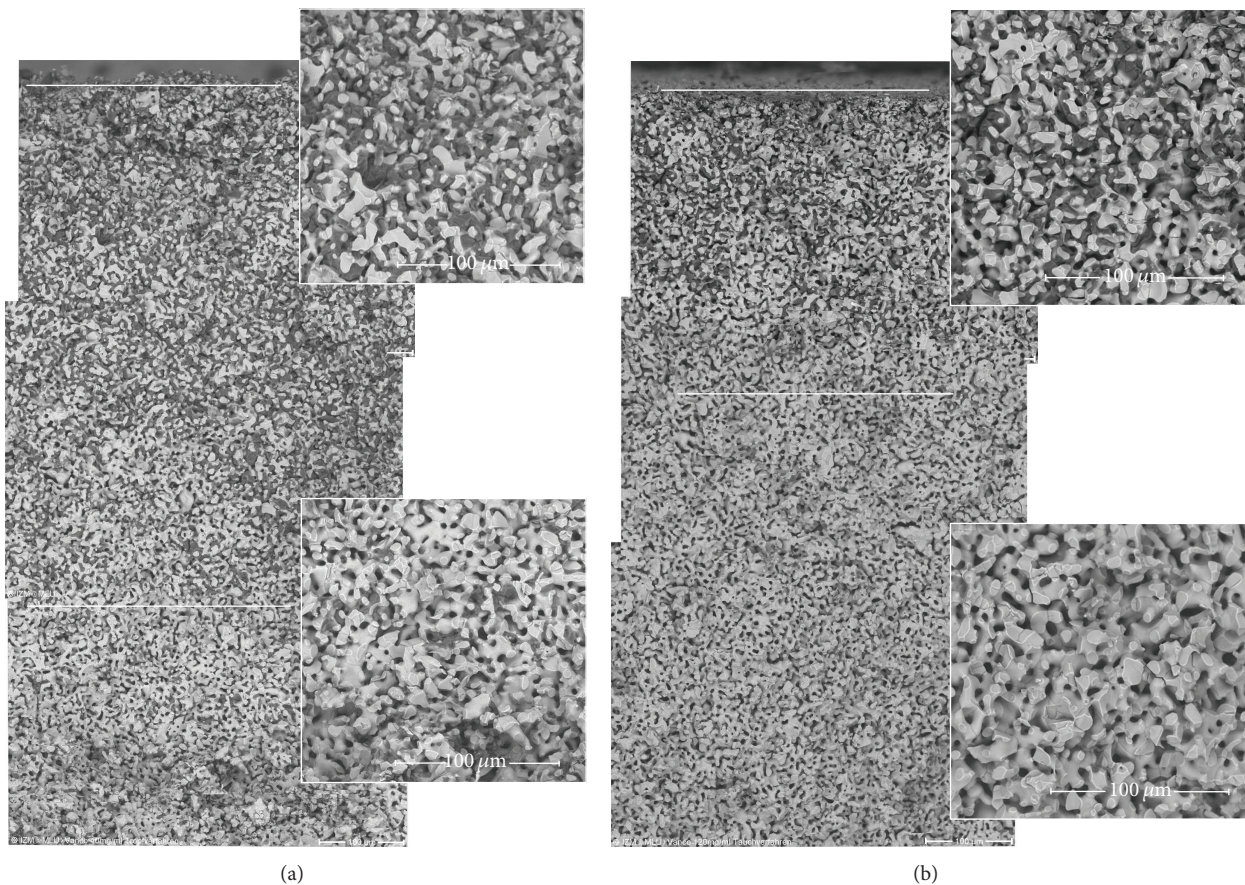


FIGURE 6: ESEM images of β -TCP. Comparison of VAN's penetration depth into the ceramics: breach area of cylindrical ceramics, breach along boresight, (a) drop coating; (b) dip coating; each image is a combination of three individual images taken with PHILIPS ESEM XL 30 FEG using a backscattered electron detector, 12 kV accelerator voltage, pressure of 100 Pa, magnification 500x, and the calcium phosphate ceramic appears (due to Ca's higher atomic number) brighter than the antibiotics, which consist mainly of hydrocarbons; top: frontal area (where the drop was placed in case of drop coating) bottom: center of ceramic cylinder and the small images are enlargements of image sections; the upper enlargement displays filled porosity and the lower empty porosity.

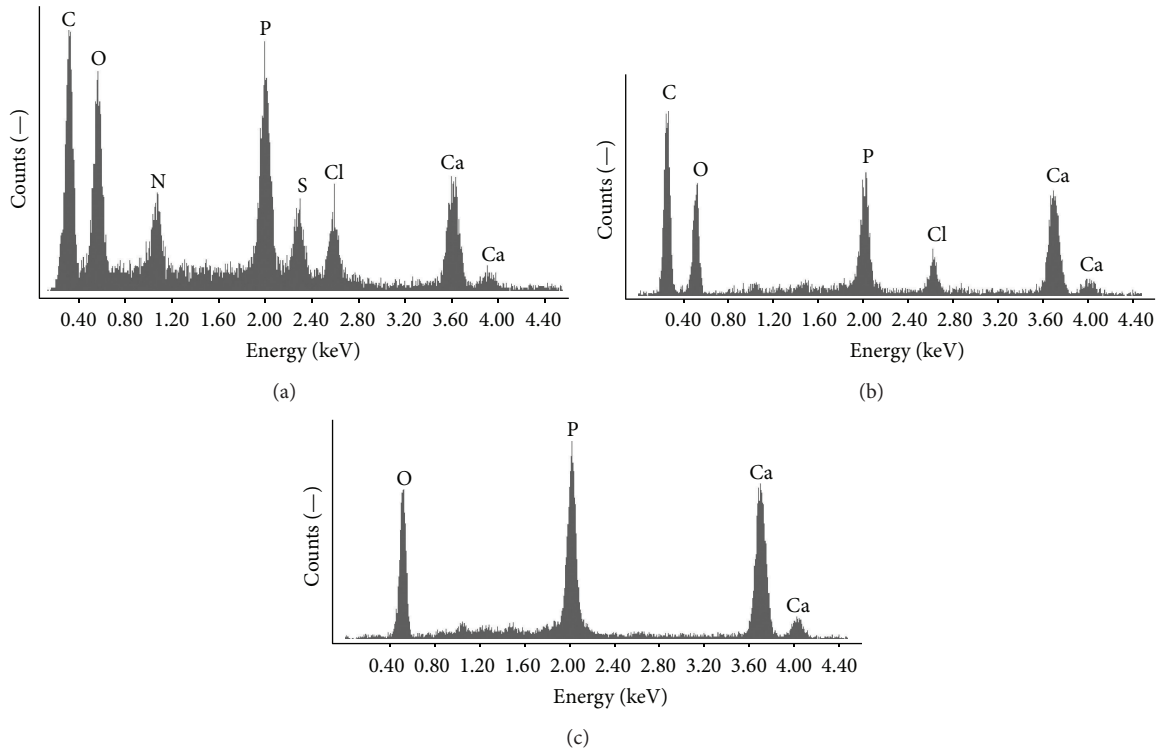


FIGURE 7: EDX spectra of clindamycin (a) and vancomycin (b) compared to β -TCP (c); spectra taken with a PHILIPS XL 30 FEG ESEM with EDX unit, with 12 kV accelerator voltage and 100 sec lifetime counting period.

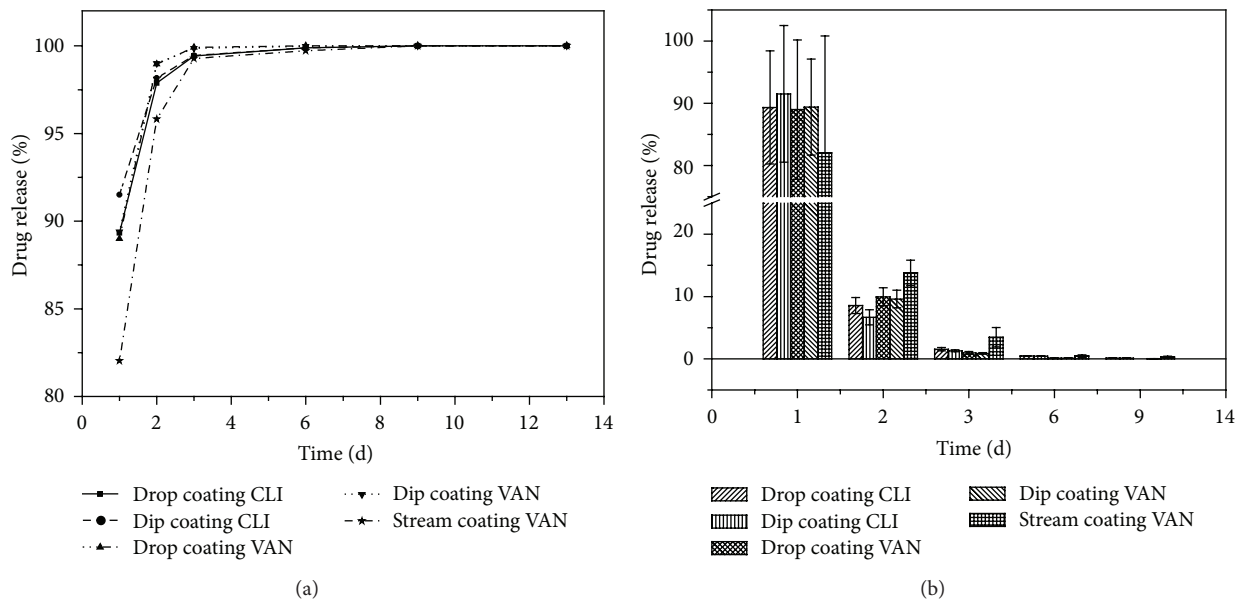


FIGURE 8: Comparison of release kinetics: (a) cumulative release; (b) daily release.

3.5. Disc Diffusion Method. The antimicrobial activity of the released VAN is shown in Table 3. We observed antimicrobial activity only on the first 3 days; at later times, the amounts released were below the MIC [27, 28] and also below the detection limit of $1 \mu\text{g/mL}$ [29].

4. Discussion

Elemental analyses proved unequivocally that the samples consist of pure phased beta-TCP. This material has also been used in previous studies [20, 21, 30] because it is more highly

TABLE 3: Released VAN concentrations and inhibition circles at different time points ($N = 3$).

Day of sampling	Vancomycin concentration (mg/mL) detected via CZE	Inhibition circle diameter (cm)
1	28.37	1.97 ± 0.23
2	2.66	1.8 ± 0.1
3	0.20	0.97 ± 0.06
6	0.02	0 ± 0
9	0.003	0 ± 0
13	0	0 ± 0

water-soluble than hydroxylapatite [16]. The sintered molded body of β -TCP exhibited a microporous structure, while in the literature β -TCP only as granules or as a powder [1, 31], incorporated in calcium phosphate cement [32, 33] or in the form of a macroporous scaffold such as macroporous DePuy Synthes chronOS.

With regard to filling the ceramics using ESEM and EDX, we detected antibiotics within the microporous ceramic; such antibiotic penetration has not been demonstrated before, as so far, the antibiotic has only been demonstrated on the ceramic's surface or barely under it.

If one compares how we loaded the ceramic with the dip coating described by Y. Zhang and M. Zhang [34] and Alkhraisat et al. [35], one observes that stream coating is superior to the latter in terms of the time it takes to load while loading the same amount of antibiotic.

(See Table 1) Hofmann et al. [33] describe results similar to ours, namely a burst of vancomycin release within the first 24 hours. Examining calcium sulfate cements, Hesaraki et al. [36] observed similar release characteristics as we did in our experiments, which barely released anything after 72 h.

Conflict of Interests

The authors declare that there is no conflict of interests regarding the publication of this paper.

Acknowledgments

The authors thank Frank Syrowatka from the Interdisciplinary Center of Materials Sciences at the Martin Luther University in Halle/Saale for the XRD measurements. They also thank Ralf Thomann from the Freiburger Research Center for Material Sciences at the Albert Ludwig University Freiburg for the ESEM measurements. The paper processing charge was funded by the open access publication fund of the Albert Ludwigs University Freiburg.

References

- [1] A. Aneja, J. Woodall, S. Wingerter, M. Tucci, and H. Benghuzzi, "Analysis of tobramycin release from beta tricalcium phosphate drug delivery system," *Biomedical Sciences Instrumentation*, vol. 44, pp. 88–92, 2008.
- [2] S. Bose and S. Tarafder, "Calcium phosphate ceramic systems in growth factor and drug delivery for bone tissue engineering: a review," *Acta Biomaterialia*, vol. 8, no. 4, pp. 1401–1421, 2012.
- [3] W. J. E. M. Habraken, J. G. C. Wolke, and J. A. Jansen, "Ceramic composites as matrices and scaffolds for drug delivery in tissue engineering," *Advanced Drug Delivery Reviews*, vol. 59, no. 4–5, pp. 234–248, 2007.
- [4] E. Verron, I. Khairoun, J. Guicheux, and J.-M. Bouler, "Calcium phosphate biomaterials as bone drug delivery systems: a review," *Drug Discovery Today*, vol. 15, no. 13–14, pp. 547–552, 2010.
- [5] O. Zamoume, S. Thibault, G. Regnié, M. O. Mecherri, M. Fiallo, and P. Sharrock, "Macroporous calcium phosphate ceramic implants for sustained drug delivery," *Materials Science and Engineering C*, vol. 31, no. 7, pp. 1352–1356, 2011.
- [6] K. Kanellakopoulou and E. J. Giamarellos-Bourboulis, "Carrier systems for the local delivery of antibiotics in bone infections," *Drugs*, vol. 59, no. 6, pp. 1223–1232, 2000.
- [7] M. J. Patzakis, K. Mazur, J. Wilkins, R. Sherman, and P. Holtom, "Septopal beads and autogenous bone grafting for bone defects in patients with chronic osteomyelitis," *Clinical Orthopaedics and Related Research*, no. 295, pp. 112–118, 1993.
- [8] Z. Pan and J. Ding, "Poly(lactide-co-glycolide) porous scaffolds for tissue engineering and regenerative medicine," *Interface Focus*, vol. 2, no. 3, pp. 366–377, 2012.
- [9] D. B. Thordarson and G. Hurvitz, "PLA screw fixation of lisfranc injuries," *Foot and Ankle International*, vol. 23, no. 11, pp. 1003–1007, 2002.
- [10] T. M. O'Shea and X. Miao, "Preparation and characterisation of plga-coated porous bioactive glass-ceramic scaffolds for subchondral bone tissue engineering," in *Proceeding of the 9th International Symposium on Ceramic Materials and Components for Energy and Environmental Applications*, Shanghai Institute of Ceramics, Shanghai Institute of Ceramics, Chinese Academy of Sciences, Shanghai, China, 2009.
- [11] W. Friess and M. Schlapp, "Sterilization of gentamicin containing collagen/PLGA microparticle composites," *European Journal of Pharmaceutics and Biopharmaceutics*, vol. 63, no. 2, pp. 176–187, 2006.
- [12] M. Schlapp and W. Friess, "Collagen/PLGA microparticle composites for local controlled delivery of gentamicin," *Journal of Pharmaceutical Sciences*, vol. 92, no. 11, pp. 2145–2151, 2003.
- [13] X. Li, X. Wang, L. Zhang, H. Chen, and J. Shi, "MBG/PLGA composite microspheres with prolonged drug release," *Journal of Biomedical Materials Research B*, vol. 89, no. 1, pp. 148–154, 2009.
- [14] C. M. Agrawal and K. A. Athanasiou, "Technique to control pH in vicinity of biodegrading PLA-PGA implants," *Journal of Biomedical Materials Research*, vol. 38, no. 2, pp. 105–114, 1997.
- [15] H. K. Koerten and J. Van Der Meulen, "Degradation of calcium phosphate ceramics," *Journal of Biomedical Materials Research*, vol. 44, no. 1, pp. 78–86, 1999.
- [16] M. Epple, *Biomaterialien und Biomineralisation*, Teubner, Wiesbaden, Germany, 2003.
- [17] J. Eitenmuller, G. Peters, and W. Golsong, "Utilising absorbable coatings for inhibition of antibiotic release from biodegradable tricalciumphosphate-ceramic beads for local treatment of osteomyelitis," *Langenbecks Archiv fur Chirurgie*, vol. 360, no. 3, pp. 193–206, 1983.
- [18] F. Laurent, A. Bignon, J. Goldnadel et al., "A new concept of gentamicin loaded HAP/TCP bone substitute for prophylactic action: in vitro release validation," *Journal of Materials Science*, vol. 19, no. 2, pp. 947–951, 2008.

- [19] J. Zhang, C. Wang, J. Wang, Y. Qu, and G. Liu, "In vivo drug release and antibacterial properties of vancomycin loaded hydroxyapatite/chitosan composite," *Drug Delivery*, vol. 19, no. 5, pp. 264–269, 2012.
- [20] H. O. Mayr, M. Dietrich, F. Fraedrich et al., "Microporous pure β -tricalcium phosphate implants for press-fit fixation of anterior cruciate ligament grafts: strength and healing in a sheep model," *Arthroscopy*, vol. 25, no. 9, pp. 996–1005, 2009.
- [21] A. Bernstein, D. Nöbel, H. O. Mayr, G. Berger, R. Gildenhaar, and J. Brandt, "Histological and histomorphometric investigations on bone integration of rapidly resorbable calcium phosphate ceramics," *Journal of Biomedical Materials Research B*, vol. 84, no. 2, pp. 452–462, 2008.
- [22] H. O. Mayr, *Mikroporöse Formkörper aus phasenreinem beta-Tricalciumphosphat zur Fixierung der vorderen Kreuzbandplastik und als Knochenersatz—biomechanische, radiologische und histologische Untersuchungen zur Erforschung der Stabilität und des Einheilverhaltens*, Medizinische Fakultät, Martin Luther Universität, Halle, Germany, 2007.
- [23] V. Menkin, "The role of hydrogen ion concentration and the cytology of an exudate," in *In Biochemical Mechanisms in Inflammation*, C. C. Thomas, Ed., pp. 66–103, Springfield, Ill, USA, 1956.
- [24] A. Lardner, "The effects of extracellular pH on immune function," *Journal of Leukocyte Biology*, vol. 69, no. 4, pp. 522–530, 2001.
- [25] R. Friebe, K. Rauscher, J. Voigt, I. Wilke, and K. -Th. Wilke, *Chemische Tabellen und Rechentafeln für Die Analytische Praxis*, Harri Deutsch, Frankfurt, Germany, 2000.
- [26] M. Böhner and F. Baumgart, "Theoretical model to determine the effects of geometrical factors on the resorption of calcium phosphate bone substitutes," *Biomaterials*, vol. 25, no. 17, pp. 3569–3582, 2004.
- [27] P. J. Jiang, S. Patel, U. Gbureck et al., "Comparing the efficacy of three bioceramic matrices for the release of vancomycin hydrochloride," *Journal of Biomedical Materials Research Part B*, vol. 93, no. 1, pp. 51–58, 2010.
- [28] G. Wang, J. F. Hindler, K. W. Ward, and D. A. Bruckner, "Increased vancomycin MICs for *Staphylococcus aureus* clinical isolates from a university hospital during a 5-year period," *Journal of Clinical Microbiology*, vol. 44, no. 11, pp. 3883–3886, 2006.
- [29] M. Seidenstuecker, "Development of a quantitative method for determination of the released antibiotics concentration out of beta TCP scaffolds by using CZE and validation of the applicability of different coating methods," in *Centre for Engineering Sciences*, Martin Luther University, Halle/S., Germany, 2010.
- [30] H. O. Mayr, R. Hube, A. Bernstein, A. B. Seibt, W. Hein, and R. V. Eisenhart-Rothe, "Beta-tricalcium phosphate plugs for press-fit fixation in ACL reconstruction—a mechanical analysis in bovine bone," *Knee*, vol. 14, no. 3, pp. 239–244, 2007.
- [31] J. Zhou, T. Fang, Y. Wang, and J. Dong, "The controlled release of vancomycin in gelatin/beta-TCP composite scaffolds," *Journal of Biomedical Materials Research Part A*, vol. 100, no. 9, pp. 2295–2301, 2012.
- [32] M. Böhner, J. Lemaître, P. Van Landuyt, P.-Y. Zambelli, H. P. Merkle, and B. Gander, "Gentamicin-loaded hydraulic calcium phosphate bone cement as antibiotic delivery system," *Journal of Pharmaceutical Sciences*, vol. 86, no. 5, pp. 565–572, 1997.
- [33] M. P. Hofmann, A. R. Mohammed, Y. Perrie, U. Gbureck, and J. E. Barralet, "High-strength resorbable brushite bone cement with controlled drug-releasing capabilities," *Acta Biomaterialia*, vol. 5, no. 1, pp. 43–49, 2009.
- [34] Y. Zhang and M. Zhang, "Calcium phosphate/chitosan composite scaffolds for controlled in vitro antibiotic drug release," *Journal of Biomedical Materials Research*, vol. 62, no. 3, pp. 378–386, 2002.
- [35] M. H. Alkhrasat, C. Rueda, J. Cabrejos-Azama et al., "Loading and release of doxycycline hyclate from strontium-substituted calcium phosphate cement," *Acta Biomaterialia*, vol. 6, no. 4, pp. 1522–1528, 2010.
- [36] S. Hesarakhi, F. Moztaaradeh, R. Nemati, and N. Nezafati, "Preparation and characterization of calcium sulfate-biomimetic apatite nanocomposites for controlled release of antibiotics," *Journal of Biomedical Materials Research B*, vol. 91, no. 2, pp. 651–661, 2009.

Review Article

Nanoparticle-Based Drug Delivery for Therapy of Lung Cancer: Progress and Challenges

Anish Babu,^{1,2} Amanda K. Templeton,^{1,2} Anupama Munshi,^{2,3} and Rajagopal Ramesh^{1,2,4}

¹ Department of Pathology, University of Oklahoma Health Sciences Center, Oklahoma City, OK 73104, USA

² Peggy and Charles Stephenson Cancer Center, University of Oklahoma Health Sciences Center, Oklahoma City, OK 73104, USA

³ Department of Radiation Oncology, University of Oklahoma Health Sciences Center, Oklahoma City, OK 73104, USA

⁴ The Graduate Program in Biomedical Sciences, University of Oklahoma Health Sciences Center, Oklahoma City, OK 73104, USA

Correspondence should be addressed to Rajagopal Ramesh; rajagopal-ramesh@ouhsc.edu

Received 26 August 2013; Accepted 28 October 2013

Academic Editor: Haifeng Chen

Copyright © 2013 Anish Babu et al. This is an open access article distributed under the Creative Commons Attribution License, which permits unrestricted use, distribution, and reproduction in any medium, provided the original work is properly cited.

The last decade has witnessed enormous advances in the development and application of nanotechnology in cancer detection, diagnosis, and therapy culminating in the development of the nascent field of “cancer nanomedicine.” A nanoparticle as per the National Institutes of Health (NIH) guidelines is any material that is used in the formulation of a drug resulting in a final product smaller than 1 micron in size. Nanoparticle-based therapeutic systems have gained immense popularity due to their ability to overcome biological barriers, effectively deliver hydrophobic therapies, and preferentially target disease sites. Currently, many formulations of nanocarriers are utilized including lipid-based, polymeric and branched polymeric, metal-based, magnetic, and mesoporous silica. Innovative strategies have been employed to exploit the multicomponent, three-dimensional constructs imparting multifunctional capabilities. Engineering such designs allows simultaneous drug delivery of chemotherapeutics and anticancer gene therapies to site-specific targets. In lung cancer, nanoparticle-based therapeutics is paving the way in the diagnosis, imaging, screening, and treatment of primary and metastatic tumors. However, translating such advances from the bench to the bedside has been severely hampered by challenges encountered in the areas of pharmacology, toxicology, immunology, large-scale manufacturing, and regulatory issues. This review summarizes current progress and challenges in nanoparticle-based drug delivery systems, citing recent examples targeted at lung cancer treatment.

1. Introduction

Worldwide lung cancer is the leading cause of cancer-related deaths with a dismal 5-year survival rate of only 15% [1]. Every year in the United States approximately 220,000 individuals are diagnosed with lung cancer of which 85% of the cases are classified as non-small-cell lung carcinoma (NSCLC) [1] while the remaining cases are diagnosed as small-cell lung carcinoma (SCLC). Current treatment strategies are strongly dependent on the type of malignancy and stage at the time of diagnosis but often involve a combination of surgery, chemotherapy, and/or radiation therapy.

Chemotherapy, a first-line treatment option for advanced-stage lung cancer, is often administered intravenously where it circulates throughout the body ultimately locating and destroying cancerous and normal tissues. Standard

first-line chemotherapy regimens for lung cancer include platinum-based drugs such as cisplatin and carboplatin. However, platinum-based chemotherapy is riddled with dose-limiting side effects including nephro- and cardiotoxicity, anemia, intestinal injury, and peripheral neuropathy as well as less serious symptoms of uneasiness, nausea, and fatigue. To mitigate many of these untoward effects, platinum drugs are used in combination with other anticancer agents. Combination therapy involving two to three drugs increases the therapeutic effectiveness and reduces the dosage of each individual drug required to produce an observable therapeutic response. Common chemotherapeutic agents for combination therapy include a platinum drug with paclitaxel, gemcitabine, etoposide, or vinblastine. However, like monotherapy, combination therapy is limited by dose-dependent side effects and patient's intolerance

to the drug combination resulting in cessation of treatment [2]. Additionally, the hydrophobic nature of the majority of the cancer chemotherapeutics makes them poorly water soluble and therefore limits their administration at high doses [3, 4]. Thus, methods to improve tumor-targeted delivery of chemotherapeutics that will result in increased drug efficacy with improved pharmacological properties and minimal toxicity to normal tissues remain a priority in cancer therapy.

Experimental therapies such as photodynamic therapy (PDT), immunotherapy, and gene therapy provide promising tools to fight lung cancer. In PDT, a photosensitizer activated by laser light reacts with molecular oxygen to form reactive oxygen species that function to annihilate cancer cells [5]. PDT is often used in combination with chemotherapy or surgery. Porfimer sodium, a first-generation photosensitizer, has been used in the treatment of early as well as advanced lung carcinomas. More improved and efficient PDT agents are currently available as a result of the extensive research efforts in the last two decades. However, many of these photosensitizers are poorly water soluble fettering their intravenous administration [6].

Immunotherapy harnesses the body's immune system to fight cancer. Biomolecules or antigens are administered to either trigger the immune system or reduce the immune suppressing activities of the tumor [7]. Administration of immunologically active agents disrupts the tumorigenic cascades by directly blocking growth factors or hormones and their receptors. Certain cancers including lung cancer overexpress growth factor receptors such as the epidermal growth factor receptor (EGFR/Her1). Binding of the ligand epidermal growth factor (EGF) to EGFR activates cell proliferation and survival signaling pathways resulting in rapid and uncontrolled tumor growth. Cetuximab, a competitive anti-EGFR monoclonal antibody, counteracts the cell proliferation signaling mediated by the endogenous EGF ligand culminating in attenuation of the cell survival signals and induction of tumor cell death. Gene therapy is a relatively new concept with a large number of research teams worldwide in active pursuit of identifying and delivering cancer-suppressing genes for clinical applications [8]. Delivery vectors are a necessity in order to protect the therapeutic genes until they reach their target site. Historically, viral vectors have been used to deliver gene-based therapeutics [9]; however, viral vector induced host immune responses limits their therapeutic potential [10]. Definitively, there is a growing need for development of safe and efficient delivery vehicles for photosensitizers, chemotherapeutics, and tumor suppressor genes.

Nanotechnology is not pervaded by some of the limitations of viral vectors providing an avenue of incredible potential for development of tumor-targeting drug delivery systems. This continuously expanding niche will revolutionize cancer treatment and management [11]. More precisely, nanoscale drug delivery systems hold great promise in successfully formulating and enhancing the therapeutic efficacy of a large number of anticancer agents [12]. Nanoparticles are known to positively alter biodistribution increasing therapeutic efficiency and reducing nonspecific toxicity of potent anticancer drugs. Their superior biocompatibility, ability to

protect nucleic acids from degradation, and ability to deliver therapeutic genes to cancer cells *in vivo* make nanoparticles the ideal delivery vehicle [13, 14]. While many nanoparticle-based therapies have been developed, such as Abraxane, an albumin-bound paclitaxel nanoformulation for the treatment of metastatic NSCLC [15], few have been translated into clinical success. It continues to be a challenge to identify ideal drug delivery systems for several classes of novel drugs with different physicochemical characteristics and varying degrees of therapeutic activities in the physiological environment. This review summarizes current progress and challenges in nanoparticle-based drug delivery systems, citing recent examples of applying nanomedicine for lung cancer treatment.

2. Progress in Nanoparticle Drug/Gene Delivery Systems

2.1. Lipid-Based Nanocarriers. Liposomes, oil dispersions (micelles), and lipid nanoparticles are the major classes of lipid-based nanocarriers for drug and gene delivery applications. Liposomes are bilayered phospholipid vesicles commonly used to deliver hydrophobic and hydrophilic drugs through either incorporation in the lipid bilayer itself or encapsulation in the inner aqueous core, respectively. Reduction of the number of lipid bilayers reduces the size of the liposomes to nanosize increasing the circulation time and tumor localization properties of encapsulated drugs [16].

Liposomes are becoming increasingly more popular delivery vehicles for anticancer therapeutics due to their strong biocompatibility properties. Over the last decade, the liposomal research field has boomed generating many new liposomal formulations such as cationic liposomes [17], virosomes [18], temperature-sensitive liposomes [19], and archaeosomes [20]. Despite these huge advances at the bench, currently there are only two FDA-approved liposomal formulations: DOXIL, a liposomal doxorubicin injection for ovarian cancer, and Marqibo, a liposomal vincristine sulphate injection for lymphoblastic leukemia.

In lung cancer treatment, liposomes may be a promising delivery system for drugs and genes. The drug of choice for the treatment of NSCLC for the last two decades, cisplatin, is implicated in the development of nephrotoxicity in 20% of patients receiving high doses [21]. In 2004, Boulikas developed a liposome-based cisplatin drug called Lipoplatin to reduce systemic toxicity of cisplatin [22]. Furthermore, these researchers also demonstrated that lipoplatin injection compared to standard therapy significantly reduced nephrotoxicity to negligible levels in multiple rat tumor models [23]. According to a recent report, lipoplatin is anticipated to complete phase III clinical trial testing in 2013 and 2014 [24]. Paclitaxel, another chemotherapeutic drug widely used in the treatment of lung cancer, was historically formulated using Cremophore EL to enhance its solubility in physiological fluids. However, this resulted in hypersensitivity reactions complicating its systemic delivery. In 2010, a phase I clinical trial in NSCLC patients with malignant pleural effusions demonstrated in all cases investigated that treatment with

paclitaxel formulated with a liposomal carrier had enhanced therapeutic efficacy [25]. Moreover, a recent preclinical study has shown that liposomal-paclitaxel formulation can be modified to target lung cancer cells to reduce the incidence of drug resistance [26]. Specifically, the liposomal surface was decorated with the mitochondrial targeting molecule d- α -tocopheryl polyethylene glycol 1000 succinate-triphenylphosphine conjugate (TPGS1000-TPP). These targeted paclitaxel liposomes could significantly enhance their cellular uptake inducing mitochondria-mediated apoptotic cell death in human A549 lung cancer cells. At present Lipusu, a paclitaxel-liposome, is commercially available with several other formulations under clinical investigation [27]. Table 1 lists current examples of liposomal formulations undergoing clinical trials intended for the treatment of cancer. In a randomized phase III multicenter trial, liposomal formulation of cisplatin and paclitaxel combination therapy reached effective therapeutic response while reducing nephrotoxicity in NSCLC patients [28]. Interestingly, this liposomal drug combination is reported to not only improve the targeting efficiency to the primary tumor but also be effective against metastasis.

Liposomes have also been used to deliver cancer vaccines for the prevention or treatment of existing cancers. Studies using therapeutic vaccine Biomira Liposomal Protein 25 (BLP25) have shown encouraging results in the treatment of advanced NSCLC [29]. BLP25 uses a liposomal carrier that targets the tumor-associated antigen MUC1 to prevent tumor growth. A preclinical study in a human MUC1 transgenic lung cancer mouse model (hMUC1.Tg) demonstrated that pretreatment with a low dose of cyclophosphamide followed by two cycles of liposome BLP25 treatment significantly reduced the number of tumor foci [30]. Importantly, phase III clinical studies using liposome BLP25 are currently underway [31].

Studies from our own laboratory have shown that lipid based nanocarriers can be effectively used for gene delivery in mouse lung cancer models. Preclinical studies using the nontargeted nanoparticle system 1,2-dioleoyl-3-Trimethylammonium Propane (DOTAP):cholesterol (Chol.) carrying tumor suppressor genes such as *p53*, *TUSC2/FUS1*, or *mda-7/IL-24* [32] efficiently delivered therapeutic genes to metastatic tumor sites culminating in a significant therapeutic effect with increased animal survival. Preclinical studies from our laboratory demonstrating efficacy and safety of the DOTAP:Chol. nanoparticle system resulted in its clinical testing for delivery of the *TUSC2/FUS1* tumor suppressor gene in NSCLC patients. Results from the phase I clinical trial demonstrated that intravenous administration of *TUSC2* encapsulated in our DOTAP:Chol. nanoparticle system was safe and well tolerated with no treatment-related toxicity. Additionally, study results showed that the nanoparticles were efficiently taken up by primary and metastatic tumors, expression of transgene and gene products occurred, and specific alterations in *TUSC2*-regulated signaling pathways were observed [32]. Results from this trial have led to discussion for initiating a phase II study for lung cancer. Additional phase I trials testing DOTAP:Chol.-based nanoparticle therapy for breast, ovarian, and pancreatic cancers are anticipated.

The therapeutic genes to be delivered will vary and depend on the cancer type.

Solid lipid nanocarriers (SLNs) are another class of vehicle for drug and gene delivery. SLNs are superior to their lipid counterparts in their enhanced stability, high drug loading, improved biocompatibility, and ease of large-scale manufacturing production. Choi et al. [33] transfected *p53*-null H1299 lung cancer cells with SLN-carrier *p53*. The authors were able to demonstrate efficient *p53* protein expression compared to commercially available Lipofectin suggesting that SLNs could be used as highly efficient gene therapy vehicles in lung cancer. In a recent report, researchers successfully loaded SLNs with Bcl-2 siRNA and paclitaxel for synergistic combination therapy as well as coencapsulated CdSe/ZnS quantum dots to bestow optical traceability [34]. Collectively, the properties of SLNs are ideally suited for combined chemo- and/or gene-therapy and molecular imaging of cancer.

2.2. Polymeric Nanoparticles. As the name suggests, polymeric nanoparticles are synthesized from polymers. More recently, biodegradable polymers such as poly(lactic acid) (PLA), poly(lactic-co-glycolic) acid (PLGA), gelatin, albumin, chitosan, polycaprolactone, and poly-alkyl-cyanoacrylates have gained popularity in use because of their controlled and sustained release properties, subcellular size, and biocompatibility. For instance, Abraxane, an FDA-approved albumin-based nanoparticle carrying paclitaxel, is indicated for first-line treatment of locally advanced or metastatic NSCLC in combination with carboplatin in patients who are not candidates for curative surgery or radiation therapy. Polymer nanoparticles have been shown to enhance the chemo- and radio-therapeutic efficacy of anticancer agents [35]. Chemoradiation therapy involves the concurrent administration of chemotherapy and radiotherapy for the treatment of many cancers, including lung cancer. Chemoradiation therapy is known to improve the local tumor control and patient survival. Polyethylene glycol- (PEG-) modified polylactic acid nanoparticles loaded with taxanes have significantly improved the efficacy of chemoradiation therapy in both *in vitro* and in an A549 lung tumor xenograft model [36]. Other research groups have developed a cremophor-free nanoformulation of paclitaxel and cisplatin using block copolymers of PEG and polylactic acid for the treatment of lung cancer [37]. This nanoformulation called Genexol-PM has entered phase II clinical trials in patients with advanced NSCLC. A separate phase II clinical trial is awaiting results for the same nanocarrier modified to deliver gemcitabine to untreated patients diagnosed with metastatic lung cancer [38].

Traditional anticancer agents are loathed for their repugnant side effects including the discomfort and pain associated with their administration. Historically, oral drug delivery methods have not been feasible for the treatment of lung cancer due to the inability of the therapeutic to penetrate lung tumor sites and achieve efficient therapeutic concentration even at high administered doses. The size, shape, and surface charge of nanoparticles provide an avenue for the development of novel routes of administration for anticancer agents. Recently, Jiang et al. [39] investigated three different

TABLE 1: Ongoing or recently completed clinical trials of a few liposomal nanoformulations used for cancer chemotherapy*.

Trade name/composition	Indication	Phase	Stage
PEGylated Liposomal Doxorubicin	AIDS-associated non-Hodgkin's lymphoma	I	Completed
Doxil/CAELYX Liposomal Doxorubicin	Malignant female reproductive system neoplasm, Ovarian cancer	I	Active
Doxil Liposomal Doxorubicin	Resistant solid malignancies	I	Completed
Liposomal Cytarabine	Central nervous system malignancies, Stage IV breast cancer	II	Active
Liposomal Entrapped Paclitaxel Easy to Use (LEP-ETU)	Advanced cancer	I	Completed
Liposomal Daunorubicin	Hematologic cancer, Chronic myelomonocytic leukemia previously treated Myelodysplastic syndromes and recurrent adult Acute myeloid leukemia	II	Completed
BLP25 Liposome Vaccine	Lung neoplasms Non-small-cell lung carcinoma	II	Completed
CPX-351 Liposomal Cytarabine-Daunorubicin	Acute myeloid leukemia	I	Active
Liposomal Vincristine	Acute lymphoblastic leukemia	II	Active
Liposomal LE-SN38	Advanced cancer	I	Completed
IHL-305 Irinotecan Liposome Injection	Advanced solid tumours	I	Active
Liposome Encapsulated Mitoxantrone (LEM)	Advanced cancer	I	Completed
Liposomal Encapsulated Docetaxel (LE-DT)	Advanced solid tumours	I	Completed

*Data retrieved from US National Institutes of Health website (<http://clinicaltrials.gov/>) on August 21, 2013.

polymer-based nanoparticles composed of polycaprolactone (PCL) that were surface modified with chitosan polymer for oral administration of chemotherapy in lung cancer. The mucoadhesive properties of the polymer increased the therapeutic effect of anticancer drugs by selectively interacting with the increased levels of mucin expressed in cancer cells compared to normal cells. Similarly, another study reported the use of PCL-based diblock copolymer nanoparticles for treating lung cancer via oral administration [40]. Interestingly, this nanoparticle showed advantages over the commercially available Taxotere, an injectable docetaxel, in terms of cytotoxicity against lung cancer cells. Another research group designed a chitosan-based controlled drug delivery system to deliver the potent antineoplastic agent lomustine. The lomustine-loaded chitosan nanoparticles demonstrated excellent control over drug release and enhanced its *in vitro* cytotoxicity against the lung cancer cell line L132 [41]. Recently, attention has turned towards polymer nanoparticles with expansile properties for the treatment of lung cancer. A Lewis lung carcinoma mouse model demonstrated that following surgical intervention paclitaxel-loaded expansile nanoparticles delayed the local recurrence of subcutaneous lesions as well as modestly improved the overall survivability of the tumor-bearing animals [42].

The advantage of combining PLA or PLGA nanoparticles with chitosan has recently materialized. Chitosan modification of drug- or gene-loaded PLGA nanoparticles imparts a positive charge to the nanoparticle surface, which aids

in cellular uptake and cytotoxicity towards lung cancer cells [43, 44]. Identifying the potential of chitosan-modified nanoparticles as drug or gene delivery vehicles provides an opportunity for combined chemo- and gene-therapeutic approaches with same or similar kinds of nanoparticle systems. Currently, our lab is developing a chitosan/PLA-hybrid-based nanoparticle system for combined delivery of chemotherapeutics and tumor suppressor genes for lung cancer. The nanoparticles are designed such that the rigid PLA polymer matrix containing the chemotherapeutic drug forms the inner core and is surface coated with siRNA or DNA containing chitosan and decorated with tumor-targeting moieties. The nanoparticle is less than 200 nm in size and is physicochemically stable for at least 10 days in solution as well as having a drug encapsulation efficiency greater than 90% (data unpublished). The ultrastructure of this drug-loaded nanoparticle system is shown in Figure 1.

Polymer nanoparticles have been extensively used in studies aimed at delivering targeted chemotherapeutics to lung cancer. Tseng et al. [45] developed a gelatin nanoparticle system decorated with EGFR-targeted biotinylated EGF (bEGF). These nanoparticles demonstrated enhanced cellular uptake in EGFR overexpressing cancer cell lines holding promise for targeted lung cancer therapy. Building on this strategy, the same group reported an aerosol-targeted therapy in a mouse model for lung cancer using bEGF-gelatin nanoparticles loaded with cisplatin [46]. The aerosol-based targeted drug delivery system resulted in enhanced drug

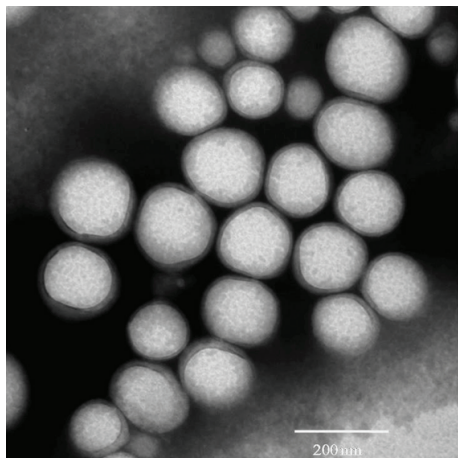


FIGURE 1: Transmission electron microscopy of cationic polymer coated poly (lactic acid) nanoparticle carrying the anticancer drug cisplatin.

concentrations in tumor tissues contributing to anticancer activity while direct tumor injection with the nanoparticles yielded high therapeutic efficacy and reduced systemic toxicity of cisplatin. Additionally, gelatin nanoparticles have also been used for the delivery of the hydrophobic drug resveratrol towards NSCLC cells [47].

Dendrimers are branched polymers with a large number of functional groups that radiate from a central core providing the opportunity to link multiple bioactive molecules. A recent study illustrated the use of dendrimer-targeting peptide conjugates as a carrier for drugs towards NSCLC [48]. These dendrimer-peptide conjugates when administered to a lung tumor-bearing athymic mouse model were efficiently taken up by the cancer cells demonstrating their potential as a drug carrier for the treatment of lung cancer [48]. In a related study, a newly designed PEGylated dendrimer nanoparticle showed promising application as an aerosol-inhaled drug delivery modality [49]. The smaller dendrimer particles are reported to enter the blood stream via inhalation while larger particles are sequestered in the lung for an extended period of time. In the future, this method of controlled drug delivery to the lungs could provide an alternative to injectable drug systems. Starpharma Holdings Ltd., Australia, released the primary data of a study utilizing delivery of dendrimer-based doxorubicin to rats burdened with metastatic breast cancer in the lungs [50]. The authors concluded that there was substantial improvement in the efficacy of doxorubicin when delivered using dendrimers.

Hybrid polymer nanoparticles composed of PLGA and chitosan demonstrated enhanced tumor uptake and cytotoxicity compared to unmodified nanoparticles in A549 cells [51]. More importantly, the modified nanoparticles administered to a lung metastatic mouse model demonstrated a lung-specific increase in biodistribution [51]. PLGA nanoparticles have also successfully been used to codeliver paclitaxel and STAT3 siRNA to the drug-resistant A549 cell line [52]. In another study, paclitaxel-loaded PLGA nanoparticles decorated with anti-EGFR demonstrated high binding affinity

to EGFR expressing cells in a mouse lung tumor model indicating the potential of these nanoparticles for targeted lung cancer therapy [53].

2.3. Metal-Based Nanoparticles. Noble metals such as gold and silver have been extensively investigated for clinical applications, including their use in sensitive diagnostic imaging, detecting, and classifying of lung cancer [54]. Peng et al. [55] developed a gold nanoparticle-based biosensor system with the capacity to detect lung cancer by analyzing an individual's exhaled breath. The sensor uses a combination of an array of chemiresistors based on gold nanoparticles and pattern recognition methods. Additionally, another research group reported the detection of picograms of enolase 1 (ENO1), an immunogenic antigen associated with NSCLC, by using an immunosensor that detects electrochemical signal probes of gold nanoparticle congregates [56]. Recently, gold nanoparticles have also successfully been tested as sensors for discriminating and classifying different lung cancer histologies. The sensor was able to distinguish between normal and cancerous cells, SCLC and NSCLC, and between two subtypes of NSCLCs [57].

Additionally, gold nanoparticles have been used to deliver anticancer drugs for enhanced therapeutic effectiveness. For example, methotrexate (MTX) has poor tumor retention ability due to its high water solubility, which likely contributes to its slow or poor therapeutic response in patients. However, gold nanoparticle conjugates of MTX have high tumor retention and enhanced therapeutic efficacy in a Lewis lung carcinoma mouse model [58]. Previously, we have shown in NSCLC cells that anti-EGFR antibody (Clone 225) conjugated hybrid plasmonic magnetic nanoparticles exhibited significant enhancement in anticancer activity by inducing autophagy and apoptosis [59]. Other studies have developed gold/iron oxide nanoclusters surface decorated with fluorescently labeled antibodies for targeting EGFR expressing epidermoid carcinoma cells [60]. Such design provides promising applications of gold-based nanoparticles in simultaneous use in magnetic resonance imaging (MRI) and therapy. Recently, gold nanoparticles have been applied in PDT for delivery of the water soluble PDT agent purpurin-18-N-methyl-D-glucamine (Pu-18-NMGA) towards A549 cells [61]. PDT using Pu-18-NMGA-gold nanoparticle resulted in higher photodynamic activity than free Pu-18-NMGA. Similarly, silver nanoparticles have demonstrated antiproliferative effects in cancer cells [62, 63]. However, *in vitro* exposure of human lung cancer cells to silver nanoparticles resulted in reactive oxygen species-induced genotoxicity raising concerns of an unfavorable risk to benefit ratio [64].

2.4. Other Nanoparticle Systems. Magnetic nanoparticles have been extensively investigated and applied in diagnosis and treatment of various cancers. Theranostic nanoparticles concurrently facilitate imaging and delivery of therapeutic agents. Magnetic hyperthermia is a noninvasive therapeutic approach for lung cancer that entails the heat-induced ablation of desired tumor tissue. When subjected to alternating currents the magnetic material, such as superparamagnetic

iron oxide (SPIO), nanoparticles generate sublethal heat that causes local tissue damage. Sadhukha et al. [65] evaluated in a mouse model the effectiveness of tumor-targeted SPIO nanoparticles for hyperthermic destruction of NSCLC. The EGFR-targeted SPIO nanoparticles showed enhanced tumor retention and significantly inhibited lung tumor growth.

Wang et al. [66] developed magnetic nanoparticles capable of detecting micrometastasis in lung cancer. Magnetic nanoparticles conjugated with the epithelial tumor cell marker pan-cytokeratin efficiently isolated circulating tumor cells (CTCs) from patients diagnosed with lung cancer. The cells were further identified using quantum dots (Qdots) coupled to the NSCLC micrometastasis marker lung-specific X protein (LUNX) and surfactant protein-A (SP-A) antibody. This is the first study that reported the detection of micrometastasis in peripheral blood of lung cancer patients. Magnetic nanoparticles have also been used to overcome drug resistance. A cisplatin-resistant A549 lung tumor xenograft model was chemosensitized with cisplatin loaded magnetic nanoparticles. Molecular studies demonstrated that cisplatin-loaded magnetic nanoparticle-treated tumors had a significant reduction in localization of lung resistance related proteins and enhanced cytotoxicity of cisplatin [67].

Mesoporous silica nanoparticles (MSNs) have been increasingly used in anticancer drug delivery research due to their dynamic capacity for drug loading, controlled drug release property, and multifunctional ability. Human lung cancer cells primarily take up MSNs by endocytosis [68]. MSNs have also been developed as a carrier for radionuclide isotope holmium-165 (Ho^{165}) and tested in a xenograft tumor model [69]. In this model, MSNs were able to hold the radionuclide without release and withstand long irradiation times. Additionally, Ho^{165} -carrying MSNs predominantly accumulated in the tumor tissue following intraperitoneal administration in tumor-bearing mice. Importantly, MSNs enhanced the radio-therapeutic efficacy of Ho^{165} and demonstrated their potential in managing ovarian cancer metastasis. MSNs have also been developed for inhalation treatment of lung cancer [70]. The elegant nanoparticle system design fully exploited the dynamic drug loading capabilities and multifunctionalization of MSNs. It was designed to simultaneously carry cisplatin, doxorubicin, and two different siRNAs targeted to MRP1 and Bcl-2. Moreover, it was surface decorated with luteinizing hormone releasing hormone (LHRH) peptide for targeted lung cancer therapy. The nanoparticle system carrying siRNA inhibited targeted mRNA causing suppression of cellular resistance to the chemotherapeutics accomplishing an enhanced therapeutic efficacy of cisplatin and doxorubicin. MSNs were also explored in targeted EGFR-based therapies. MSNs modified with the cationic polymer polyethyleneimine (PEI) and surface attached with EGFR ligands selectively targeted EGFR overexpressing NSCLC cells [71]. Moreover, these nanoparticles when loaded with the anticancer agent pyrrolidine-2 had enhanced targeting and therapeutic efficiencies compared to free drug in a subcutaneous lung cancer model.

3. Challenges for Nanoparticle-Based Drug Delivery in Lung Cancer Therapy

The past decade has witnessed tremendous growth and development of drug delivery technology utilizing nanoparticle systems. It is expected that the ongoing research efforts in nanomedicine will continue to lead towards safe, efficient, and feasible drug delivery and highly sensitive and improved imaging agents for diagnostic and disease monitoring applications. However, nanomedicine research is facing numerous challenges in bridging rapidly developing novel ideas and translating them into clinical practice. Synthesizing nanoparticle drug delivery systems has always been complicated by designing an appropriate size to carry effective drug/gene payload and ability to target to the right place. Inappropriate size distribution, undefined structure/shape, poor biocompatibility, and improper surface chemistry are possible risk factors in the biological environment. It has been operose to devise the ideal nanoparticle system for drug delivery to the lungs due to the variability in the physicochemical properties and biological behavior of the particles. A number of obstacles including immune reaction, rate of clearance from circulation, efficiency in targeting, and ability to cross biological barriers will follow when these nanoparticle systems enter the preclinical and clinical testing arenas. Having a solid understanding of the biological behavior of nanoparticles is imperative to achieve the highest drug delivery efficiency.

Identification of Physicochemical parameters are absolutely critical in determining the particle-particle interaction within a biological environment, aggregation tendencies, adsorption of proteins on nanoparticle surface, and intracellular trafficking of nanoparticles. A substantial variation in any of these factors can contribute to poor drug delivery, loss of therapeutic efficiency, and/or toxicity. Thus, the efficacy-toxicity balance of nanoparticle systems largely depends on their physicochemical properties. Particles larger than 500 nm are not recommended for intravenous administration since these particles are rapidly eliminated from the circulation. The ideal nanoparticle for delivering conventional therapeutics to solid tumors is less than 200 nm in size with a spherical shape and a smooth texture in order to easily transport through tumor vasculature and into tumor cells. Such physical characteristics are likely advantageous to the nanoparticles in exploiting the enhanced permeation and retention (EPR) effect associated with solid tumors. Passively targeted nanoparticles enter through leaky vasculature of the solid tumors and are retained in the tumor tissue for extended periods of time due to impaired lymphatic flow. This unique microphysiology of tumors is exploited by many FDA-approved nanoformulations such as Doxil and Abraxane. In solid tumors, such as lung cancer, the EPR effect plays an important role in determining the efficacy of the nanoparticle-based drug delivery system [72]. The presence of a highly fenestrated blood vasculature in the tumor facilitates the EPR effect allowing the enhanced entry of colloidal nanoparticles into the tumor (Figure 2). Additionally, the poor lymphatic flow in the tumor tissue adds to this effect and results in enhanced retention of

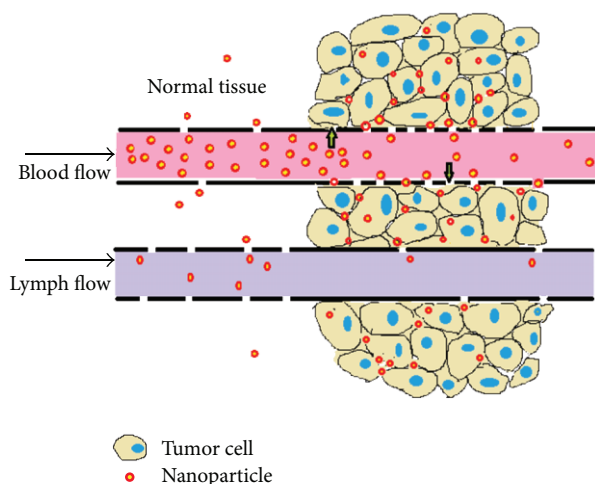


FIGURE 2: A schematic representation of the EPR effect. The leaky vasculature and dysfunctional lymphatics of solid tumors allow the preferential accumulation and retention of colloidal nanoparticles in contrast to the tight vasculature of normal tissue, which excludes nanoparticles.

nanoparticles within the tumor site. In contrast to tumor tissues, the blood vasculature in normal tissues is intact and less permeable attenuating the uptake of nanoparticles by normal tissues. Furthermore, the size, shape, and surface properties of nanoparticles are critically important for passive targeting of solid tumors. The EPR effect usually applies to particles that are less than 200 nm in size. However, particles less than 50 nm in size frequently undergo extravasation from the tumor through the fenestrations and are thus less likely to be retained in the tumor tissue for extended periods of time. Moreover, active targeting of nanoparticles is accomplished by decorating the surface of the nanoparticle with specific ligands to promote the binding and interaction with overexpressed protein receptors on cancer cell surfaces. This approach leads to preferential binding, uptake, and intracellular accumulation of the drug or gene in the targeted cells. However, the overall tumor accumulation and therapeutic effect of targeted nanoparticles may be principally controlled by the EPR effect [73].

Fabrication of polymeric nanoparticles with uniform and sub-200 nm size requires critical control over each and every step in the synthesis procedure, which is always challenging. The size distribution of liposomes or vesicular nanoparticles can be narrowed using common extrusion procedures. However, burst release of the drug and poor stability layer additional challenges in the development of such nanoparticles.

Surface charge determines the fate of nanoparticles *in vivo*. Particle-particle interactions and aggregation tendencies are largely dependent on the zeta potential of the nanoparticles. Positively charged nanoparticles have an increased affinity for the negatively charged cellular membranes of all cells in the body. Most nanoparticles designed for gene delivery applications use positively charged polymers or lipids to achieve enhanced DNA to

nanoparticle interaction. Unfortunately, some cationic nanoparticles have enhanced hemolytic properties inciting concern for their safe use in gene delivery. For example, cationic lipid composition of N [1-(2,3-dioleoyloxy) propyl]-N,N,N-trimethylammonium chloride and dioleoylphosphatidylethanolamine (DOTMA/DOPE) are reported to be highly hemolytic while 3 beta-[N-(N',N'-dimethylaminoethane)-carbamoyl]-cholesterol (DC-chol)/DOPE liposomes are moderately hemolytic [74].

Biocompatible polymer nanoparticles are an alternative to cationic lipids for the charge-specific delivery of drugs and/or genes. However, little is known in lung tumor models about the effect of surface charge on biodistribution of nanoparticles. PEGylation is routinely used to mask the surface charge effectively camouflaging the nanoparticle from opsonin proteins and significantly extending the half-life of the nanoparticle in the circulation. Another important issue in drug delivery is nanoparticle stability. Poor stability of nanoparticle systems has been attributed to their aggregation tendencies in the physiological environment. Once aggregated, it is virtually impossible to redisperse the particles into their original distribution pattern. While shear forces can be used to redisperse the particles, this may lead to enhanced drug leaching from the particles and ultimately affect the drug loading and therapeutic efficiencies.

Additionally, further consideration must be given to the complexity of nanoparticles and how this may have a negative impact on drug delivery. Multifunctional nanoparticles are hot topics in the field of nanomedicine [75]. A nanoparticle with a large number of surface functional groups provides an avenue for the attachment of multiple kinds of biomolecules for targeted drug delivery and diagnostic applications for lung cancer. A careful analysis of these nanoparticle systems, however, is necessary prior to testing in an *in vivo* system. Multifunctionalization generally increases the complexity of the nanoparticle. While a large number of multifunctional nanoparticles, such as theranostic systems targeted to lung cancer are under development, Aurimune (CYT-6091) is currently the only known multifunctional nanoparticle system with diagnostic and therapeutic properties that has entered the clinical setting [76]. Aurimune consists of tumor necrosis factor (TNF), a tumor growth inhibiting agent, bound to colloidal gold nanoparticles for simultaneous imaging and therapy.

Interestingly, increased scientific contributions to the field of nanomedicine have resulted in the emergence of a new area of research, nanotoxicology [77]. Even though nanoparticles of various compositions have displayed strong therapeutic properties towards various types of cancer in preclinical studies, they also carry the risk of inducing toxicity to normal cells. Emphases in particular towards inorganic- and metal-based nanoparticles have demonstrated that some nanoparticles induce toxicity to normal cells. For example, silica nanoparticles in their amorphous state have the potential to cause inflammatory reactions on target organs resulting in apoptotic cell death [78]. Thus, the use of silica-based nanoparticles for cancer therapy is limited to low concentrations (0.1 mg/mL) *in vitro* [78]. The toxicity of titanium oxide (TiO₂) nanoparticles towards healthy cells is also a

matter of concern considering its biological applications [79]. Carbon nanotubes (CNTs) have also been reported to exhibit toxicity to normal cells. CNTs upon interaction with live cells generate reactive oxygen species causing mitochondrial dysfunction and lipid peroxidation [80]. Therefore, stringent *in vitro* and *in vivo* toxicity studies for each of the novel nanoparticle systems must be conducted to ensure safety prior to their application in humans.

4. Conclusion and Future Perspectives

Nanoparticle-based medicine has infinite potential with novel applications continuously being developed for use in cancer diagnosis, detection, imaging, and treatment. These systems are already helping to address key issues with traditional anticancer agents such as nonspecific targeting, low therapeutic efficiencies, untoward side effects, and drug resistance as well as surpassing their predecessors with the ability to detect early metastasis. The ability of nanoparticles to be tailored for a personalized medicine strategy makes them ideal vehicles for the treatment of lung cancer. Numerous nanoparticle-based experimental therapeutics for lung cancer utilize a combinatorial approach balancing the design with targeting and tracking moieties and anticancer agents. In general, nanoparticles with multicomponent structures allow design flexibility in drug delivery of poorly water soluble molecules as well as imparting the ability to overcome biological barriers and selectively target desired sites within the body.

However, many challenges must be overcome in order to expedite the translation of nanoparticle-based therapies from the bench to the bedside. Nanomedicines are three-dimensional structures of multiple components with preferred spatial arrangement to impart their function. Subtle changes in the synthesis process or composition of the complex that alter the physical and/or chemical properties can have adverse effects resulting in pharmacological and immunological challenges. Pharmacokinetics (PK) and biodistribution are known to be effected by small compositional differences in nanoparticles [81]. Moreover, nanoparticles oftentimes require higher bioavailability than traditional small molecules since they are routinely designed for novel routes of delivery such as by nasal or oral administration. *In vivo* clearance of nanoparticles and release kinetics of the active drug are also complicated by their physical and chemical properties. PEGylation is oftentimes used to mask the nanoparticle to evade detection by macrophages and avoid opsonization and destruction. This strategy effectively increases the circulation time enhancing the distribution and accumulation of nanoparticles at the intended target site. Ultimately, small molecules are cleared by the kidney while larger particles are cleared by Kupffer cells and macrophages in the liver and spleen [82]. Researches are also challenged with nanoparticle induced immune responses, which can be elicited by the nanocarrier, the payload, or both [83]. These findings enumerate the importance for identifying key characteristics of each component and developing a thorough understanding of the physicochemical properties to ensure

high reproducibility throughout the formulation process and minimize pharmacological and immunological challenges.

Aside from the difficulty of nanoparticle design and discovery, scientists must also battle the lack of standards in the examination of nanomedicines, including manufacturing processes, functional testing, and safety measurements. Conceptually nanoparticle-based therapy must overcome the same hurdles faced by any new drug: optimal design of components and properties, reproducible manufacturing processes, institution of analysis methods for sufficient characterization, favorable pharmacology and toxicity profiles, and demonstration of safety and efficacy in clinical trials. Standard drugs are usually composed of a single active agent. Nanoparticles are complex in nature with multiple active components that can affect the pharmacological behavior. Such complexity necessitates the modification of standard testing of pharmacokinetic, bioequivalence, and safety measurements. There is an immediate need for regulatory agencies to develop an exhaustive list of tests and a streamlined approval process to proactively address the emergence of new products based on new technologies and facilitate nanomedicine delivery to the clinic.

References

- [1] S. S. Ramalingam, T. K. Owonikoko, and F. R. Khuri, "Lung cancer: new biological insights and recent therapeutic advances," *CA Cancer Journal for Clinicians*, vol. 61, no. 2, pp. 91–112, 2011.
- [2] L. C. Pronk, G. Stoter, and J. Verweij, "Docetaxel (Taxotere): single agent activity, development of combination treatment and reducing side-effects," *Cancer Treatment Reviews*, vol. 21, no. 5, pp. 463–478, 1995.
- [3] J. Lu, M. Liang, J. I. Zink, and F. Tamanoi, "Mesoporous silica nanoparticles as a delivery system for hydrophobic anticancer drugs," *Small*, vol. 3, no. 8, pp. 1341–1346, 2007.
- [4] A. Kumar, S. K. Sahoo, K. Padhee et al., "Review on solubility enhancement techniques for hydrophobic drugs," *International Journal of Comprehensive Pharmacy*, vol. 3, no. 3, pp. 1–7, 2011.
- [5] P. Agostinis, K. Berg, K. A. Cengel et al., "Photodynamic therapy of cancer: an update," *CA Cancer Journal for Clinicians*, vol. 61, no. 4, pp. 250–281, 2011.
- [6] A. Babu, J. Periasamy, A. Gunasekaran et al., "Polyethylene glycol-modified gelatin/poly(lactic acid) nanoparticles for enhanced photodynamic efficacy of a hypocrellin derivative *in vitro*," *Journal of Biomedical Nanotechnology*, vol. 9, no. 2, pp. 177–192, 2013.
- [7] M. Dougan and G. Dranoff, "Immune therapy for cancer," *Annual Review of Immunology*, vol. 27, pp. 83–117, 2009.
- [8] M. A. Kay, "State-of-the-art gene-based therapies: the road ahead," *Nature Reviews Genetics*, vol. 12, no. 5, pp. 316–328, 2011.
- [9] M. Giacca and S. Zacchigna, "Virus-mediated gene delivery for human gene therapy," *Journal of Controlled Release*, vol. 161, no. 2, pp. 377–388, 2012.
- [10] S. Nayak and R. W. Herzog, "Progress and prospects: immune responses to viral vectors," *Gene Therapy*, vol. 17, no. 3, pp. 295–304, 2010.
- [11] J. H. Grossman and S. E. McNeil, "Nanotechnology in cancer medicine," *Physics Today*, vol. 65, pp. 38–42, 2012.

- [12] A. Z. Wang, R. Langer, and O. C. Farokhzad, "Nanoparticle delivery of cancer drugs," *Annual Review of Medicine*, vol. 63, pp. 185–198, 2012.
- [13] K. Ahmad, "Gene delivery by nanoparticles offers cancer hope," *The Lancet Oncology*, vol. 3, no. 8, p. 451, 2002.
- [14] R. Ramesh, "Nanoparticle-mediated gene delivery to the lung," *Methods in Molecular Biology*, vol. 434, pp. 301–331, 2008.
- [15] D. Yuan, Y. Lv, Y. Yao et al., "Efficacy and safety of Abraxane in treatment of progressive and recurrent non-small cell lung cancer patients: a retrospective clinical study," *Thoracic Cancer*, vol. 3, no. 4, pp. 341–347, 2012.
- [16] R. M. Schiffelers, J. M. Metselaar, M. H. A. M. Fens, A. P. C. A. Janssen, G. Molema, and G. Storm, "Liposome-encapsulated prednisolone phosphate inhibits growth of established tumors in mice," *Neoplasia*, vol. 7, no. 2, pp. 118–127, 2005.
- [17] S. Simões, A. Filipe, H. Faneca et al., "Cationic liposomes for gene delivery," *Expert Opinion on Drug Delivery*, vol. 2, no. 2, pp. 237–254, 2005.
- [18] M. Adamina, U. Guller, L. Bracci, M. Heberer, G. C. Spagnoli, and R. Schumacher, "Clinical applications of virosomes in cancer immunotherapy," *Expert Opinion on Biological Therapy*, vol. 6, no. 11, pp. 1113–1121, 2006.
- [19] L. H. Lindner, M. E. Eichhorn, H. Eibl et al., "Novel temperature-sensitive liposomes with prolonged circulation time," *Clinical Cancer Research*, vol. 10, no. 6, pp. 2168–2178, 2004.
- [20] L. Krishnan, L. Deschatelets, F. C. Stark, K. Gurnani, and G. D. Sprott, "Archaeosome adjuvant overcomes tolerance to tumor-associated melanoma antigens inducing protective CD8+ T cell responses," *Clinical and Developmental Immunology*, vol. 2010, Article ID 578432, 13 pages, 2010.
- [21] X. Yao, K. Panichpisal, N. Kurtzman, and K. Nugent, "Cisplatin nephrotoxicity: a review," *American Journal of the Medical Sciences*, vol. 334, no. 2, pp. 115–124, 2007.
- [22] T. Boulikas, "Low toxicity and anticancer activity of a novel liposomal cisplatin (Lipoplatin) in mouse xenografts," *Oncology Reports*, vol. 12, no. 1, pp. 3–12, 2004.
- [23] P. Devarajan, R. Tarabishi, J. Mishra et al., "Low renal toxicity of lipoplatin compared to cisplatin in animals," *Anticancer Research*, vol. 24, no. 4, pp. 2193–2200, 2004.
- [24] "Liposomal cisplatin (Nanoplatin) for advanced non-small cell lung cancer—first line (2012)," <http://www.hsc.nihr.ac.uk/topics/liposomal-cisplatin-nanoplatin-for-advanced-non-sm/>.
- [25] X. Wang, J. Zhou, Y. Wang et al., "A phase I clinical and pharmacokinetic study of paclitaxel liposome infused in non-small cell lung cancer patients with malignant pleural effusions," *European Journal of Cancer*, vol. 46, no. 8, pp. 1474–1480, 2010.
- [26] J. Zhou, W. Y. Zhao, X. Ma et al., "The anticancer efficacy of paclitaxel liposomes modified with mitochondrial targeting conjugate in resistant lung cancer," *Biomaterials*, vol. 34, no. 14, pp. 3626–3638, 2013.
- [27] S. Koudelka and J. Turánek, "Liposomal paclitaxel formulations," *Journal of Control Release*, vol. 163, no. 3, pp. 322–334, 2012.
- [28] G. P. Stathopoulos, D. Antoniou, J. Dimitroulis et al., "Liposomal cisplatin combined with paclitaxel versus cisplatin and paclitaxel in non-small-cell lung cancer: a randomized phase III multicenter trial," *Annals of Oncology*, vol. 21, no. 11, pp. 2227–2232, 2010.
- [29] S. North and C. Butts, "Vaccination with BLP25 liposome vaccine to treat non-small cell lung and prostate cancers," *Expert Review of Vaccines*, vol. 4, no. 3, pp. 249–257, 2005.
- [30] G. T. Wurz, A. M. Gutierrez, B. E. Greenberg et al., "Antitumor effects of L-BLP25 Antigen-Specific tumor immunotherapy in a novel human MUC1 transgenic lung cancer mouse model," *Journal of Translational Medicine*, vol. 11, no. 1, pp. 64–77, 2013.
- [31] Y.-L. Wu, K. Park, R. A. Soo et al., "INSPIRE: a phase III study of the BLP25 liposome vaccine (L-BLP25) in Asian patients with unresectable stage III non-small cell lung cancer," *BMC Cancer*, vol. 11, article 430, 2011.
- [32] C. Lu, D. J. Stewart, J. J. Lee et al., "Phase I clinical trial of systemically administered TUSC2(FUS1)-nanoparticles mediating functional gene transfer in humans," *Plos One*, vol. 7, no. 4, Article ID e34833, 2012.
- [33] S. H. Choi, S.-E. Jin, M.-K. Lee et al., "Novel cationic solid lipid nanoparticles enhanced p53 gene transfer to lung cancer cells," *European Journal of Pharmaceutics and Biopharmaceutics*, vol. 68, no. 3, pp. 545–554, 2008.
- [34] K. H. Bae, J. Y. Lee, S. H. Lee, T. G. Park, and Y. S. Nam, "Optically traceable solid lipid nanoparticles loaded with siRNA and paclitaxel for synergistic chemotherapy with in situ imaging," *Advanced Healthcare Materials*, vol. 2, no. 4, pp. 576–584, 2013.
- [35] A. Z. Wang, K. Yuet, L. Zhang et al., "ChemoRad nanoparticles: a novel multifunctional nanoparticle platform for targeted delivery of concurrent chemoradiation," *Nanomedicine*, vol. 5, no. 3, pp. 361–368, 2010.
- [36] J. Jung, S. J. Park, H. K. Chung et al., "Polymeric nanoparticles containing taxanes enhance chemoradiotherapeutic efficacy in non-small cell lung cancer," *International Journal of Radiation Oncology Biology Physics*, vol. 84, pp. e77–e83, 2012.
- [37] D.-W. Kim, S.-Y. Kim, H.-K. Kim et al., "Multicenter phase II trial of Genexol-PM, a novel Cremophor-free, polymeric micelle formulation of paclitaxel, with cisplatin in patients with advanced non-small-cell lung cancer," *Annals of Oncology*, vol. 18, no. 12, pp. 2009–2014, 2007.
- [38] "A Phase II Trial of Genexol-PM and Gemcitabine in Patients With Advanced Non-small-cell Lung Cancer," 2013, <http://clinicaltrials.gov/show/NCT01770795>.
- [39] L. Jiang, X. Li, L. Liu, and Q. Zhang, "Thiolated chitosan-modified PLA-PCL-TPGS nanoparticles for oral chemotherapy of lung cancer," *Nanoscale Research Letters*, vol. 8, no. 1, p. 66, 2013.
- [40] T. Zhao, H. Chen, L. Yang et al., "DDAB-modified TPGS-b-(PCL-ran-PGA) Nanoparticles as oral anticancer drug carrier for lung cancer chemotherapy," *Nano*, vol. 8, no. 2, Article ID 1350014, 10 pages, 2013.
- [41] A. Mehrotra, R. C. Nagarwal, and J. K. Pandit, "Lomustine loaded chitosan nanoparticles: characterization and in-vitro cytotoxicity on human lung cancer cell line L132," *Chemical and Pharmaceutical Bulletin*, vol. 59, no. 3, pp. 315–320, 2011.
- [42] R. Liu, O. V. Khullar, A. P. Griset et al., "The pax-eNP placed at the time of surgical resection delayed local tumor recurrence and modestly prolonged survival in a murine Lewis lung carcinoma recurrence model," *Annals of Thoracic Surgery*, vol. 91, no. 4, pp. 1077–1083, 2011.
- [43] R. Yang, S.-G. Yang, W.-S. Shim et al., "Lung-specific delivery of paclitaxel by chitosan-modified PLGA nanoparticles via transient formation of microaggregates," *Journal of Pharmaceutical Sciences*, vol. 98, no. 3, pp. 970–984, 2009.
- [44] K. Tahara, H. Yamamoto, N. Hirashima, and Y. Kawashima, "Chitosan-modified poly(D,L-lactide-co-glycolide) nanospheres for improving siRNA delivery and gene-silencing effects," *European Journal of Pharmaceutics and Biopharmaceutics*, vol. 74, no. 3, pp. 421–426, 2010.

- [45] C.-L. Tseng, T.-W. Wang, G.-C. Dong et al., "Development of gelatin nanoparticles with biotinylated EGF conjugation for lung cancer targeting," *Biomaterials*, vol. 28, no. 27, pp. 3996–4005, 2007.
- [46] C.-L. Tseng, W.-Y. Su, K.-C. Yen, K.-C. Yang, and F.-H. Lin, "The use of biotinylated-EGF-modified gelatin nanoparticle carrier to enhance cisplatin accumulation in cancerous lungs via inhalation," *Biomaterials*, vol. 30, no. 20, pp. 3476–3485, 2009.
- [47] S. Karthikeyan, N. R. Prasad, A. Ganamani, and E. Balamurugan, "Anticancer activity of resveratrol-loaded gelatin nanoparticles on NCI-H460 non-small cell lung cancer cells," *Biomedicine and Preventive Nutrition*, vol. 3, no. 1, pp. 64–73, 2013.
- [48] J. Liu, J. Liu, L. Chu et al., "Novel peptide-dendrimer conjugates as drug carriers for targeting nonsmall cell lung cancer," *International Journal of Nanomedicine*, vol. 6, no. 1, pp. 59–69, 2010.
- [49] G. M. Ryan, L. M. Kaminskas, B. D. Kelly, D. J. Owen, M. P. McIntosh, and C. J. H. Porter, "Pulmonary administration of PEGylated polylysine dendrimers: absorption from the lung versus retention within the lung is highly size-dependent," *Molecular Pharmaceutics*, vol. 10, no. 8, pp. 2986–2995, 2013.
- [50] "Dendrimers improve anticancer efficacy in lung metastasis model," 2013, <http://www.starpharma.com/news/150>.
- [51] R. Yang, S.-G. Yang, W.-S. Shim et al., "Lung-specific delivery of paclitaxel by chitosan-modified PLGA nanoparticles via transient formation of microaggregates," *Journal of Pharmaceutical Sciences*, vol. 98, no. 3, pp. 970–984, 2009.
- [52] W. P. Su, F. Y. Cheng, D. B. Shieh, C. S. Yeh, and W. C. Su, "PLGA nanoparticles codeliver paclitaxel and Stat3 siRNA to overcome cellular resistance in lung cancer cells," *International Journal of Nanomedicine*, vol. 7, pp. 4269–4283, 2012.
- [53] N. Karra, T. Nassar, A. N. Ripin et al., "Antibody conjugated PLGA nanoparticles for targeted delivery of paclitaxel palmitate: efficacy and biofate in a lung cancer mouse model," *Small*, 2013.
- [54] J. Conde, G. Doria, and P. Baptista, "Noble metal nanoparticles applications in cancer," *Journal of Drug Delivery*, vol. 2012, Article ID 751075, 12 pages, 2012.
- [55] G. Peng, U. Tisch, O. Adams et al., "Diagnosing lung cancer in exhaled breath using gold nanoparticles," *Nature Nanotechnology*, vol. 4, no. 10, pp. 669–673, 2009.
- [56] J.-A. A. Ho, H.-C. Chang, N.-Y. Shih et al., "Diagnostic detection of human lung cancer-associated antigen using a gold nanoparticle-based electrochemical immunosensor," *Analytical Chemistry*, vol. 82, no. 14, pp. 5944–5950, 2010.
- [57] O. Barash, N. Peled, U. Tisch, P. A. Bunn Jr., F. R. Hirsch, and H. Haick, "Classification of lung cancer histology by gold nanoparticle sensors," *Nanomedicine: Nanotechnology, Biology, and Medicine*, vol. 8, no. 5, pp. 580–589, 2012.
- [58] Y.-H. Chen, C.-Y. Tsai, P.-Y. Huang et al., "Methotrexate conjugated to gold nanoparticles inhibits tumor growth in a syngeneic lung tumor model," *Molecular Pharmaceutics*, vol. 4, no. 5, pp. 713–722, 2007.
- [59] T. Yokoyama, J. Tam, S. Kuroda et al., "Egfr-targeted hybrid plasmonic magnetic nanoparticles synergistically induce autophagy and apoptosis in non-small cell lung cancer cells," *PLoS ONE*, vol. 6, no. 11, Article ID e25507, 2011.
- [60] L. L. Ma, J. O. Tam, B. W. Willsey et al., "Selective targeting of antibody conjugated multifunctional nanoclusters (nanoroses) to epidermal growth factor receptors in cancer cells," *Langmuir*, vol. 27, no. 12, pp. 7681–7690, 2011.
- [61] B. Lkhagvadulam, J. H. Kim, I. Yoon, and Y. K. Shim, "Size-dependent photodynamic activity of gold nanoparticles conjugate of water soluble purpurin-18-N-methyl-D-glucamine," *BioMed Research International*, vol. 2013, Article ID 720579, 10 pages, 2013.
- [62] R. Govender, A. Phulukdaree, R. M. Gengan, K. Anand, and A. A. Chuturgoon, "Silver nanoparticles of *Albizia adianthifolia*: the induction of apoptosis in human lung carcinoma cell line," *Journal of Nanobiotechnology*, vol. 11, no. 5, pp. 1477–3155, 2013.
- [63] W. G. Zhou and W. Wang, "Synthesis of silver nanoparticles and their antiproliferation," *The Oriental Journal of Chemistry*, vol. 28, no. 2, pp. 651–655, 2012.
- [64] R. Foldbjerg, D. A. Dang, and H. Autrup, "Cytotoxicity and genotoxicity of silver nanoparticles in the human lung cancer cell line, A549," *Archives of Toxicology*, vol. 85, no. 7, pp. 743–750, 2011.
- [65] T. Sadhukha, T. S. Wiedmann, and J. Panyam, "Inhalable magnetic nanoparticles for targeted hyperthermia in lung cancer therapy," *Biomaterials*, vol. 34, no. 21, pp. 5163–5171, 2013.
- [66] Y. Wang, Y. Zhang, Z. Du, M. Wu, and G. Zhang, "Detection of micrometastases in lung cancer with magnetic nanoparticles and quantum dots," *International Journal of Nanomedicine*, vol. 7, pp. 2315–2324, 2012.
- [67] K. Li, B. Chen, L. Xu et al., "Reversal of multidrug resistance by cisplatin-loaded magnetic Fe₃O₄ nanoparticles in A549/DDP lung cancer cells in vitro and in vivo," *International Journal of Nanomedicine*, vol. 8, pp. 1867–1877, 2013.
- [68] W. Sun, N. Fang, B. G. Trewyn et al., "Endocytosis of a single mesoporous silica nanoparticle into a human lung cancer cell observed by differential interference contrast microscopy," *Analytical and Bioanalytical Chemistry*, vol. 391, no. 6, pp. 2119–2125, 2008.
- [69] A. J. Di Pasqua, M. L. Miller, X. Lu, L. Peng, and M. Jay, "Tumor accumulation of neutron-activatable holmium-containing mesoporous silica nanoparticles in an orthotopic non-small cell lung cancer," *Inorganica Chimica Acta*, vol. 393, no. 1, pp. 334–336, 2012.
- [70] O. Taratula, O. B. Garbuzenko, A. M. Chen, and T. Minko, "Innovative strategy for treatment of lung cancer: targeted nanotechnology-based inhalation co-delivery of anticancer drugs and siRNA," *Journal of Drug Targeting*, vol. 19, no. 10, pp. 900–914, 2011.
- [71] S. Sundarraj, "EGFR antibody conjugated mesoporous silica nanoparticles for cytosolic phospholipase A2 α targeted non-small lung cancer therapy," *Journal of Cell Science and Therapy*, vol. 3, no. 7, 2012.
- [72] H. Maeda, "The enhanced permeability and retention (EPR) effect in tumor vasculature: the key role of tumor-selective macromolecular drug targeting," *Advances in Enzyme Regulation*, vol. 41, pp. 189–207, 2001.
- [73] N. Dinauer, S. Balthasar, C. Weber, J. Kreuter, K. Langer, and H. Von Briesen, "Selective targeting of antibody-conjugated nanoparticles to leukemic cells and primary T-lymphocytes," *Biomaterials*, vol. 26, no. 29, pp. 5898–5906, 2005.
- [74] H. Schreier, L. Gagné, T. Bock et al., "Physicochemical properties and in vitro toxicity of cationic liposome cDNA complexes," *Pharmaceutica Acta Helvetica*, vol. 72, no. 4, pp. 215–223, 1997.
- [75] G. Bao, S. Mitragotri, and S. Tong, "Multifunctional nanoparticles for drug delivery and molecular imaging," *Annual Review of Biomedical Engineering*, vol. 15, pp. 253–282, 2013.
- [76] R. Wang, P. S. Billone, and W. M. Mullet, "Nanomedicine in action: an overview of cancer nanomedicine on the market and

- in clinical trials,” *Journal of Nanomaterials*, vol. 2013, Article ID 629681, 12 pages, 2013.
- [77] A. F. Hubbs, R. R. Mercer, S. A. Benkovic et al., “Nanotoxicology—a pathologist’s perspective,” *Toxicologic Pathology*, vol. 39, no. 2, pp. 301–324, 2011.
- [78] J. McCarthy, I. Inkielewicz-Stepmiak, J. J. Corbalan, and M. W. Radomski, “Mechanisms of toxicity of amorphous silica nanoparticles on human using submucosal cells in vitro: protective effects of fisetin,” *Chemical Research in Toxicology*, vol. 25, no. 10, pp. 2227–2235, 2012.
- [79] B. Trouiller, R. Reliene, A. Westbrook, P. Solaimani, and R. H. Schiestl, “Titanium dioxide nanoparticles induce DNA damage and genetic instability in vivo in mice,” *Cancer Research*, vol. 69, no. 22, pp. 8784–8789, 2009.
- [80] A. Make, L. Wang, and Y. Rojanasakul, “Mechanisms of nanoparticle-induced oxidative stress and toxicity,” *BioMed Research International*, vol. 2013, Article ID 942916, 15 pages, 2013.
- [81] D. F. Emerich and C. G. Thanos, “The pinpoint promise of nanoparticle-based drug delivery and molecular diagnosis,” *Biomolecular Engineering*, vol. 23, no. 4, pp. 171–184, 2006.
- [82] S. M. Moghimi, A. C. Hunter, and J. C. Murray, “Long-circulating and target-specific nanoparticles: theory to practice,” *Pharmacological Reviews*, vol. 53, no. 2, pp. 283–318, 2001.
- [83] M. A. Dobrovolskaia, P. Aggarwal, J. B. Hall, and S. E. McNeil, “Preclinical studies to understand nanoparticle interaction with the immune system and its potential effects on nanoparticle biodistribution,” *Molecular Pharmaceutics*, vol. 5, no. 4, pp. 487–495, 2008.

Research Article

Magnetic and Structural Studies of CoFe_2O_4 Nanoparticles Suspended in an Organic Liquid

Branka Babić-Stojić,¹ Vukoman Jokanović,¹ Dušan Milivojević,¹ Zvonko Jagličić,²
Darko Makovec,³ Nataša Jović,¹ and Milena Marinović-Cincović¹

¹ Vinča Institute of Nuclear Sciences, University of Belgrade, P.O. Box 522, 11001 Belgrade, Serbia

² Institute of Mathematics, Physics and Mechanics, Jadranska 19, 1000 Ljubljana, Slovenia

³ Department for Materials Synthesis, Jožef Stefan Institute, Jamova 39, 1000 Ljubljana, Serbia

Correspondence should be addressed to Branka Babić-Stojić; babic@vinca.rs

Received 16 September 2013; Accepted 17 October 2013

Academic Editor: Haifeng Chen

Copyright © 2013 Branka Babić-Stojić et al. This is an open access article distributed under the Creative Commons Attribution License, which permits unrestricted use, distribution, and reproduction in any medium, provided the original work is properly cited.

We present a study of magnetic and structural properties of CoFe_2O_4 nanoparticles suspended in an organic liquid. Transmission electron microscopy shows that the nanoparticles have a narrow size distribution of average particle size 5.9 ± 1.0 nm. X-ray diffraction shows that the particles are of cubic spinel crystal structure. Dynamic light scattering measurements reveal the existence of an organic shell around the CoFe_2O_4 nanoparticles with an average hydrodynamic diameter of 14.4 nm. Coercive magnetic field at $T = 5$ K is found to be 11.8 kOe. Disappearance of the coercive field and remanent magnetization at about 170 K suggests that the CoFe_2O_4 nanoparticles are superparamagnetic at higher temperatures which is confirmed by the room temperature Mössbauer spectrum analysis. Saturation magnetization of the nanoparticles of 80.8 emu/g(CoFe_2O_4) at 5 K reaches the value detected in the bulk material and remains very high also at room temperature. The cobalt ferrite nanoparticle system synthesized in this work exhibits magnetic properties which are very suitable for various biomedical applications.

1. Introduction

Ferrofluids are stable colloidal suspensions of single domain magnetic particles in a carrier liquid. Stability of the magnetic colloid depends on the thermal contribution and on the balance between attractive and repulsive interactions. Magnetic dipole and van der Waals interactions have tendency to agglomerate the particles. In order to prevent agglomeration, the magnetic particles should be small enough (usually about 10 nm in size) and coated with a shell of an appropriate material. This coating can be a surfactant made of long chained molecules or ionic if it is an electric shell [1–3]. The particles are usually made of maghemite $\gamma\text{-Fe}_2\text{O}_3$, magnetite Fe_3O_4 , and other ferrites of the type MFe_2O_4 , where $\text{M} = \text{Mn}, \text{Co}, \text{Ni}, \text{Cu}$. The carrier liquid is usually an organic solvent or water. Ferrofluids respond to an external magnetic field. This enables the ferrofluid's location to be controlled through the application of a magnetic field. Ferrofluids have a wide range of applications. They can be used to improve the

performance of loud speakers [2]. Ferrofluids are also used in high-speed computer disk drives to eliminate harmful dust particles or other impurities that can cause the data-reading heads to crash into the disks. In recent years, a lot of research work has been devoted to biomedical applications of ferrofluids. In magnetic resonance imaging (MRI), ferrofluids are used as contrast agents [3–5]. Ferrofluids specially designed can carry drugs to specific locations in the living body through the use of applied magnetic fields [3, 6]. Heat treatment of organs or tissues called hyperthermia uses the property of ferrofluids of absorbing electromagnetic energy. This allows heating of a localized part of a living body, such as malignant tumor, up to temperature 42–46°C which reduces the viability of cancerous cells [3, 4, 6]. For various applications, particularly in biomedicine, magnetic particles in ferrofluids, besides the requirement for small sizes, must have large enough magnetization. Depending on the relative magnitude of anisotropy energy with respect to thermal energy, the particles exhibit superparamagnetic

behavior when magnetic moment of the particle overcomes the anisotropy energy barrier by thermal activation. For a given temperature T and time τ characteristic to a specific measurement, there is a critical particle diameter D_{sp} (assuming spherical shape) that separates smaller particles $D < D_{sp}$ exhibiting superparamagnetism from larger particles $D > D_{sp}$ which have ferro(ferri)magnetic properties. For cubic magnetocrystalline anisotropy, the energy barrier is $E = KV/4$, where V is the particle volume. The critical size of the CoFe_2O_4 particles with anisotropy constant $K = 2 \times 10^6 \text{ erg cm}^{-3}$ at $T = 300 \text{ K}$ [7] and for $\tau = 10^2 \text{ s}$ can be estimated [8] as $D_{sp} \approx 16 \text{ nm}$. In the case of axial magnetocrystalline anisotropy, the energy barrier is $E = KV$, and, for the same values of the parameters K , T , and τ , the critical particle size is $D_{sp} \approx 10 \text{ nm}$.

There are two dominant mechanisms of magnetic relaxation in a ferrofluid, the Brownian relaxation and Néel relaxation. When the relaxation is dominated by the Brownian mechanism, the magnetic moment is rotated together with the nanoparticle in the carrier liquid under the influence of an external magnetic field [9]. Relaxation time for the Brownian rotational motion is

$$\tau_B = \frac{3V_h\eta}{k_B T}, \quad (1)$$

where V_h is the hydrodynamic volume of the particle, η is the dynamic viscosity of the carrier liquid, and T is the temperature. At temperatures below the freezing point of the carrier liquid, the particles are immobilized, and in that case relaxation of the particle magnetic moment can take place only by rotation of the moment within the particle. Relaxation time for this rotation, known as the Néel relaxation, is

$$\tau_N = \tau_0 \exp\left(\frac{E}{k_B T}\right), \quad (2)$$

where τ_0 is the characteristic time of the system.

Up to now, the research attention has been focused mainly on magnetic properties and magnetic relaxation in ferrofluids with iron oxide nanoparticles (NPs) [10–15]. These materials are already in use as contrast agents for MRI and are under investigation for several other applications. On the other hand, the use of materials with larger magnetic anisotropy and larger magnetic moment is considered since it may allow the reduction of particle size. The bulk cobalt ferrite is a magnetic material with almost the same saturation magnetization as the bulk iron oxide Fe_3O_4 , but with one order of magnitude higher magnetocrystalline anisotropy compared to magnetite. Because of these properties the cobalt ferrite nanoparticle systems are promising materials for high-density magnetic recording media and also very interesting for various biomedical applications [16–20]. In this work, we have synthesized CoFe_2O_4 NPs in an organic carrier liquid. Microstructure, morphology, and static and dynamic magnetic properties of the prepared nanomaterial were studied using X-ray diffraction (XRD), transmission electron microscopy (TEM), dynamic light scattering (DLS), Fourier-transform infrared (FTIR) spectroscopy, differential scanning calorimetry (DSC), dc magnetization, ac susceptibility measurements, and Mössbauer spectroscopy. We found

that the properties of this NPs system correspond to ferrofluids: it is stable for months, magnetic nanoparticles do not agglomerate and have reproducible magnetic properties. Its main characteristics are high saturation magnetization at low temperatures close to that of the bulk material and superparamagnetic properties of most of the CoFe_2O_4 nanoparticles at room temperature.

2. Experimental Details

2.1. Synthesis. Synthesis of the CoFe_2O_4 nanoparticles was carried out via the polyol route using Co(II) acetate, Fe(III) acetylacetonate, and diethylene glycol (DEG) from Aldrich Chemical Co as starting materials. These precursors were taken in stoichiometric ratio for obtaining the CoFe_2O_4 phase: 22.3775 g Fe(III) acetylacetonate and 7.8870 g Co(II) acetate were mixed as solutions inside of diethylene glycol solvent which has been previously divided in two parts, the first volume of 150 mL for dissolution of Fe(III) acetylacetonate and the second volume of 50 mL for dissolution of Co(II) acetate. The mixture of both solutions was magnetically stirred under the flow of nitrogen. After that, the space of the vessel filled with nitrogen was closed and the mixture was heated firstly to 120°C with a heating rate of 4°C per minute, and then the temperature was increased to 160°C and maintained at this level for 3 h. Finally, the temperature was increased to 180°C and after one hour was abruptly lowered with a high cooling rate by cold water introduced through corresponding inlet. The water flowed with a high flux around the working volume of the vessel causing a fast change of temperature from the top temperature to the room temperature. The particle solution was filtered to exclude aggregates. A Vivaspin filter (polyethersulfone (PES), Vivascience Sartorius, Hannover, Germany) with pore size $0.2 \mu\text{m}$ was used and the filtering process was performed by centrifuging the sample at 1750 rpm for about 30 min until all fluid had passed the filter. Besides the liquid sample, a powder sample was also prepared by drying the suspension of CoFe_2O_4 NPs at 200°C for 10 h.

2.2. Experimental Technique. X-ray characterization of the sample was carried out on a Philips PW 1050 powder diffractometer using $\text{Cu K}\alpha$ radiation. The X-ray diffraction (XRD) pattern was taken in the 17° – $70^\circ 2\theta$ range with a step of 0.05° at a slow scan rate of 40 s per step. For transmission electron microscopy (TEM) measurements, the sample was prepared by drying a drop of the diluted suspension on a copper-grid-supported perforated transparent carbon foil. High-resolution transmission electron microscopy (HRTEM) and energy dispersive X-ray spectroscopy (EDXS) were carried out using a field-emission electron-source transmission electron microscope JEOL 2010 equipped with an EDXS microanalysis system (LINK ISIS EDS 300) operated at 200 kV. Average Fe/Co ratio in the composition of the nanoparticles was obtained from quantification of a large number of EDXS spectra using the Oxford ISIS software. The spectra were collected from areas of the sample containing several hundreds of the nanoparticles. For the quantification of the

spectra, the CoFe_2O_4 ceramics were used as a standard. The relative standard deviation of the method calculated from 20 measurements of the Fe/Co ratio on the standard was found to be inside $\pm 2.6\%$ ($\text{Fe}/\text{Co}_{\text{standard}} = 1.992 \pm 0.052$). The size distribution of the CoFe_2O_4 nanoparticles was measured by dynamic light scattering (DLS) using Zetasizer Nano ZS (Malvern, UK) equipped with green laser (532 nm). Intensity of scattered light was detected at the angle of 173° . All measurements were conducted at room temperature. Ten measurements were performed for each sample. All data processing was done by the Zetasizer software 6.20 (Malvern instruments). The size distribution is reported as distribution by number. Fourier-transform infrared (FTIR) transmission spectrum was taken at room temperature on a Perkin-Elmer 983 G spectrophotometer in the range $600\text{--}3900\text{ cm}^{-1}$. Differential scanning calorimetry (DSC) measurements were performed using Setaram 151 R (softer SETSOFT 2000) instrument in the temperature range $150\text{--}240\text{ K}$ under helium atmosphere. Magnetic measurements were carried out on a SQUID magnetometer (MPMS XL-5, Quantum Design) equipped with an *ac* option. Zero-field-cooled (ZFC) and field-cooled (FC) measurements of magnetization were performed at applied magnetic fields from 100 to 10000 Oe in the temperature range from 2 to 300 K. Magnetic field dependence of magnetization was measured at applied magnetic fields up to 50 kOe in the temperature range from 5 to 300 K. The *ac* magnetization measurements were made under an *ac* exciting field with amplitude of 6.5 Oe using different frequencies in the range $1\text{--}1500\text{ Hz}$. ^{57}Fe Mössbauer spectrum was recorded at room temperature using a conventional transmission Mössbauer spectrometer operating in constant acceleration mode. The source was ^{57}Co in Rh matrix. Experimental data were fitted to Lorentzian absorption lines by using a least square based method. The spectrometer was calibrated using $\alpha\text{-Fe}$ foil at room temperature. All the isomer shifts are given relative to the center of the $\alpha\text{-Fe}$ spectrum.

3. Results and Discussion

3.1. Structure Analysis. Figure 1 shows the XRD pattern of dry powder sample. The diffraction peaks are consistent with those of the cubic spinel phase (space group $\text{Fd}3\text{m}$). The lattice parameter obtained from Rietveld analysis was found to be $a = 8.390\text{ \AA}$. The average crystallite size determined from the width of the X-ray diffraction lines using Scherrer's formula was estimated as 5 nm.

The morphology, particle size, and chemical composition of the CoFe_2O_4 nanoparticles deposited from organic liquid dispersion were characterized by TEM, HRTEM, and EDXS. TEM analysis (Figure 2(a)) shows that the sample contains the nanoparticles with a narrow size distribution. The measurement of approximately 500 nanoparticles from TEM images gave equivalent diameter of $5.9 \pm 1.0\text{ nm}$. HRTEM imaging showed good crystallinity of the nanoparticles (Figure 2(b)). The electron diffraction pattern (inset of Figure 2(a)) corresponds to a spinel structure. The EDXS spectra analysis confirmed stoichiometric composition of the

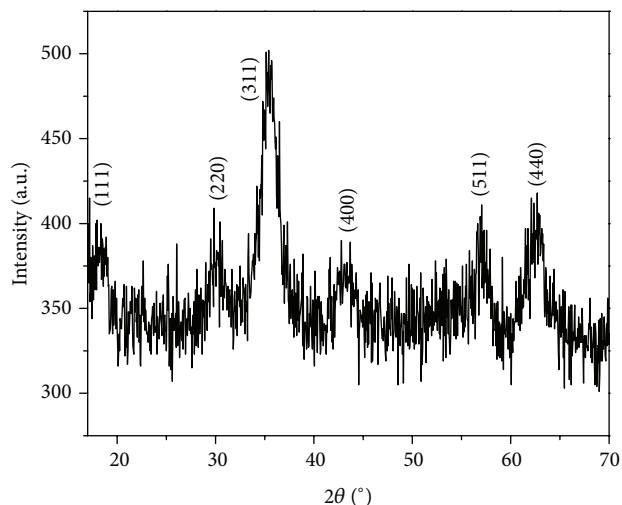


FIGURE 1: Powder X-ray diffraction pattern of the CoFe_2O_4 dried powder sample indexed with the (hkl) reflections of the cubic spinel.

cobalt ferrite nanoparticles in the margins of the experimental uncertainty. The measured Fe/Co ratio was 2.08 ± 0.14 .

The size distribution of the CoFe_2O_4 nanoparticles in the organic liquid was studied using dynamic light scattering (DLS). The result is presented in Figure 3. Measured number of particles as a function of hydrodynamic particle diameter can be well described by a log-normal distribution:

$$f(d) = \frac{1}{\sqrt{2\pi}\sigma d} \exp\left[-\frac{\ln^2(d/d_0)}{2\sigma^2}\right]. \quad (3)$$

The best fit yields the distribution width $\sigma = 0.22$ and median of the distribution $d_0 = 14.1\text{ nm}$ related to the average hydrodynamic diameter $d_{\text{av}} = d_0 \exp(\sigma^2/2) = 14.4\text{ nm}$. The hydrodynamic diameters are larger than those measured by TEM. This is because DLS measures the size of the particles together with organic shell which cannot be observed in the TEM images due to poor contrast with respect to the background as a result of low electron density of the organic structure. Difference between the average hydrodynamic diameter of the particles and equivalent TEM diameter gives a measure of the thickness of the organic shell. The organic shell thickness thus estimated is about 4 nm.

FTIR transmission spectrum of the organic liquid suspension of CoFe_2O_4 NPs was measured at room temperature in the region from $600\text{ to }3900\text{ cm}^{-1}$ (Figure 4). The band at 2350 cm^{-1} can be assigned to (Co, Fe)-OH vibrations caused by the interaction of the $\text{CoFe}_2\text{O}_{4-x}(\text{OH})_x$ surface layer of the nanoparticles with polar group chains of the diethylene glycol (DEG). Almost negligible band at 2331 cm^{-1} belongs probably to the symmetric stretching mode of the $\nu_s\text{ CH}_2$. The band at 1625 cm^{-1} belongs to the $\nu_s(\text{COO}^-)$ asymmetric stretching mode of carboxyl acids. A slightly pronounced band at 1316 cm^{-1} belongs to the C-O-C stretching vibrations inside of residual DEG chains [17, 21]. The slightly pronounced band arising from the residual DEG chains with missing other characteristic bands for DEG at 1050 and 1080 cm^{-1} shows

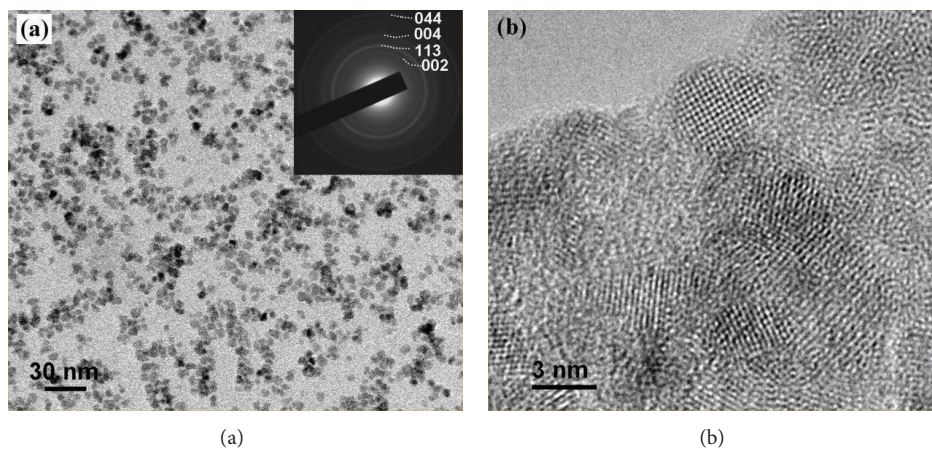


FIGURE 2: TEM (a) and HRTEM (b) images of the CoFe_2O_4 nanoparticles. Electron diffraction pattern in the inset of Figure 2(a) was indexed according to the spinel structure.

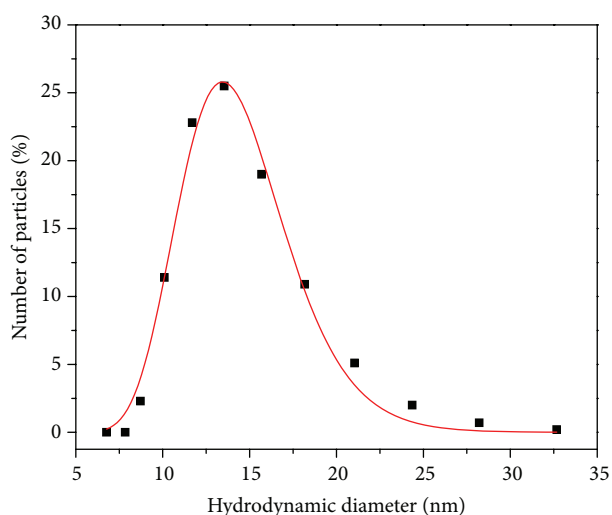


FIGURE 3: Hydrodynamic size distribution of the CoFe_2O_4 nanoparticles suspended in the organic liquid measured by dynamic light scattering. The solid curve is the fit of the dependence (3) to the experimental data.

that DEG is mostly changed probably into diethylene glycol acetate (ester compound) and diethylene glycol acetylacetonate. The band at 2350 cm^{-1} proves the existence of significant interaction between the $\text{CoFe}_2\text{O}_{4-x}(\text{OH})_x$ surface layer of the nanoparticles and organic shell. It can be noticed also that a very small fraction of DEG remained unreacted due to excess of DEG compared to carboxyl acid groups inside of starting mixture for the synthesis of the organic liquid suspension of CoFe_2O_4 NPs.

3.2. Magnetic Properties

3.2.1. *dc* Magnetization. The temperature dependence of zero-field-cooled and field-cooled magnetization curves for the organic liquid suspension of CoFe_2O_4 NPs was measured at applied magnetic fields from 100 to 10000 Oe.

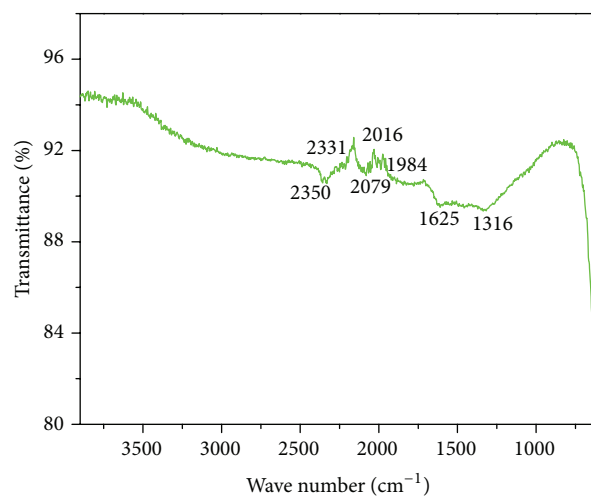


FIGURE 4: Fourier-transform infrared transmission spectrum of the organic liquid suspension of CoFe_2O_4 nanoparticles at room temperature.

The concentration of the CoFe_2O_4 phase in the liquid sample was 0.045 g/mL which corresponds to the volume fraction of 0.84% . Magnetization values are expressed per unit mass of CoFe_2O_4 taking into account the mass fraction of the CoFe_2O_4 nanoparticles in the liquid. The representative ZFC-FC curves for several selected magnetic field values are shown in Figure 5. To explore possible aging effects, we compared these measurements with the previous runs performed several months ago. Measured magnetizations were reproduced within a few percent of precision. As can be seen, the ZFC and FC magnetizations of the liquid sample bifurcate at a certain temperature and show a broad peak in the ZFC curve with a maximum at temperature T_{max} . The broad peak in the ZFC magnetization is characteristic of superparamagnetic nanoparticles with size distribution where the temperature of the maximum T_{max} represents the average blocking temperature. The temperature T_{max} for the

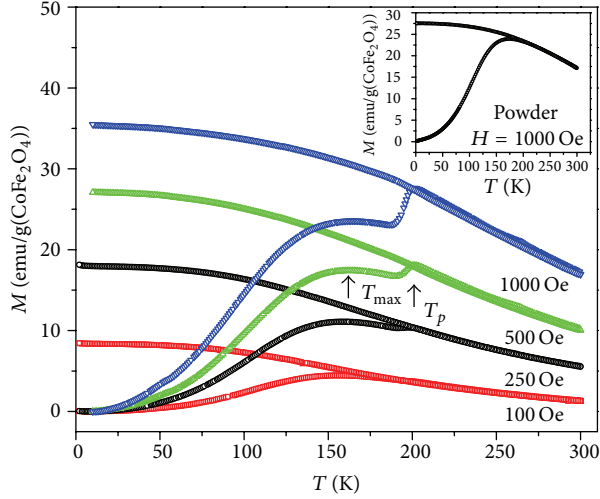


FIGURE 5: Temperature dependence of the zero-field-cooled (ZFC) and field-cooled (FC) magnetization curves for the organic liquid suspension of CoFe₂O₄ nanoparticles at several selected magnetic field values. The inset shows the temperature dependence of the ZFC-FC magnetization of dry powder at $H = 1000$ Oe.

liquid sample extends in the range 156–164 K depending on the magnetic field values in the range $H \leq 1000$ Oe. Besides the broad peak in the ZFC magnetization, a cusp at about $T_p \approx 200$ K was also detected, which can be clearly seen for magnetic fields $H \geq 500$ Oe (Figure 5).

In order to get some insight into the origin of the cusp in the ZFC magnetization of the organic liquid suspension of CoFe₂O₄ NPs at about 200 K, we have measured the ZFC-FC magnetization of dry powder at $H = 1000$ Oe which is shown in the inset of Figure 5. As can be seen, there is no cusp in the ZFC magnetization of the powder sample in contrast to the liquid sample where this cusp is clearly observed. This finding suggests that the origin of the cusp in the ZFC magnetization of the liquid sample at about 200 K is associated with the carrier liquid. We performed differential scanning calorimetry (DSC) measurements on the liquid sample and the result is presented in Figure 6. Three distinct peaks in DSC graph were found. The first peak at about 204 K indicates the temperature where a part of the organic liquid enters the frozen or so called mixed state [11]. The second peak at about 183 K probably is due to freezing of the remaining part of the organic liquid. The peak at about 164 K indicates transition temperature of the liquid from the partly frozen (mixed) state to the completely frozen (solid) state. It can be noticed that the temperature of the cusp observed in the ZFC magnetization at about $T_p \approx 200$ K is just below the temperature 204 K where the organic liquid enters the frozen state. The fact that the magnetization of the magnetic nanoparticles dispersed in the liquid is sensitive to the Brownian motion of the particles in that liquid and that there is no anomalous behavior of the magnetization in the dry powder gives evidence that the cusp in the ZFC magnetization of the organic liquid suspension of CoFe₂O₄ NPs is due to the freezing of the organic liquid.

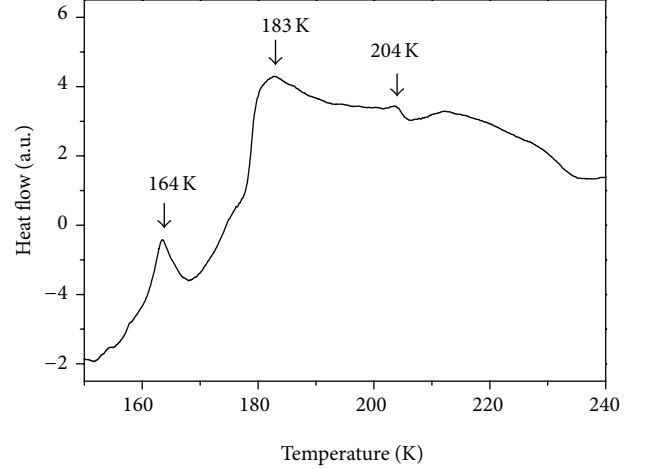


FIGURE 6: Differential scanning calorimetry curve for the liquid sample of the CoFe₂O₄ nanoparticles in the temperature range 150–240 K.

The magnetic field dependence of magnetization for the suspension of the CoFe₂O₄ NPs at $T = 5$ K and 300 K is presented in Figure 7. The $M(H)$ curve at $T = 300$ K exhibits superparamagnetic behavior: the coercive field H_c and remanent magnetization M_r are zero and the saturation magnetization, estimated by extrapolation of the M versus $1/H$ curve in the limit $1/H \rightarrow 0$, is 50.1 emu/g (CoFe₂O₄). For comparison, saturation magnetization of the bulk CoFe₂O₄ at 300 K is M_s (bulk) ≈ 76 emu/g [22]. At $T = 5$ K, the liquid sample exhibits hysteresis loop. The $M(H)$ measurements carried out at magnetic fields in the range of ± 50 kOe gave $H_c = 11.8$ kOe, $M_r = 39.1$ emu/g(CoFe₂O₄), and $M_s = 80.8$ emu/g(CoFe₂O₄) which was estimated also by the extrapolation of the M versus $1/H$ dependence in the limit $1/H \rightarrow 0$. The saturation magnetization at $T = 5$ K falls into the region of the M_s values for the bulk CoFe₂O₄ ranging from 80 to 94 emu/g [23]. The saturation magnetization of the CoFe₂O₄ NPs in the liquid sample at 5 K, as well as that at room temperature, is considerably higher than that for the CoFe₂O₄ NPs obtained by either thermal decomposition [24, 25], or microemulsion route [26], or mechanical milling [27]. It appears that the method of synthesis applied in the present work favors good crystallinity and magnetic ordering resulting in a high saturation magnetization.

Saturation magnetization of 80.8 emu/g(CoFe₂O₄) for the CoFe₂O₄ NPs in the liquid sample at $T = 5$ K corresponds to $\mu_s = 3.4\mu_B$ per unit chemical formula which is only slightly larger than that for inverse spinel ($3\mu_B$). Utilizing the formula (Co_{1- δ} Fe _{δ})[Co _{δ} Fe_{2- δ}]O₄ to describe the cation distribution in the spinel structure of the CoFe₂O₄ nanoparticles, where δ is the inversion parameter, and assuming that Fe³⁺ and Co²⁺ ions have a magnetic moment of $5\mu_B$ and $3\mu_B$, respectively, we find that $\delta = 0.91$. The value of the inversion parameter δ indicates that the crystal structure of the CoFe₂O₄ NPs is very close to the inverse spinel.

Coercive field and saturation magnetization of the liquid sample as a function of temperature are presented in the

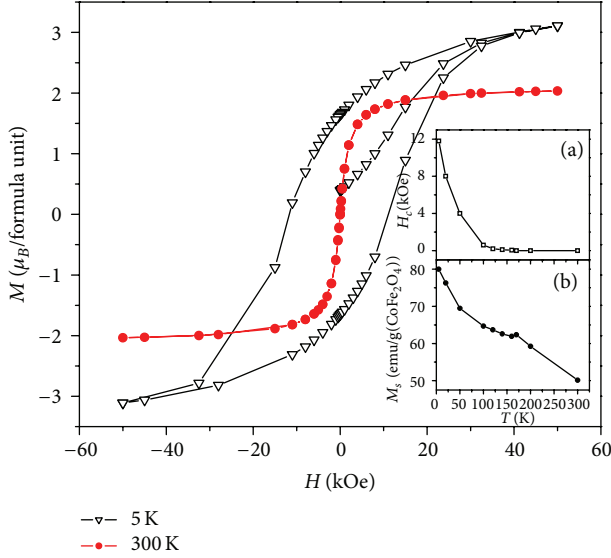


FIGURE 7: Magnetic field dependence of the magnetization for the organic liquid suspension of the CoFe_2O_4 nanoparticles at 5 K and 300 K. The inset shows the temperature dependence of (a) coercive field and (b) saturation magnetization.

inset of Figure 7. The coercive field decreases with increasing temperature and vanishes at about 170 K. The saturation magnetization exhibits specific properties. First, there is a small kink in the M_s versus T plot at 170 K where the coercive field vanishes, and, second, the character of the function $M_s(T)$ is changed at this temperature. Remanent magnetization (not shown) also decreases with increasing temperature and vanishes at about 170 K.

The broad peak in the ZFC magnetization at T_{\max} extending from 156 to 164 K for the magnetic field in the range $H \leq 1000$ Oe as well as the disappearance of the coercive field and remanent magnetization at about 170 K suggests that a large fraction of the CoFe_2O_4 nanoparticles in the organic liquid are subject to the blocking process at temperatures below 170 K.

3.2.2. *ac* Magnetic Susceptibility. Figure 8 shows the temperature dependence of (a) the real part χ' and (b) the imaginary part χ'' of the *ac* magnetic susceptibility for the suspension of the CoFe_2O_4 NPs at different frequencies in the range 1–1500 Hz. It can be seen that the real component χ' has a maximum at a temperature T_{m1} in the vicinity of 200 K which shifts towards higher temperatures with increasing frequency. The imaginary part χ'' has a maximum at a temperature T_{m2} around 160 K which also shifts towards higher temperatures with increasing frequency. This property is not only characteristic of most of the spin glass systems but also of the interacting and noninteracting superparamagnetic nanoparticles. It should be noticed that the temperature T_{m1} falls into the temperature region of freezing of the organic liquid, while T_{m2} falls into the temperature region of the broad peak in the ZFC magnetization of the liquid sample. In fact, the temperature T_{m2} is significantly

lower than the temperatures around 200 K where the organic liquid enters the frozen (mixed) state. Therefore, we could expect that at T_{m2} the particles are mainly frozen and cannot move, and relaxation of the particle magnetic moments in that case should occur relative to the particle through the Néel relaxation.

According to Néel [28] magnetic moment of noninteracting single domain particles with uniaxial magnetic anisotropy relaxes via an activated process, $\tau = \tau_0 \exp(E/k_B T)$, that is, the Arrhenius law, where E is the barrier due to anisotropy energy required for reversal of magnetic moment orientation and τ is the relaxation time. At temperatures where the relaxation time is comparable to the experimental time scale, the spins will seem to be frozen. Thus, the blocking temperature depends on the relaxation time $\tau \sim 1/f$, where f is the frequency of the experiment. We assume that the temperature of the maximum in χ'' is the blocking temperature of the CoFe_2O_4 particle magnetic moments. Taking $\tau = 1/2\pi f$, the relation between T_{m2} and frequency f is $f = f_0 \exp(-E/k_B T_{m2})$, where $f_0 = 1/2\pi\tau_0$. We find that T_{m2} can be fitted to the Arrhenius law. However, the fitted parameters are large or even have unphysical values: $\tau_0 = 1/2\pi f_0 = 2.9 \times 10^{-18}$ s and $E/k_B = 5360$ K.

In the further analysis, we take the interparticle interactions into account and describe the relaxation time of the particles in the vicinity of the temperature T_{m2} by the Vogel-Fulcher law,

$$\tau = \tau_0 \exp \left[\frac{E}{k_B (T - T_0)} \right], \quad (4)$$

where E is the energy barrier and the parameter T_0 depends on the interparticle interactions [11]. Now, the relation between T_{m2} and frequency f is $f = f_0 \exp[-E/k_B (T_{m2} - T_0)]$. A good fit of the Vogel-Fulcher law, (4), to the experimental data $\ln f$ versus $T_{m2}(f)$ is obtained with physically meaningful parameters, and the result is shown in Figure 9. The best fit yields $f_0 = (1.6 \pm 0.3) \times 10^{11}$ Hz, $\tau_0 = 1/2\pi f_0 = (1.0 \pm 0.3) \times 10^{-12}$ s, $E/k_B = (2300 \pm 300)$ K and $T_0 = (46.5 \pm 5)$ K. The parameter T_0 presents the average value of the interparticle interactions observed in the $\chi''(T)$ dependence in the measured frequency range. In the case of axial magnetocrystalline anisotropy, the energy barrier of superparamagnetic particles is related to the anisotropy constant, $E = KV$. For $E/k_B = 2300$ K and average volume of the particles assuming spherical geometry $\langle V \rangle = 1.075 \times 10^{-19}$ cm³, $K = 3 \times 10^6$ erg/cm³, which is somewhat larger than that in the bulk material [23]. High saturation magnetization of the synthesized CoFe_2O_4 NPs with a narrow size distribution in combination with superparamagnetic properties observed at room temperature makes these particles, with appropriate coating and functionalization, very promising materials for biomedical applications, especially in magnetic targeted drug delivery and in magnetic fluid hyperthermia.

Temperature of the maximum in the real part of the *ac* magnetic susceptibility T_{m1} appears in the vicinity of 200 K, Figure 8(a), that is, in the region where the organic liquid enters the frozen (mixed) state. In the mixed state, the system is not yet a rigid solid and the nanoparticles

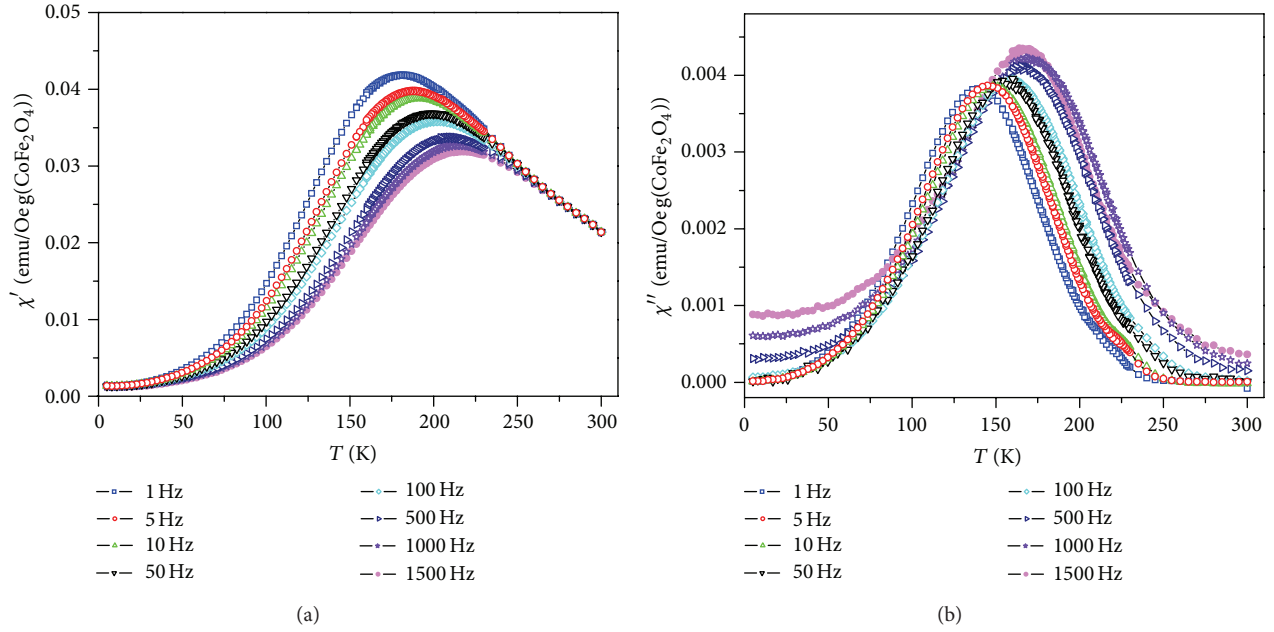


FIGURE 8: Temperature dependence of (a) the real part χ' and (b) the imaginary part χ'' of the ac magnetic susceptibility for the organic liquid suspension of the CoFe_2O_4 nanoparticles at different frequencies in the range 1–1500 Hz.

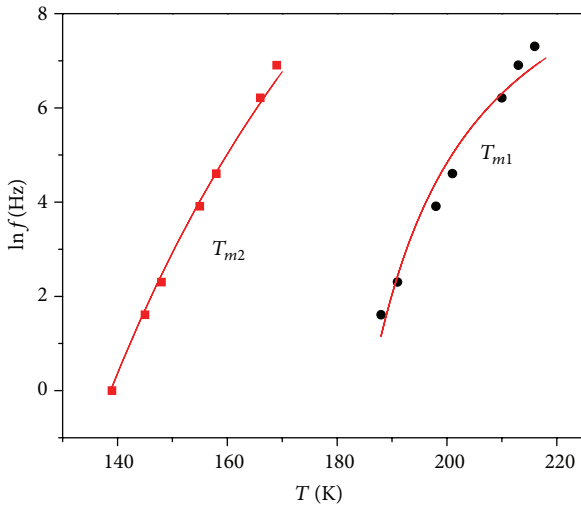


FIGURE 9: Frequency dependent temperature T_{m1} of the maximum in the real part χ' and temperature T_{m2} of the maximum in the imaginary part χ'' of the ac magnetic susceptibility. The solid curves represent fit of the Vogel-Fulcher law, (4), to the experimental data.

are free to move locally. Brownian relaxation arises as a response of the nanoparticles magnetic moments to the external magnetic field through the particle movement. The Vogel-Fulcher law was found to describe successfully the Brownian relaxation in the ferrofluids containing magnetite nanoparticles [11, 15]. The exponential temperature dependence of τ_B is attributed to divergence of the viscosity of the liquid at the characteristic temperature T'_0 , as found in many glass-forming liquids [29]. Using the Brownian relaxation

time in the form $\tau_B = \tau'_0 \exp[E'/k_B(T - T'_0)]$, the relation between T_{m1} and frequency f is $f = f'_0 \exp[-E'/k_B(T_{m1} - T'_0)]$. We find that the Vogel-Fulcher law can be fitted to the experimental data $\ln f$ versus $T_{m1}(f)$ with the following parameters: $\tau'_0 = 1/2\pi f'_0 = (2.6 \pm 1.0) \times 10^{-6}$ s, $E'/k_B = (2.0 \pm 0.2) \times 10^2$ K, and $T'_0 = (168 \pm 10)$ K. The result of this fit is shown also in Figure 9. Difference between the parameters in the Vogel-Fulcher law describing the Néel relaxation and the Brownian relaxation can be seen immediately. The characteristic time of the system τ'_0 in the Brownian relaxation is much larger than τ_0 in the Néel relaxation. The large difference between the parameters E' associated with the viscosity of the liquid [11] and E in the Néel relaxation also indicates different nature of the two relaxations. The parameter T'_0 should correspond to the temperature of the divergence of the viscosity, that is, to the temperature where the organic liquid passes from the partly frozen (mixed) state to the completely frozen (solid) state. It is interesting to note that $T'_0 = 168$ K obtained from the Vogel-Fulcher expression for the Brownian relaxation time as a fitting parameter is in good agreement with $T = 164$ K identified as transition temperature from the mixed state to the solid state of the organic liquid recorded in the DSC measurements.

3.2.3. Mössbauer Spectroscopy. ^{57}Fe Mössbauer measurement was performed on the CoFe_2O_4 nanoparticles with average particle size of 5.9 nm. The experimental spectrum collected at room temperature is presented in Figure 10. The main contribution to the spectrum belongs to a quadrupolar doublet characteristic of a paramagnetic compound showing that the quadrupole interaction is much stronger than the magnetic hyperfine interaction. This quadrupolar doublet is ascribed to

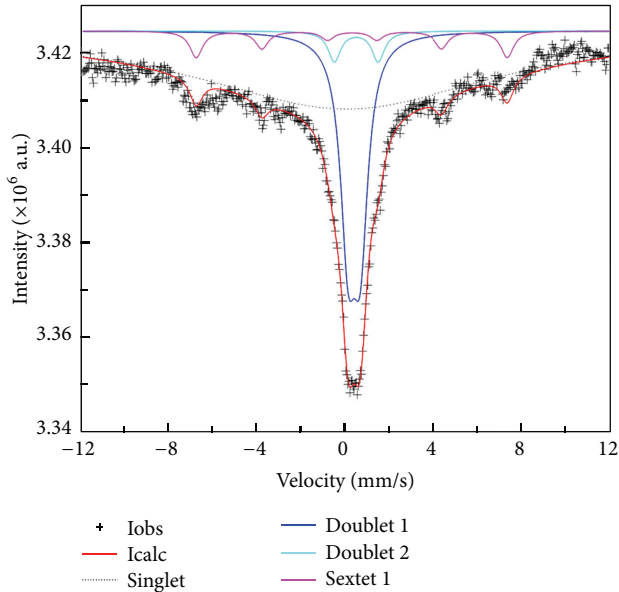


FIGURE 10: Mössbauer spectrum of the CoFe_2O_4 nanoparticles in the dried powder sample at room temperature.

the superparamagnetic CoFe_2O_4 nanoparticles. Besides the quadrupolar doublet, a six-line hyperfine pattern of lower intensity was also recorded. The presence of both the doublets and sextets in the Mössbauer spectrum is usually detected in an assembly of ultrafine particles with a size distribution. The Mössbauer spectrum of the CoFe_2O_4 powder sample has been fitted as a superposition of a broad singlet, two quadrupolar doublets, and one sextet. The broad singlet is introduced to delineate process of magnetic relaxations in some grains due to the particle size distribution. The isomer shift values of two doublets, (0.34 ± 0.01) mm/s and (0.43 ± 0.06) mm/s, indicate the presence of the Fe^{3+} ions in two different local environments. The quadrupolar splitting values of these doublets are (0.55 ± 0.03) mm/s and (1.98 ± 0.19) mm/s, respectively. Therefore, both doublets are assigned to the Fe^{3+} ions, one located in the particle core and the other located at the particle surface. The doublet with more positive isomer shift (0.43 mm/s) and higher quadrupolar splitting (1.98 mm/s) can be ascribed to the iron ions located at the surface layer of the particles. The hyperfine field is obtained as $B_{\text{hyp}} = (437 \pm 1)$ kOe. This hyperfine field is somewhat lower than the minimal value of the B-site hyperfine field found in the bulk cobalt ferrite [30]. Lower values of the hyperfine fields, compared to those usually reported for the cobalt ferrite nanoparticles [31, 32], were obtained to be about 440 kOe at the room temperature Mössbauer spectrum of the CoFe_2O_4 NPs with average diameter of 9.6 nm [33]. In a detailed analysis of the Mössbauer spectra of the CoFe_2O_4 NPs with average particle size of 5.1, 8.6, and 12.2 nm, acceptable fitting data were obtained only when the B-site pattern was assumed to be a superposition of more than one sextet, including those with lower hyperfine fields [27]. The Mössbauer spectrum of the CoFe_2O_4 powder sample studied in the present work indicates that most of the CoFe_2O_4

nanoparticles are superparamagnetic at room temperature, while a minor fraction of the nanoparticles have blocked magnetic moments with blocking temperatures above 300 K. Because the contribution of the CoFe_2O_4 particles with blocked magnetic moments is minor in the spectrum, more detailed analysis concerning the hyperfine fields is unreliable.

4. Conclusion

The synthesis procedure of the organic liquid suspension of the CoFe_2O_4 nanoparticles applied in the present work appears to be very promising from the aspect of the tailoring of these particles with well-pronounced magnetic properties. The narrow size distribution of the particles, high saturation magnetization, and superparamagnetic properties at room temperature make them very attractive and suitable for application in biomedicine, especially in magnetic targeted drug delivery and in magnetic fluid hyperthermia.

Acknowledgment

Financial support for this study was granted by the Ministry of Education, Science and Technological Development of Serbia (Project no. 172026).

References

- [1] S. Odenbach, "Magnetic fluids—suspensions of magnetic dipoles and their magnetic control," *Journal of Physics Condensed Matter*, vol. 15, no. 15, pp. S1497–S1508, 2003.
- [2] S. Odenbach, "Recent progress in magnetic fluid research," *Journal of Physics Condensed Matter*, vol. 16, no. 32, pp. R1135–R1150, 2004.
- [3] C. Scherer and A. M. Figueiredo Neto, "Ferrofluids: properties and applications," *Brazilian Journal of Physics*, vol. 35, no. 3, pp. 718–727, 2005.
- [4] C. C. Berry, "Progress in functionalization of magnetic nanoparticles for applications in biomedicine," *Journal of Physics D*, vol. 42, no. 22, Article ID 224003, 9 pages, 2009.
- [5] H. Tan, J. M. Xue, B. Shuter, X. Li, and J. Wang, "Synthesis of PEOlated $\text{Fe}_3\text{O}_4/\text{SiO}_2$ nanoparticles via bioinspired silyfication for magnetic resonance imaging," *Advanced Functional Materials*, vol. 20, no. 5, pp. 722–731, 2010.
- [6] R. Rahisuddin, P. K. Sharma, M. Salim, and G. Garg, "Application of ferrofluid: as a targeted drug delivery system in nanotechnology," *International Journal of Pharmaceutical Sciences Review and Research*, vol. 5, no. 3, pp. 115–119, 2010.
- [7] R. Skomski and J. M. D. Coey, *Permanent Magnetism*, Institute of Physics Publishing, Bristol, UK, 1999.
- [8] M. Walker, P. I. Mayo, K. O'Grady, S. W. Charles, and R. W. Chantrell, "The magnetic properties of single-domain particles with cubic anisotropy. I. Hysteresis loops," *Journal of Physics*, vol. 5, no. 17, pp. 2779–2792, 1993.
- [9] E. Blums, A. Cebers, and M. M. Maiorov, *Magnetic Fluids*, Walter de Gruyter, Berlin, Germany, 1997.
- [10] T. Jonsson, J. Mattsson, C. Djurberg, F. A. Khan, P. Nordblad, and P. Svedlindh, "Aging in a magnetic particle system," *Physical Review Letters*, vol. 75, no. 22, pp. 4138–4141, 1995.

- [11] J. Zhang, C. Boyd, and W. Luo, "Two mechanisms and a scaling relation for dynamics in ferrofluids," *Physical Review Letters*, vol. 77, no. 2, pp. 390–393, 1996.
- [12] A. Skumiel, A. Józefczak, T. Hornowski, and M. Labowski, "The influence of the concentration of ferroparticles in a ferrofluid on its magnetic and acoustic properties," *Journal of Physics D*, vol. 36, no. 24, pp. 3120–3124, 2003.
- [13] M. Blanco-Mantecón and K. O'Grady, "Interaction and size effects in magnetic nanoparticles," *Journal of Magnetism and Magnetic Materials*, vol. 296, no. 2, pp. 124–133, 2006.
- [14] L.-Y. Zhang, Y.-H. Dou, L. Zhang, and H.-C. Gu, "Magnetic behaviour and heating effect of Fe_3O_4 ferrofluids composed of monodisperse nanoparticles," *Chinese Physics Letters*, vol. 24, no. 2, pp. 483–486, 2007.
- [15] M. B. Morales, M. H. Phan, S. Pal, N. A. Frey, and H. Srikanth, "Particle blocking and carrier fluid freezing effects on the magnetic properties of Fe_3O_4 -based ferrofluids," *Journal of Applied Physics*, vol. 105, no. 7, Article ID 07B511, 3 pages, 2009.
- [16] G. Baldi, D. Bonacchi, C. Innocenti, G. Lorenzi, and C. Sangregorio, "Cobalt ferrite nanoparticles: the control of the particle size and surface state and their effects on magnetic properties," *Journal of Magnetism and Magnetic Materials*, vol. 311, no. 1, pp. 10–16, 2007.
- [17] G. Baldi, D. Bonacchi, M. C. Franchini et al., "Synthesis and coating of cobalt ferrite nanoparticles: a first step toward the obtainment of new magnetic nanocarriers," *Langmuir*, vol. 23, no. 7, pp. 4026–4028, 2007.
- [18] G. Baldi, G. Lorenzi, and C. Ravagli, "Hyperthermic effect of magnetic nanoparticles under electromagnetic field," *Processing and Applications of Ceramics*, vol. 3, no. 1-2, pp. 103–109, 2009.
- [19] M. C. Franchini, G. Baldi, D. Bonacchi et al., "Bovine serum albumin-based magnetic nanocarrier for MRI diagnosis and hyperthermic therapy: a potential theranostic approach against cancer," *Small*, vol. 6, no. 3, pp. 366–370, 2010.
- [20] V. Cabuil, V. Dupuis, D. Talbot, and S. Neveu, "Ionic magnetic fluid based on cobalt ferrite nanoparticles: influence of hydrothermal treatment on the nanoparticle size," *Journal of Magnetism and Magnetic Materials*, vol. 323, no. 10, pp. 1238–1241, 2011.
- [21] H. Guo, X. Yang, T. Xiao, W. Zhang, L. Lou, and J. Mugnier, "Structure and optical properties of sol-gel derived Gd_2O_3 waveguide films," *Applied Surface Science*, vol. 230, no. 1–4, pp. 215–221, 2004.
- [22] H. Shenker, "Magnetic anisotropy of cobalt ferrite ($\text{Co}_{1.01}\text{Fe}_{2.00}\text{O}_{3.62}$) and nickel cobalt ferrite ($\text{Ni}_{0.72}\text{Fe}_{0.20}\text{Co}_{0.08}\text{Fe}_2\text{O}_4$)," *Physical Review*, vol. 107, no. 5, pp. 1246–1249, 1957.
- [23] V. A. Brabers, "Progress in spinel ferrite research," in *Handbook of Magnetic Materials*, K. H. J. Buschow, Ed., vol. 8, North-Holland, Amsterdam, The Netherlands, 1995.
- [24] M. Grigorova, H. J. Blythe, V. Blaskov et al., "Magnetic properties and Mössbauer spectra of nanosized CoFe_2O_4 powders," *Journal of Magnetism and Magnetic Materials*, vol. 183, no. 1-2, pp. 163–172, 1998.
- [25] V. Blaskov, V. Petkov, V. Rusanov et al., "Magnetic properties of nanophase CoFe_2O_4 particles," *Journal of Magnetism and Magnetic Materials*, vol. 162, no. 2-3, pp. 331–337, 1996.
- [26] N. Moumen, P. Veillet, and M. P. Pileni, "Controlled preparation of nanosize cobalt ferrite magnetic particles," *Journal of Magnetism and Magnetic Materials*, vol. 149, no. 1-2, pp. 67–71, 1995.
- [27] E. Manova, B. Kunev, D. Paneva et al., "Mechano-synthesis, characterization, and magnetic properties of nanoparticles of cobalt ferrite, CoFe_2O_4 ," *Chemistry of Materials*, vol. 16, no. 26, pp. 5689–5696, 2004.
- [28] L. Néel, "Thermoremanent magnetization of fine powders," *Review of Modern Physics*, vol. 25, no. 1, pp. 293–295, 1953.
- [29] N. Menon and S. R. Nagel, "Evidence for a divergent susceptibility at the glass transition," *Physical Review Letters*, vol. 74, no. 7, pp. 1230–1233, 1995.
- [30] G. A. Sawatzky, F. van der Woude, and A. H. Morrish, "Mössbauer study of several ferrimagnetic spinels," *Physical Review*, vol. 187, no. 2, pp. 747–757, 1969.
- [31] N. Moume, P. Bonville, and M. P. Pileni, "Control of the size of cobalt ferrite magnetic fluids: Mössbauer spectroscopy," *Journal of Physical Chemistry*, vol. 100, no. 34, pp. 14410–14416, 1996.
- [32] A. Hutlova, D. Niznansky, J.-L. Rehspringer, C. Estournès, and M. Kurmoo, "High coercive field for nanoparticles of CoFe_2O_4 in amorphous silica sol-gel," *Advanced Materials*, vol. 15, no. 19, pp. 1622–1625, 2003.
- [33] S. R. Ahmed, S. B. Ogale, G. C. Papaefthymiou, R. Ramesh, and P. Kofinas, "Magnetic properties of CoFe_2O_4 nanoparticles synthesized through a block copolymer nanoreactor route," *Applied Physics Letters*, vol. 80, no. 9, pp. 1616–1618, 2002.

Research Article

pH Responsive Self-Assembly of Cucurbit[7]urils and Polystyrene-Block-Polyvinylpyridine Micelles for Hydrophobic Drug Delivery

Basem A. Moosa, Afnan Mashat, Wengang Li, Karim Fhayli, and Niveen M. Khashab

Controlled Release and Delivery Lab, Advanced Membranes and Porous Materials Center, King Abdullah University of Science and Technology (KAUST), Thuwal 23955-6900, Saudi Arabia

Correspondence should be addressed to Niveen M. Khashab; niveen.khashab@kaust.edu.sa

Received 25 June 2013; Revised 7 September 2013; Accepted 9 September 2013

Academic Editor: Haifeng Chen

Copyright © 2013 Basem A. Moosa et al. This is an open access article distributed under the Creative Commons Attribution License, which permits unrestricted use, distribution, and reproduction in any medium, provided the original work is properly cited.

Polystyrene-block-polyvinylpyridine (PS-*b*-P4VP) polypseudorotaxanes with cucurbit[7]urils (CB[7]) were prepared from water soluble PS-*b*-P4VPH⁺ polymer and CB[7] in aqueous solution at room temperature. At acidic and neutral pH, the pyridinium block of PS-*b*-P4VP is protonated (PS-*b*-P4VPH⁺) pushing CB[7] to preferably host the P4VP block. At basic pH (pH 8), P4VP is not charged and thus is not able to strongly complex CB[7]. This phenomenon was verified further by monitoring the release of pyrene, a hydrophobic cargo model, from a PS-*b*-P4VPH⁺/CB[7] micellar membrane. Release study of UV active pyrene from the membrane at different pH values revealed that the system is only operational under basic conditions and that the host-guest interaction of CB[7] with P4VPH⁺ significantly slows down cargo release.

1. Introduction

Self-assembly of polystyrene-block-poly(4-vinylpyridine) PS-*b*-P4VP amphiphilic block copolymer has been studied extensively with different metals (because a variety of metal salts can be selectively coordinated to the PVP block) and at different temperatures and pH values [1–8]. PS-*b*-P4VP is a well-known block copolymer that is commercially available and can be easily synthesized by sequential anionic polymerization of styrene followed by 4-vinylpyridine (4VP) in tetrahydrofuran (THF) at -78°C under nitrogen [9]. Multiple changes in aggregate morphology (spheres, rods, lamellae, and mixture of aggregates) of this block copolymer have been described as a function of pH [7]. The reason for this behavior or morphological complexity can be ascribed to the amphiprotic nature of P4VP where the addition of acid or base introduces ionic groups into the corona chains. Polymer micellar morphologies are useful in the field of controlled drug release, and so we reported the morphological changes and Dox release from PS-*b*-P4VP micellar membrane at different pH values [8].

Cucurbit[*n*]urils (CB[*n*], $n = 5-8$ of glycoluril units) are a class of barrel-shaped macrocyclic hosts with symmetric carbonyl-lined portals [10–16]. They are capable of forming inclusion complexes with appropriately sized guest compounds in water with high affinity ($K_a > 10^5 \text{ M}^{-1}$) [17]. Cucurbit[7]uril (CB[7]) has been shown to form a variety of strong, stable complexes with pyridinium cation type compounds. Polymers with such aromatic moieties promote the creation of a wide range of macromolecular architectures in water, which are held together by host-guest interaction with CB[7]. Pseudorotaxanes, a class of supramolecular species in which a molecular thread is encircled by a molecular bead, have been studied extensively [18–21]. Many reports on CB[7] have been published, including the recognition of CB[7] towards the aliphatic amines ions, pyridylmethyl-ended alkylammonium ions, and other guest molecules. The formation of pseudorotaxanes, rotaxanes, pseudopolyrotaxanes, polyrotaxanes, molecular machines, molecular necklaces, and so forth from CB[7] has also been reported [18–20, 22–24]. Inclusion complexes with CB[7] can induce self-assembly of block copolymer complexes

and result in the formation of systems of pseudorotaxane with different morphologies and physical properties [25]. By complexing stimuli-responsive polymers with CB[7], a wide variety of polymer/CB[7] complexes with amphiphilic properties may be produced. We recently reported the pH sensitive behavior of PS-*b*-P4VP micelles; however, the host-guest interaction and self-assembly of this block copolymer with macrocycles such as CB[7] have not been reported before [8]. Herein, self-assembly of PS-*b*-P4VPH⁺ with CB[7] to afford a controlled release system for hydrophobic cargo is reported. It is a supramolecular approach using CB[7] to slow cargo release, which can be very crucial for drug delivery systems. PS-*b*-P4VPH⁺ was used in this study because its self-assembly and morphology at different pH values are extensively studied in the literature. Pyrene was chosen as the cargo as it is a neutral, UV active, and hydrophobic molecule (most drugs are hydrophobic) that is too big to be enclosed by CB[7]. Moreover, CB[7] does not absorb at 245 nm, so it will not affect UV measurements [26]. PS-*b*-P4VP/CB[7] micellar solution was casted into a membrane and tested under different pH values (Figure 1).

2. Experimental Section

2.1. Materials. Polystyrene-*b*-poly(4-vinylpyridine) block copolymer (PS-*b*-P4VP, 81 000-*b*-57 000 g/mol) was purchased from Polymer Source, Inc. Dimethylformamide (DMF), CB[7], pyrene, and other buffer solutions were used as purchased from Sigma-Aldrich, USA.

2.2. PS-*b*-P4VPH⁺-CB[7] Polypseudorotaxanes Complex for NMR. To a stirred solution of 5 mg CB[7] in 1 mL, D₂O/DCl (pD 3) was added a solution of 10 mg of PS-*b*-P4VP in 0.5 mL d₇-DMF and stirred for 10 hours at room temperature. The solution was filtered and the filtrate was characterized by ¹H-NMR, SEM, and TEM.

2.3. pH Responsive Micellar Membrane Preparation. A micellar solution containing 20 wt% PS-*b*-P4VP block copolymer was loaded with pyrene (0.005 μg per 2 μg polymer) in DMF. Water (0.5 mL) was then added dropwise to the DMF solution and stirred overnight. The mixture was then transferred into a dialysis bag where it was dialyzed in water (pH 3) and CB[7] (5 mg) aqueous solution at room temperature (20°C) overnight. The dialysis bag was then removed and washed with water three times before the contents were lyophilized for 48 hrs. The mixture was then redissolved in a minimum amount of DMF and casted on a glass plate using casting blades with 200 μm gate height. The room temperature was 20°C with 60% relative humidity. The glass plate was then immersed in water to peel the membrane off. The membrane was finally air dried overnight before UV testing. The control solution was prepared using the same method but without incorporating CB[7]. The release test was carried out using 2 mg of the casted membrane and using UV spectrometer Cary 5000, at 245 nm at a series of pH values (pH 4.0 to 8.0) two times on duplicate.

2.4. Instruments. Pyrene release from micellar membrane was measured using UV-Vis spectrophotometer Cary 5000, at 245 nm. Scanning electron microscopy (SEM) images were obtained using a Quanta 600 FEG scanning electron microscope (SEM) from FEI company, USA. The ¹H NMR spectrum was recorded on Bruker Avance III (400 MHz) spectrometer, using DMF-d₇ as the solvent. Dynamic light scattering (DLS) measurements were done using the Zetasizer Nano from Malvern Instruments. Transmission electron microscope (TEM) images were obtained using Titan 3 80–300 electron microscope (TEM) from FEI company, USA.

3. Results and Discussion

The complexation of CB[7] with PS-*b*-P4VPH⁺ was first verified by NMR. Figure 2 revealed (i) disappearance of styrene peaks, (ii) shifting of pyridine peaks in acidic media, and (iii) broadening of all peaks. This suggests that the motion of both blocks in an aqueous solution is highly restricted and the absence of the styrene peaks (Figure 2(b)) proves the formation of what is called a “frozen micelle” [22, 23], as the NMR cannot detect the hydrophobic core of the particles. When CB[7] was added (Figure 2(c)), a clear shift of the pyridinium block was observed which suggests a complexation between the protonated pyridine and CB[7].

PS-*b*-P4VPH⁺ and PS-*b*-P4VPH⁺/CB[7] micelles were then characterized using SEM and TEM. More aggregates were observed using TEM in PS-*b*-P4VPH⁺/CB[7] sample (Figure 3(b)) versus PS-*b*-P4VPH⁺ (Figure 3(a)). A slight difference in terms of morphology between the nanoparticles with and without CB[7] can be seen using SEM. The surface of the polymeric micelles was smooth (Figure 4(a)), while that of the complex was coarse (Figure 4(b)).

DLS measurements showed a distribution of the hydrodynamic diameter with mean values of 76 and 66 nm for PS-P4VPH⁺ nanoparticles and PS-P4VPH⁺/CB[7] nanoparticles, respectively (Figure 4). The difference in size of nanoparticles in the dried and solvated phase is consistent with that of a swollen composite polymeric system in aqueous media. The diameter distribution observed by DLS can be explained by interparticle interactions or the statistical distribution of the number of macromolecules within individual particles [27].

3.1. Payload Release Investigation. To investigate the host-guest effect of CB[7] complexation on hydrophobic cargo release, pyrene was loaded into PS-P4VPH⁺ micelles as described in the experimental section. UV spectrometer was employed to measure the amount of pyrene released into the aqueous solution at a series of pH values (pH 4.0 to 8.0) at room temperature (Figure 5).

Two types of pyrene-loaded membranes were prepared, one with (pH 4'–8') and the other without CB[7] (pH 4–8) (control experiment). PS-*b*-P4VP micellar membrane (2 mg) was placed in the bottom of a UV spectrometer cell without stirring. At pH 4–5, negligible amount of pyrene was released from both samples, where at pH 6–7, a very small amount of pyrene <5% was released during a long period of time (Figure 5), which suggests that (i) the encapsulation efficiency

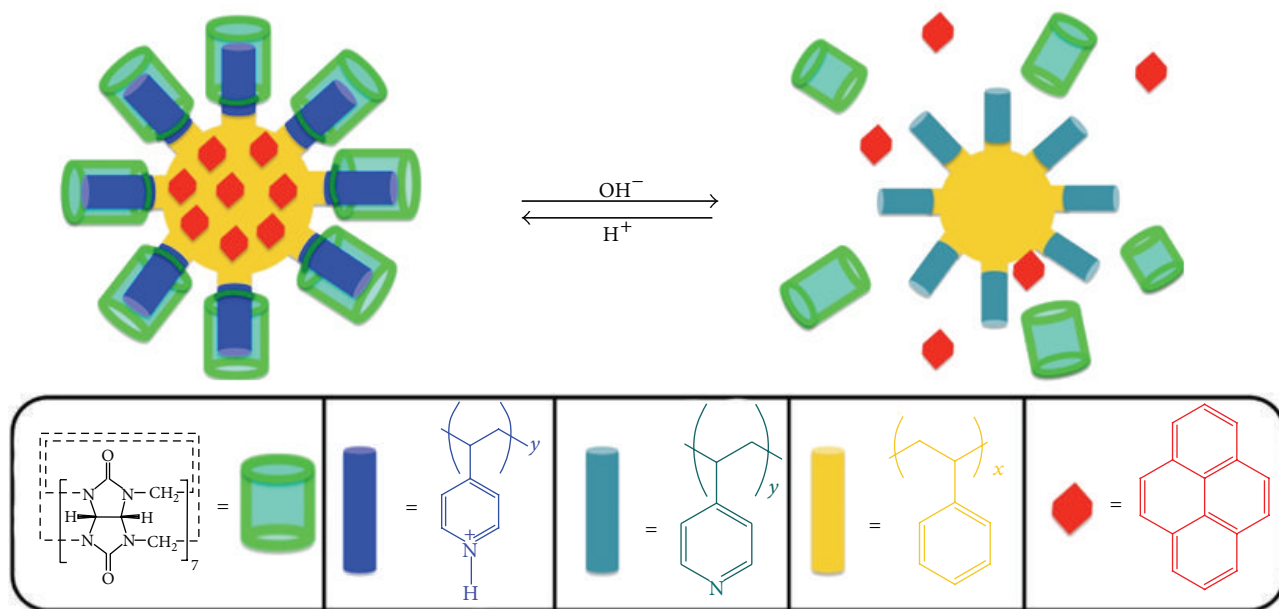


FIGURE 1: Schematic representation of pyrene-loaded micelles and their release mechanism.

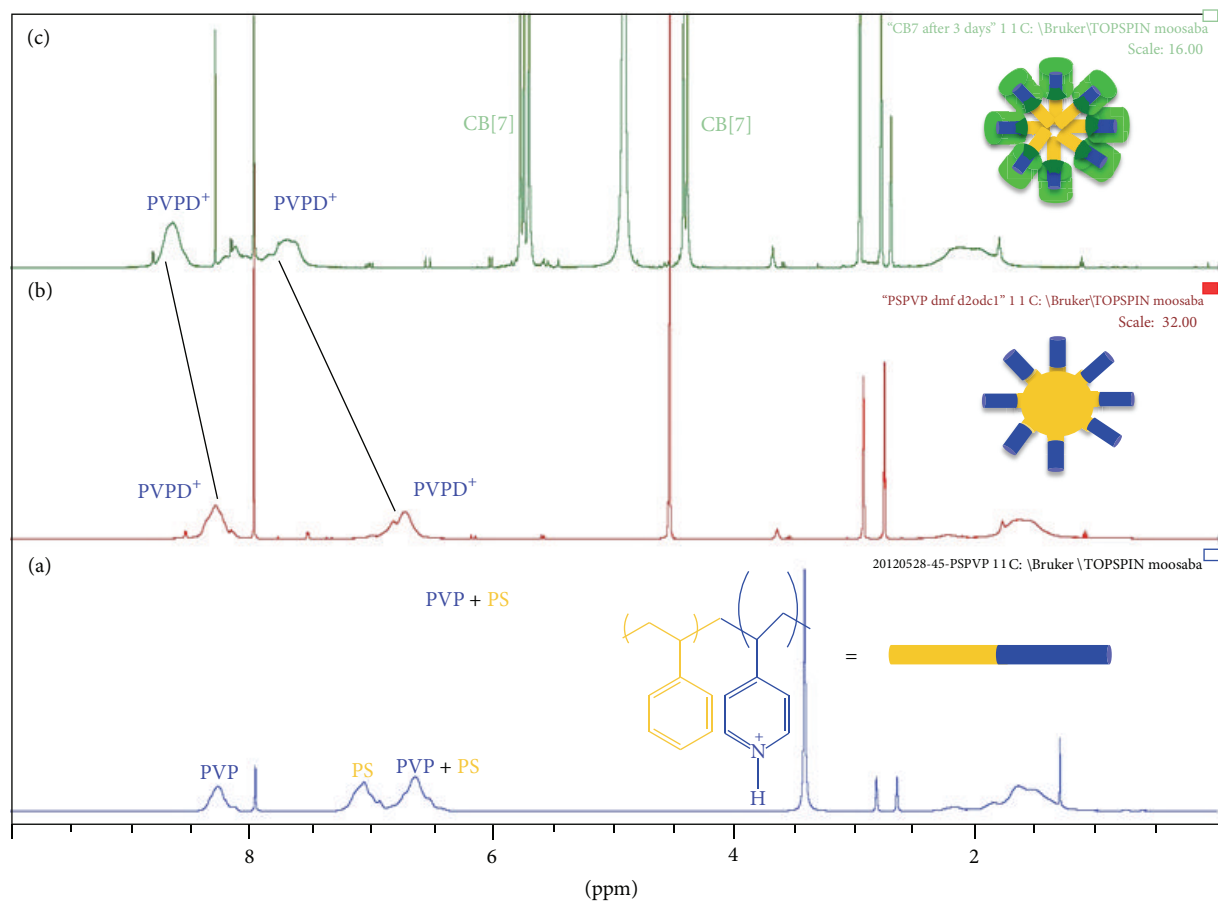


FIGURE 2: $^1\text{H-NMR}$ spectra (500 MHz) of (a) PS-P4VPH ($d_7\text{-DMF}$), (b) PS-P4VPH⁺ (1 mM in D_2O), and (c) PS-P4VPH⁺ (1 mM in D_2O) + 0.4 equiv CB[7].

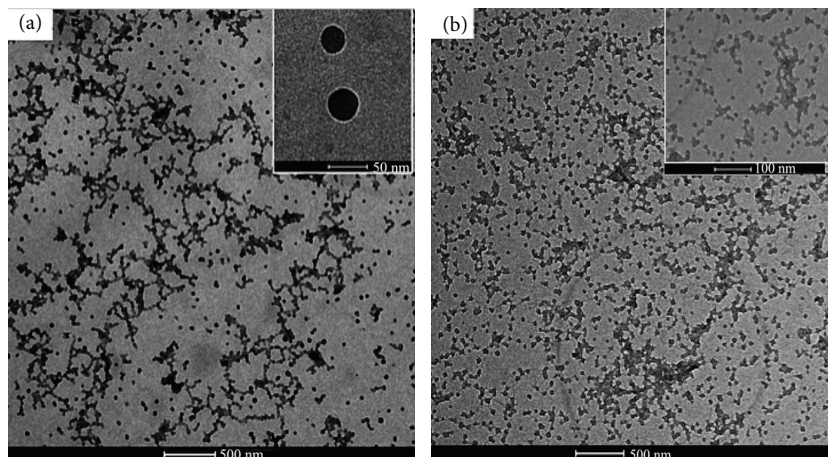


FIGURE 3: TEM images of (a) PS-P4VPH⁺ and (b) PS-P4VPH⁺CB[7] complex where more aggregates can be observed.

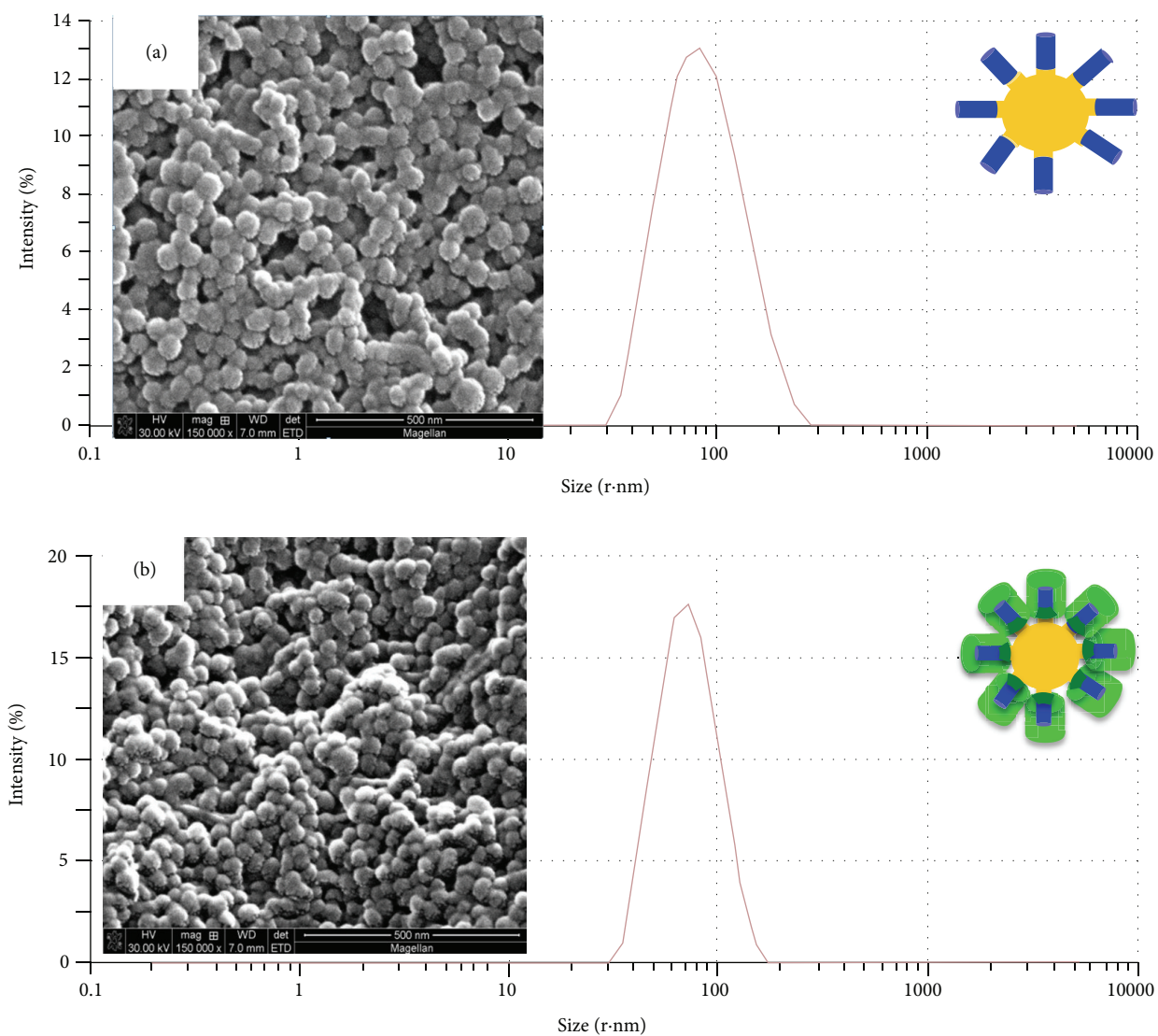


FIGURE 4: SEM images of (a) PS-P4VPH⁺ and (b) PS-P4VPH⁺CB[7] complex.

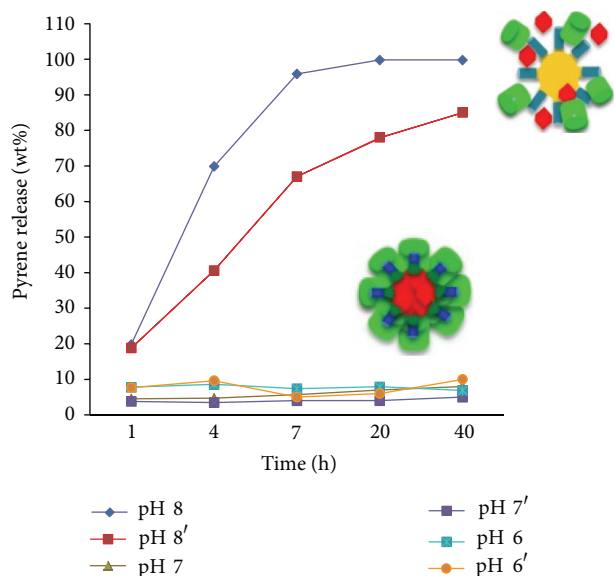


FIGURE 5: Release profile of pyrene at different pH with CB[7] pH(4'–8') and without CB[7] pH(4–8).

of this membrane is ~95% (no major leakage) and (ii) it is very stable at physiological pH 7.4. At pH 8, a clear release of pyrene was observed which is due to the deprotonation of the pyridinium ion block, which forms the corona shell of the micelle at high pH as we previously reported [8]. The pyridinium molecules shrink and expose the pyrene-loaded PS core to the buffer solution, resulting in a substantial pyrene release (Figure 5). The major difference between the two profiles pH 8 and pH 8' is that the pyrene release was slower in the presence of CB[7]. This is due to CB[7] threading the pyridinium block which will decrease the deprotonation rate and thus hinders the release of pyrene. To calculate the loading efficiency, the membrane was digested at pH 1 and the amount of released pyrene was measured by UV. Pyrene was loaded into the micellar membrane with a loading efficiency of about 0.02 wt%, which means that every 2 mg of the micellar membrane contains 0.4 μg of pyrene.

4. Conclusion

A supramolecular approach for building a potential controlled drug delivery system is both simple and efficient. CB[7] strongly complexes P4VPH⁺, making up the corona shell of the micelle, at acidic and neutral pH which affords a closed delivery system with minimal leakage. Under basic conditions, the micelles will shrink and cargo release will be initiated. The presence of CB[7] slows down the release rate and thus provides more control over this system. Designing drug delivery systems that offer prolonged drug release and are only operational under basic pH, such that the pancreatic cancer duct can afford both controlled and targeted release to diseased tissues [28, 29]. Further studies are now underway to incorporate this concept into biocompatible block copolymers for *in vivo* applications.

Acknowledgments

The authors thank King Abdullah University of Science and Technology (KAUST) for the financial support. There is no financial gain from any commercial material used.

References

- [1] R. P. Zhu, Y. M. Wang, and W. D. He, "Multiple morphological micelles formed from the self-assembly of poly(styrene)-*b*-poly(4-vinylpyridine) containing cobalt dodecyl benzene sulfonate," *European Polymer Journal*, vol. 41, pp. 2088–2096, 2005.
- [2] J. T. Zhu, H. Z. Yu, and W. Jiang, "Morphological transition of aggregates from ABA amphiphilic triblock copolymer induced by hydrogen bonding," *Macromolecules*, vol. 38, no. 17, pp. 7492–7501, 2005.
- [3] J. Ruokolainen, G. ten Brinke, and O. Ikkala, "Supramolecular polymeric materials with hierarchical structure-within-structure morphologies," *Advanced Materials*, vol. 11, pp. 777–780, 1999.
- [4] O. Ikkala and G. Ten Brinke, "Functional materials based on self-assembly of polymeric supramolecules," *Science*, vol. 295, no. 5564, pp. 2407–2409, 2002.
- [5] O. Ikkala and G. Ten Brinke, "Hierarchical self-assembly in polymeric complexes: towards functional materials," *Chemical Communications*, vol. 19, pp. 2131–2137, 2004.
- [6] Z. Gao, S. K. Varshney, S. Wong, and A. Eisenberg, "Block copolymer "crew-cut" micelles in water," *Macromolecules*, vol. 27, no. 26, pp. 7923–7927, 1994.
- [7] H. Shen, L. Zhang, and A. Eisenberg, "Multiple pH-induced morphological changes in aggregates of polystyrene-block-poly(4-vinylpyridine) in DMF/H₂O mixtures," *Journal of the American Chemical Society*, vol. 121, pp. 2728–2740, 1999.
- [8] X. Yang, B. A. Moosa, L. Deng, L. Zhao, and N. M. Khashab, "PH-triggered micellar membrane for controlled release microchips," *Polymer Chemistry*, vol. 2, no. 11, pp. 2543–2547, 2011.
- [9] J. Zhu, A. Eisenberg, and R. B. Lennox, "Interfacial behavior of block polyelectrolytes. 1. Evidence for novel surface micelle formation," *Journal of the American Chemical Society*, vol. 113, no. 15, pp. 5583–5588, 1991.
- [10] H.-K. Lee, K. M. Park, Y. J. Jeon et al., "Vesicle formed by amphiphilic cucurbit[6]uril: versatile, noncovalent modification of the vesicle surface, and multivalent binding of sugar-decorated vesicles to lectin," *Journal of the American Chemical Society*, vol. 127, no. 14, pp. 5006–5007, 2005.
- [11] J. Kim, I.-S. Jung, S.-Y. Kim et al., "New cucurbituril homologues: syntheses, isolation, characterization, and X-ray crystal structures of cucurbit[n]uril (n = 5, 7, and 8)," *Journal of the American Chemical Society*, vol. 122, no. 3, pp. 540–541, 2000.
- [12] A. I. Day, A. P. Arnold, R. J. Blanch, and B. Snushall, "Controlling factors in the synthesis of cucurbituril and its homologues," *Journal of Organic Chemistry*, vol. 66, no. 24, pp. 8094–8100, 2001.
- [13] G. Celtek, M. Artar, O. A. Scherman, and D. Tuncel, "Sequence-specific self-sorting of the binding sites of a ditopic guest by cucurbituril homologues and subsequent formation of a hetero[4]pseudorotaxane," *Chemistry*, vol. 15, no. 40, pp. 10360–10363, 2009.
- [14] F. W. L. Vögtle, *Mock in Comprehensive Supramolecular Chemistry*, vol. 2, Pergamon Press, Oxford, UK, 1996.

- [15] K. Kim, "Mechanically interlocked molecules incorporating cucurbituril and their supramolecular assemblies," *Chemical Society Reviews*, vol. 31, pp. 96–107, 2002.
- [16] J. Lagona, P. Mukhopadhyay, S. Chakrabarti, and L. Isaacs, "The cucurbit[n]uril family," *Angewandte Chemie (International Edition)*, vol. 44, no. 31, pp. 4844–4870, 2005.
- [17] S. Y. Jon, N. Selvapalam, D. H. Oh et al., "Facile synthesis of cucurbit[n]uril derivatives via direct functionalization: expanding utilization of cucurbit[n]uril," *Journal of the American Chemical Society*, vol. 125, no. 34, pp. 10186–10187, 2003.
- [18] M. Sempere, G. Fernandez, and F. Wurthner, "Self-sorting phenomena in complex supramolecular systems," *Chemical Reviews*, vol. 111, pp. 5784–5814, 2011.
- [19] B. Rosen, C. Wilson, D. Wilson, M. Peterca, M. Imam, and V. Percec, "Dendron-mediated self-assembly, disassembly, and self-organization of complex systems," *Chemical Reviews*, vol. 109, pp. 6275–6540, 2009.
- [20] A. Harada, A. Hashidzume, H. Yamaguchi, and Y. Takashima, "Polymericrotaxanes," *Chemical Reviews*, vol. 109, pp. 5974–6023, 2009.
- [21] N. Momčilović, P. Clark, A. Boydston, and R. Grubbs, "One-pot synthesis of polyrotaxanes via acyclic diene metathesis polymerization of supramolecular monomers," *Journal of the American Chemical Society*, vol. 133, pp. 19087–19089, 2011.
- [22] S. I. Yoo, B.-H. Sohn, W.-C. Zin, J. C. Jung, and C. Park, "Mixtures of diblock copolymer micelles by different mixing protocols," *Macromolecules*, vol. 40, no. 23, pp. 8323–8328, 2007.
- [23] M. Jacquin, P. Muller, H. Cottet, and O. Théodoly, "Self-assembly of charged amphiphilic diblock copolymers with insoluble blocks of decreasing hydrophobicity: from kinetically frozen colloids to macrosurfactants," *Langmuir*, vol. 26, no. 24, pp. 18681–18693, 2010.
- [24] B. P. Bastakoti, S. Guragain, Y. Yokoyama, S.-I. Yusa, and K. Nakashima, "Incorporation and release behavior of amitriptylene in core-shell-corona type triblock copolymer micelles," *Colloids and Surfaces B*, vol. 88, no. 2, pp. 734–740, 2011.
- [25] G. Chen and M. Jiang, "Cyclodextrin-based inclusion complexation bridging supramolecular chemistry and macromolecular self-assembly," *Chemical Society Reviews*, vol. 40, pp. 2254–2266, 2011.
- [26] Y. Ling and A. E. Kaifer, "Complexation of poly(phenylenevinylene) precursors and monomers by cucurbituril hosts," *Chemistry of Materials*, vol. 18, no. 25, pp. 5944–5949, 2006.
- [27] Z. Keresztesy, M. Bodnár, E. Ber et al., "Self-assembling chitosan/poly- γ -glutamic acid nanoparticles for targeted drug delivery," *Colloid and Polymer Science*, vol. 287, no. 7, pp. 759–765, 2009.
- [28] H. Ishiguro, M. C. Steward, R. W. Wilson, and R. M. Case, "Bicarbonate secretion in interlobular ducts from guinea-pig pancreas," *Journal of Physiology*, vol. 495, no. 1, pp. 179–191, 1996.
- [29] D. Tuveson and D. Hanahan, "Translational medicine: cancer lessons from mice to humans," *Nature*, vol. 471, no. 7338, pp. 316–317, 2011.

Research Article

Development of Lecithin Nanoemulsion Based Organogels for Permeation Enhancement of Metoprolol through Rat Skin

J. Varshosaz,^{1,2} S. Andalib,¹ M. Tabbakhian,¹ and N. Ebrahimzadeh¹

¹ Department of Pharmaceutics and Novel Drug Delivery Systems Research Centre, School of Pharmacy and Pharmaceutical Sciences, Isfahan University of Medical Sciences, Isfahan 81746-73461, Iran

² Department of Pharmaceutics, Faculty of Pharmacy and Novel Drug Delivery Systems Research Centre, Isfahan University of Medical Sciences, P.O. Box 81745-359, Isfahan 81746-73461, Iran

Correspondence should be addressed to J. Varshosaz; varshosaz@pharm.mui.ac.ir

Received 26 July 2013; Revised 18 September 2013; Accepted 23 September 2013

Academic Editor: Patricia Murray

Copyright © 2013 J. Varshosaz et al. This is an open access article distributed under the Creative Commons Attribution License, which permits unrestricted use, distribution, and reproduction in any medium, provided the original work is properly cited.

Background. Drugs with low oral bioavailability due to the first pass metabolism are good candidates for transdermal delivery. **Objectives.** The aim of this work was preparation of transdermal nanoemulsion of metoprolol which has high first pass metabolism. **Methods.** Three commercially available types of lecithin (200, 100p, and 170), three short chain alcohol (n-butanol, isopropyl alcohol, and n-propanol), and isopropyl myristate (IPM) were used as surfactant, cosurfactant, and oil phase, respectively. The aqueous phase was composed of metoprolol tartrate. Nanoemulsions with different surfactant/cosurfactant weight ratio, various amounts of drug, and different types of alcohol were prepared, and their phase diagrams were studied. Drug release, permeability, and diffusion coefficient of the drug were studied using hairless rat skin. **Results.** A significant increase in drug solution rate was observed with increasing the metoprolol content in the nanoemulsions, while it decreased when lecithin concentration increased from 40% to 60%. Increasing the water content resulted in a significant increase in metoprolol release. N-butanol enhanced the drug flux from nanoemulsions more than n-propanol and isopropyl alcohol. The o/w nanoemulsions of metoprolol showed high flux and permeability through the skin. **Conclusion.** Both w/o and o/w nanoemulsions of metoprolol could enhance permeation and diffusion of metoprolol through rat skin.

1. Introduction

The human skin is a readily accessible area for drug delivery. It covers a surface of 2 m² in an average adult body with the thickness of about 2.97 ± 0.28 mm that uptakes one-third of whole blood circulation [1, 2]. Skin is a barrier that protects the body against chemical and microbial agents; it also controls body temperature and has some roles in controlling blood pressure [2]. Skin consists of three layers: epidermis, dermis, and hypoderm. The epidermis has four regions: basal layer, spiny layer, stratum granulosum, and upper most stratum corneum; the latter consists of keratinized, dehydrated, and highly cornified cells which are inlaid in continuous matrix of lipid membranous sheets constantly replacing internal layers. The water intake of stratum corneum is about 20%. The human skin surface contains average 10–70 hair follicles and 200–250 sweat ducts on every square centimeter

area of the skin [1, 3, 4]. Currently, skin is a good candidate for drug delivery and systemic pharmacological approach. Transdermal drug delivery has some benefits: skipping first pass metabolism in liver, steady infusion of a drug over an extended period of time, better compliance of the patient due to ease of usage and reduced frequency of use, a choice for drugs with low therapeutic index and short half life, and so easy elimination of drug when toxicity occurs during the application [3, 5, 6]. Also transdermal drug delivery has some disadvantages such as the possibility of local irritation and skin's low permeability. Considering that variability may occur due to differences in skin permeation due to differences in subcutaneous fat deposition the reduction of inconstancy in the plasma concentration of drug may be restricted. The release of drug from its carrier depends on the concentration of drug in the carrier, physiochemical properties, and presence of polar groups and molecular weight of the drug. Its

absorbance depends on the application site of use, thickness, temperature, hydration status, and integrity of skin, pH of the drug, and its molecular size [1, 2, 6, 7].

Nanoemulsions are multiphase systems consisting of water, oil, surfactant, and alcohol, which form a transparent solution. In fact, they are small-scale of emulsions whether oil in water or water in oil with a size range in the order of 5–50 nm, while particle size of dispersed phase in emulsions is $>0.1\ \mu\text{m}$, so the emulsions seem milky. The average droplet size in traditional emulsions grows continuously with time, leading to separation of phases due to gravity, but the nanoemulsions are stable, and the particle size does not change during storage [8]. Their ability to solubilize the insoluble drugs and their transparency and constancy make nanoemulsions suitable carriers for transdermal drug delivery [9, 10].

The nanoemulsions include four types according to the Winsor's classification: (I) the surfactant is preferentially soluble in water causing the formation of oil-in-water (o/w) nanoemulsions, (II) the surfactant is remarkably soluble in the oil phase and forms water-in-oil (w/o) nanoemulsions, (III) there is a middle phase having lots of surfactant that coexists with water and oil phases with low amount of surfactant, and (IV) the fourth type is a single-phase micellar solution that forms when a sufficient quantity of amphiphile (an alcohol) is added [11].

Lecithin is a natural surfactant isolated from eggs or soya bean. It can form gels when combined with water and nonpolar solvents. Organogels have gelling agent molecules such as lecithin as a surfactant, a continuous phase of nonpolar solvent, and a polar solvent that is water in most cases [12, 13]. They have the properties of oil and aqueous based formulations and are clear, viscoelastic, thermodynamically stable, and biocompatible. The organogels have a jelly-like structure with three-dimensional network. A lot of organic solvents such as linear or cyclic alkanes, esters of fatty acids, and amines can be used to form organogels in the presence of lecithin [13]. Lecithin molecules assemble to each other and form enormous cylindrical micelles when a little amount of water, formamide or glycerin is added to the nonpolar media [12]. Lecithin has a wide variety of roles in food industries, pharmaceuticals, and cosmetics as a viscosity modifier, solubilizer, emulsifier, stabilizer, and penetration enhancer [14]. Lecithin consists of phosphatidyl choline, phosphatidyl ethanolamine, phosphatidyl serine, and phosphatidyl inositol and some other substances such as triglycerides and fatty acids [15].

When lecithin is added to the organic media it is dispersed randomly. By adding the trace amount of water the lecithin molecules will assemble in spherical reverse micellar form. Tubular or cylindrical micellar aggregates of lecithin molecules will form when the amount of water is increased. Next step is formation of long, flexible, and worm-like tubular micelle structures in the presence of much more water, and at last these tubular microstructures overlap and entangle with each other to form a three-dimensional gel network among which the organic solvent is entrapped. Some other beneficial properties of organogels are the ability of solving a wide variety of different molecules, resistance to microbial

contamination, and optical transparency [12], so they have the essential criteria for transdermal drug delivery.

Microemulsions are homogenous systems by some unique characteristics which make them a good choice for delivering drugs and are widely used in pharmaceutical companies. They have been also used for oral and intramuscular injection routes [16–18]. The lecithin organogels have been used for preparation of local sodium salicylate [16], methimazole [19], and ketoprofen [20].

Intravenous nanoemulsions have been on the market for parenteral nutrition since the 1950s; meanwhile, they have also been used successfully for IV drug delivery [21].

Nanoemulsions were tested on surfaces by the US Army in December 1999 for a broad-spectrum decontamination of anthrax spore surrogates. It was tested again in March 2001 as a chemical decontamination agent. All tests were successful. The technology has been tested on gangrene and *Clostridium botulism* spores and can even be used on contaminated wounds to salvage limbs. The nanoemulsion technology can be formulated into a cream, foam, liquid, or spray to decontaminate a variety of materials marketed as NANOSTAT (NanoBio Corp.) [22].

Nanoemulsions are being used to deliver either recombinant proteins or inactivated organisms to a mucosal surface to produce an immune response. The first applications, an influenza vaccine and an HIV vaccine, can proceed to clinical trials. Additional research is ongoing to complete the proof of concept in animal trials for other vaccines including hepatitis B and anthrax. The University of Michigan has exclusively licensed this technology to NanoBio [22].

Metoprolol is a potent β_1 -selective adrenergic blocking agent. The β_1 -adrenoceptor antagonists are extensively used in various cardiovascular disorders. The oldest drug of this family is propranolol, but because of its blocking effect on smooth and skeletal muscles it is contraindicated in patients with asthma and should be used with caution in diabetic individuals [23]. Now metoprolol is widely used as a first choice drug in the treatment of mild to moderate hypertension and stable angina and is helpful in postinfarction patients [24]. These benefits are gained due to blocking peripheral adrenoceptors, decreasing rennin secretion from kidneys, and decreasing oxygen use in myocard [25].

Unfortunately, this drug undergoes a wide first pass metabolism but this deactivation can be overcome by fabricating the drug in transdermal therapeutic systems [26]. Nair et al. [27] used the combination of iontophoresis with sodium lauryl sulfate and showed augmented metoprolol delivery which rendered skin drug depot eventually released over a period of time. The transdermal matrix films of metoprolol tartrate were also prepared by casting on mercury substrate employing different ratios of polymers, ethyl cellulose (EC) and polyvinyl pyrrolidone (PVP), using dibutyl phthalate (DBT) as a plasticizer [28]. Based on the physical evaluation, *in vitro* drug release, and permeation characteristics, it was concluded that, for potential therapeutic use, monolithic drug matrix films composed of EC:PVP, may be suitable for the development of a transdermal drug delivery system of metoprolol [28]. Matrix and membrane controlled transdermal therapeutic systems were prepared from methacrylic

TABLE 1: Formulation of the different types of metoprolol nanoemulsions.

Formulation	Metoprolol tartrate (mg)	Lecithin 170 (g)	Lecithin 200 (g)	Lecithin 100p (g)	Isopropyl myristate (g)	Butanol (mL)	Isopropyl alcohol (mL)	n-Propanol (mL)
F ₁	40	0.64	—	—	0.96	—	0.3	—
F ₂	80	0.48	—	—	0.72	—	1.1	—
F ₃	100	0.4	—	—	0.6	—	1.4	—
F ₄	10	0.64	—	—	0.96	—	—	0.4
F ₅	20	0.64	—	—	0.96	—	—	0.2
F ₆	40	0.64	—	—	0.96	—	—	0.6
F ₇	60	0.64	—	—	0.96	—	—	0.2
F ₈	40	—	0.64	—	0.96	—	—	0.3
F ₉	40	—	—	0.64	0.96	—	—	0.8
F ₁₀	131	—	0.51	—	0.17	—	—	0.65
F ₁₁	40	—	—	—	—	—	—	—
F ₁₂	80	0.64	—	—	0.96	—	0.4	—
F ₁₃	80	0.4	—	—	0.6	—	0.4	—
F ₁₄	40	—	0.51	—	0.17	—	—	0.4
F ₁₅	40	0.48	—	—	1.12	—	—	0.6
F ₁₆	40	0.8	—	—	0.8	—	—	0.1
F ₁₇	40	0.64	—	—	0.96	0.7	—	—

polymers (Eudragit NE) applying different sucrose fatty acid esters to control the drug release and cutaneous absorption of metoprolol [29]. Eudragit RL-100 and polyvinyl acetate have also been used in production of the matrix type transdermal drug delivery systems of metoprolol by film casting technique which showed statistically significant reduction in mean blood pressure in methyl prednisolone-induced hypertensive rats [30]. Ghosh et al. [23] studied the effect of n-decyl methyl sulfoxide (nonionic surfactant) as a percutaneous absorption enhancer in permeation rate of metoprolol across human cadaver skin. They used 1.5 mm polyacrylate patches (10% w/w) containing varying concentrations of n-decyl methyl sulfoxide and tested for skin permeation potential. It was found that incorporation of n-decyl methyl sulfoxide up to 3% w/w concentration did not produce any significant change in skin permeation rate. A concentration of 5% w/w of this surfactant showed 40% enhancement in metoprolol permeation rate. They concluded that metoprolol permeated quite efficiently through both hairless mouse and human cadaver skin when applied from the polyacrylate patch with no significant lag time. Use of electrical outflow has also been reported for increasing drug permeation due to opening skin pores [30].

Considering the different reports on transdermal delivery of metoprolol and the good results obtained by other drugs used in the basis of nanoemulsions for enhanced permeation in the skin, the aim of the present work was to prepare lecithin nanoemulsion for transdermal delivery of metoprolol in the treatment of hypertension. To our knowledge there is no report on the production of metoprolol lecithin based nanoemulsions and, its designing is novel.

2. Material and Methods

2.1. Materials. Lecithin 200, 100p were from Locus Meyer industry, Germany, lecithin 170 was from Degussa, Germany,

n-butanol, isopropyl alcohol, n-propanol, potassium monohydrogen phosphate (K_2HPO_4), NaOH, and sodium lauryl sulphate (SLS) were from Merck Chemical Company, Germany, cellulose membrane from Biocin industry, Belgium, isopropyl myristate from Aldrich company, Germany, and metoprolol was from Alborz Darou, Iran, as a gift sample. All the materials were of analytical grades.

2.2. Animals. Healthy male Wistar albino rats weighing 180–280 g were purchased from Pastur Institute, Tehran, Iran. Animals had free access to standard rat chow and tap water *ad libitum*. They were kept in a temperature-controlled environment in animal house of Isfahan University of Medical Science at $23 \pm 2^\circ C$ with an alternating cycle of 12 h light and dark.

2.3. Preparation of Lecithin Organogels of Metoprolol. For preparation of lecithin organogels of metoprolol lecithin was added to $40^\circ C$ water while being stirred on a magnetic stirrer at 300 rpm. After complete dissolution of lecithin isopropyl myristate was added at room temperature leading to the formation of a turbid lotion. Finally, by adding one of the three short chain alcohols of n-butanol, isopropyl alcohol, or n-propanol as cosurfactants, the organogel was achieved. After the preliminary tests 16 formulations were selected according to the ratio of lecithin/isopropyl myristate and metoprolol percent that are shown in Table 1. Among these formulations one that had the least amount of alcohol was selected as the optimum formulae.

2.4. Lecithin-Oil-Water Phase Diagram. Different amounts of water were added to the lotion of lecithin/isopropyl myristate in fixed ratio of 1:1.5. The studied variables were the percent of metoprolol in solution, the type of alcohol (n-propanol, isopropyl alcohol, and n-butanol), and the different amounts of lecithin. Finally, the effect of lecithin amount, metoprolol percent, alcohol type, and the ratio of lecithin/isopropyl

myristate on the transparent region of nanoemulsion was estimated. As the amount of water increases, the microemulsion turned to a viscous gel. Phase diagrams for the organogel system also demonstrate the behavior of organogel system such as cloudiness, isotropicity, optical transparency, and viscosity.

2.5. The Nanoemulsion Characteristic of Metoprolol Organogels

2.5.1. Particle Size Measurements. The mean particle size of nanoemulsions was measured by photon correlation spectroscopy (PCS) at a fixed angle of 90° (Zetasizer, ZEN 3600, Malvern Instrumental, UK). Nanodispersion was suitably diluted to measure mean particle size and polydispersity index. Dynamic light scattering (also known as photon correlation spectroscopy or quasielastic light scattering) is a technique in physics that can be used to determine the size distribution profile of small particles in suspension or polymers in solution. It can also be used to probe the behavior of complex fluids such as concentrated polymer solutions. So, none of the ingredients of the formulation interfered with the particle size measurements.

2.5.2. Turbidity of Nanoemulsions. All the samples were tested with spectrophotometer at the wave length of 580 nm, and the absorbance was read. Then the absorbance was changed to transmittance.

2.5.3. Birefringency. The microemulsions were assessed through the polarizing microscope. The rotation of scaled sheet shows the birefringency of the system.

2.5.4. Rheologic Characteristics. For investigation of rheologic behavior of the samples a Rheomat device (RM/180 model, Mettler, Germany) was used. The measuring tube diameter was 15.18 mm, the measuring bob diameter was 14 mm, the shear rate was in the range of 6.5–129 (S⁻¹), and the fill volume was 9 mL. For drawing the rheogram, shear rate was increased for the samples till maximum. The shearing stress was plotted against shear rate.

2.5.5. Drug Release Studies In Vitro. *In vitro* permeation studies were performed using Franz diffusion cell. The cellulose membrane was previously soaked for 24 h in PBS in order to open the pores. These membranes were mounted between the donor and receptor compartment of the diffusion cell. 2 g of the formulated nanoemulsions was placed over the membranes. The receptor compartment of the diffusion cell was filled with phosphate buffer pH 7.4. The solution in the receptor compartment was constantly and continuously stirred using magnetic stirrer at 37 ± 2°C. 2 mL samples were withdrawn at predetermined time intervals of 30, 60, 120, 180, 240, and 300 min and replaced with an equal volume of fresh phosphate buffer with the same temperature. The samples were suitably diluted and analyzed to determine drug content using UV spectrophotometer at a wave length of 275.9 nm. All tests were done in triplicate. For each sample there was a

blank. The actual concentration of samples was calculated by using

$$C_n = C + \frac{C_{n-1} \times V}{V_t}, \quad (1)$$

where C_n is the actual concentration of sample n , C is the apparent concentration, C_{n-1} is the actual concentration of sample $n - 1$, V is the volume of sample, and V_t is the volume of total sample.

2.5.6. Measurement of Drug Penetration from Rat Skin. All test conditions in this experiment were as mentioned earlier in previous section but with some modifications; the freshly excised full thickness hairless abdomen skin of male Wistar rat was mounted on glass diffusion cells with the stratum corneum side in intimate contact with donor phase and the dermal side facing the receptor solution. Samples from the receptor compartment were withdrawn at predetermined time intervals, and the concentration of drug released was measured.

2.5.7. The Diffusion Coefficient and Permeation Coefficient Measurements. Flux of drug was estimated from Fick's first law of diffusion:

$$J_s = \frac{1}{S} \frac{dQ}{dt}, \quad (2)$$

in which S is the surface area of diffusion cell and dQ/dt is the slope of drug release curve [5]. For determination of diffusion coefficient the following equation was used:

$$K = 2C_o \times S \left(\frac{D}{\pi} \right)^{1/2}, \quad (3)$$

where K is the slope of the cumulative drug release profile, C_o is the amount of primary drug, S is the surface area of diffusion cell, and D is drug diffusion.

For calculating the permeation of drug, the following was used:

$$M = PSC_d t, \quad (4)$$

where M is the amount of drug released, P is the permeation coefficient, S is the surface area through which drug permeates, and C_d is the amount of drug in donor phase [5].

2.6. Data Analysis. For the evaluation of drug release kinetics Excel 2007 software was used, and the statistical analysis was done using SPSS software version 10. All data were expressed as mean ± SD and were compared by analysis of variance (ANOVA) test followed by the post hoc test of LSD. A significant level of $P < 0.05$ was considered in all cases.

3. Results and Discussion

3.1. Metoprolol in a Lecithin Base Organogel for Transdermal Delivery in Hypertension. Transdermal drug delivery has its advantages in drug delivery such as elimination of first pass

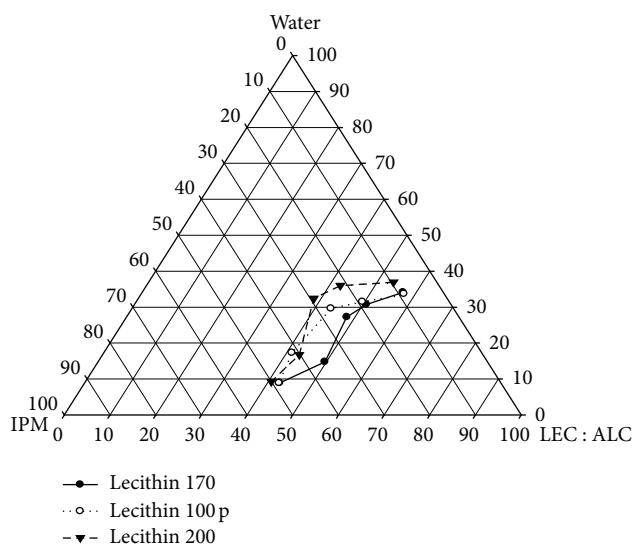


FIGURE 1: The effect of lecithin type on the transparent region of w/o metoprolol nanoemulsion containing IPM/lecithin/isopropyl alcohol/and 0.4 g of 10% metoprolol solution (LEC : ALC represents the mixture of lecithin and alcohol used as the surfactant and cosurfactant).

metabolism, ease of application and reduction of inconstancy in the plasma concentration of drug. Metoprolol is an antihypertensive drug with short half life which needs to be used, frequently; meanwhile it goes under a high first pass metabolism so that its oral bioavailability is just 50%. Bioavailability is reduced by about 20–30% for the controlled release preparation compared to the conventional tablets. Therefore, this drug is a good candidate for transdermal delivery [27–29].

3.2. Formulation Types. In order to increase the permeation of metoprolol, different ratio of soya lecithin and isopropyl myristate (from 90:10 to 10:90) was used. The best ratios of lecithin/IPM were 40:60, 50:50, and 30:70. The formulations containing more than 50% of lecithin and less than 30% could not be prepared, since more than 50% of lecithin could not be dissolved in IPM, and when its concentration was less than 30% too much alcohol was needed to prepare the nanoemulsion [31].

3.3. Phase Diagram. Phase diagrams seen in Figures 1–4 show the effect of lecithin type, alcohol type, drug content, and lecithin/isopropyl myristate ratio on the transparent region of nanoemulsions, respectively.

By increasing purity of lecithin (type 200 was the most pure one and type 100p had the lowest purity) the transparent region increased (Figure 1) as Nasser and coworkers [32] also showed in their study. By increasing alcohol chain (Figure 2) the transparent region decreased. Trotta et al. [33] reported such a phenomenon in their study too. Increasing drug content (Figure 3) did not change the transparent region, but 15% of metoprolol decreased the transparent region because of decreasing the surface tension [33]. Changing

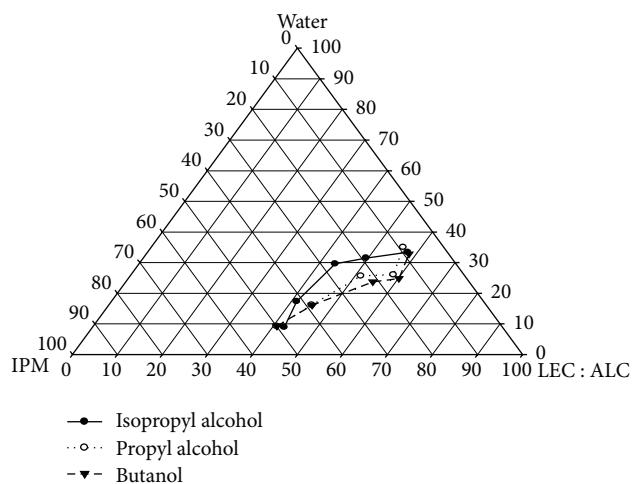


FIGURE 2: The effect of alcohol type on the transparent region of w/o metoprolol nanoemulsion containing IPM/lecithin 170/isopropyl alcohol/and 0.4 g of 10% metoprolol solution (LEC : ALC represents the mixture of lecithin and alcohol used as the surfactant and cosurfactant).

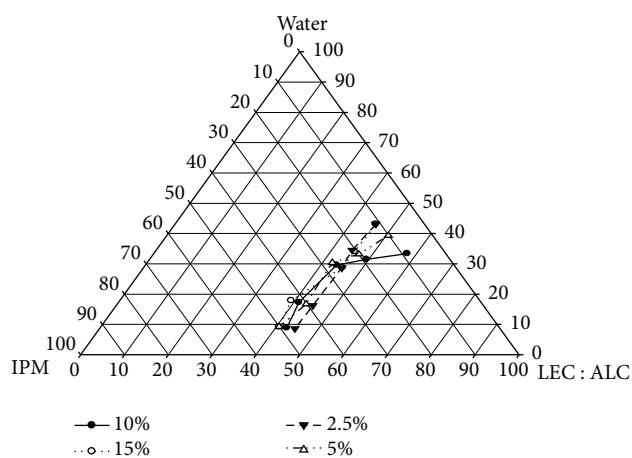


FIGURE 3: The effect of drug content in aqueous solution on the transparent region of w/o metoprolol nanoemulsion containing IPM/lecithin 170/isopropyl alcohol/and aqueous solution of different drug contents (LEC : ALC represents the mixture of lecithin and alcohol used as the surfactant and cosurfactant).

in IPM/lecithin ratio did not change the transparent region (Figure 4).

3.4. Characteristics of the Nanoemulsions of Metoprolol Organogel

3.4.1. Turbidity and Particle Size of Nanoemulsions. There is a close and direct relationship between transparency and the particle size. All samples were transparent when seen with eyes and showed a particle size between 17 and 49 nm except F_3 and F_{15} which had larger particle size. Table 2 shows the transmittance and particle size of the samples. The samples with more transparency and smaller particle size

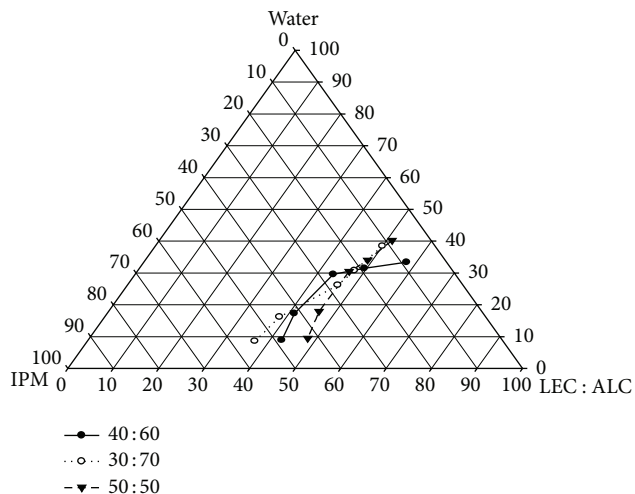


FIGURE 4: The effect of lecithin/IPM ratio on the transparent region of w/o metoprolol nanoemulsion containing IPM/lecithin 170/isopropyl alcohol/and 0.4 g of 10% metoprolol solution (LEC:ALC represents the mixture of lecithin and alcohol used as the surfactant and cosurfactant).

TABLE 2: The results of turbidity measurement of nanoemulsions according to the transmittance of light.

Formulation	Particle size (nm)	Transmittance (%)
F ₁	34	60
F ₂	20	71
F ₃	256	40
F ₄	44	50
F ₅	42	53
F ₆	40	53
F ₇	49	50
F ₈	17	85
F ₉	47	52
F ₁₀	19	75
F ₁₁	—	90
F ₁₂	18	73
F ₁₃	37	60
F ₁₅	301	32
F ₁₆	32	65
F ₁₇	41	57

were better choices for studying the drug release parameters. The most transparent formulation was the aqueous solution of metoprolol (F₁₁) after that the nanoemulsion of F₈ had the highest transparency while F₁₅ was the most turbid one. Both these formulations have similar amounts of drug and are prepared using n-propanol as the cosurfactant, but F₈ contains more lecithin 200 which has higher purity than the type of lecithin 170 used in less amounts in F₁₁. The former has also lower amounts of IPM.

DLS method may be used even for suspensions which are dispersed systems with micrometric particles and quite turbid so turbidity of some samples does not interfere with

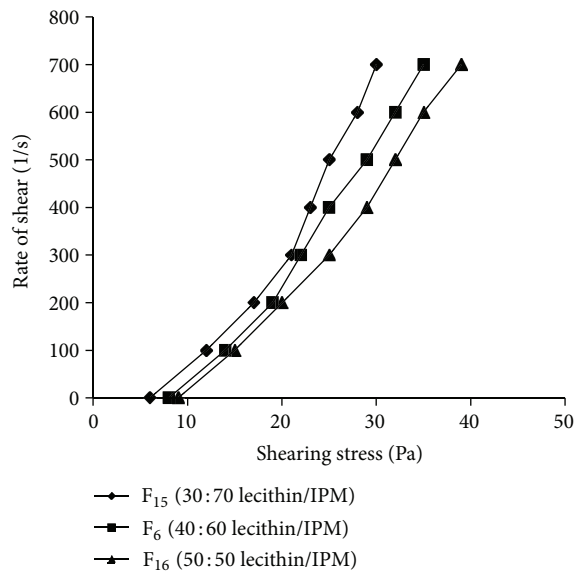


FIGURE 5: The rheogram of w/o metoprolol nanoemulsion containing IPM/lecithin/isopropyl alcohol/and 0.4 g of 10% metoprolol solution with different ratios of lecithin 170 : IPM.

the PCS measurements. Moreover, as mentioned in the methods all samples were diluted suitably before particle size measurements.

3.4.2. Birefringency. The microemulsions were assessed through the polarizing microscope; none of the samples showed light scattering; the background was dark; and no birefringency was seen, representing the production of nanoemulsions.

3.4.3. Rheologic Behavior. Flow properties of different nanoemulsions are shown in Figures 5–7. Initially, the flow of organogels did not change by changing the shearing stress, but after a while with the increasing in the rate of shear, shearing stress increased linearly too. Adding the amount of lecithin increased shearing stress (Figure 5), while increased amounts of water decreased it (Figure 6). Changing the amount of drug did not change the shearing stress (Figure 7).

Rheologic behavior is a sign of flow and dispersion of a system and also affects the release process [34, 35]. So knowledge of the rheologic behavior of a transdermal drug delivery system is obviously important. Lecithin organogels show Newtonian behavior before they become gels but by adding water they show non-Newtonian behavior [36]. Three types of flow are seen in these systems: plastic, pseudoplastic, and dilatant flow. As seen in Figures 5–7 all studied formulations had plastic flow behavior; when the organogels were sheared at low shear rates, they behaved like a solid and show elasticity. With a subsequent increase in shear rate, the tubular structures are weakened. The gelling molecules break the physical interactions of the tubules until the shear stress is high enough to destroy the organogel structure, so they flow in linear form [12]. Increasing the ratio of lecithin/IPM from 30 : 70 (F₁₅) to 40 : 60 (F₆) and 50 : 50 (F₁₆) increased

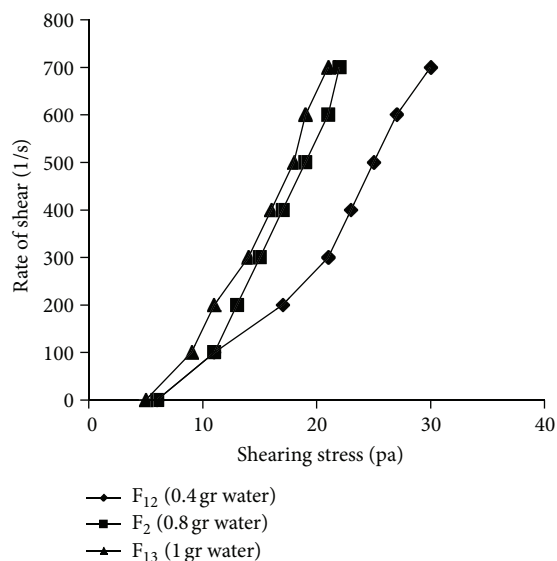


FIGURE 6: The rheogram of w/o metoprolol nanoemulsion containing IPM/lecithin/isopropyl alcohol/and 0.4 g of 10% metoprolol solution with different water contents.

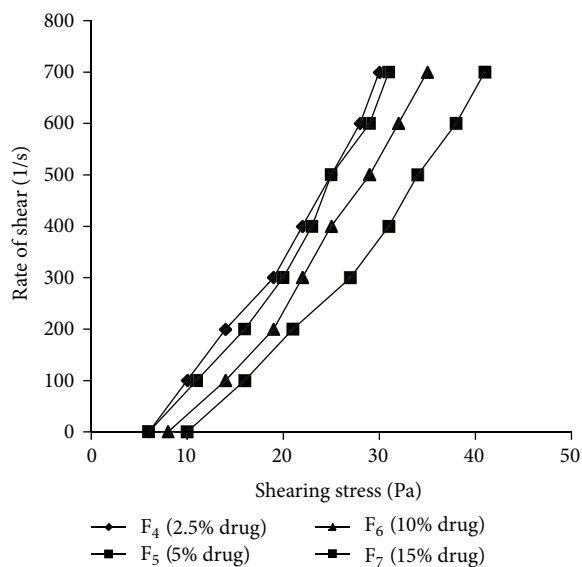


FIGURE 7: The rheogram of w/o metoprolol nanoemulsion containing IPM/lecithin/isopropyl alcohol/and 0.4 g of different concentrations of metoprolol solution.

viscosity and shearing stress of the formulations (Figure 5). By changing the water content of nanoemulsions from 0.4 g in F₁₂ to 0.8 g in F₂ and 1 g in F₁₃ the viscosity and shearing stress decreased too (Figure 6). Nasser and coworkers achieved similar results in their study on the ketorolac thrometamine organogels in which, by increasing the water content of nanoemulsions, the viscosity and shearing stress decreased [31]. Changing the drug content from 2.5 to 15% did not have significant effect on the rheologic behavior of nanoemulsions, and no change in viscosity was observed (Figure 7).

3.5. In Vitro Drug Release. The results of flux calculation, regression coefficient, and permeation and diffusion of different formulations are written in Table 3.

As Table 3 indicates in formulations of F₁₆, F₁₅ and F₆ the flux and drug release rate is the lowest. In formulation of F₁₅ by increasing the ratio of lecithin:IPM, the coefficients of permeation and diffusion decreased (Table 3). Increasing the lecithin:IPM from 30:70 to 40:60 and 50:50 drug release (flux) decreased; it can be interpreted in this way that thermodynamic activity of drug is decreased in higher concentration of lecithin. In higher concentrations of lecithin there are cylindrical micelles which trap the drug, so the flux of drug and its release rate decreased (Table 3) ($P < 0.05$) (cf. F₁₆, F₁₅, and F₆). Aboofazeli and coworkers achieved similar results in their study on the ketorolac thrometamine organogels [31]. By increasing the drug content from 2.5 to 10% the rate of drug release enhanced (F₄, F₅, and F₆), and after that by increasing the drug content to 15% the rate of release declined again (Table 3) ($P < 0.05$) (compare F₇ and F₆). These results confirm the fact that release profile is attributed to drug concentration. The explanation for this phenomenon is that the thermodynamic activity increases by increasing drug concentration until it reaches the saturated concentration, and after this concentration the thermodynamic activity decreases, and accordingly the release declines. Santoyo and coworkers [37] achieved similar results in their study on piroxicam release from propylene glycol gels. Also Henmi et al. [38] reported that indomethacin release from oily gels consisting of soya phospholipid was directly contributed to the drug concentration.

Increasing water content increased the flux and drug release rate from the formulations (Table 3) (cf. F₂, F₁₂, and F₁₃). This is because water can enhance drug permeation from cellulose acetate pores [31]. According to the type of alcohol it was observed that flux was lower in formulations which were prepared by n-propanol and isopropanol than those by n-butanol ($P < 0.05$) (Table 3) (cf. F₁, F₁₇, and F₆). N-propanol and isopropanol are dispersed majorly in aqueous phase, so drug was trapped in inner phase of w/o emulsions, and consequently its release decreased, but water solubility of n-butanol is lower than the other two alcohols [16]; therefore, it may be concluded that the drug was entrapped more in the outer phase causing the faster and increased flux.

Comparing the drug release rate, flux, permeation, and diffusion from formulations containing 0.4 g of a 10% metoprolol solution with nanoemulsions containing the same amount of drug but with a different type of nanoemulsion revealed that o/w nanoemulsion formulations released the drug faster than w/o types, because w/o nanoemulsions trap drug more and prevent their fast release; that is, representing drug is passed more in time [10] (compare F₈ and F₁₄) (Table 3).

Increasing the purity of lecithin decreased the release from formulation where lecithin 100p increased drug permeability more than other lecithin types ($P < 0.05$) (cf. F₉, F₈, and F₆) (Table 3). This result is contrary to Aboofazeli and coworkers' [16] results that can be interpreted in this way that the more pure lecithin can absorb more water in the core of nanoemulsion and decrease drug release rate as discussed

TABLE 3: Flux, release rate (dQ/dt), regression coefficient (R^2) of the curve plotted from changes of dQ against dt , permeation (P), and diffusion coefficient (D) of different formulations through cellulose acetate membrane and (†) rat skin.

Formulation	Flux ($\mu\text{g}/\text{cm}^2/\text{min}$) \pm SD	dQ/dt ($\mu\text{g}/\text{min}$) \pm SD	* $R^2 \pm$ SD	P (cm/min) \pm SD	D (cm^2/min) \pm SD
F ₁	0.29 \pm 0.01	1.53 \pm 0.08	0.971 \pm 0.002	(2.46 \pm 0.28) $\times 10^{-4}$	(6.60 \pm 0.88) $\times 10^{-9}$
F ₂	9.66 \pm 0.30	51.38 \pm 1.59	0.993 \pm 0.001	(1.63 \pm 0.04) $\times 10^{-4}$	(2.67 \pm 0.16) $\times 10^{-6}$
F ₃	21.21 \pm 0.21	112.83 \pm 1.12	0.995 \pm 0.005	92.24 \pm 0.02) $\times 10^{-4}$	(6.38 \pm 0.16) $\times 10^{-6}$
F ₆	1.58 \pm 0.01	6.16 \pm 0.09	0.938 \pm 0.001	(2.76 \pm 0.04) $\times 10^{-5}$	(2.01 \pm 0.06) $\times 10^{-7}$
F ₇	0.93 \pm 0.03	4.96 \pm 0.19	0.991 \pm 0.002	(1.89 \pm 0.05) $\times 10^{-5}$	(4.83 \pm 0.39) $\times 10^{-8}$
F ₈	0.70 \pm 0.03	3.73 \pm 0.18	0.964 \pm 0.006	(1.98 \pm 0.09) $\times 10^{-5}$	(4.31 \pm 0.50) $\times 10^{-8}$
F ₉	1.25 \pm 0.02	6.66 \pm 0.13	0.995 \pm 0.002	(2.92 \pm 0.061) $\times 10^{-5}$	(2.03 \pm 0.07) $\times 10^{-7}$
F ₁₀	7.38 \pm 0.26	39.26 \pm 1.39	0.998 \pm 0.001	(4.61 \pm 0.20) $\times 10^{-5}$	(6.21 \pm 0.52) $\times 10^{-7}$
F ₁₁	43.00 \pm 1.03	228.68 \pm 5.46	0.964 \pm 0.003	(1.59 \pm 0.03) $\times 10^{-3}$	(2.65 \pm 0.52) $\times 10^{-4}$
F ₁₂	4.50 \pm 0.16	24.02 \pm 0.81	0.957 \pm 0.007	(4.64 \pm 0.19) $\times 10^{-5}$	(5.32 \pm 0.40) $\times 10^{-7}$
F ₁₃	9.00 \pm 0.13	47.92 \pm 0.70	0.993 \pm 0.001	(1.59 \pm 0.01) $\times 10^{-4}$	(2.87 \pm 0.07) $\times 10^{-6}$
F ₁₄	5.32 \pm 0.16	28.30 \pm 0.91	0.993 \pm 0.007	(1.33 \pm 0.11) $\times 10^{-6}$	(3.43 \pm 0.55) $\times 10^{-6}$
F ₁₅	5.32 \pm 0.16	28.30 \pm 0.91	0.987 \pm 0.001	(2.96 \pm 0.25) $\times 10^{-5}$	(2.11 \pm 0.30) $\times 10^{-7}$
F ₁₆	0.65 \pm 0.02	3.46 \pm 0.12	0.986 \pm 0.001	(1.93 \pm 0.06) $\times 10^{-5}$	(4.37 \pm 0.36) $\times 10^{-8}$
F ₁₇	2.62 \pm 0.03	13.96 \pm 0.17	0.993 \pm 0.001	(5.19 \pm 0.08) $\times 10^{-5}$	(7.11 \pm 0.24) $\times 10^{-7}$
†F ₂	3.38 \pm 0.17	18.00 \pm 0.89	0.961 \pm 0.001	(3.68 \pm 0.21) $\times 10^{-5}$	(8.29 \pm 0.27) $\times 10^{-7}$
†F ₁₁	22.24 \pm 0.21	118.30 \pm 1.21	0.987 \pm 0.001	(4.53 \pm 0.06) $\times 10^{-4}$	(2.76 \pm 0.05) $\times 10^{-5}$
†F ₁₀	3.07 \pm 0.20	16.37 \pm 1.04	0.960 \pm 0.001	(2.47 \pm 0.15) $\times 10^{-5}$	(5.32 \pm 0.83) $\times 10^{-8}$

earlier about the effect of water content of nanoemulsions on the drug release rate and flux.

Comparing the drug release rate through the cellulose acetate membrane and rat skin (†F₂, †F₁₀, and †F₁₁) it was observed that in all formulations the flux and drug release rate was higher when using cellulose acetate membrane ($P < 0.05$) (Table 3). It is similar to the study of Malaz et al. [39] on release profile of tretinoin gels through synthetic membrane and rat skin. This low release of drug through rat skin relates to complexity of skin texture which does not allow drug molecules to penetrate.

The release rate and flux of metoprolol from an aqueous solution (F₁₁) through rat skin was more than both w/o (F₂) and o/w (F₁₀) types of nanoemulsions ($P < 0.05$) (Table 3) due to drug entrapment in nanoemulsions. Drug release rate, or flux in rat skin did not differ so much in w/o (†F₂) and o/w (†F₁₀) nanoemulsions type ($P > 0.05$) (Table 3).

Increase in the amount of flux enhances drug permeation and diffusion coefficient. Drug permeation and diffusion coefficient were more in the formulations studied by cellulose acetate membrane than rat skin (Table 3) (cf. F₂, F₁₀, and F₁₁ with †F₂, †F₁₀, and †F₁₁). The highest flux and permeation was seen in F₁₁ (aqueous drug solution) and the lowest was seen in F₁₀ (o/w types of nanoemulsion) ($P < 0.05$).

In spite of promising results obtained from nanoemulsions for transdermal uses attention to toxicological aspects of nanosized delivery systems should not be ignored. Lipid-based nanoparticles such as liposomes, micelles, and nanoemulsions are platforms that must be compatible with the physiological environment and prevent undesirable interactions with the immune system. At present there is little experimental evidence on the potential toxicity of nanoemulsions [40]. Nevertheless, there are a number of

physicochemical and physiological mechanisms associated with the small particle size in nanoemulsions that could potentially cause toxicity. Avoiding immune stimulation or suppression is an important consideration when developing new strategies in drug and gene delivery. The organic solvents are usually removed by evaporation during the preparation of the nanoemulsions, but some residual solvent may remain in the final product. It is therefore important to be aware of the potential toxic effects associated with any residual organic solvents if nanoemulsions are produced using this approach. The potential toxicity of emulsifiers and solvents that are suitable for utilization within foods, pharmaceuticals, and other consumer products has been published by various organizations, including the World Health Organization [41]. In the present study all FDA accepted ingredients were used, and no toxicity has been reported for them so far. There are also many reports on the safety of transdermal nanoemulsions. For example, the *in vivo* toxicity of meloxicam nanoemulsion gel was assessed by histopathological examination in rat which turned out to be nonirritant and biocompatible [42]. Also there was no observed mortality or any signs of toxicity during the experimental period of using thymoquinone-rich fraction nanoemulsions [43].

4. Conclusion

O/w nanoemulsion released higher amount of metoprolol through cellulose acetate membrane compared to w/o nanoemulsions; however, permeation and diffusion of drug through rat skin from w/o and o/w nanoemulsion did not differ significantly. Formulations containing 10% aqueous solution of metoprolol had higher drug release rate, and those containing lecithin 200 were preferred because of using less alcohol for elucidating the systems.

Conflict of Interests

The authors declare no conflict of interests.

Acknowledgment

The authors acknowledge the financial support of Isfahan University of Medical Sciences.

References

- [1] E. Keleb, R. K. Sharma, E. B. Mosa, and A. A. Zaljahwi, "Transdermal drug delivery system-design and evaluation," *International Journal of Advances in Pharmaceutical Sciences*, vol. 1, no. 3, pp. 201–211, 2010.
- [2] L. Brunton, B. Chabner, and B. Knollman, *Goodman and Gilman's the Pharmacological Basis of Therapeutics*, McGraw-Hill, New York, NY, USA, 12th edition, 2010.
- [3] M. Omranifard, M. R. Ardakani, A. Abbasi, and A. S. Moghadam, "Follicular isolation technique with de-epithelialization for eyebrow and eyelash reconstruction," *Plastic and Reconstructive Surgery*, vol. 130, no. 3, pp. 571–578, 2012.
- [4] E. C. Paes, H. J. L. J. M. Teepen, W. A. Koop, and M. Kon, "Perioral wrinkles: histologic differences between men and women," *Aesthetic Surgery Journal*, vol. 29, no. 6, pp. 467–472, 2009.
- [5] R. Aboofazeli, H. Zia, and G. T. Needham, "Transdermal delivery of nicardipine: an approach to in vitro permeation enhancement," *Drug Delivery*, vol. 9, no. 4, pp. 239–247, 2002.
- [6] N. Sharma, B. Parashar, S. Sharma, and U. Mahajan, "Blooming pharma industry with transdermal drug delivery system," *Indo Global Journal of Pharmaceutical Sciences*, vol. 2, pp. 262–278, 2012.
- [7] G. A. van Buskirk, M. A. González, V. P. Shah et al., "Scale-up of adhesive transdermal drug delivery systems," *Pharmaceutical Research*, vol. 14, no. 7, pp. 848–852, 1997.
- [8] R. Y. Parapat, M. Wijaya, M. Schwarze, S. Selve, M. Willinger, and R. Schomäcker, "Particle shape optimization by changing from an isotropic to an anisotropic nanostructure: preparation of highly active and stable supported Pt catalysts in nanoemulsions," *Nanoscale*, vol. 5, no. 2, pp. 796–805, 2013.
- [9] L. Chen, F. Tan, J. Wang, and F. Liu, "Nanoemulsion: a novel transdermal delivery system to facilitate skin penetration of indomethacin," *Pharmazie*, vol. 67, no. 4, pp. 319–323, 2012.
- [10] D. W. Osborne, A. J. I. Ward, and K. J. O'Neill, "Nanoemulsions as topical drug delivery vehicles: characterization of a model system," *Drug Development and Industrial Pharmacy*, vol. 14, no. 9, pp. 1203–1219, 1988.
- [11] P. A. Winsor, "Hydrotropy, solubilisation and related emulsification processes—part I," *Transactions of the Faraday Society*, vol. 44, pp. 376–398, 1948.
- [12] S. Raut, S. S. Bhadoriya, V. Uplanchiwar, V. Mishra, S. K. Jain, and A. Gahane, "Lecithin organogel: a unique micellar system for the delivery of bioactive agents in the treatment of skin aging," *Acta Pharmaceutica Sinica B*, vol. 2, no. 1, pp. 8–15, 2012.
- [13] A. Bhatia, B. Singh, K. Raza, S. Wadhwa, and O. P. Katare, "Tamoxifen-loaded lecithin organogel (LO) for topical application: development, optimization and characterization," *International Journal of Pharmaceutics*, vol. 444, no. 1–2, pp. 47–59, 2013.
- [14] B. F. Szuhaj, *Lecithins: Sources, Manufacture and Uses*, American Oil Chemist's Society, Champaign, Ill, USA, 1989.
- [15] W. Martindale and J. E. E. Reynolds, *Martindale, the Complete Drug Reference*, Royal Pharmaceutical Society, London, UK, 37th edition, 2011.
- [16] R. Aboofazeli, S. A. Mortazavi, and P. Khoshnevis, "In vitro release study of sodium salicylate from lecithin based phospholipid microemulsions," *Iranian Journal of Pharmaceutical Research*, vol. 2, pp. 95–101, 2003.
- [17] W. A. Ritschel, "Microemulsions for improved peptide absorption from the gastrointestinal tract," *Methods and Findings in Experimental and Clinical Pharmacology*, vol. 13, no. 3, pp. 205–220, 1991.
- [18] J. M. Sarciaux, L. Acar, and P. A. Sado, "Using microemulsion formulations for oral drug delivery of therapeutic peptides," *International Journal of Pharmaceutics*, vol. 120, no. 2, pp. 127–136, 1995.
- [19] S. B. Hoffman, A. R. Yoder, and L. A. Trepanier, "Bioavailability of transdermal methimazole in a pluronic lecithin organogel (PLO) in healthy cats," *Journal of Veterinary Pharmacology and Therapeutics*, vol. 25, no. 3, pp. 189–193, 2002.
- [20] D. Paolino, C. A. Ventura, S. Nisticò, G. Puglisi, and M. Fresta, "Lecithin microemulsions for the topical administration of ketoprofen: percutaneous adsorption through human skin and in vivo human skin tolerability," *International Journal of Pharmaceutics*, vol. 244, no. 1–2, pp. 21–31, 2002.
- [21] C. M. Keck, M. Jansch, and R. H. Müller, "Protein adsorption patterns and analysis on IV nanoemulsions—the key factor determining the organ distribution," *Pharmaceutics*, vol. 5, no. 1, pp. 36–68, 2013.
- [22] P. Shah, D. Bhalodia, and P. Shelat, "Nanoemulsion: a pharmaceutical review," *Systematic Reviews in Pharmacy*, vol. 1, no. 1, pp. 24–32, 2010.
- [23] T. K. Ghosh, M. J. Habib, K. Childs, and M. Alexander, "Transdermal delivery of metoprolol—I: comparison between hairless mouse and human cadaver skin and effect of n-decylmethyl sulfoxide," *International Journal of Pharmaceutics*, vol. 88, no. 1–3, pp. 391–396, 1992.
- [24] H. Fares, C. J. Lavie, and H. O. Ventura, "Vasodilating versus first-generation β -blockers for cardiovascular protection," *Postgraduate Medicine*, vol. 124, no. 2, pp. 7–15, 2012.
- [25] G. K. McEvoy and E. K. Snow, *AHFS Drug Information*, American Society of Health System Pharmacists, 54th edition, 2013.
- [26] G. S. Anisree, C. Ramasamy, J. I. Wesley, and B. M. Koshy, "Formulation of transdermal drug delivery system of metoprolol tartrate and its evaluation," *Journal of Pharmaceutical Sciences and Research*, vol. 4, pp. 1939–1942, 2012.
- [27] A. Nair, H. Vyas, J. Shah, and A. Kumar, "Effect of permeation enhancers on the iontophoretic transport of metoprolol tartrate and the drug retention in skin," *Drug Delivery*, vol. 18, no. 1, pp. 19–25, 2011.
- [28] D. C. Bhatt, A. S. Dhake, R. K. Khar, and D. N. Mishra, "Development and in vitro evaluation of transdermal matrix films of metoprolol tartrate," *Yakugaku Zasshi*, vol. 128, no. 9, pp. 1325–1331, 2008.
- [29] G. Csóka, S. Marton, R. Zelko, N. Otomo, and I. Antal, "Application of sucrose fatty acid esters in transdermal therapeutic systems," *European Journal of Pharmaceutics and Biopharmaceutics*, vol. 65, no. 2, pp. 233–237, 2007.
- [30] R. Vanbever, N. Lecouturier, and V. Preat, "Transdermal delivery of metoprolol by electroporation," *Pharmaceutical Research*, vol. 11, no. 11, pp. 1657–1662, 1994.

- [31] A. A. Nasser, R. Aboofazeli, H. Zia, and T. E. Needham, "Lecithin stabilized nanoemulsion based organogels for topical application of ketorolac tromethamine—II: in vitro release study," *Iranian Journal of Pharmaceutical Research*, vol. 2, pp. 117–124, 2003.
- [32] A. A. Nasser, R. Aboofazel, H. Zia, and T. G. Needham, "Lecithin stabilized nanoemulsions: an organogel for topical application of ketorolac tromethamine—I: phase behavior studies," *Iranian Journal of Pharmaceutical Research*, vol. 2, no. 1, pp. 59–63, 2003.
- [33] M. Trotta, F. Pattarino, and G. Grosa, "Formation of lecithin-based microemulsions containing n-alkanol phosphocholines," *International Journal of Pharmaceutics*, vol. 174, no. 1-2, pp. 253–259, 1998.
- [34] G. Betageri and P. Sunil, "Semisolid preparation," in *Encyclopedia of Pharmaceutical Technology*, J. Swarbrick and J. C. Boylan, Eds., pp. 2436–2438, Marcel Dekker, London, UK, 2nd edition, 2002.
- [35] J. Wagner, *Biopharmaceutics and Relevant Pharmacokinetics*, Drug Intelligence Publications, Hamilton, Ill, USA, 1st edition, 1971.
- [36] R. Kumar and O. P. Katare, "Lecithin organogels as a potential phospholipid-structured system for topical drug delivery: a review," *AAPS PharmSciTech*, vol. 6, no. 2, pp. E298–E310, 2005.
- [37] S. Santoyo, A. Arellano, P. Ygartua, and C. Martín, "In vitro percutaneous absorption of piroxicam through synthetic membranes and abdominal rat skin," *Pharmaceutica Acta Helvetiae*, vol. 71, no. 2, pp. 141–146, 1996.
- [38] T. Henmi, M. Fujii, K. Kikuchi, N. Yamanobe, and M. Matsumoto, "Application of an oily gel formed by hydrogenated soybean phospholipids as a percutaneous absorption-type ointment base," *Chemical and Pharmaceutical Bulletin*, vol. 42, no. 3, pp. 651–655, 1994.
- [39] M. Malaz, N. Tavakoli, and R. Ebrahimi, "Physicochemical evaluation, stability and release stability studies of tertinoil local products," *Medical Journal of Hormozgan University*, vol. 8, no. 4, pp. 199–207, 2005.
- [40] F. Shakeel, S. Shafiq, N. Haq, F. K. Alanazi, and I. A. Alsarra, "Nanoemulsions as potential vehicles for transdermal and dermal delivery of hydrophobic compounds: an overview," *Expert Opinion on Drug Delivery*, vol. 9, no. 8, pp. 953–974, 2012.
- [41] D. J. McClements and J. Rao, "Food-grade nanoemulsions: formulation, fabrication, properties, performance, biological fate, and potential toxicity," *Critical Reviews in Food Science and Nutrition*, vol. 51, no. 4, pp. 285–330, 2011.
- [42] S. Khurana, N. K. Jain, and P. M. Bedi, "Nanoemulsion based gel for transdermal delivery of meloxicam: physico-chemical, mechanistic investigation," *Life Sciences*, vol. 92, no. 6-7, pp. 383–392, 2013.
- [43] Z. Tubesha, M. U. Imam, R. Mahmud, and M. Ismail, "Study on the potential toxicity of a thymoquinone-rich fraction nanoemulsion in sprague dawley rats," *Molecules*, vol. 18, no. 7, pp. 7460–7472, 2013.

Research Article

In Vivo Study of Ligament-Bone Healing after Anterior Cruciate Ligament Reconstruction Using Autologous Tendons with Mesenchymal Stem Cells Affinity Peptide Conjugated Electrospun Nanofibrous Scaffold

Jingxian Zhu,^{1,2} Xin Zhang,² Zhenxing Shao,² Linghui Dai,¹ La Li,² Xiaoqing Hu,² Xiaokun Wang,³ Chunyan Zhou,¹ and Yingfang Ao²

¹ Department of Biochemistry and Molecular Biology, Peking University School of Basic Medical Sciences, 38 Xueyuan Road, Haidian District, Beijing 100191, China

² Institute of Sports Medicine, Peking University Third Hospital, 49 North Garden Road, Haidian District, Beijing 100191, China

³ Department of Biomedical Engineering, College of Engineering, Peking University, No. 5 Yiheyuan Road, Haidian District, Beijing 100871, China

Correspondence should be addressed to Chunyan Zhou; chunyanzhou@bjmu.edu.cn and Yingfang Ao; yingfang.ao@gmail.com

Received 22 July 2013; Revised 23 September 2013; Accepted 2 October 2013

Academic Editor: Patricia Murray

Copyright © 2013 Jingxian Zhu et al. This is an open access article distributed under the Creative Commons Attribution License, which permits unrestricted use, distribution, and reproduction in any medium, provided the original work is properly cited.

Electrospinning nanofibrous scaffold was commonly used in tissue regeneration recently. Nanofibers with specific topological characteristics were reported to be able to induce osteogenic differentiation of MSCs. In this *in vivo* study, autologous tendon grafts with lattice-like nanofibrous scaffold wrapping at two ends of autologous tendon were used to promote early stage of ligament-bone healing after rabbit ACL reconstruction. To utilize native MSCs from bone marrow, an MSCs specific affinity peptide E7 was conjugated to nanofibrous meshes. After 3 months, H-E assessment and specific staining of collagen type I, II, and III showed direct ligament-bone insertion with typical four zones (bone, calcified fibrocartilage, fibrocartilage, and ligament) in bioactive scaffold reconstruction group. Diameters of bone tunnel were smaller in nanofibrous scaffold conjugated E7 peptide group than those in control group. The failure load of substitution complex also indicated a stronger ligament-bone insertion healing using bioactive scaffold. In conclusion, lattice-like nanofibrous scaffold with specific MSCs affinity peptide has great potential in promoting early stage of ligament-bone healing after ACL reconstruction.

1. Introduction

Tissue engineering technique emerges as a new tool in tissue regeneration these years. Nanosized material was frequently used as scaffold in tissue engineering because of its superior characteristics like huge surface area and superior biological compatibility. Nanofibrous scaffold fabricated by electrospinning technique has been used in bone, neuron, and ligament regeneration. We developed a specific nanotopographical electrospun scaffold which could induce osteogenesis of rat bone marrow derived mesenchymal stem cells (MSCs) *in vitro*. And now we want to testify the ability of this scaffold in accelerating bone formation at the ligament-bone insertion sites after rabbit ACL reconstruction.

Nanofibrous scaffolds are appropriated for cell adhesion and growing because of the huge surface area and fibers in nanoscale which can mimic natural extracellular matrix [1, 2]. Among the methods of fabricating nanofibrous scaffolds, electrospinning is the most widely used given its simplicity and efficiency. However, mechanical properties of electrospun meshes render it impossible to be a substitution for ACL reconstruction alone. Therefore some researchers designed composite scaffold combining firm artificial material with nanofibrous surface made by electrospinning [3, 4]. But autologous tendons especially hamstring tendons, which were commonly used in clinical surgery, were still verified to be better than artificial scaffolds for their good biocompatibility

and mechanical properties [5, 6]. So combining autologous tendon and electrospun meshes to form a new scaffold should satisfy both the mechanical and cell growth requirements.

MSCs have been widely used in tissue engineering studies and have been proved to have great potential in clinical application because of their convenience in isolation, lack of significant immunogenicity, high capacity of expansion, and potential to differentiate into tissue-specific cell types [7–9]. However MSCs should be first homed and entrapped into the site of tissue damage so as to allow MSCs to properly perform their functions during the whole repair process [10]. In our previous research we screened an affinity peptide of bone marrow-derived MSCs using phage display technique to solve the problem of low efficiency and engraftment of MSCs in tissue engineering [11]. As a result, covalently conjugating the peptide E7 on the synthetic electrospun mesh significantly enhanced the MSC recruitment of scaffold *in vivo*. Therefore we used this technique for the same purpose in our study.

As new bone formation is of vital importance for ligament-bone healing after ACL reconstruction, many composite scaffolds were designed to promote osteogenesis of MSCs at the insertion site. In bone tissue engineering, composition mimic native extracellular matrix like hydroxyapatite, collagen, chitosan, and so forth was added to promote osteogenic differentiation of MSCs [12, 13]. Also, bioactive cytokines like BMP2 were used as chemical inductive agents, and mechanical stimulation can promote osteogenic differentiation of MSCs as well [14]. In recent years, topological characteristics of nanofibrous scaffold was confirmed to be an important factor in deciding the destiny of cell growing on them. Specific topographical scaffold can promote cell adhesion, migration, proliferation, and differentiation [15, 16]. In our previous research, we found that the lattice-like nanofibrous mesh can promote osteogenesis of rat MSCs by regulating integrin $\beta 1$ (ITGB1), ras homolog gene family member A (RhoA)/Rho-associated protein kinase (ROCK), extracellular regulated protein kinases (ERK), and runt related transcription factor 2 (Runx2) expression [17]. However, few studies were available that have tested the osteoinductive ability of electrospun meshes *in vivo*. In this study, we designed a new scaffold, which is combined lattice-like nanofibrous meshes with bone marrow MSCs affinity peptide, and was used in rabbit ACL reconstruction model together with autologous hamstring tendon. The aim of this study is to compare the osteogenic ability of tendon grafts with or without nanofibrous scaffolds and to explore the potential application of electrospun scaffolds in ligament tissue engineering.

2. Methods and Materials

2.1. Electrospinning PLLA Nanofibrous Scaffold. Lattice-like patterned poly-L-lactide (PLLA) nanofibrous scaffolds were fabricated as described in our previous research. The polymer solution was prepared by dissolving 1.0 g of PLLA powders in 10 mL tetrafluoroethylene and stirred overnight. The solution was electrospun from a 20 mL syringe with a steel needle (inner diameter of 0.5 mm) at a rate of 0.5 mL/h continuously

with a programmable syringe pump (Top 5300, Japan). A voltage (12 kV) was applied to the tip of the needle by the use of a high-voltage supply (DW-P303-1AC, China) when a fluid jet was ejecting. To obtain patterned PLLA nanofibrous scaffolds, a copper wire grid ($r = 10$ cm) was used as a collector at a distance of 15 cm from the tip of the needle. Before using, all scaffolds were exposed to a vacuum oven (DZF-6210, Bluepard, China) at room temperature for 2 weeks to remove residual solvent.

2.2. MSCs Affinity Peptide E7 Biopanning and Conjugation. The bone marrow MSCs of Wistar rats were harvested using standard protocol in our lab. MSCs were derived from two lower extremities of rats with the approval of the Animal Ethics Committee of Peking University Third Hospital. MSC specific affinity peptide was biopanning by the phage display technique following a previously described procedure with modifications [11, 18]. In brief, first a peptide phage display library was commercially constructed (Ph.D.-7 phage display library, NEB, Beverly, MA, USA) and incubated with MSCs, synovial cells were used as negative control. Then the phage clones binding MSCs were amplified, titrated and, purified according to the manufacturer's standard protocol. Three to four rounds of selection were performed until the optimal results were obtained. The experiments were duplicated for verification. A specific peptide was identified in the MSC-affinity clones and designated as E7. The peptides were dissolved in DMSO to yield a 2 mg/mL concentration before usage.

The PLLA meshes were immersed into a 10% w/v solution of 1,6-hexanediamine (Sigma, St. Louis, MO, USA) prepared in isopropanol at 37°C for 1 h. After the exposure, the PLLA meshes were thoroughly washed in ultrapure water and dried under vacuum at room temperature. For the conjugation of E7 peptides to the surface of meshes, the aminated PLLA meshes were washed thrice with activation buffer (0.1 M PBS containing 0.15 M NaCl, pH 7.2) before treatment, and sulfo-succinimidyl-4- (N-maleimidomethyl) cyclohexane-1-carboxylate (sulfo-SMCC) (Thermo Fisher Scientific Inc., Rockford, IL, USA) was used as a cross-linker. A total of 500 mL (2 mg/mL) sulfo-SMCC solution was added onto the aminated PLLA meshes, incubated for 1 h at room temperature, and washed with conjugation buffer (activation buffer containing 0.1 M EDTA, pH 7.0). The peptides were dissolved in conjugation buffer at a concentration of 0.1 mM. Up to 500 mL of the peptide solution was applied onto the sulfo-SMCC-treated PLLA scaffold and incubated overnight at 4°C. The peptide conjugated PLLA meshes were thoroughly washed thrice with ultrapure water and dried under vacuum at room temperature. The whole mesh was cut into 1 cm², sterilized by immersing in 75% ethanol over-night, washed thrice with ultrapure water, and immersed in PBS over 4 h. Before implantation, the meshes were kept in 4°C refrigerator.

2.3. MSCs Attachment on Different Scaffolds. The MSCs at passage 3 were seeded onto the blank or E7-conjugated lattice PLLA meshes. After 24 h of incubation, the PLLA meshes were washed from three to five times with PBS

and fixed with 4% paraformaldehyde for 10 min at room temperature. Cells were then preincubated in 100 μL of primary blocking solution (PBS, 1% BSA, and 0.1% NP-40) for 20 min and then incubated with 10^{-7} M Alexa Fluor 488 phalloidin conjugate (Molecular Probes) for 1 h. After three washes in PBS, nuclei were stained with 10 $\mu\text{g}/\text{mL}$ Hoechst 33342 at room temperature for 30 min. Mounting medium (35 μL , Zhongshan) was dispensed onto the cells, and a glass coverslip was placed on the slide before placing it in the freezer prior to observation. Actin structures were examined by laser confocal scanning microscopy (FV 1000 Olympus IX-81). Cell attachment was observed by confocal microscope at both ridge regions and nonwoven regions of lattice. And percentage of cell attachment to material within each group were measured using Image-Pro Plus 6.0 software (Media Cybernetics, Silver Spring, MD, USA) by 5 random areas were used in one photograph.

2.4. ACL Reconstruction Surgery. Animal experiments were approved by Ethical Committee of third hospital, Peking University. Forty-eight New Zealand white rabbits (12 weeks old, 2.5–3.0 kg) were divided into three groups: BIO group (lattice-like PLLA scaffold with MSCs affinity peptide; n 16), PLLA group (lattice-like PLLA scaffold alone; n 16), and control group with single reconstruction surgery. Hamstring tendon grafts were harvested from both two knees of each rabbit. Then two tendons were bound by braiding two ends with 3–0 braided nylon thread. Nanofibrous meshes were braiding together with tendon in BIO or PLLA reconstruction groups at this time. The right knee joint of each rabbit was exposed using a midline skin incision, and lateral parapatellar arthrotomy was performed. The patella was dislocated totally with the knee extended. With the knee placed in its hyperflexive state, the original ACL was removed by sharp dissection of the tibial and femoral attachment sites, while the fat pad was left intact. Using a 2.0 mm diameter Kirschner wire and a drill, bone tunnels were made from the ACL femur attachment sites to the lateral femoral condyles, as well as from the ACL tibial attachment sites to the medial tibia. The tibial sites were distal and lateral to the tibial tubercles. After placing the grafts into two bone tunnels, both two ends were fixed by bone bridge (Figures 3(a)–3(f)). This was done with the knee at 45° of flexion, while the constructs were manually exposed to maximum tension. Penicillin (200000 U/kg) was subcutaneously administered to prevent postoperative infection. Enhanced antibiotic was used for 3 days after surgery. At 1 or 3 months after surgery, the knee joints were harvested for histological and mechanical examinations. At the specified times, rabbits were sacrificed by intravenous air embolism.

2.5. Measurement of Bone Tunnel by CT Scanning. All 48 hind limbs were harvest after rabbit was sacrificed immediately. Whole limb was scanned by 64-row CT scanner (LightSpeed VCT; GE Medical System, Chalfont St Giles, UK) using the same parameter of human hands scanning. Both the femoral and tibial tunnels were measured by one and

the same technician, to ensure no operating errors. The cross-section of bone tunnel was determined by 3 steps: first step, confirm the middle of articular according the patellar position; then draw the long axis of bone tunnel in femora or tibia by adjusting the sagittal and coronal plane to show the longest tunnel; at last the cross sectional images were taken perpendicular to the long axis of bone tunnel (Figure 4). All slices of each sample were scanned and the minimal diameter of bone tunnel could be calculated by 3-dimensional reconstruction. All data were analyzed by 3-different researchers and both femoral and tibial tunnel diameter was taken as one specimen.

2.6. Histological and Immunohistological Assessment. Eight of specimens in each group were prepared for histological assessment. Ligament-bone insertion was harvested by cutting from sagittal plane 1 cm away articular. After all soft tissue removing, transplanted ligament was cut off in the middle part, fixed in formalin (4% formalin in phosphate-buffered saline), and embedded in paraffin. Six micron thick tissue sections were cut from these paraffin blocks. All of the specimens were stained with hematoxylin and eosin (H-E), sirius red, and immunohistochemical staining to display the histological characteristics and distribution of collagen type I, II, and III. Distribution of collagen type I and III was displayed by sirius red staining and observed by polarized light microscope (Laica DM2500, Wetzlar, Germany). Distribution of collagen II was evaluated with a specific antibody to rabbit collagen type II (Calbiochem, Darmstadt, Germany). Before staining, the samples were treated with pepsin working solution (ZhongShanJinQiao, Beijing, China) for 15 min and then incubated with primary antibody overnight. Following PBS washing, biotinylated secondary antibodies were added for 1 hour at 37°C , then the samples were colorated with 3,3-diaminobenzidine (DAB). Each specimen was viewed by light microscopy (Olympus BH-2, Tokyo, Japan) and photographs were taken from 3 randomly chosen representative microscopic fields at a magnification of 40–200x.

2.7. Biomechanical Test of Substitution Complex. After CT scanning, the lower extremities of another 8 animals in each group were disarticulated at the hip joint and stored at -80°C refrigerator. Before mechanical testing, each knee was thawed overnight at 4°C and all soft tissues around the knee were carefully removed except the ACL. The prepared femur-ACL-tibia complex was then mounted onto a conventional tensile tester. The femur and the tibia were fixed in cupreous holders using 2 Kirschner wires. The knee was fixed at 45° of flexion with maximal tensile resistance during testing. The specimen was cycled between 0 and 0.5 mm deformation 10 times at a rate of 5 mm/min for pretension. Subsequently, the specimen was stretched to failure at a rate of 0.1 mm/s. The load-deformation curve was recorded and the ultimate load was then obtained. The linear stiffness was defined as the best-fitting straight line drawn through the linear portion of the load-deformation curve. The specimens were kept moist at

all times during preparation and testing with normal saline solution.

2.8. Statistical Analysis. All data were shown as the mean with standard deviation. One-way analysis of variance was performed when comparing data of 3 groups. Other statistical comparisons were performed with the paired-samples *t*-test. SPSS 14.0 software was used for statistical calculation. The significance level was set at $P < 0.05$.

3. Results

3.1. Lattice-Like PLLA Nanofibrous Meshes Synthesis and Observation. Propelled by electrostatic forces, lattice-like fibrous PLLA meshes could be obtained by using copper wire grid as collector (Figure 1(a)). The lattice-like mesh macroscopically resembled gauzes and followed the pattern of grid (Figure 1(b)). Detailed structure of nanofibers in the scaffolds was observed by scanning electron microscopy (Figures 1(c), 1(e), and 1(f)). Fibers depositing on the ridge regions were parallel-aligned (Figure 1(e)) while in those regions between ridges were randomly distributed (Figure 1(f)). The diameter of nano fibers ranged from 200 to 1200 nm (Figure 1(e)).

3.2. MSCs Attachment on PLLA Nanofibrous Meshes. The attachment of MSCs on scaffolds with or without affinity peptide was observed by laser scanning confocal microscope. Staining of cytoskeleton and nuclei of MSCs showed well attaching and spreading of cells on both two kinds of scaffolds. But the cell number was obviously different on E7 conjugated PLLA meshes at different regions of lattice meshes (Figures 2(a) and 2(c)). Cell morphology of MSCs growing on E7 conjugated PLLA meshes appeared better organized and was more compliance with the nanofiber distribution than on PLLA meshes (Figures 2(b) and 2(d)). Percentage of cell attachment to different kinds of scaffolds was obviously different, which was $89.72 \pm 1.66\%$ and $60.24 \pm 10.42\%$ ($P < 0.05$) on PLLA meshes with or without E7 peptide.

3.3. Gross Observation. Twenty-four rabbits were sacrificed at 1 or 3 months after ACL reconstruction surgery, respectively. Gross morphology of knee joint was compared after operation between three groups. At 12 weeks the regenerated ligament showed a stable fixation in all three groups without any ends pulling out of tunnels. There was not obvious infection in joint cavity; meanwhile synovial fluid was clear in three groups. But all joints exhibited a little degeneration with cartilage injury, to some extent, which might because of the damage in surgery procedure or instability after reconstruction of ACL. The gross findings revealed that reconstructed ligament was wrapped by synovial membrane, but two bundles of tendon were still distinguishable (Figures 3(g)–3(i)).

3.4. Bone Tunnel Measurement. The cross-sectional images perpendicular to the longitudinal axis of bone tunnel were reconstructed in high-resolution CT. The newly formed mineralized tissue could be examined by screening all slices of

TABLE 1: Bone tunnel measured by CT and failure load of grafts.

Group	Bone tunnel (mm)		Failure load (N)
	1 M	3 M	3 M
REC	7.50 ± 1.80	$10.16 \pm 2.62^*$	34.58 ± 4.08
PLLA	5.96 ± 0.90	6.72 ± 1.66	$82.59 \pm 3.33^*$
BIO	5.32 ± 2.45	4.20 ± 1.87	$141.50 \pm 3.90^*$

REC: reconstruction group, PLLA: reconstruction with PLLA scaffold, and BIO: reconstruction with E7 peptide conjugated PLLA scaffold. Student's test was used and significance of $^*P < 0.05$.

each sample and the minimal diameter of bone tunnel could be calculated. In both control group and PLLA reconstruction group, the bone tunnel was larger at 3 months after surgery than 1 month, which was known as the “enlargement of bone tunnel.” Though in BIO reconstruction group there was no obvious enlargement at 3 months, bone tunnel was smaller than the other two groups both at 1 and 3 months, which was 5.32 ± 2.45 and 4.20 ± 1.87 mm, respectively (Table 1). The consecutive CT images showed that there was no obvious mineralized tissue formed in tibial and femoral bone tunnels after 4 and 12 weeks in all groups (Figures 4(b) and 4(d)). After CT scan, the biomechanical test or histological staining was performed to further examine the changes of ligament-bone insertion.

3.5. Biomechanical Analysis. Four specimens in each group at 3 months after surgery were tested to evaluate tensional properties of the reconstructed ACL. Results showed that all substitution complex in BIO reconstruction group were broken in the midpart of regenerated ligaments during mechanical test. Two of four specimens in PLLA group were pulled out of ligament insertion sites, while in control group there was one. The load-deformation curves changed smoothly from a flat slope to a steep one with extension of implants and suddenly fell at failure load. The control group recorded a maximum tensile load of 34.58 ± 4.08 N, while the PLLA reconstruction group had a failure load of 82.59 ± 3.33 N. The failure load in BIO reconstruction group was 141.50 ± 3.90 N at 12 weeks postoperatively, which was also significantly higher than that of control ($P < 0.05$) (Table 1).

3.6. Histological Assessment of Ligament-Bone Insertion. Histological observation demonstrated that the fibrovascular connective tissue, fibrocartilage, and the Sharpey's fibers were gradually developed between the implants and bone tunnel in BIO reconstruction group. At 4 weeks postoperatively, only a thin layer of fibrovascular connective tissue was observed on the interface of regenerated ligament in control and PLLA reconstruction groups (Figures 5(a) and 5(b)). But in BIO reconstruction group the implant-bone interface was filled with loose fibrocartilage tissue with a few chondrocytes scattered between bone and regenerated ligament (Figure 5(c)). After 12 weeks, the thin layer of connective tissue became much denser in PLLA reconstruction group (Figure 5(e)) while in control group, the more organized perpendicular collagen fibers resembling the Sharpey's fibers were observed to form the indirect junction between ligament and bone

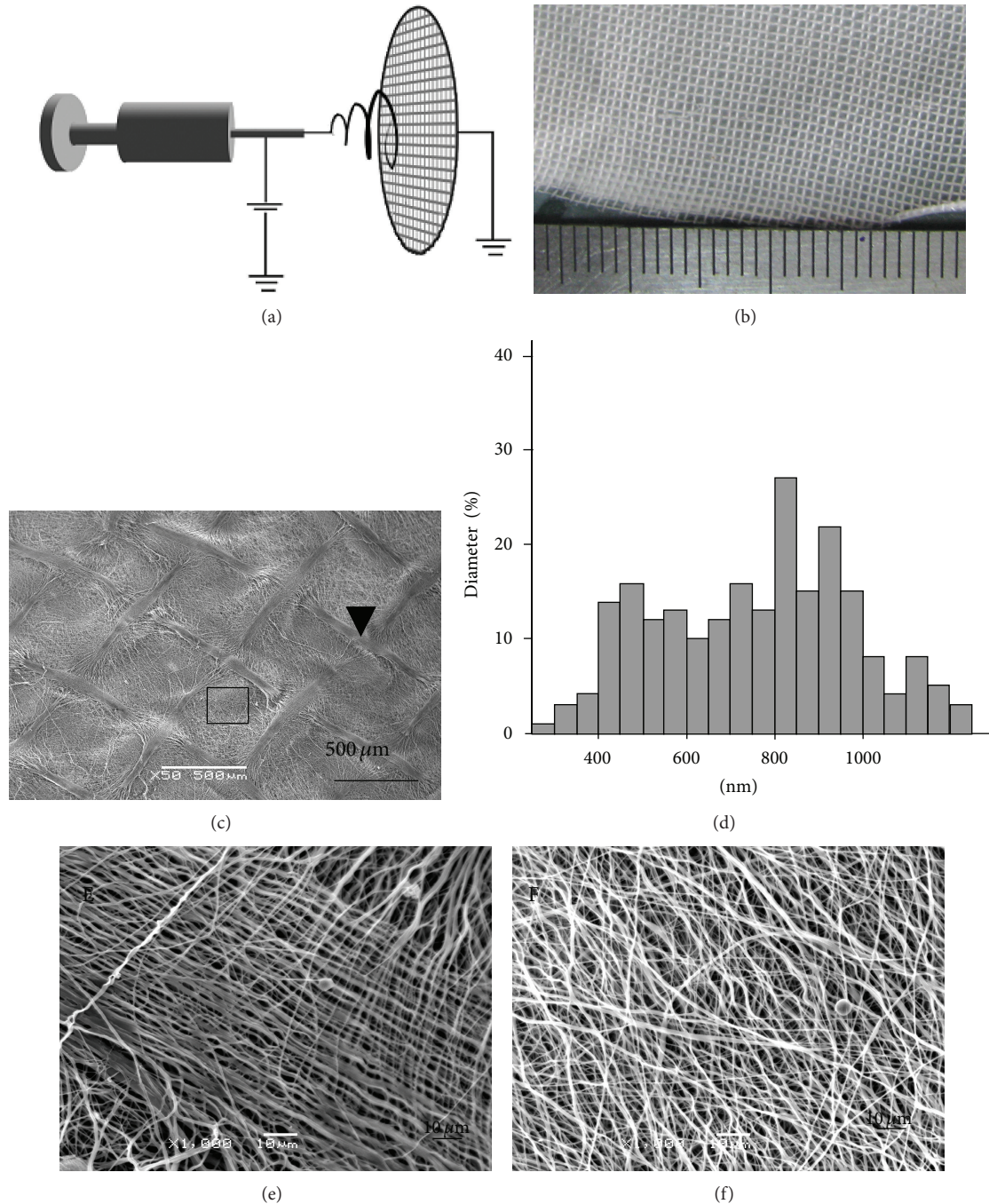


FIGURE 1: Schematic illustration of electrospinning devices and scanning electron microscope observation of nanofibers characteristics in lattice-like electrospun scaffolds. (a) Schematic diagram of electrospun scaffold device showed lattice-like fibers collecting by copper wire grid. (b) Picture of scaffold showed general view of lattice-like PLLA meshes. ((c), (e), and (f)) Micrographs showed nanofibers distribution in different regions of lattice-like PLLA meshes. Detailed view showed local enlarged fibers on ridge (e) and nonwoven region (f) of each lattice. (d) Histogram showed distribution of nanofibers' diameter in scaffolds.

at 12 weeks (Figure 5(d)). At the same time, fibrocartilage appeared with tide line mark between ligament and bone in BIO reconstruction group. A gradual transition from bone, mineralized fibrocartilage and fibrocartilage, into the tendon substance was successfully reconstructed (Figure 5(f)).

At 3 months after surgery, collagen type II, I, and III distribution of insertion site was detected by immunohistochemical and Sirius red staining, respectively. Results

indicated that a large amount of collagen fibers making up of type III and I grow from ligament to bone in control group (Figure 6(a)), while little mature cartilage tissue was found at insertion site in this group by collagen II staining (Figure 6(d)). In PLLA and BIO reconstruction groups, collagen III amount decreased at insertion site while collagen I increased (Figures 6(b) and 6(c)). Meanwhile fibrocartilage with aligned chondrocytes was found in BIO group

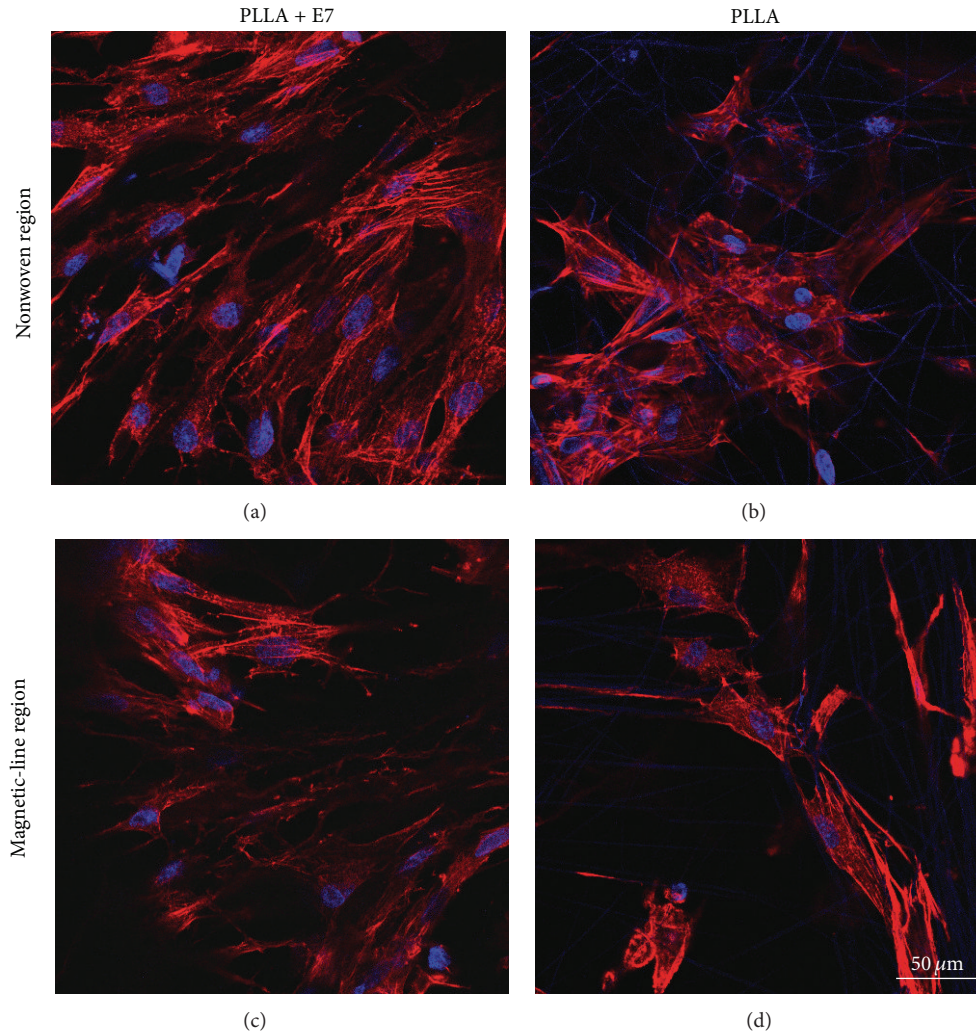


FIGURE 2: Laser scanning confocal microscopy image showed attachment of MSCs on different scaffolds. Morphology of MSCs was displayed by F-actin (red) and nuclei (blue). Cell attachment and spreading on E7 conjugated PLLA meshes were shown in both nonwoven and near ridge regions of lattice ((a), (c)). MSCs that grew on PLLA meshes were shown as control ((b), (d)).

by immunohistochemical staining (Figure 6(f)). In PLLA group, few collagen II fibers and chondrocytes indicated an immature insertion site (Figure 6(e)).

4. Discussion

The ligament-bone insertion is important for the effective transmission of mechanical force and the reduction in stress gradient between the soft ligament and hard bone tissue. The healing of ligament-bone insertion after ACL reconstruction is of vital importance for the stability of implantation especially at early stage. Many kinds of approaches like cytokines, biomaterials, biological and chemistry reagents, stem cells, and genes were added to strengthen the healing of ligament-bone insertion [19–23]. Their objectives were the same, which is to promote local bone formation. While drilling bone tunnel, many bone marrow MSCs and cytokines were released and leaked out into the articular cavity. Using these mixture would be more convenient and effective than using extrinsic MSCs supplement. In our study, nanofibrous

meshes which wrapped two ends of tendon graft can fill the interspace between tendon and bone tunnel and increase the contact area to absorb the leaking MSCs from bone marrow. Meanwhile our results indicated higher adhesion level of MSCs on nanofibrous meshes conjugated with E7 peptide which was proved to have specific affinity to MSCs. The specific affinity peptide together with physical absorption ability of nanofibrous scaffold promoted the utilization of endogenous bone marrow MSCs.

The ultimate goal in the design of biomimetic materials for use in tissue engineering is to generate biocompatible scaffolds with appropriate mechanical and chemical properties. Recent efforts have therefore been focused on the construction and modification of surfaces targeted to support tissue-specific cell functions including adhesion, growth, differentiation, motility, and the expression of tissue-specific genes [24]. There are three types of modification of biomimetic surfaces to mimic natural ECM: physical properties, chemical signals, and the nanoscale topography of microenvironmental adhesive sites. Recently, the development of new



FIGURE 3: Pictures showing rabbit ACL reconstruction surgery procedure and gross morphology of reconstructed ACL at 3 months after surgery. Hamstring tendon grafts were harvested from both two knees of each rabbit (a). PLLA scaffold or PLLA scaffold with E7 peptide conjugation was wrapped at two ends of tendons in PLLA reconstruction group and BIO reconstruction group (b) and braided with nylon thread (c). The right knee joint of each rabbit was exposed and original ACL was removed. Bone tunnels were made from the ACL femur attachment sites to the lateral femoral condyles (d), as well as from the ACL tibial attachment sites to the medial tibia (e). After placing the transplants into two bone tunnels, both two ends were fixed by bone bridge (f). At 90 degree flexion of knee joint, both reconstructed ACL and cartilage of femoral condyle could be exposed in control group (g), PLLA reconstruction group (h), and BIO reconstruction group (i).

nanotechnologies allowing the construction of a geometrically defined microenvironment for cells at the nanoscale could induce specifically differentiation of MSCs. In others' researches, aligned nanofibrous scaffolds can induce MSCs to differentiate into ligament, tendon fibroblasts, or fibrochondrocytes [25–27]. In our and others' research, lattice-like nanofibrous meshes can induce osteogenic differentiation of MSCs, which is more important in ligament-bone healing, through integrin signaling *in vitro* [28]. So we testified it by these *in vivo* experiments. Histological staining indicated

a fibrous tissue connection of ligament to bone in control group with tendon grafts only, while in PLLA scaffold groups with or without peptide there was fibrocartilage formation at different levels. This was confirmed by specific stain of collagen type I, II, and III. It has been known that normal ligament and bone were mainly composed of type I collagen while repaired scar tissue was mainly made up of type III collagen. In control group, the insertion site was filled with disorderly arranged collagen III and I which formed an indirect junction. That coincided with early stage healing of

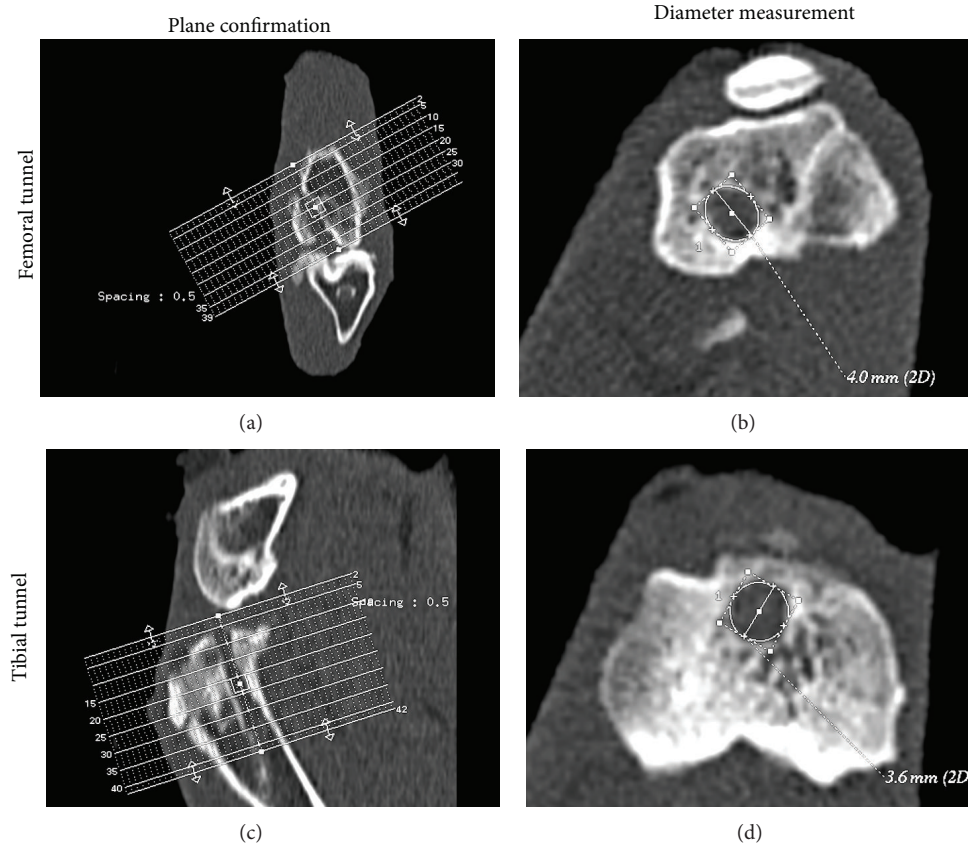


FIGURE 4: Femoral and tibial tunnels measured by CT scanning. Scanning plane confirmed in femora (a) and tibia (c). Minimum diameter of bone tunnel was measured in cross-section of femoral (b) or tibial (d) tunnel. Spacing between cross-sections was 0.5 mm.

ligament to bone in clinic [29], while at insertion sites of BIO reconstruction groups, chondrocytes and collagen type II were found indicating a process of endochondral ossification.

Mechanical property is another key point in early healing of ACL reconstruction. After surgery the ligament bone healing process needs more than a year in clinic. During this time, patients are not allowed to participate in strenuous exercise. And the mechanical properties during this time are important for prospective knee joint stability. In our study, at 3 months after surgery, mechanical properties of substitution complex were significantly different among 3 groups. Failure load of complexes in both PLLA group and BIO group was significantly higher than that in control group. But only in BIO group, all implantations were broken from the middle of tendons, while in other two groups there were specimens pulling out of bone tunnel. These results showed stronger early stage healing of ligament to bone using autologous tendon and PLLA scaffold with E7 peptide conjugation transplantation. In rabbit, the reported maximum ACL force is about 138.6% of body weight [30]. According to this data, the maximum native ACL force in this study is about 40 N (rabbit weight: 2.5–3.0 kg). The average failure load of control group was under 40 N. And the PLLA and BIO scaffold groups were higher than it, 82.59 ± 3.33 and 141.50 ± 3.90 N, respectively.

Results of bone tunnel measurement showed no significant statistical differences in PLLA group and BIO group at 1 and 3 months. Only in control group there was significant enlargement of bone tunnel. But the diameter was smaller in BIO scaffolds implantation groups than that in control group. Both results indicated that composite scaffold of lattice-like nanofibrous meshes can promote early stage healing of ligament-bone insertion site after ACL reconstruction of rabbit by narrowing bone tunnel and accelerating collagen structure remodeling to form direct junction.

5. Conclusions

In the present study, a substitution complex was designed by incorporating electrospinning nanofibrous meshes into autologous tendon. By modification of nanotopographical properties to lattice-like, the scaffold was suitable for MSCs proliferation, osteogenic differentiation, and active function. To absorb native MSCs from bone marrow, MSCs specific affinity peptide E7 was conjugated to nanofibrous meshes. After implantation of grafts for 3 months, the regenerated ligament-bone insertion exhibited abundant ECM (collagen I, II, and III) and fibrocartilage growth. The tensile strength of substitution complex was shown to be better than control. The findings of this study imply that nanofibrous scaffold with specific MSCs affinity peptide has great potentials

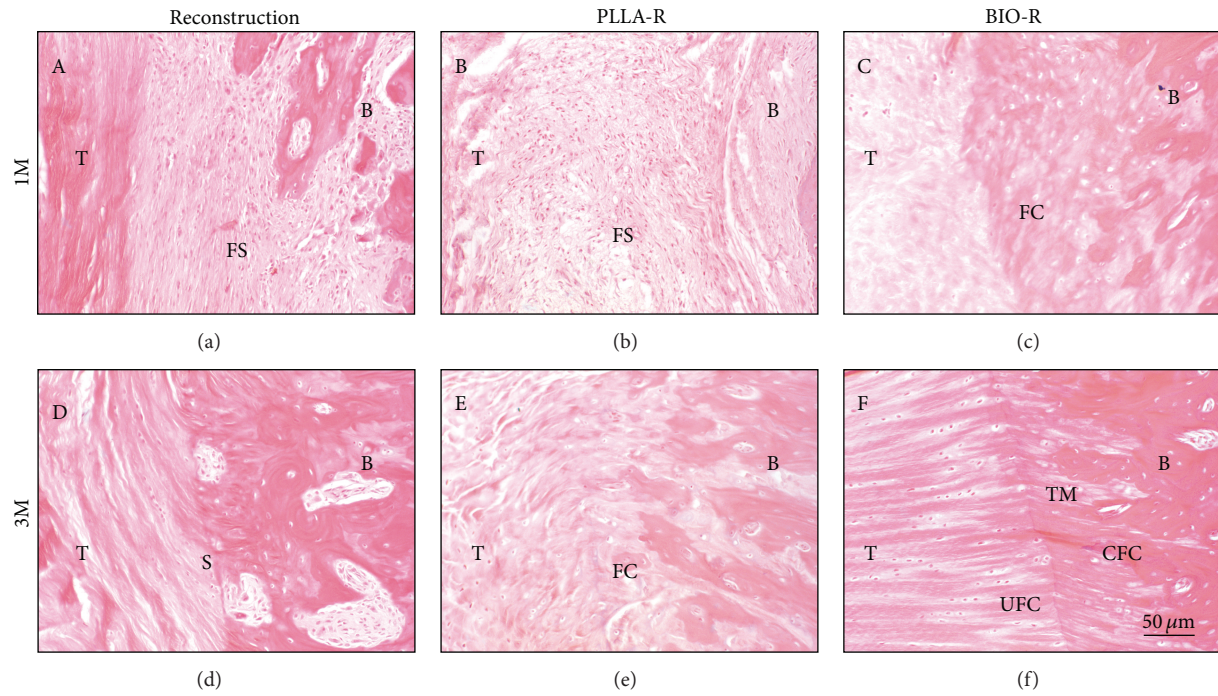


FIGURE 5: Histological assessment of ligament-bone insertion at 1 and 3 months after reconstruction surgery. H-E staining indicated connective tissues growing in ligament-bone insertion of control group, PLLA reconstruction group, and BIO reconstruction group at 1 month ((a)–(c)) and 3 months ((d)–(f)). Magnification: 200x. T: tendon; B: bone; FS: fibrous synovium; FC: fibrocartilage; S: Sharpey’s fiber; UFC: uncalcified fibrocartilage; CFC: calcified fibrocartilage; TM: tide line mark.

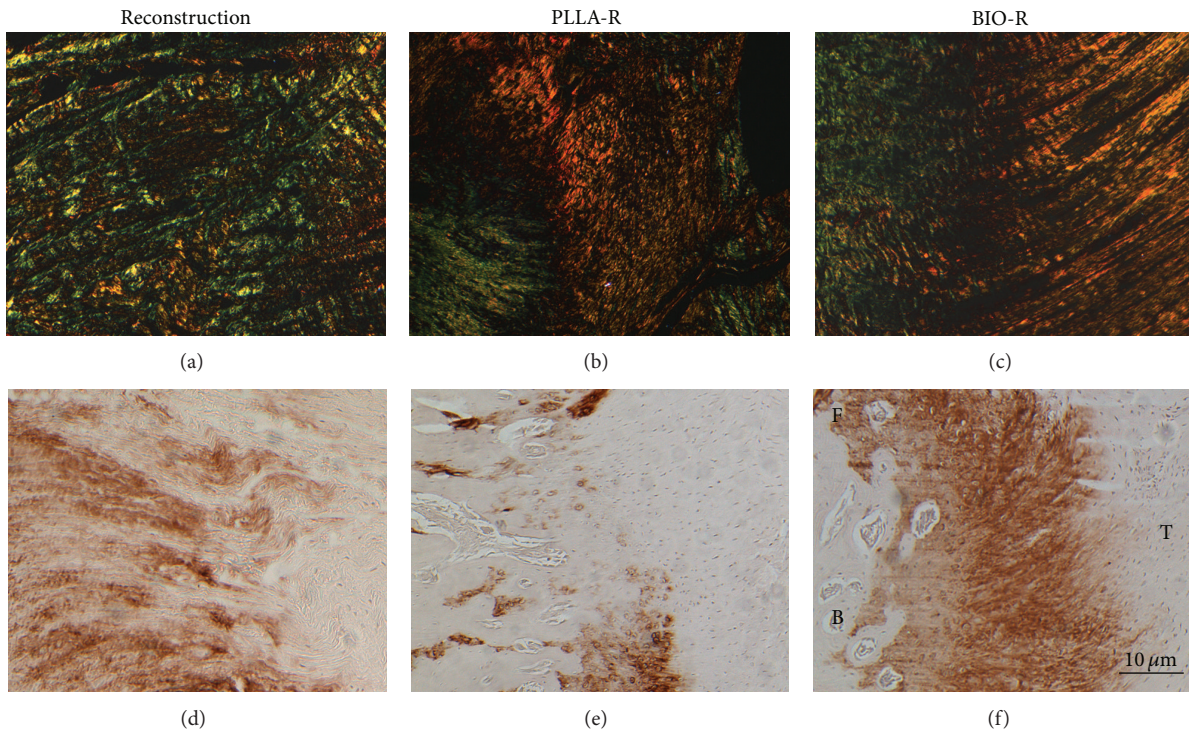


FIGURE 6: Sirius red and immunohistochemical staining of ligament-bone insertion at 3 months after ACL reconstruction surgery. Sirius red staining observed by polarized light microscope indicated distribution of collagen type I (red) and III (green) of control group, PLLA reconstruction group, and BIO reconstruction group ((a)–(c)). Specific immunohistochemical staining showing distribution of collagen type II at ligament-bone insertion in 3 groups ((d)–(f)). Magnification: 100x. T: tendon; B: bone.

in accelerating ligament-bone healing process after ACL reconstruction.

Conflict of Interests

All authors declare that there is no conflict of interests regarding the publication of this paper.

Acknowledgments

This work was supported by the National Natural Science Foundation of China (Grant nos. 81171726, 81101390), the National Basic Research Program of China (2012CB933903), and the China Postdoctoral Science Foundation.

References

- [1] M. M. Stevens and J. H. George, "Exploring and engineering the cell surface interface," *Science*, vol. 310, no. 5751, pp. 1135–1138, 2005.
- [2] Y. Z. Zhang, B. Su, J. Venugopal, S. Ramakrishna, and C. T. Lim, "Biomimetic and bioactive nanofibrous scaffolds from electrospun composite nanofibers," *International Journal of Nanomedicine*, vol. 2, no. 4, pp. 623–638, 2007.
- [3] C. K. Kuo, J. E. Marturano, and R. S. Tuan, "Novel strategies in tendon and ligament tissue engineering: advanced biomaterials and regeneration motifs," *Sports Medicine, Arthroscopy, Rehabilitation, Therapy and Technology*, vol. 2, article 20, 2010.
- [4] S. Sahoo, J. G. Cho-Hong, and T. Siew-Lok, "Development of hybrid polymer scaffolds for potential applications in ligament and tendon tissue engineering," *Biomedical Materials*, vol. 2, no. 3, article 001, pp. 169–173, 2007.
- [5] K. R. Reinhardt, I. Hetsroni, and R. G. Marx, "Graft selection for anterior cruciate ligament reconstruction: a level I systematic review comparing failure rates and functional outcomes," *Orthopedic Clinics of North America*, vol. 41, no. 2, pp. 249–262, 2010.
- [6] F. A. Petrigliano, D. R. McAllister, and B. M. Wu, "Tissue engineering for anterior cruciate ligament reconstruction: a review of current strategies," *Arthroscopy*, vol. 22, no. 4, pp. 441–451, 2006.
- [7] E. M. Horwitz, K. Le Blanc, M. Dominici et al., "Clarification of the nomenclature for MSC: the International Society for Cellular Therapy position statement," *Cytotherapy*, vol. 7, no. 5, pp. 393–395, 2005.
- [8] M. F. Pittenger, A. M. Mackay, S. C. Beck et al., "Multilineage potential of adult human mesenchymal stem cells," *Science*, vol. 284, no. 5411, pp. 143–147, 1999.
- [9] A. I. Caplan and D. Correa, "The MSC: an injury drugstore," *Cell Stem Cell*, vol. 9, no. 1, pp. 11–15, 2011.
- [10] J. M. Karp and G. S. Leng Teo, "Mesenchymal stem cell homing: the devil is in the details," *Cell Stem Cell*, vol. 4, no. 3, pp. 206–216, 2009.
- [11] Z. Shao, X. Zhang, Y. Pi et al., "Polycaprolactone electrospun mesh conjugated with an MSC affinity peptide for MSC homing in vivo," *Biomaterials*, vol. 33, no. 12, pp. 3375–3387, 2012.
- [12] J. Buschmann, L. Harter, S. Gao et al., "Tissue engineered bone grafts based on biomimetic nanocomposite PLGA/amorphous calcium phosphate scaffold and human adipose-derived stem cells," *Injury*, vol. 43, no. 10, pp. 1689–1697, 2012.
- [13] N. Hild, O. D. Schneider, D. Mohn et al., "Two-layer membranes of calcium phosphate/collagen/PLGA nanofibres: in vitro biomineralisation and osteogenic differentiation of human mesenchymal stem cells," *Nanoscale*, vol. 3, no. 2, pp. 401–409, 2011.
- [14] M. D. Schofer, P. P. Roessler, J. Schaefer et al., "Electrospun plla nanofiber scaffolds and their use in combination with bmp-2 for reconstruction of bone defects," *PLoS ONE*, vol. 6, no. 9, Article ID e25462, 2011.
- [15] X. H. Zou, Y. L. Zhi, X. Chen et al., "Mesenchymal stem cell seeded knitted silk sling for the treatment of stress urinary incontinence," *Biomaterials*, vol. 31, no. 18, pp. 4872–4879, 2010.
- [16] M. J. Dalby, N. Gadegaard, R. Tare et al., "The control of human mesenchymal cell differentiation using nanoscale symmetry and disorder," *Nature Materials*, vol. 6, no. 12, pp. 997–1003, 2007.
- [17] J. Zhu, Q. Cai, X. Zhang et al., "Biological characteristics of mesenchymal stem cells grown on different topographical nanofibrous poly-L-lactide meshes," *Journal of Biomedical Nanotechnology*, vol. 9, no. 10, pp. 1757–1767, 2013.
- [18] Y. Pi, X. Zhang, J. Shi et al., "Targeted delivery of non-viral vectors to cartilage in vivo using a chondrocyte-homing peptide identified by phage display," *Biomaterials*, vol. 32, no. 26, pp. 6324–6332, 2011.
- [19] C. B. Ma, S. Kawamura, X.-H. Deng et al., "Bone morphogenetic proteins-signaling plays a role in tendon-to-bone healing: a study of rhBMP-2 and noggin," *The American Journal of Sports Medicine*, vol. 35, no. 4, pp. 597–604, 2007.
- [20] C. N. Manning, H. M. Kim, S. Sakiyama-Elbert, L. M. Galatz, N. Havlioglu, and S. Thomopoulos, "Sustained delivery of transforming growth factor beta three enhances tendon-to-bone healing in a rat model," *Journal of Orthopaedic Research*, vol. 29, no. 7, pp. 1099–1105, 2011.
- [21] X. Huangfu and J. Zhao, "Tendon-bone healing enhancement using injectable tricalcium phosphate in a dog anterior cruciate ligament Reconstruction Model," *Arthroscopy*, vol. 23, no. 5, pp. 455–462, 2007.
- [22] A. Bedi, D. Kovacevic, C. Hettrich et al., "The effect of matrix metalloproteinase inhibition on tendon-to-bone healing in a rotator cuff repair model," *Journal of Shoulder and Elbow Surgery*, vol. 19, no. 3, pp. 384–391, 2010.
- [23] L. V. Gulotta, D. Kovacevic, J. D. Packer, X. H. Deng, and S. A. Rodeo, "Bone marrow-derived mesenchymal stem cells transduced with scleraxis improve rotator cuff healing in a rat model," *The American Journal of Sports Medicine*, vol. 39, no. 6, pp. 1282–1289, 2011.
- [24] K. von der Mark, J. Park, S. Bauer, and P. Schmuki, "Nanoscale engineering of biomimetic surfaces: cues from the extracellular matrix," *Cell and Tissue Research*, vol. 339, no. 1, pp. 131–153, 2010.
- [25] T. K. H. Teh, S.-L. Toh, and J. C. H. Goh, "Aligned hybrid silk scaffold for enhanced differentiation of mesenchymal stem cells into ligament fibroblasts," *Tissue Engineering C*, vol. 17, no. 6, pp. 687–703, 2011.
- [26] Z. Yin, X. Chen, J. L. Chen et al., "The regulation of tendon stem cell differentiation by the alignment of nanofibers," *Biomaterials*, vol. 31, no. 8, pp. 2163–2175, 2010.
- [27] B. M. Baker, A. S. Nathan, A. O. Gee, and R. L. Mauck, "The influence of an aligned nanofibrous topography on human mesenchymal stem cell fibrochondrogenesis," *Biomaterials*, vol. 31, no. 24, pp. 6190–6200, 2010.

- [28] A. Martins, M. L. Alves da Silva, S. Faria, A. P. Marques, R. L. Reis, and N. M. Neves, "The influence of patterned nanofiber meshes on human mesenchymal stem cell osteogenesis," *Macromolecular Bioscience*, vol. 11, no. 7, pp. 978–987, 2011.
- [29] H. Robert, J. Es-Sayeh, D. Heymann, N. Passuti, S. Eloit, and E. Vaneenoge, "Hamstring insertion site healing after anterior cruciate ligament reconstruction in patients with symptomatic hardware or repeat rupture: a histologic study in 12 patients," *Arthroscopy*, vol. 19, no. 9, pp. 948–954, 2003.
- [30] D. L. Gushue, J. Houck, and A. L. Lerner, "Rabbit knee joint biomechanics: motion analysis and modeling of forces during hopping," *Journal of Orthopaedic Research*, vol. 23, no. 4, pp. 735–742, 2005.

Research Article

Enhanced Ca^{2+} Entry and Tyrosine Phosphorylation Mediate Nanostructure-Induced Endothelial Proliferation

Michaela Scherthaner,¹ Gerd Leitinger,² Heimo Wolinski,³
Sepp D. Kohlwein,³ Bettina Reisinger,⁴ Ruxandra-A. Barb,⁴
Wolfgang F. Graier,⁵ Johannes Heitz,⁴ and Klaus Groschner¹

¹ Institute of Biophysics, Medical University Graz, 8010 Graz, Austria

² Department of Cell Biology, Histology and Embryology, Core Facility Ultrastructure Analysis, Center for Medical Research, Medical University Graz, 8010 Graz, Austria

³ Institute of Molecular Biosciences, University of Graz, 8010 Graz, Austria

⁴ Institute of Applied Physics, Johannes Kepler University Linz, 4040 Linz, Austria

⁵ Institute of Molecular Biology and Biochemistry, Medical University Graz, 8010 Graz, Austria

Correspondence should be addressed to Johannes Heitz; johannes.heitz@jku.at
and Klaus Groschner; klaus.groschner@medunigraz.at

Received 23 August 2013; Accepted 6 October 2013

Academic Editor: Krasimir Vasilev

Copyright © 2013 Michaela Scherthaner et al. This is an open access article distributed under the Creative Commons Attribution License, which permits unrestricted use, distribution, and reproduction in any medium, provided the original work is properly cited.

Nanostructured substrates have been recognized to initiate transcriptional programs promoting cell proliferation. Specifically β -catenin has been identified as transcriptional regulator, activated by adhesion to nanostructures. We set out to identify processes responsible for nanostructure-induced endothelial β -catenin signaling. Transmission electron microscopy (TEM) of cell contacts to differently sized polyethylene terephthalate (PET) surface structures (ripples with 250 to 300 nm and walls with 1.5 μm periodicity) revealed different patterns of cell-substrate interactions. Cell adhesion to ripples occurred exclusively on ripple peaks, while cells were attached to walls continuously. The Src kinase inhibitor PP2 was active only in cells grown on ripples, while the Abl inhibitors dasatinib and imatinib suppressed β -catenin translocation on both structures. Moreover, Gd^{3+} sensitive Ca^{2+} entry was observed in response to mechanical stimulation or Ca^{2+} store depletion exclusively in cells grown on ripples. Both PP2 and Gd^{3+} suppressed β -catenin nuclear translocation along with proliferation in cells grown on ripples but not on walls. Our results suggest that adhesion of endothelial cells to ripple structured PET induces highly specific, interface topology-dependent changes in cellular signalling, characterized by promotion of Gd^{3+} -sensitive Ca^{2+} entry and Src/Abl activation. We propose that these signaling events are crucially involved in nanostructure-induced promotion of cell proliferation.

1. Introduction

Understanding the basic mechanisms by which cells recognize and respond to specific surface topologies is of outstanding importance for the development of novel biomaterials to advance tissue engineering applications. We and others have demonstrated that growth of vascular endothelial cells is governed not only by the type of culture substrate and its surface chemistry but also by surface topography [1–3]. Many studies have focused on optimisation of the biocompatibility of polymer substrates to improve cell adhesion and promote

proliferation [4], while mechanisms underlying the control of cell functions by nanoarchitected substrates remain elusive.

Micro- and nanostructures on polyethylene terephthalate (PET) substrates produced by laser irradiation were recently discovered to activate endothelial β -catenin signaling which leads to nuclear translocation of the transcriptionally active protein and enhanced proliferation of human microvascular endothelial cells (HMEC). The extent of these effects was dependent on size and periodicity of surface structure topography. In particular, transcription levels of the β -catenin target gene cyclin D1 were significantly different on ripples

and walls. This observation led to the hypothesis that cell growth on various surface structures on PET substrates differentially activates specific pools of β -catenin [5].

β -catenin is an important signaling molecule in endothelial cells and part of adherens junctions. When released from contact sites or as newly synthesized protein, cytosolic β -catenin is phosphorylated by a destruction complex that includes glycogen synthase kinase 3 β (GSK3 β) which marks the protein for degradation by the proteasome [6]. Upon inhibition of this destruction, complex β -catenin accumulates and translocates to the nucleus where it binds to transcription factors and induces target gene transcription [7–10]. β -catenin possesses a multitude of regulatory phosphorylation sites, which are substrates of serine/threonine and tyrosine kinases [11]. Cell attachment to the extracellular matrix (ECM) can initiate clustering of integrins and activation of downstream targets such as integrin-linked kinase (ILK) [12], focal adhesion kinase (FAK) [13], or Src kinases [14, 15]. Src and FAK are able to phosphorylate β -catenin directly [16–18] or block its proteasomal degradation by inhibiting its phosphorylation by GSK3 β via the phosphatidylinositol 3-kinase (PI3K)/Akt pathway [19]. Phosphorylation of FAK and β -catenin may also be controlled by stimulation of mechanosensitive ion channels [20] as well as by mechanical stress, which leads to enhanced calcium influx downstream of Src [21].

In this study, we set out to identify cellular mechanisms that trigger β -catenin translocation and consequently proliferation in endothelial cells growing on nanopatterned substrates. We demonstrate that adhesion of endothelial cells to nanostructured PET substrates activates β -catenin by enhanced tyrosine phosphorylation and calcium signaling through mechanosensitive ion channels.

2. Material and Methods

Laser generation and characterization of structured PET substrates, cell culture of HMEC, immunocytochemistry, and confocal microscopy were performed as described recently [5].

In short: for immunostainings, HMEC-1 cells [22, 23] were seeded on the different substrates and fixed and immunostained with the anti- β -catenin antibody (1:150, BD Biosciences), anti-Ki67 antibody (1:300, Abcam), anti-P397-FAK antibody (1:250, Abcam), or anti-VE-cadherin (1:150, BD Biosciences) after 48 h of culture. For the inhibitor experiments, inhibitors were added to the culture medium 6 h prior to fixation.

Nuclear to cytosolic ratios of β -catenin were determined by marking ROIs (regions of interest) in the phase contrast image for the nuclei and cytosols. The ROIs were then transferred to the corresponding fluorescence image and the mean fluorescence intensity for every ROI was determined, using Image J software. Finally, the ratio of nuclear to cytosolic intensity was calculated.

2.1. Reagents and Antibodies. All chemicals were purchased from Sigma Aldrich (Steinheim, Germany) unless otherwise

stated: anti-Ki67 (1:300, Abcam, Cambridge, MA), anti-Tyr397-FAK (1:250, Abcam), PP2 (4-amino-5-(4-chlorophenyl)-7-(dimethylethyl) pyrazolo[3,4-*d*]pyrimidine; Calbiochem/Merck, Darmstadt, Germany), imatinib (Cayman Chemical, Tallinn, Estonia), FuraRed AM (Molecular Probes, Life Technologies Corporation, UK), and BHQ (2,5-di-*t*-butyl-1,4-benzohydrochinone).

2.2. Transmission Electron Microscopy (TEM). Cells cultivated on the different substrates were embedded with a small piece of their substrate. For this, they were fixed in a mixture of 2% formaldehyde, 2.5% glutardialdehyde in 0.1 M sodium cacodylate buffer, pH 7.4 for 1 h at room temperature. They were then rinsed in the same buffer, treated with 2% osmium tetroxide (in the same buffer) for 1 h, rinsed, and dehydrated in a series of graded alcohols. They were then embedded in TAAB epoxy resin (TAAB laboratories Equipment Ltd, Aldermaston, UK) with propylene oxide as an intermediate. Sections of 70 nm thickness were counterstained with uranyl acetate and lead citrate and visualised using an FEI Tecnai 20 (FEI, Hillsboro, OR, USA) transmission electron microscope operated at 120 kV acceleration voltage. Electron micrographs were made with a Gatan Ultrascan 1000 CCD camera (Gatan, Inc, Pleasanton, CA, USA).

2.3. Measurement of Intracellular Calcium Levels Using FuraRed AM. Cells cultivated on the different substrates were loaded for 40 min at 37°C with FuraRed AM. Base levels of calcium content were recorded for 1 min before perfusion was started. Cells were continuously perfused with buffer containing 140 mM NaCl, 15 mM HEPES, 10 mM glucose, 2 mM MgCl₂, and 2 mM CaCl₂ and treated with 15 μ M 2,5-di-*t*-butyl-1,4-benzohydrochinone (BHQ) for 5 min as indicated. For preincubation, cells were treated with 10 μ M gadolinium chloride (Gd³⁺) for 6 h before the experiment was started, and Gd³⁺ was present throughout the experiment. Measurements were carried out on a Till iMIC microscope (Till Photonics, Gräfing, Germany).

3. Results

3.1. Ripples and Wall Structures Generate a Divergent Pattern of Physical Contact with the Basal Membrane of Endothelial Cells. Experiments were performed with HMEC cultured on two different types of structured PET surfaces representing distinct range of pattern size. Ripples characterized by a periodicity of 250 to 300 nm were compared to walls with a periodicity of 1.5 μ m [5]. Electron micrographs of these structures are shown in Figure 1. Flat, pristine PET was used as a control to evaluate potential effects induced by the polymer itself. Lower panel of Figure 1 shows TEM images of HMEC grown on the different nanoarchitectures with focus on the contact area between cell membranes and the surface of the substrate.

Contact between the basal membrane of the endothelial cells and flat, pristine PET surfaces is continuous and straight, whereas punctual contact sites are exclusively observed between the basal endothelial membrane and the peaks on

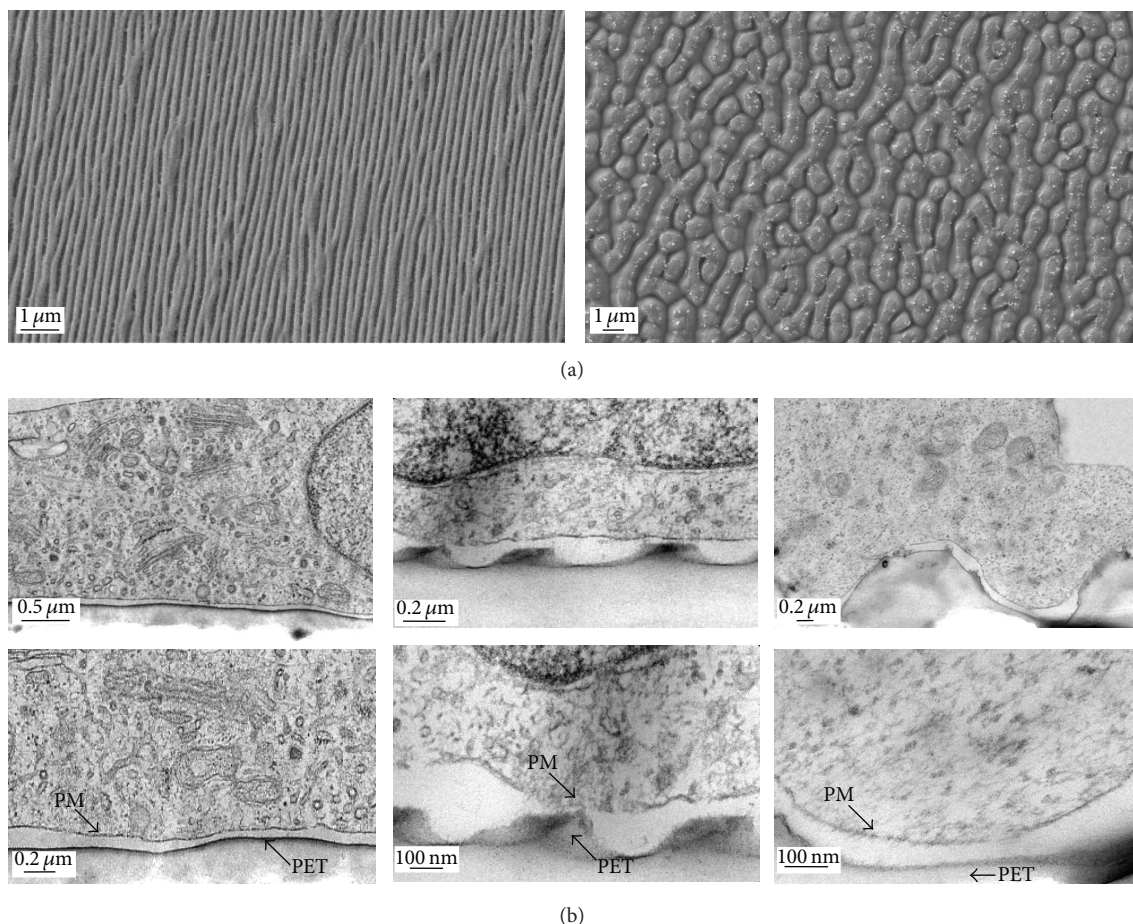


FIGURE 1: Electron microscopy of laser-irradiated PET substrates. Upper panel: SEM images of resulting structures after excimer laser irradiation of PET substrates. Left: ripples, 6000 pulses of linear polarized KrF laser radiation ($\lambda = 248$ nm) at a fluence of 9 mJ cm^{-2} . Right: walls, 30 pulses of ArF laser radiation ($\lambda = 193$ nm) at fluences of 30 mJ cm^{-2} . Lower panel: TEM images of HMEC grown on pristine PET (flat, left) or laser irradiated with surface topography (ripples, middle; walls, right); PM and arrow indicate basal plasma membrane; PET and arrow indicate border of PET substrate.

the ripple surface, and cells do not adhere to ripple valleys. In contrast, on wall structures, the basal plasma membrane was found continuously attached to the surface, thereby forming contact on peaks and in valleys of the structure. This observation suggests that divergent attachment architectures of endothelial membranes are generated by contact to these substrates, resulting in the initiation of divergent signaling pathways.

3.2. Promotion of β -Catenin Translocation by Ripple Structures Involves Tyrosine Phosphorylation. Divergent mechanisms of β -catenin activation by differently sized nanostructures were already suggested by the previously reported observation that both ripples and wall structures are capable of initiating nuclear translocation of β -catenin, albeit with divergent consequences for β -catenin target gene expression [5]. To analyse the role of tyrosine kinase activation in detail, we characterized transcriptional activation of cells grown on different surface structures in response to kinase inhibitors. Figures 2(a)–2(d) show inhibition of β -catenin nuclear translocation in HMEC cultured on the different substrates in the presence

of the tyrosine kinase inhibitors PP2 (50 nM), an inhibitor of the Src family of kinases [24], dasatinib ($3 \mu\text{M}$), which inhibits Src, ILK, and Abl kinases [25–27], and imatinib ($2 \mu\text{M}$), which inhibits Abl kinases only [28].

To quantify translocation levels, the nuclear to cytosolic ratios of β -catenin immunofluorescence were calculated (Figure 2(e)). Translocation on ripples was significantly reduced by all three inhibitors, indicating that both Src as well as Abl kinases are essential for that process. The translocation on wall structures, by contrast, was sensitive to Abl kinase inhibition by dasatinib and imatinib, while PP2 was barely effective. These findings further strengthen our hypothesis that differently sized structures activate β -catenin signaling by divergent mechanisms involving alternative tyrosine kinases.

To test for involvement of focal adhesion kinase (FAK) which is phosphorylated on Tyr397 in response to integrin signaling as a potential initial step of enhanced tyrosine phosphorylation, we immunostained the cells with an antibody against the active form of FAK (Figure 3). Interestingly, we observed high immunoreactivity on flat, pristine PET and on

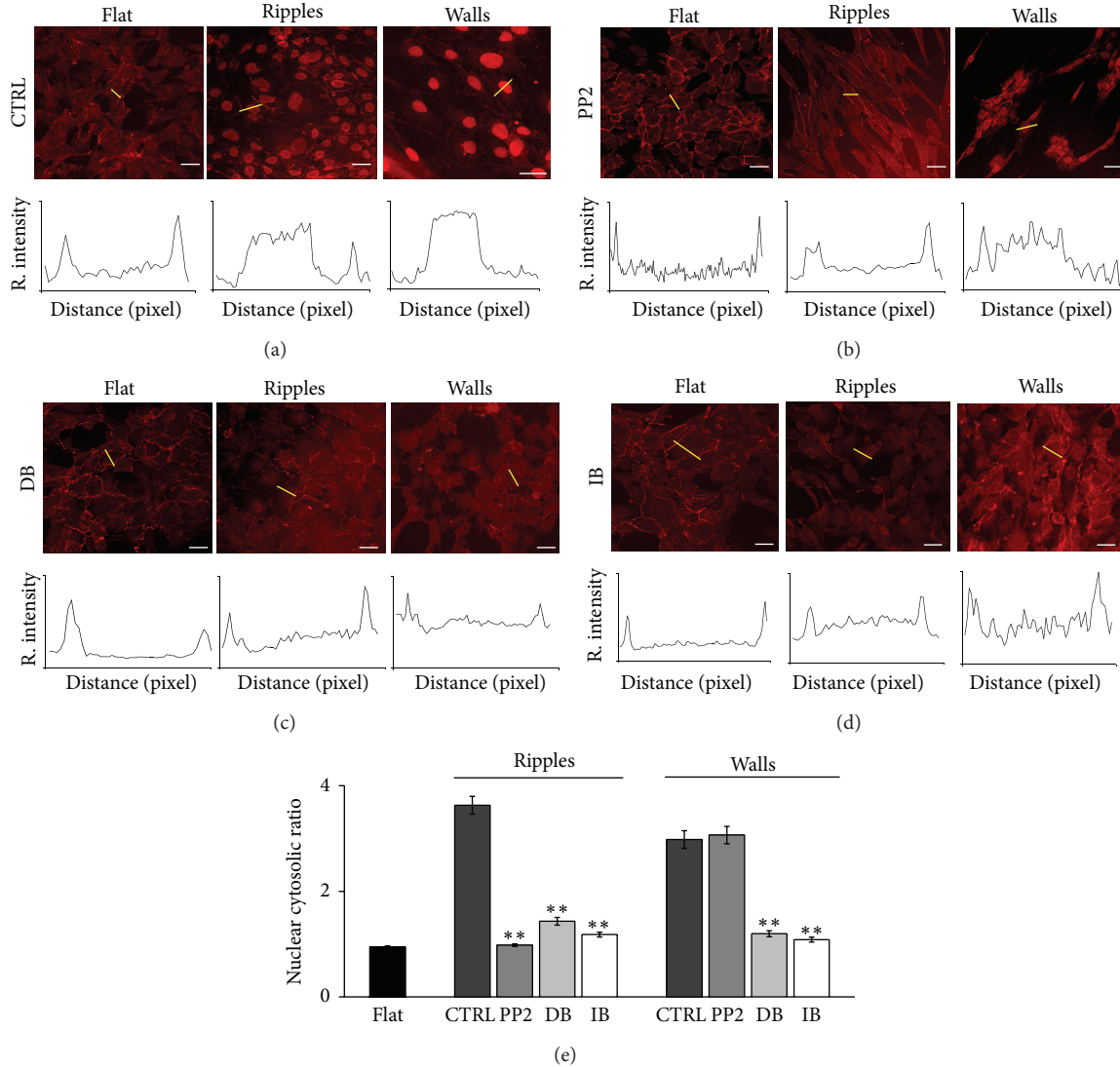


FIGURE 2: Nanostructure-induced β -catenin translocation involves tyrosine phosphorylations. Confocal microscopy images of β -catenin distribution (red) in HMEC grown on the indicated substrate. Lower panels: representative profile plots along the indicated cell section (yellow line) show intensity distribution of β -catenin as relative immunofluorescence intensity (y -axis) along the distance in pixel (x -axis). Scale bars represent $10 \mu\text{m}$. CTRL (a); for inhibitor experiments, cells were incubated for 6 h at 37°C with 50 nM PP2 (b), $3 \mu\text{M}$ dasatinib (DB, (c)), $2 \mu\text{M}$ imatinib (IB, (d)). Bar graphs representing the nuclear to cytosolic ratio of β -catenin immunofluorescence (e); values \pm SEM; $n \geq 60$ cells from 3 independent experiments, calculated from 3 different images of each experiment; * $P < 0.05$; ** $P < 0.001$ compared to CTRL.

ripples, but none on walls. This result further supports the concept that different molecular mechanisms of transcriptional control are initiated by ripples and walls structures. Nonetheless, activation of FAK alone is not sufficient to explain the observed enhancement of β -catenin translocation and proliferation by cell adhesion to ripples.

3.3. Divergent Impact of Ripples and Wall Structures on Endothelial Ca^{2+} Signaling—Evidence for Promotion of Mechanosensitive Ca^{2+} Entry by Ripples. Another potential mechanism associated with enhanced tyrosine phosphorylation is Ca^{2+} signaling. Ca^{2+} entry was reported to control Src activity and Src phosphorylation, which appears as

a hallmark of endothelial cells grown on ripples. In turn, Src was found essential for certain mechanisms of Ca^{2+} entry [19, 21, 29]. This evidence and the observed differences in cell substrate adhesion architecture (Figure 1(b)) led us to hypothesize that mechanosensitive Ca^{2+} entry may be affected in a specific manner by structured PET substrates. To test our hypothesis, we stimulated cells grown on the different substrates by perfusion-induced shear stress and by depletion of intracellular stores with BHQ as a selective inhibitor of sarcoplasmic/endoplasmic reticulum calcium ATPase (SERCA), [30]. Involvement of mechanosensitive and/or store-operated Ca^{2+} entry (SOCE) was tested with Gd^{3+} , a common blocker of these cation channels [31, 32].

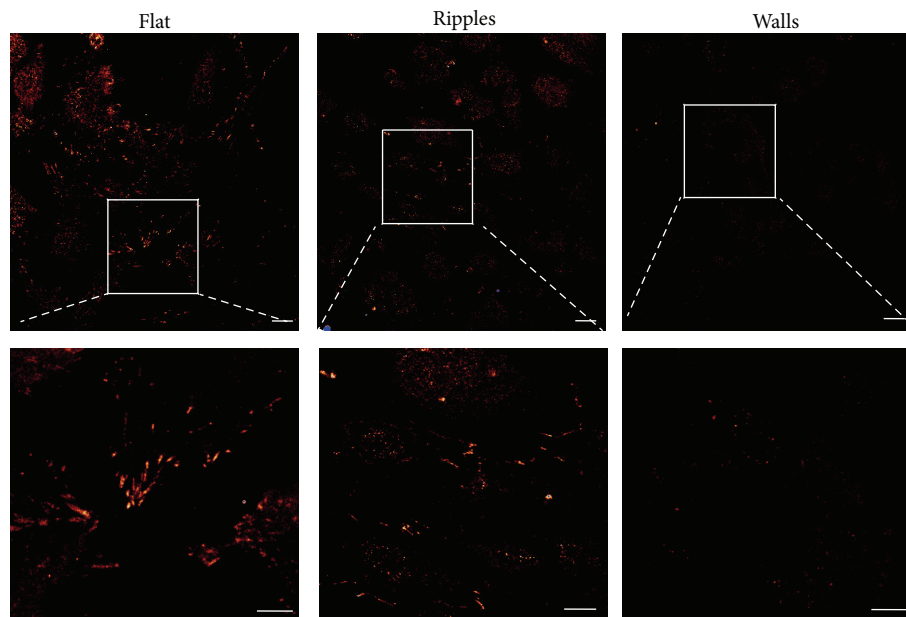


FIGURE 3: Activation of focal adhesion kinase (FAK) is observed on flat and ripples but not on wall structures. Confocal microscopy images show HMEC grown on the indicated substrate, fixed and immunostained with an antibody against the active form of FAK phosphorylated on Tyr397 (red). White square indicates the magnified part (lower panel, microscopic zoom in). Scale bars represent $10\ \mu\text{m}$. In Supplementary Figure 2 available online at <http://dx.doi.org/10.1155/2013/251063>, the images of Figure 3 are shown at enhanced brightness to visualize cell borders and the cell number.

We observed enhanced content of Ca^{2+} stores by FuraRed AM measurements in cells cultured on ripples as compared to wall structures or flat substrate. Our experiments revealed significant differences in mechanosensitive Ca^{2+} signaling. Figure 4(a) illustrates basal levels of cytosolic calcium recorded before and after activation of flow-induced shear by perfusion (2 min). Flow-induced mechanical stress initiated a significant elevation of cytosolic Ca^{2+} in cells on all three substrates. When cells were preincubated with Gd^{3+} ($10\ \mu\text{M}$), flow-induced Ca^{2+} elevation on ripples and on flat substrates was abolished, while Ca^{2+} signals on cells attached to walls remained elevated. Another difference in endothelial Ca^{2+} signaling was observed when Ca^{2+} entry was promoted by BHQ-induced store depletion. BHQ elicited a profound cellular Ca^{2+} response in cells grown on ripples (Figures 4(b) and 4(c)), while cells grown on walls displayed a modest response to BHQ. Gd^{3+} sensitivity of Ca^{2+} entry into cells grown on ripples was also clearly evident during stimulation with BHQ. Collectively, these results suggest that mechanosensitive channels, which may be linked to Src kinase activation, govern Ca^{2+} homeostasis in cells grown on ripples.

3.4. Gd^{3+} Inhibits β -Catenin Translocation and Proliferation Induced by Ripples but Not by Wall Structures. The observation of Gd^{3+} sensitive calcium signaling on ripples prompted us to test whether Gd^{3+} also had an impact on nuclear translocation of β -catenin. In fact, preincubation with Gd^{3+} ($10\ \mu\text{M}$) for 6 h significantly reduced nuclear translocation of cells grown on ripples, while there was no effect observed in cells grown on wall structures (Figure 5).

As reported recently [5], culture of HMEC on ripples as well as on wall structures results in enhanced proliferation levels. To investigate the correlation of nuclear β -catenin translocation and enhanced proliferation, we tested the effects of Gd^{3+} and tyrosine kinase inhibition by PP2, dasatinib, and imatinib on the expression levels of the proliferation marker Ki67.

By preventing the translocation of β -catenin, either by inhibiting tyrosine phosphorylation or blocking the mechanosensitive ion channels, proliferation in cells grown on ripples was significantly reduced down to levels in cells grown on flat substrates. Src kinase inhibition again showed no effect on cells grown on wall structures, whereas Abl kinase inhibition led to reduced cell proliferation. Consistent with the observed differences in Ca^{2+} signaling, Gd^{3+} failed to inhibit proliferation in cells adherent to walls (Figure 6).

4. Discussion

4.1. Periodicity of Substrate Topography Determines Basal Membrane Architecture. Increasing evidence suggests that cell proliferation is strongly affected by specific interactions with the culture substrate. Topographical characteristics appear as important determinants of this interaction and govern cell growth through multiple signaling pathways.

Our results from Figure 1(b) are in line with findings of Teixeira et al. [33], who reported that lamellipodia of cells were able to adhere to valleys of grooves with a width of $2.1\ \mu\text{m}$ but not with narrower valleys only $330\ \text{nm}$ wide. They further observed that cells could be elongated and aligned along the structures without focal adhesions and suggested

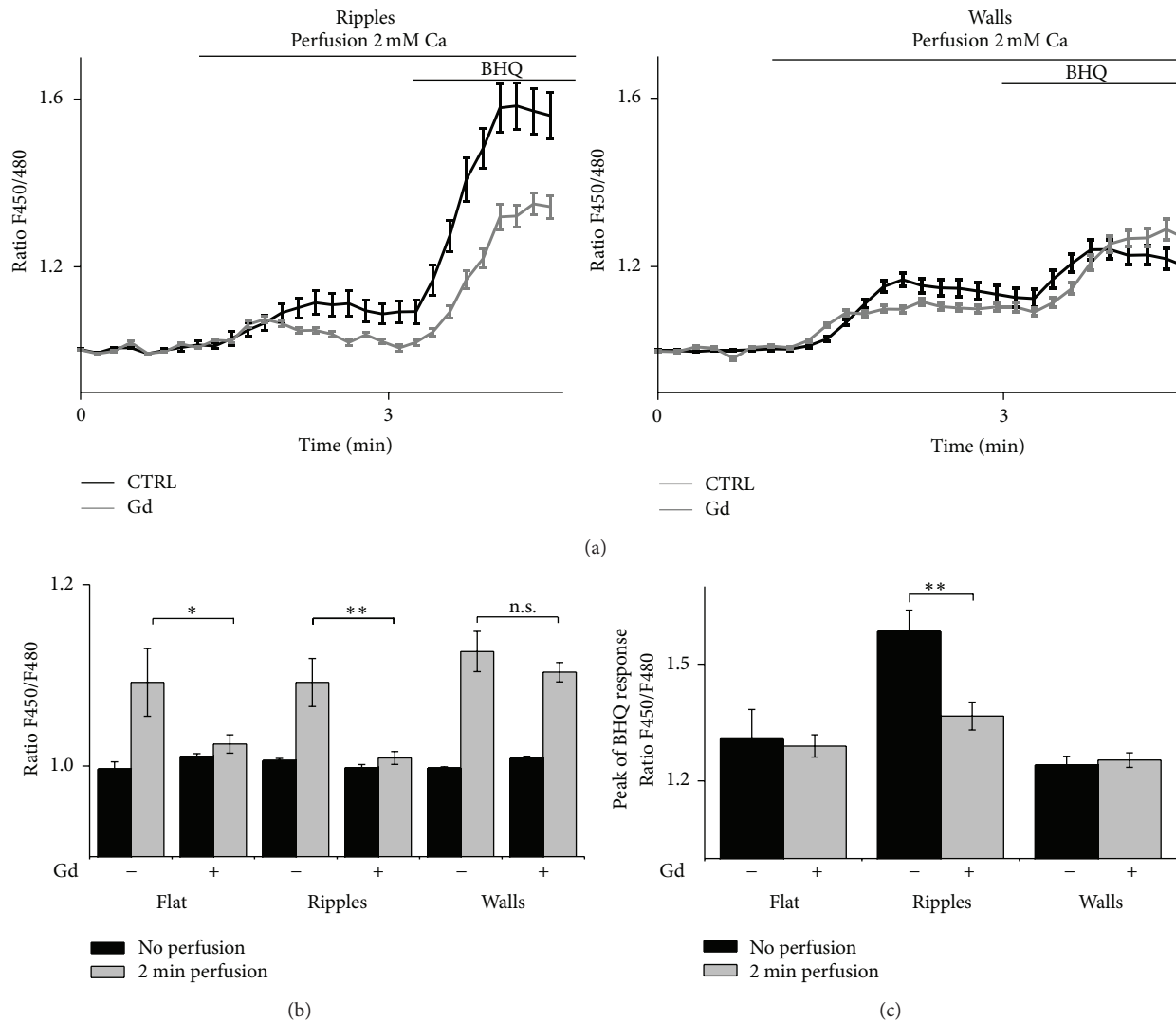


FIGURE 4: Ripples structures promote a Gd^{3+} -sensitive Ca^{2+} entry pathway in endothelial cells. Substrates were fixed in a perfusion chamber and after recording the base line for 1 min perfusion with 2 mM calcium buffer was started. All experiments were carried out with or without Gd^{3+} preincubation for 6 h. Then, 15 μM BHQ was applied. Time course of FuraRed AM measurement of cells grown on the indicated substrate is shown in (a). Data are calculated in 10 sec intervals and averaged. Bar graphs show calcium levels at 30 sec (no perfusion) and after 2 min perfusion (b). The maximum peak after 15 μM BHQ stimulation in CTRL and preincubated cells is shown in (c). $n \geq 40$ cells from 3 independent experiments; values for FuraRed AM ratios \pm SEM; * $P < 0.05$; ** $P < 0.001$; n.s. = not significant.

that the assembly of these structures was not necessary for contact guidance of epithelial cells. Consistent with these morphological observations, we failed to detect formation of focal adhesions in terms of phosphorylated FAK (Tyr397) when cells were grown on wall structures (Figure 3), which substantially promote alignment of HMEC [5]. Ohara and Buck [34] proposed that focal adhesion contacts are constrained to the peaks of closely spaced nanostructures since limited flexibility of the cell membrane leads to bridging the valleys. Thus focal adhesions were located almost exclusively on top of ridges. This is consistent with our observations that cells growing on ripples had contact to the structure on peaks only (Figure 1(b)).

We conclude that spacing of parallel surface structures is an essential determinant of cell-substrate contact and of

formation of focal adhesions. Our results clearly demonstrate size-dependent differences in endothelial cell-substrate interactions and formation of adhesion contacts on nanostructured PET.

4.2. Role of Tyrosine Kinase Phosphorylations in β -Catenin Nuclear Translocation. Recently, β -catenin was identified as a key player in nanostructure-induced control of cell proliferation [5]. The functions of β -catenin correspond to certain subcellular localizations of the protein and are governed by a multitude of regulatory phosphorylations [11]. ILK, FAK as well as Src kinases are able to phosphorylate β -catenin directly and/or influence the cytoplasmic availability of β -catenin by phosphorylation of GSK3 β or, even more indirectly, via impact on the PI3K/Akt pathway [16–18, 35].

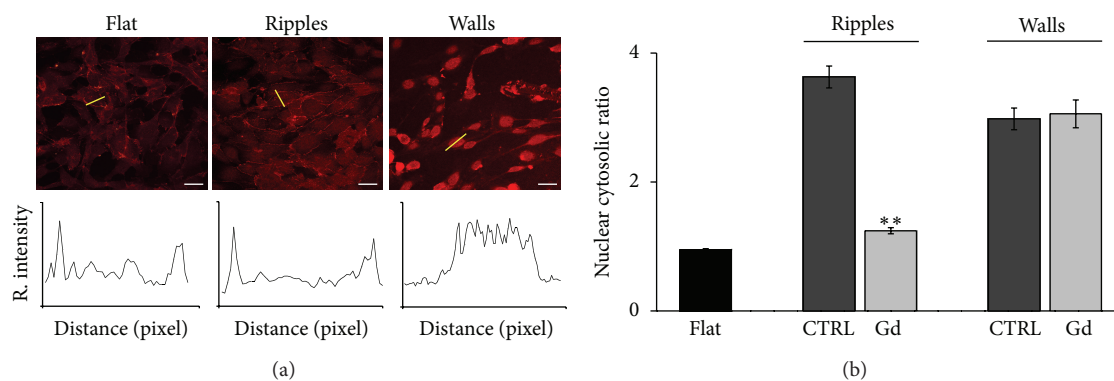


FIGURE 5: Nuclear translocation of β -catenin on ripples is sensitive to Gd^{3+} . Confocal microscopy images of β -catenin distribution (red) in HMEC grown on the indicated substrate. Cells were incubated with $10 \mu M Gd^{3+}$ for 6 h at $37^\circ C$ (a). Lower panels: representative profile plots along the indicated cell section (yellow line) show intensity distribution of β -catenin as relative immunofluorescence intensity (y-axis) along the distance in pixel (x-axis). Scale bars represent $10 \mu m$. Bar graphs representing the nuclear to cytosolic ratio of β -catenin immunofluorescence (b); values \pm SEM; $n \geq 60$ from 3 independent experiments, calculated from 3 different images of each experiment; * $P < 0.05$; ** $P < 0.001$ compared to CTRL.

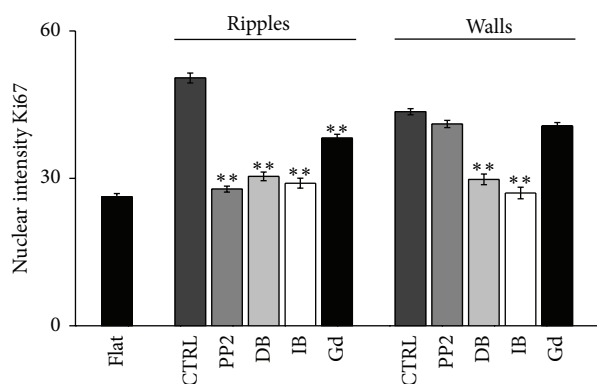


FIGURE 6: Sensitivity of endothelial proliferation on ripples and wall structures to kinase inhibitors, and Gd^{3+} . Bar graphs represent the nuclear immunofluorescence intensity levels of the proliferation marker Ki67. Cells were grown on the indicated substrate and incubated for 6 h at $37^\circ C$ with $50 nM PP2$, $3 \mu M$ dasatinib (DB), $2 \mu M$ imatinib (IB), $10 \mu M Gd^{3+}$ (Gd), or without inhibitor for control (Values \pm SEM; $n \geq 120$ from 3 independent experiments, calculated from 3 different images of each experiment; * $P < 0.05$; ** $P < 0.001$ compared to CTRL) (representative confocal images of HMEC immunolabeled with an antibody against Ki67 are shown in Supplementary Figure 3).

Our results provide compelling evidence for the induction of divergent β -catenin phosphorylation states by differently sized micro/nanostructures. We cannot exclude that β -catenin distribution is in part disturbed via a reduction of junctional stability. Nonetheless, HMEC cells are able to form mature cell-cell adhesions when grown on nanostructured surfaces (Supplementary Figure 1). Based on our pharmacological analysis, it is suggested that the mechanism which initiates β -catenin nuclear translocation on ripples involves both Src and Abl kinases, while Src kinases are not involved on wall structures. An interference of these mechanisms with the Wnt/ β -catenin pathway is likely and requires further investigation.

4.3. Periodicity of Substrate Topography Determines Calcium Signaling. Numerous studies reported the involvement of Src kinase signaling in cyclin D1 regulation, cell cycle progression and proliferation [36–38]. Src activity and phosphorylation are strongly dependent on Ca^{2+} [19, 21, 29]. Moreover, it has been reported that the activity of Src, in turn, is able to promote SOCE fluxes [39–41], which represent an important Ca^{2+} entry mechanism in endothelial cells relevant for proliferation [42]. Mechanical stress is another factor reported to induce Ca^{2+} influx downstream of Src [21].

Interestingly, we observed a similar level of shear-induced Ca^{2+} elevation on all three substrates. Nonetheless, on flat substrates and on ripples, this Ca^{2+} influx was abolished by Gd^{3+} , a common blocker of mechanosensitive cation channels, while Gd^{3+} failed to suppress flow-induced Ca^{2+} rises in cells grown on wall structures. This observation further substantiates the divergent signaling characteristics of cells grown on the different surface topologies. Our results indicate the expression of a particular Gd^{3+} insensitive subset of mechanosensitive channels in cells grown on wall structures. It is tempting to speculate that such a Gd^{3+} -insensitive subset is formed by K^+ channels [32], which may confer hyperpolarisation of the plasma membrane and thereby promote Ca^{2+} influx into endothelial cells [43].

Endothelial cells grown on ripples display a substantially enhanced SOCE. This phenomenon may well be related to the enhanced Src activity [39–41, 44]. It is important to note that Src and Ca^{2+} entry are mutually amplifying signaling processes, with Src activity being Ca^{2+} dependent and SOCE being promoted by Src tyrosine phosphorylation [19, 21, 39–41]. At present, we cannot tell which of these processes is initially triggered by the substrate topology. Nonetheless, it appears conceivable to conclude a feed-forward interaction between tyrosine phosphorylation and SOCE being involved in the effects of ripple structures on endothelial gene transcription. Concomitantly enhanced SOCE and Src activity are likely to generate a positive feedback mechanism that promotes β -catenin tyrosine phosphorylation (Figure 7).

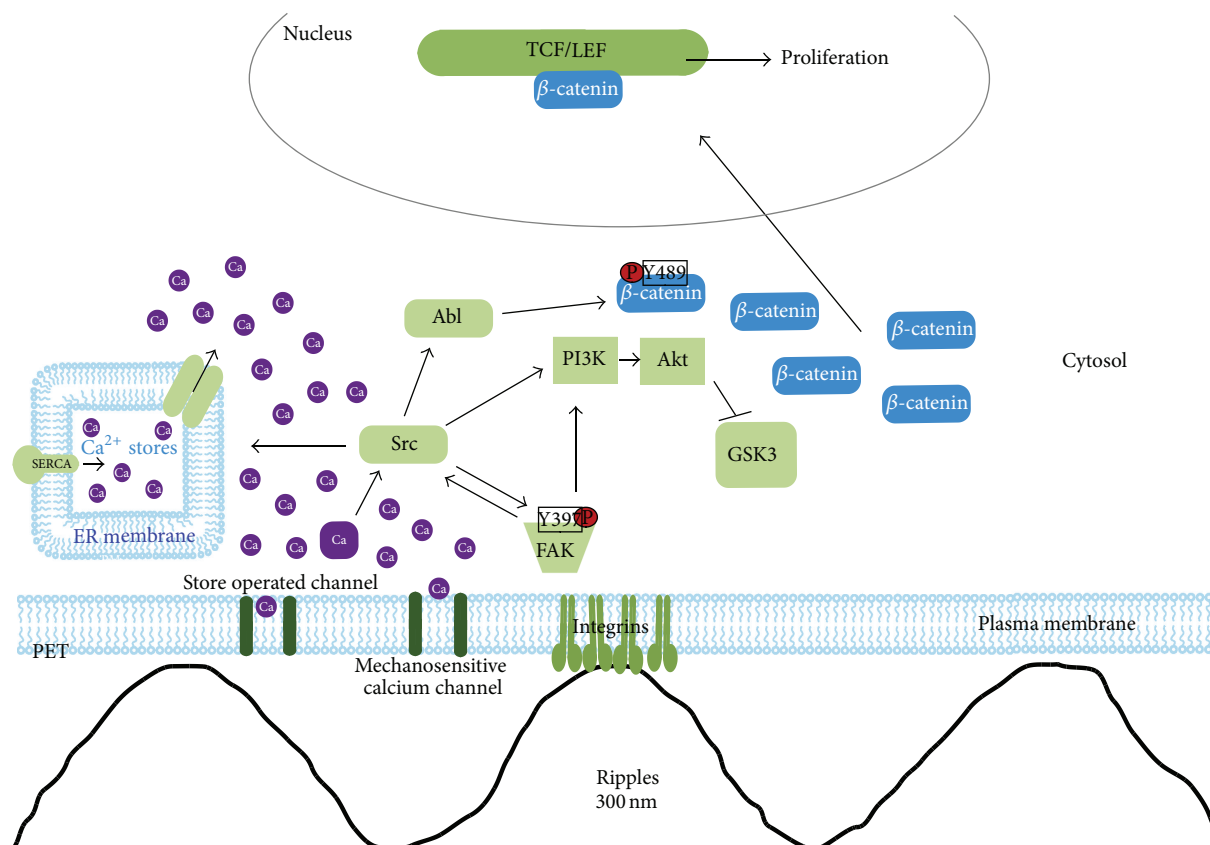


FIGURE 7: Scheme pathway. TCF: T-cell factor; LEF: lymphoid enhancer factor; SERCA: sarcoplasmic/endoplasmic reticulum ATPase; PI3K: phosphatidylinositol 3 kinase; GSK3 β : glycogen synthase kinase 3 β ; Ca: calcium.

4.4. Tyrosine Phosphorylation and Calcium Signaling Are Essential for Nanostructure-Induced Cell Proliferation. Our experiments identified Src and SOCE activation as key upstream signals involved in β -catenin activation in endothelial cells grown on ripples, while these processes appear irrelevant for the effects of wall structures. Consistently, inhibition of Src kinases by PP2 or inhibition of Ca^{2+} entry by Gd^{3+} had no effect on expression of the proliferation marker Ki67 in cells adherent to wall structures but significantly suppressed Ki67 expression in cells grown on ripples. Inhibition of Abl kinases by dasatinib and imatinib on the other hand elicited profound effects on proliferation in cells grown on both types of structures.

In aggregate, our results suggest that enhanced endothelial proliferation initiated by ripples is mediated by joint promotion of tyrosine kinase activity with a leading role of Src and calcium signaling.

5. Conclusion

We report significant differences in signalling events initiated by 250 to 300 nm ripples and 1.5 μm wall structures and demonstrate that activation of β -catenin signaling is strongly dependent on periodicity of PET surface structures. Both micro-(walls-) and nano-(ripple-) structures induce endothelial β -catenin signaling and proliferation by

enhanced tyrosine phosphorylation. Nanostructured ripples control β -catenin via activation of multiple tyrosine kinases, including Src and promotion of SOCE calcium signaling.

Acknowledgments

We would like to thank Drs. E. Ades and F. J. Candal of CDC and Dr. T. Lawley of Emory University for making the HMEC-1 cell line available. We would also like to thank E. Bock and S. Blass for excellent technical assistance. Dasatinib was a kind gift from Dr. Veronika Sexl. The support by the Austrian Science Funds FWF by funding Project F3005 LIPOTOX to Heimo Wolinski and Sepp D. Kohlwein and project P21925-B19 to Klaus Groschner and by the Austrian Research Promotion Agency FFG by Project 838955 Cell-Stretch to Johannes Heitz and Ruxandra-A. Barb is gratefully acknowledged.

References

- [1] E. Martínez, A. Lagunas, C. A. Mills et al., "Stem cell differentiation by functionalized micro- and nanostructured surfaces," *Nanomedicine*, vol. 4, no. 1, pp. 65–82, 2009.
- [2] S. Kruss, T. Wolfram, R. Martin, S. Neubauer, H. Kessler, and J. P. Spatz, "Stimulation of cell adhesion at nanostructured teflon interfaces," *Advanced Materials*, vol. 22, no. 48, pp. 5499–5506, 2010.

- [3] M. Ventre, F. Causa, and P. A. Netti, "Determinants of cell-material crosstalk at the interface: towards engineering of cell instructive materials," *Journal of the Royal Society, Interface/the Royal Society*, vol. 9, no. 74, pp. 2017–2032, 2012.
- [4] S. Pernagallo, O. Tura, M. Wu et al., "Novel biopolymers to enhance endothelialisation of intra-vascular devices," *Advanced Healthcare Materials*, vol. 1, no. 5, pp. 646–656, 2012.
- [5] M. Scherthner, B. Reisinger, H. Wolinski et al., "Nanopatterned polymer substrates promote endothelial proliferation by initiation of β -catenin transcriptional signaling," *Acta Biomaterialia*, vol. 8, no. 8, pp. 2953–2962, 2012.
- [6] F. H. Brembeck, M. Rosário, and W. Birchmeier, "Balancing cell adhesion and Wnt signaling, the key role of β -catenin," *Current Opinion in Genetics and Development*, vol. 16, no. 1, pp. 51–59, 2006.
- [7] T. J. C. Harris and M. Peifer, "Decisions, decisions: β -catenin chooses between adhesion and transcription," *Trends in Cell Biology*, vol. 15, no. 5, pp. 234–237, 2005.
- [8] F. H. Brembeck, T. Schwarz-Romond, J. Bakkers, S. Wilhelm, M. Hammerschmidt, and W. Birchmeier, "Essential role of BCL9-2 in the switch between β -catenin's adhesive and transcriptional functions," *Genes and Development*, vol. 18, no. 18, pp. 2225–2230, 2004.
- [9] C. J. Gottardi and B. M. Gumbiner, "Distinct molecular forms of β -catenin are targeted to adhesive or transcriptional complexes," *The Journal of Cell Biology*, vol. 167, no. 2, pp. 339–349, 2004.
- [10] T. P. Rao and M. Kühl, "An updated overview on wnt signaling pathways: a prelude for more," *Circulation Research*, vol. 106, no. 12, pp. 1798–1806, 2010.
- [11] T. Valenta, G. Hausmann, and K. Basler, "The many faces and functions of beta-catenin," *The EMBO Journal*, vol. 31, no. 12, pp. 2714–2736, 2012.
- [12] G. E. Hannigan, C. Leung-Hagesteijn, L. Fitz-Gibbon et al., "Regulation of cell adhesion and anchorage-dependent growth by a new β 1-integrin-linked protein kinase," *Nature*, vol. 379, no. 6560, pp. 91–96, 1996.
- [13] S. K. Hanks, M. B. Calalb, M. C. Harper, and S. K. Patel, "Focal adhesion protein-tyrosine kinase phosphorylated in response to cell attachment to fibronectin," *Proceedings of the National Academy of Sciences of the United States of America*, vol. 89, no. 18, pp. 8487–8491, 1992.
- [14] Y. Wang, G. Jin, H. Miao, J. Y.-S. Li, S. Usami, and S. Chien, "Integrins regulate VE-cadherin and catenins: dependence of this regulation on Src, but not on Ras," *Proceedings of the National Academy of Sciences of the United States of America*, vol. 103, no. 6, pp. 1774–1779, 2006.
- [15] S. Huvneers and E. H. J. Danen, "Adhesion signaling—crosstalk between integrins, Src and Rho," *Journal of Cell Science*, vol. 122, part 8, pp. 1059–1069, 2009.
- [16] J. Lilien and J. Balsamo, "The regulation of cadherin-mediated adhesion by tyrosine phosphorylation/dephosphorylation of β -catenin," *Current Opinion in Cell Biology*, vol. 17, no. 5, pp. 459–465, 2005.
- [17] X. Chen, J. Nam, C. Jean et al., "VEGF-induced vascular permeability is mediated by FAK," *Developmental Cell*, vol. 22, no. 1, pp. 146–157, 2012.
- [18] C. Bertocchi, M. V. Rao, and R. Zaidel-Bar, "Regulation of adherens junction dynamics by phosphorylation switches," *Journal of Signal Transduction*, vol. 2012, Article ID 125295, 14 pages, 2012.
- [19] H. Rangaswami, R. Schwappacher, T. Tran et al., "Protein kinase G and focal adhesion kinase converge on Src/Akt/beta-catenin signaling module in osteoblast mechanotransduction," *The Journal of Biological Chemistry*, vol. 287, no. 25, pp. 21509–21519, 2012.
- [20] H. S. Lee, S. J. Millward-Sadler, M. O. Wright, G. Nuki, and D. M. Salter, "Integrin and mechanosensitive ion channel-dependent tyrosine phosphorylation of focal adhesion proteins and β -catenin in human articular chondrocytes after mechanical stimulation," *Journal of Bone and Mineral Research*, vol. 15, no. 8, pp. 1501–1509, 2000.
- [21] S. Katz, R. Boland, and G. Santillán, "Modulation of ERK 1/2 and p38 MAPK signaling pathways by ATP in osteoblasts: Involvement of mechanical stress-activated calcium influx, PKC and Src activation," *International Journal of Biochemistry and Cell Biology*, vol. 38, no. 12, pp. 2082–2091, 2006.
- [22] E. W. Ades, F. J. Candal, R. A. Swerlick et al., "HMEC-1: establishment of an immortalized human microvascular endothelial cell line," *Journal of Investigative Dermatology*, vol. 99, no. 6, pp. 683–690, 1992.
- [23] A. Graziani, M. Poteser, W. Heupel et al., "Cell-cell contact formation governs Ca^{2+} signaling by TRPC4 in the vascular endothelium: evidence for a regulatory TRPC4- β -catenin interaction," *The Journal of Biological Chemistry*, vol. 285, no. 6, pp. 4213–4223, 2010.
- [24] J. Bain, L. Plater, M. Elliott et al., "The selectivity of protein kinase inhibitors: a further update," *Biochemical Journal*, vol. 408, no. 3, pp. 297–315, 2007.
- [25] M. Maydan, P. C. McDonald, J. Sanghera et al., "Integrin-linked kinase is a functional Mn^{2+} -dependent protein kinase that regulates glycogen synthase kinase-3 β (gsk-3 β) phosphorylation," *PLoS ONE*, vol. 5, no. 8, Article ID e12356, 2010.
- [26] S. Michels, M. Trautmann, E. Sievers et al., "SRC signaling is crucial in the growth of synovial sarcoma cells," *Cancer Research*, vol. 73, no. 8, pp. 2518–2528, 2013.
- [27] N. P. Shah, C. Tran, F. Y. Lee, P. Chen, D. Norris, and C. L. Sawyers, "Overriding imatinib resistance with a novel ABL kinase inhibitor," *Science*, vol. 305, no. 5682, pp. 399–401, 2004.
- [28] M. J. Mauro and B. J. Druker, "ST1571: targeting BCR-ABL as therapy for CML," *Oncologist*, vol. 6, no. 3, pp. 233–238, 2001.
- [29] Z. Xie, P. A. Singleton, L. Y. W. Bourguignon, and D. D. Bikle, "Calcium-induced human keratinocyte differentiation requires src- and fyn-mediated phosphatidylinositol 3-kinase-dependent activation of phospholipase C- γ 1," *Molecular Biology of the Cell*, vol. 16, no. 7, pp. 3236–3246, 2005.
- [30] G. A. Moore, D. J. McConkey, G. E. N. Kass, P. J. O'Brien, and S. Orrenius, "2,5-Di(tert-butyl)-1,4-benzohydroquinone—a novel inhibitor of liver microsomal Ca^{2+} sequestration," *FEBS Letters*, vol. 224, no. 2, pp. 331–336, 1987.
- [31] D. A. Murtazina, D. Chung, A. Ulloa, E. Bryan, H. L. Galan, and B. M. Sanborn, "TRPC1, STIM1, and ORAI influence signal-regulated intracellular and endoplasmic reticulum calcium dynamics in human myometrial cells," *Biology of Reproduction*, vol. 85, no. 2, pp. 315–326, 2011.
- [32] O. P. Hamill and D. W. McBride Jr., "The pharmacology of mechanogated membrane ion channels," *Pharmacological Reviews*, vol. 48, no. 2, pp. 231–252, 1996.
- [33] A. I. Teixeira, G. A. Abrams, P. J. Bertics, C. J. Murphy, and P. F. Nealey, "Epithelial contact guidance on well-defined micro- and nanostructured substrates," *Journal of Cell Science*, vol. 116, part 10, pp. 1881–1892, 2003.

- [34] P. T. Ohara and R. C. Buck, "Contact guidance in vitro. A light, transmission, and scanning electron microscopic study," *Experimental Cell Research*, vol. 121, no. 2, pp. 235–249, 1979.
- [35] A. Oloumi, S. Syam, and S. Dedhar, "Modulation of Wnt3a-mediated nuclear β -catenin accumulation and activation by integrin-linked kinase in mammalian cells," *Oncogene*, vol. 25, no. 59, pp. 7747–7757, 2006.
- [36] J. Xing, Z. Zhang, H. Mao, R. G. Schnellmann, and S. Zhuang, "Src regulates cell cycle protein expression and renal epithelial cell proliferation via PI3K/Akt signaling-dependent and -independent mechanisms," *American Journal of Physiology—Renal Physiology*, vol. 295, no. 1, pp. F145–F152, 2008.
- [37] X. Liu, L. Du, and R. Feng, "c-Src regulates cell cycle proteins expression through protein kinase B/glycogen synthase kinase 3 beta and extracellular signal-regulated kinases 1/2 pathways in MCF-7 cells," *Acta Biochimica et Biophysica Sinica*, vol. 45, no. 7, pp. 586–592, 2013.
- [38] D. Riley, N. O. Carragher, M. C. Frame, and J. A. Wyke, "The mechanism of cell cycle regulation by v-Src," *Oncogene*, vol. 20, no. 42, pp. 5941–5950, 2001.
- [39] G. Babnigg, S. R. Bowersox, and M. L. Villereal, "The role of pp60(c-src) in the regulation of calcium entry via store-operated calcium channels," *The Journal of Biological Chemistry*, vol. 272, no. 47, pp. 29434–29437, 1997.
- [40] J. A. Rosado, D. Graves, and S. O. Sage, "Tyrosine kinases activate store-mediated Ca^{2+} entry in human platelets through the reorganization of the actin cytoskeleton," *Biochemical Journal*, vol. 351, part 2, pp. 429–437, 2000.
- [41] J. A. Rosado and S. O. Sage, "Regulation of plasma membrane Ca^{2+} -ATPase by small GTPases and phosphoinositides in human platelets," *The Journal of Biological Chemistry*, vol. 275, no. 26, pp. 19529–19535, 2000.
- [42] I. F. Abdullaev, J. M. Bisailon, M. Potier, J. C. Gonzalez, R. K. Motiani, and M. Trebak, "Stim1 and orail mediate crac currents and store-operated calcium entry important for endothelial cell proliferation," *Circulation Research*, vol. 103, no. 11, pp. 1289–1299, 2008.
- [43] W. F. Graier, W. R. Kukovetz, and K. Groschner, "Cyclic AMP enhances agonist-induced Ca^{2+} entry into endothelial cells by activation of potassium channels and membrane hyperpolarization," *Biochemical Journal*, vol. 291, part 1, pp. 263–267, 1993.
- [44] I. Bogeski, M. Bozem, L. Sternfeld, H. W. Hofer, and I. Schulz, "Inhibition of protein tyrosine phosphatase 1B by reactive oxygen species leads to maintenance of Ca^{2+} influx following store depletion in HEK 293 cells," *Cell Calcium*, vol. 40, no. 1, pp. 1–10, 2006.

Research Article

Novel Caffeic Acid Nanocarrier: Production, Characterization, and Release Modeling

Milad Fathi,¹ Maryam Mirlohi,² Jaleh Varshosaz,³ and Golnoosh Madani⁴

¹ Department of Food Science and Technology, Faculty of Agriculture, Isfahan University of Technology (IUT), Isfahan 84156-83111, Iran

² Food Security Research Center, School of Nutrition and Food Science, Isfahan University of Medical Science (MUI), Isfahan 8174-73461, Iran

³ Faculty of Pharmacy, Isfahan University of Medical Science (MUI), Isfahan 81746-73461, Iran

⁴ Department of Biotechnology, Faculty of Agriculture, Isfahan University of Technology (IUT), Isfahan 84156-83111, Iran

Correspondence should be addressed to Maryam Mirlohi; m_mirlohi@hlth.mui.ac.ir

Received 9 June 2013; Revised 9 September 2013; Accepted 10 September 2013

Academic Editor: Krasimir Vasilev

Copyright © 2013 Milad Fathi et al. This is an open access article distributed under the Creative Commons Attribution License, which permits unrestricted use, distribution, and reproduction in any medium, provided the original work is properly cited.

This paper deals with the development of novel nanocarriers using layer by layer carbohydrate coating of caffeic acid loaded solid lipid nanoparticles (SLNs) to improve stability and colon delivery of the poorly water-soluble caffeic acid. Three biopolymers (chitosan, alginate, and pectin) in different concentrations (0.1, 0.25, and 0.5%) were electrostatically coated over the SLN surface. The size and zeta potential of produced nanocarriers were measured using photon correlation spectroscopy. Mathematical models (i.e., zero-order, first-order, Higuchi, Ritger-Peppas, reciprocal powered time, Weibull, and quadratic models) were used to describe the release and kinetic modeling in gastrointestinal solution (GIS). Also, antioxidant activity of caffeic acid during the release in GIS was investigated using DPPH and reducing activity methods. The prepared treatments coated by alginate-chitosan as well as pectin-chitosan coated SLN at the concentration of 0.1% showed nanosized bead; the latter efficiently retarded the release of caffeic acid in gastric media up to 2.5 times higher than that of SLN. Zeta potential values of coated samples were found to significantly increase in comparison to SLN indicating the higher stability of produced nanocarriers. Antioxidant activity of caffeic acid after gastric release did not result in the same trend as observed for caffeic acid release from different treatments; however, in line with less caffeic acid release in the intestine solution by the effect of coating, lower antioxidant activity was determined at the end stage of the experiment.

1. Introduction

Caffeic acid (3,4-dihydroxycinnamic acid) is a natural antioxidant found in various agricultural products such as fruits, vegetables, tea, olive oil, and coffee bean [1]. It acts as an antioxidant by scavenging oxygen-free radicals and chelating prooxidant metal ions [2]. Caffeic acid has also shown antimicrobial properties against *Escherichia coli*, *Bacillus cereus*, *Staphylococcus aureus*, *Listeria monocytogenes*, and some yeast [3]. However, it suffers from low stability in UV irradiation and oxygen presence [2, 3]. On the other hand, low aqueous solubility and bitter taste limit its application for food fortification.

Nanoencapsulation of food bioactives possesses different advantages including masking unpleasant taste, possibility of application of low soluble compounds, and protection against unfavorable environmental and processing conditions [4]. It is also supposed that colon delivery of food bioactives, particularly in nanocarriers is favorable due to higher bioavailability and positive effect on natural intestine flora. Solid lipid nanoparticles (SLNs) are new generation of nanocarriers which attract increasing attention due to their advantages such as high encapsulation efficiency, slow degradation rate, and possibility of large scale production [5]. They have been produced and characterized for encapsulating of hesperetin for food fortification. In spite of the different

benefits, there are some limitations possess to SLN including their initial rapid release (burst release) and their low stability [6]. Therefore, modification of nanocarriers is necessary to overcome these limitations.

Chitosan (poly[β -(1-4)-2-amino-2-deoxy-d-glucopyranose]; CH) is the second most abundant polysaccharides in nature after cellulose. There are some valuable characteristics possess to chitosan (e.g., biocompatibility, biodegradability, bioadhesiveness, and antimicrobial properties) which lead to its application for encapsulation of food bioactives [5, 7, 8]. However as a weak base with a pK_a value of the d-glucosamine residue of about 6.2–7.0, it is soluble in acidic media [9]. Hence, chitosan cannot be considered as a protective biopolymer for encapsulating of bioactives against the gastric media and therefore might not be alone applied for colon delivery.

Alginate (AL) is a water soluble linear anionic polysaccharide formed from alternating blocks of 1-4 linked α -L-guluronic and β -D-mannuronic acid residues. It has been reported to be mucoadhesive, biodegradable, and biocompatible [10, 11]. Gel formation of AL is induced using cross-linking with divalent cations such as Ca^{+2} . The gelation and cross-linking of the AL are mainly achieved by exchanging of sodium ions from the guluronic acids with the Ca^{+2} ions, and zipping of guluronic groups to form the egg-box-like conformation [12]. Alginate also shows pH sensitivity, while in contrast to chitosan, the release of encapsulated bioactive could be postponed in low pH, which is advantageous for colon delivery of acidic sensible bioactive ingredients [8, 13, 14].

Pectin (PEC) is a linear anionic polysaccharide, mainly consisting of linearly connected α -(1 \rightarrow 4)-d-galacturonic acid residues and is considered as a biocompatible, biodegradable, nontoxic, and mechanically resistant against physical shear. Pectin is classified as low methoxyl (LM, with a 25–50% degree of methoxylation) and high methoxyl (HM, with a 50–80% degree of methoxylation). LM pectin can also form an egg-box-like conformation gel by ionotropic gelation in presence of divalent Ca^{2+} ions [15]. Similar to alginate, LM pectin is pH sensitive and is favorable for food bioactive oral delivery.

Caffeic acid is a sensitive compound against oxidative degradation and also shows poor aqueous solubility and bitter taste. Therefore, its protection is necessary before its application for food fortification. To our knowledge, there is not any effort to enhance stability of caffeic acid. Therefore, the aims of this work were to produce and characterize novel nanocarriers for entrapment of caffeic acid and investigate the effect of encapsulation on caffeic acid antioxidant properties after release in gastrointestinal condition.

2. Materials and Methods

2.1. Materials. Caffeic acid was purchased from Sigma-Aldrich (USA). Chitosan (low molecular weight, MW 150000), sodium alginate, and LM pectin were supplied by Sigma-Aldrich Company (Canada). Glycerol monostearate (GMS; Condea, Germany), glycerol behenate (*Compritol* 888;

Gattefossé, France), and Tween 80 (Merck, Germany) were applied at analytical grade. All other chemicals and reagents were at least of analytical grade.

2.2. Methods

2.2.1. SLN Production. The SLN production method was adjusted based on the procedure mentioned in a previous study [6]. Briefly, the aqueous phase was added to caffeic acid containing melted lipid phase at 80°C and stirred in 2000 rpm for 1 min. To form coarse and nanoemulsions the preemulsion was subjected to bath (10 min; PowerSonic 505; Hwashin Technology, Gyeonggi-do, Republic of Korea) and probe (1 min, in amplitude 50% and power of 100 W-TT13 probe; Bandelin, Germany, Berlin) sonication, respectively. In order to prevent temperature increase, the probe sonicator was inactive in 2 second intervals. The attained emulsion was cooled down in an ice bath for 30 minutes to recrystallize lipid forming SLN. The encapsulation load and efficiency were determined using centrifugation method [6].

2.2.2. SLN Layer by Layer Coating. Chitosan solution was prepared by dissolving into acetic acid (0.1%) and stirring overnight. Alginate and pectin were dissolved in distilled water. SLNs were coated layer by layer coating of alginate or pectin with chitosan. A solution of 7.5 mL chitosan (0.1%) was added dropwise into a beaker containing 15 mL SLN solution under 1000 rpm stirring. Then, 15 mL of alginate or pectin solution (0.1, 0.25, and 0.5%) was dropped into the SLN-chitosan solution. Finally, appropriate amount of 18 mM calcium chloride solution was dropped into resulted solution, the pH was set on 5.2, and prepared nanoparticles were held with an additional stirring for 30 min to form uniform particle size. Subsequently, for future characterization, nanoparticles were freeze-dried at -80°C in 0.001 mbar for 48 h using a freeze-dryer (Christ Alpha LD, Germany).

2.2.3. Particle Size and Zeta Potential. The average particle size and zeta potential were determined by photon electron spectroscopy (PCS) using Zetasizer (NanoSizer 3000, Malvern Instruments, Malvern, UK). The size measurements were performed at a fixed angle of 90 degrees using the volume distribution. The polydispersity index (PDI) measures the size distribution of the nanocarriers. The lower the PDI, the narrower the size distribution. Zeta potential which is an indicator of surface charge was measured based on mean electrostatic mobility applying Helmholtz-Smoluchowski equation [16].

2.2.4. Morphology Characterization. Morphological study of the SLN and coated nanoparticles was performed using transmission electron microscopy (TEM). Samples were negatively stained with uranyl acetate (2%) and dried on carbon coated grids at room temperature.

2.2.5. Caffeic Acid Release and Kinetic Modeling. Caffeic acid release was studied in gastric and intestinal solutions applying dialysis bag method at 37°C and 100 rpm. Two milliliters

caffeic acid loaded SLN or solution of freeze-dried coated samples (with equal amount of caffeic acid) were sealed into dialysis bag (Sigma, Canada) with a 12 kDa cut-off. The bag was then placed into a 40 mL gastric buffer for 2 h. It was subsequently subjected to the intestinal buffer (50 mL) for 6 h. At appropriate time intervals, the amount of released caffeic acid was determined spectrophotometrically at wavelength of 295 nm. The release data were kinetically evaluated by zero-order, first-order, Higuchi, Rigter-Peppas, reciprocal powered time, Weibull, and quadratic models (see (1)–(7)) [6, 17, 18]:

$$C = Kt, \quad (1)$$

$$C = [1 - \exp(-Kt)] \times 100, \quad (2)$$

$$C = Kt^{0.5}, \quad (3)$$

$$C = Kt^n, \quad (4)$$

$$\left(\frac{1}{C} - 1\right) = \frac{K}{t^a}, \quad (5)$$

$$\ln[-\ln(1 - C)] = a_w \ln t - \ln b_w, \quad (6)$$

$$C = 100(K_1 t^2 + K_2 t), \quad (7)$$

where C is caffeic acid concentration (%) at time t , K is kinetic constant, and n is release exponent. The latest is used to characterize different release mechanisms. Encapsulant release from spherical carriers with $0.43 \leq n$ is controlled by Fickian diffusion mechanism, and $n \geq 0.85$ is commanded for dissolution phenomenon, and $0.43 < n < 0.85$ is governed by combination of two mechanisms [19].

The shape parameter, a_w , in Weibull model characterizes the curve as either exponential ($a_w = 1$) (Case 1), sigmoid, S-shaped, with upward curvature followed by a turning point ($a_w > 1$) (Case 2), or parabolic, with a higher initial slope and after that consistent with the exponential ($a_w < 1$) (Case 3) [18].

2.2.6. Reducing Activity Measurement. Either the gastric or intestinal buffers were subjected to reducing activity test as an indicator for antioxidative capability of the released caffeic acid. The method was adopted from Rekha [20]. A test sample or distilled water (control) (0.5 mL) was added to 0.5 mL potassium ferricyanide solution 1% (Merck, Germany) and 0.5 mL sodium phosphate buffer (0.02 M, pH 7). The mixture was incubated at 50°C for 20 min and then 0.5 mL trichloroacetic acid (0.5 mL, Merck, Germany) was added. The mixture was centrifuged at 780 g for 5 min. The upper layer (1.5 mL) was mixed with 0.1% ferri chloride (0.2 mL, Merck, Germany) and the absorbance was measured at 700 nm. The higher absorbance of the given mixture would present the higher reducing activity. The following equations were used to indicate the concentrations of caffeic acid

balanced with the reducing activity of the released caffeic acid.

Reducing activity standard curve in gastric buffer:

$$x = 32.3y - 1.25. \quad (8)$$

Reducing activity standard curve in intestinal buffer:

$$x = 55y - 7.5.$$

2.2.7. DPPH Radical Scavenging Activity. Free radical scavenging activity of the gastric and intestinal solution containing caffeic acid was measured by DPPH method, as described by Shinde et al. with minor modifications [21]. Briefly, 0.2 mL of each sample was added to 3.8 mL DPPH ethanol solution (final concentration was adjusted at 0.1 mM) in a test tube. The mixture was mixed vigorously for 1 min by vortexing and was left to stand at room temperature in the dark for 30 min. Thereafter, the absorbance of the sample was measured using the UV-visible spectrophotometer at 517 nm against ethanol blank. A negative control (control) was taken after adding DPPH solution to 0.2 mL of the respective gastric or intestinal buffer. The percent of DPPH discoloration of the sample was calculated according to the following equation:

$$\text{Percentage of discoloration} = \left[1 - \left(\frac{A_{\text{sample}}}{A_{\text{control}}}\right)\right] \times 100. \quad (9)$$

The scatter plots of absorbance against different concentration of caffeic acid in gastric and intestinal condition were provided individually, and the following equations were used for each of the media.

DPPH discoloration standard curve in gastric buffer:

$$x = 126 - 53.9y.$$

DPPH discoloration standard curve in intestinal buffer:

$$x = 182 - 355y. \quad (10)$$

2.2.8. Statistical Analysis. All experiments were performed at least with 3 replications, and the average values were reported. Statistical analyses were carried out using MSTAT software (version C). Data were subjected to analysis of variance (ANOVA), and means were compared using “Duncan” test at 5% significant level.

3. Results and Discussion

SLN, AL-CH, and PEC-CH coated SLNs were produced to enhance stability and functionality of caffeic acid. Encapsulation efficiency and load of produced SLN were $71.21 \pm 1.2\%$ and $4.73 \pm 0.35\%$, respectively. It is noteworthy that in a previous paper, it has been indicated that chemical compositions of the materials did not change during layer by layer coating [8]. In the following subsections, some features of developed nanocarriers such as size, zeta potential,

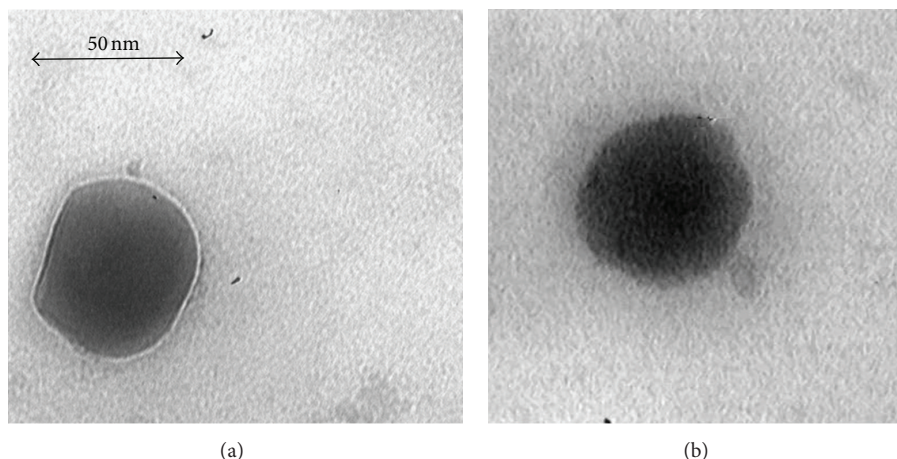


FIGURE 1: TEM morphology of caffeic acid loaded SLN (b) and PEC-CH coated SLN (a).

morphology, and release behavior are studied; the effect of different treatments on antioxidant activity of caffeic acid is discussed afterwards.

3.1. Size, Zeta Potential, and Morphological Characterization. Size, PDI, and zeta potential values of produced nanocarriers were tabulated in Table 1.

As expected, the SLN showed the smallest size (49.65 ± 1.12 nm). The developed SLNs are significantly small in comparison to some produced SLN [6, 22] and NLC [23, 24]. The smaller size of the particles leads to their faster movement due to Brownian motion and therefore higher dispersion stability against the gravity. On the other hand, zeta potential value of produced SLN was found to be near zero (-2.57 ± 1.03 mV). This low zeta potential in comparison to the literature data [25, 26] is due to the fact that there is almost the same positive and negative electron charge over the nano carriers' surface. Zeta potential is a crucial factor in nanoparticle stability. The particles with higher zeta potential show bigger repulsion force which leads to higher dispersion stability against aggregation. The low zeta potential of caffeic acid loaded SLN could be attributed to the neutral nature of applied lipid. Therefore, surface coating of nanoparticle using charged biopolymer could enhance their zeta potential. The results indicated that coating lead to increase of size and zeta potential. With the increasing coating concentration, the sizes of nanocarriers significantly ($P < 0.05$) increased in consequence. The negatively charged calcium alginate complex in pregel state can interact with positively charged chitosan [27]. The negative zeta potential of AL-CH coated SLN shows that Ca-AL properly covered the chitosan surface and therefore could be well protected against acidic condition in the gastric medium. Similar results were obtained by Mladenovska research team [28, 29] who showed AL-CH biopolymer had negative zeta potential. The absolute values of zeta potential of AL-CH coated nanoparticles increased by alginate concentration.

PEC-CH coated SLN in 0.1% pectin concentration showed size of 52.60 ± 0.31 nm (Table 1). However, in higher

concentrations of pectin, the micron size beads were constructed; therefore, their size and zeta potential were not reported due to the unreliability of the applied instrument. Similar results were obtained in our previous study for hesperetin loaded nanoparticles [8]. The micron size PEC-CH beads were also reported in the literature [30, 31]. The surface charge of pectin was found to be negative [32]. The positive zeta potential of 0.1% pectin-chitosan coated nanoparticles might be attributed to low pectin concentration and presence of chitosan on the surface of nanoparticles. Luo et al. produced chitosan coated NLC and observed that the zeta potential of NLC (-0.45 mV) increased by chitosan coating ($+20.70$ mV) [33].

The PDI values of all produced nanocarriers were found to be lower than 0.5 indicating their narrow size distribution.

The morphological images of SLN and PEC-CH coated nanoparticles obtained from transmission electron microscopy were depicted in Figure 1.

The obtained sized from TEM was in accordance with PCS analysis. Both SLN and coated nanoparticles showed spherical shape. The double shell layer in coated carrier could be obviously observed in TEM image.

3.2. Caffeic Acid Release. Two drawbacks of SLN, namely, low zeta potential and rapid release in gastric media motivated us to produce coated SLN. The release profiles of developed nanocarriers were shown in Figure 2.

Release and absorption of encapsulated food bioactives are supposed to be in intestine for higher bioavailability. More than 55% of caffeic acid released from SLN during the first two hours in gastric media (Figure 2(a)), and therefore, it was necessary to modify SLN for bioactive protection against gastric condition. AL-CH and PEC-CH coated nanoparticles could both retard caffeic acid release in gastric condition. Caffeic acid releases from AL-CH coated nanoparticles in the first 2 hours were found to be 30.32 ± 0.08 , 24.66 ± 1.00 , and 29.05 ± 0.99 for alginate concentrations of 0.1, 0.25, and 0.5%, respectively (Figure 2(b)). No significant difference was observed among

TABLE 1: Size, PDI, and zeta potential of developed caffeic acid loaded nanocarriers.

Nanocarrier	Size (nm)	Polydispersity index (PDI)	Zeta potential (mV)
SLN	49.65 ± 1.12	0.47 ± 0.02	-2.57 ± 1.03
AL-CH coated SLN-0.1%	74.26 ± 8.26	0.45 ± 0.07	-21.87 ± 3.04
AL-CH coated SLN-0.25%	109 ± 7.22	0.49 ± 0.05	-31.60 ± 2.32
AL-CH coated SLN-0.5%	235.93 ± 24.1	0.33 ± 0.03	-35.20 ± 3.41
PEC-CH coated SLN-0.1%	52.60 ± 0.31	0.42 ± 0.01	14.75 ± 0.35

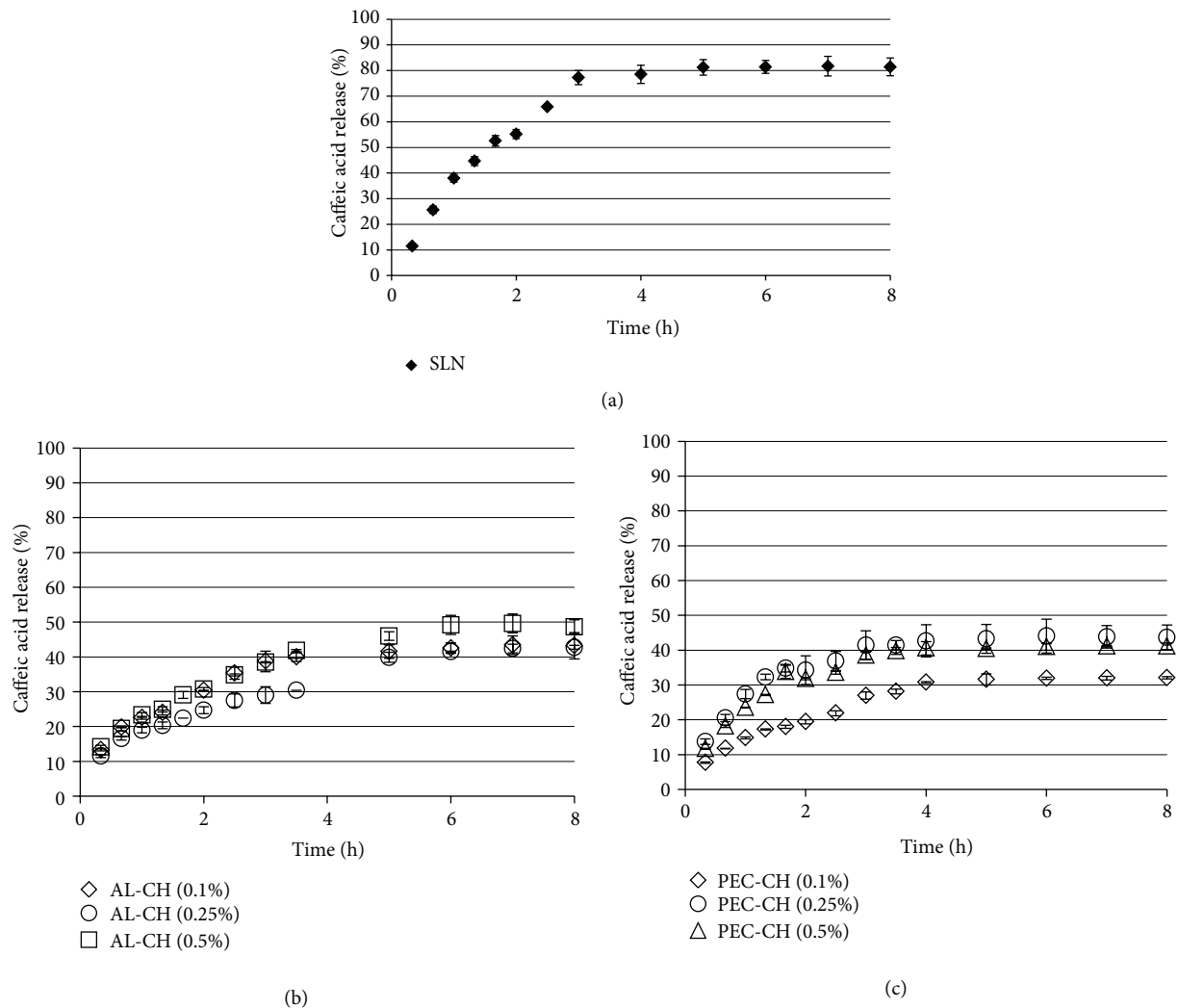


FIGURE 2: Caffeic acid release profile of SLN (a), coated AL-CH (b), and PEC-CH (c) SLN in gastrointestinal conditions.

caffeic acid release for the three applied concentrations. The release in gastric solution from AL-CH was found to be delayed due to cross-linking of guluronic acids with the Ca^{+2} ions and the amino groups of chitosan. On the other hand, in the intestinal condition, the slower release could be attributed to the insoluble chitosan blended in the gel structure. PEC-CH coated carriers in pectin concentration of 0.1% were found to be the most efficient against caffeic acid release in gastric media ($19.43 \pm 0.59\%$ of caffeic acid release) (Figure 2(c)). At higher concentrations, it seems that pectin

could not properly cover the particle surface and therefore was not capable of decelerating caffeic acid release in gastric media. The micron size of pectin coated carriers in concentrations of 0.25 and 0.50% shows that additional pectin tends to be aggregated and failed to completely cover the particle surface. Pectin can form a rigid gels by the action of calcium ions cross-linking the galacturonic acid chains [34].

It is also said to resist the proteases and amylase which are active in the upper gastrointestinal tract.

TABLE 2: Kinetic parameters of caffeic acid release.

Nanocarrier	Zero order		First order		Higuchi		Ritger-Peppas		Reciprocal powered time		Weibull		Quadratic					
	K	R	K	R	K	R	K	n	K	a	R	a_w	b_w	K_1	K_2	R		
SLN	14.605	0.738	0.399	0.958	34.960	0.906	40.467	0.399	0.912	1.677	1.202	0.981	4.5×10^{-5}	0.105	0.508	-3.0×10^{-4}	3.3×10^{-3}	0.962
AL-CH coated SLN (0.1%)	7.606	0.721	0.112	0.790	18.550	0.908	23.848	0.328	0.960	3.821	0.663	0.982	4.1×10^{-5}	0.102	0.517	-1.6×10^{-4}	1.7×10^{-3}	0.918
AL-CH coated SLN (0.25%)	7.074	0.80	0.097	0.859	16.688	0.979	18.615	0.424	0.990	4.449	0.601	0.989	3.0×10^{-5}	0.102	0.511	-1.1×10^{-4}	1.4×10^{-3}	0.931
AL-CH coated SLN (0.5%)	8.478	0.762	0.129	0.844	20.214	0.956	23.908	0.382	0.983	3.772	0.539	0.995	1.8×10^{-5}	0.102	0.515	-1.5×10^{-4}	1.8×10^{-3}	0.933
PEC-CH coated SLN (0.1%)	5.723	0.763	0.073	0.814	13.445	0.944	15.460	0.402	0.957	5.585	0.537	0.967	4.6×10^{-6}	0.102	0.508	-1.0×10^{-4}	1.2×10^{-3}	0.957
PEC-CH coated SLN (0.25)	8.276	0.666	0.127	0.738	19.990	0.847	27.530	0.272	0.935	2.674	0.438	0.955	2.0×10^{-5}	0.102	0.518	-1.8×10^{-4}	1.9×10^{-3}	0.871
PEC-CH coated SLN (0.5%)	7.733	0.678	0.114	0.747	18.601	0.860	24.804	0.296	0.925	3.088	0.458	0.945	7.1×10^{-6}	0.102	0.515	-1.7×10^{-4}	1.8×10^{-3}	0.893

TABLE 3: Antioxidant activity changes^a of released caffeic acid from nanocarriers in gastric and intestinal simulated condition.

Treatment	DPPH assay (%)		Reducing activity ($\mu\text{g/mL}$ of caffeic acid)	
	Gastric media	Intestine media	Gastric media	Intestine media
T1	5.85 ± 1.34	8.39 ± 2.56	12.44 ± 0.61	4.7 ± 0.34
T2	0.00	0.19 ± 0.09	5.3 ± 0.19	1.23 ± 0.10
T3	9.16 ± 1.04	3.7 ± 0.61	9.36 ± 1.07	0.96 ± 0.05
T4	0.00	2.15 ± 0.88	21.48 ± 0.11	0.38 ± 0.33
T5	11.24 ± 0.21	7.8 ± 1.86	5.6 ± 0.93	2.3 ± 1.28
T6	15.6 ± 3.37	0.00	0.27 ± 0.1	0.83 ± 0.23
T7	3.07 ± 0.23	3.2 ± 0.73	4.78 ± 1.16	3.84 ± 0.68

T1: caffeic acid released from solid lipid nanoparticles.

T2: caffeic acid released from solid lipid nanoparticles coated with 0.1% PEC-CH.

T3: caffeic acid released from solid lipid nanoparticles coated with 0.25% PEC-CH.

T4: caffeic acid released from solid lipid nanoparticles coated with 0.5% PEC-CH.

T5: caffeic acid released from solid lipid nanoparticles coated with 0.1% AL-CH.

T6: caffeic acid released from solid lipid nanoparticles coated with 0.25% AL-CH.

T7: caffeic acid released from solid lipid nanoparticles coated with 0.5% AL-CH.

^aResults are expressed as the means of three replications \pm standard error of mean.

The modeling results for four different kinetic models are tabulated in Table 2.

Rigter-Peppas and reciprocal powered time models provided better capability to describe release behavior of caffeic acid. The poor ability of zero-order model demonstrated that the release mechanism was concentration dependent. Low correlation coefficients of Higuchi model for pectin coated SLN in concentrations of 0.25% and 0.5% could be attributed to the swelling nature of these nanocarriers and weakness of this model for swellable polymers. Rigter-Peppas was found to be the most appropriate model describing release of hesperetin from coated nanostructure lipid carriers and Higuchi the least appropriate model due to swellability of biopolymers [8]. The n values of the Rigter-Peppas model were found to be lower than 0.43 indicating that the release mechanism is governed by the Fickian mechanism. Kinetic study of Weibull model demonstrated that a_w values are lower than 1 which indicated a parabolic release curve with a higher initial slope and then a consistent exponential release. These results showed that although burst release was decreased by carbohydrate coating, however, initial release is still exist.

3.3. Antioxidant Activity. The results of antioxidant properties of released caffeic acid in the gastric and intestine solutions for different treatments measured by a couple of distinct experimental methods are presented in Table 3.

Among different treatments, the highest antioxidant activity of the released caffeic acid in the intestine solution obtained for the trial contained noncoated particles (T1) was in line with the highest concentration of caffeic acid excreted in intestine simulated buffer in the given treatment. Instead, in the former phase, in the gastric solution, the measured antioxidant activity in each trial did not represent the trend observed in the caffeic acid release. It seems that the determined antioxidant activity was influenced by the nature of the coated material used in this study. Based on a previous study, pure caffeic acid is an effective DPPH-free radical scavenger and showed appropriate total reducing

power [35]. In accordance with the results of PEC-CH (0.1%) coated treatment in retarding caffeic acid diffusion in gastric solution, antioxidant activity was shown to be lower in this treatment than in noncoated nanocarriers (control). Though, the given treatment did not give rise to the enhancement of this property in the latter step as well. It is noteworthy that the results obtained from reducing activity method were concentration dependent, and therefore, their comparison for different release values might be imprecise.

The results was also shown to be highly influenced by the pH of the media; thus, in the present study, two individual conditions were considered for assessing the DPPH-free radicals scavenging capability of caffeic acid in different gastrointestinal conditions that unlikely contributes the test's precision. In vitro liberation of encapsulated phenolic component bioactive has been shown to be pH dependent and acidic environment accelerate the diffusion of protected bioactive [36].

Antioxidant property is defined as the ability of compounds to inhibit or suppress the oxidation process by scavenging the free radicals and/or reactive oxygen species. Methods to determine overall antioxidant activities are divided into two major categories; (i) methods in which the measurement is carried out based on transition of one electron from an antioxidant molecule to an oxidizing agent and (ii) methods in which the hydrogen releasing power of antioxidant molecule is regarded as the antioxidant capability [37]. In the present study, both methods were applied; however, the negative charge on the surface of coated nanoparticles (pectin and alginate) may interfere with the hydrogen donation properties of caffeic acid, leading to sophisticated results.

Based on previous studies, examining a distinct food sample by different antioxidative evaluation methods does not necessarily end up to similar results, and different experiments may result in different responses in quantity and even quality of antioxidant characteristic of a tested sample [38]. Here, in this study, such difference was seen

between DPPH assay and reducing activity test for both kinds of media, particularly in the gastric buffer, convening that the methodology for evaluating antioxidative characteristics of these structures need to be optimized in future studies. The necessity of application of modified DPPH assay for the determination of antioxidant properties of nanoparticles was also stated by others [39]. Using polymeric nanoparticles of L, D lactid-co-glycolid, Pool et al. [36] showed that encapsulation of antioxidant biochemical like quercetin and catechin resulted in the higher antioxidant capability than their free forms. Inhibition of superoxide production and chelating the prooxidant ions were used in their study as the antioxidative indexes; however, the corresponded protocols were adjusted upon the tests condition.

4. Conclusions

In this study, development and release kinetic modeling of novel nanocarriers encasing caffeic acid were pursued. Solid lipid nanoparticles were first used for encapsulation of caffeic acid, while its burst release and low zeta potential made them inappropriate carriers for colon delivery. Layer by layer coating of SLN was therefore performed using alginate-chitosan and pectin-chitosan in different concentrations. Micron size carriers were constructed in higher concentrations (0.25 and 0.5%) of pectin-chitosan treatments, and nanosize particles with capability of control release were achieved using alginate-chitosan and 0.1% pectin-chitosan samples. However, the antioxidant properties of the produced nanocarriers in the intestine simulated buffer were not improved by any of the employed treatments which may root by the nature of the coating material. Since bioavailability of nutraceuticals is improved by their colon delivery, developed nanocarriers could be applied for the production of functional fortified food.

References

- [1] F. Shahidi and M. Naczki, *Food Phenolics: Sources, Chemistry, Effects, Applications*, Taylor & Francis, London, UK, 2003.
- [2] S. Ou and K. Kwok, "Ferulic acid: pharmaceutical functions, preparation and applications in foods," *Journal of the Science of Food and Agriculture*, vol. 84, no. 11, pp. 1261–1269, 2004.
- [3] A. Saija, A. Tomaino, R. Lo Cascio et al., "Ferulic and caffeic acids as potential protective agents against photooxidative skin damage," *Journal of the Science of Food and Agriculture*, vol. 79, no. 3, pp. 476–480, 1999.
- [4] M. Fathi, M. R. Mozafari, and M. Mohebbi, "Nanoencapsulation of food ingredients using lipid based delivery systems," *Trends in Food Science and Technology*, vol. 23, no. 1, pp. 13–27, 2012.
- [5] W. Klaypradit and Y. Huang, "Fish oil encapsulation with chitosan using ultrasonic atomizer," *LWT-Food Science and Technology*, vol. 41, no. 6, pp. 1133–1139, 2008.
- [6] M. Fathi, J. Varshosaz, M. Mohebbi, and F. Shahidi, "Hesperetin-loaded solid lipid nanoparticles and nanostructure lipid carriers for food fortification: preparation, characterization, and modeling," *Food and Bioprocess Technology*, vol. 6, no. 6, pp. 1464–1475, 2013.
- [7] G. Y. Park, S. Mun, Y. Park et al., "Influence of encapsulation of emulsified lipids with chitosan on their in vivo digestibility," *Food Chemistry*, vol. 104, no. 2, pp. 761–767, 2007.
- [8] M. Fathi and J. Varshosaz, "Novel hesperetin loaded nanocarriers for food fortification: production and characterization," *Journal of Functional Foods*, vol. 53, pp. 1382–1391, 2013.
- [9] R. Hejazi and M. Amiji, "Chitosan-based gastrointestinal delivery systems," *Journal of Controlled Release*, vol. 89, no. 2, pp. 151–165, 2003.
- [10] T. Espevik, M. Otterlei, G. Skjak-Braek, L. Ryan, S. D. Wright, and A. Sundan, "The involvement of CD14 in stimulation of cytokine production by uronic acid polymers," *European Journal of Immunology*, vol. 23, no. 1, pp. 255–261, 1993.
- [11] W. R. Gombotz and S. F. Wee, "Protein release from alginate matrices," *Advanced Drug Delivery Reviews*, vol. 31, no. 3, pp. 267–285, 1998.
- [12] M. George and T. E. Abraham, "Polyionic hydrocolloids for the intestinal delivery of protein drugs: alginate and chitosan—a review," *Journal of Controlled Release*, vol. 114, no. 1, pp. 1–14, 2006.
- [13] S. Sugawara, T. Imai, and M. Otagiri, "The controlled release of prednisolone using alginate gel," *Pharmaceutical Research*, vol. 11, no. 2, pp. 272–277, 1994.
- [14] C.-K. Kim and E.-J. Lee, "The controlled release of blue dextran from alginate beads," *International Journal of Pharmaceutics*, vol. 79, no. 1, pp. 11–19, 1992.
- [15] R. H. Walter and S. Taylor, *The Chemistry and Technology of Pectin*, Elsevier Science, Amsterdam, The Netherlands, 1992.
- [16] R. A. Nash and B. E. Haeger, "Zeta potential in the development of pharmaceutical suspensions," *Journal of Pharmaceutical Sciences*, vol. 55, no. 8, pp. 829–837, 1966.
- [17] G. Singhvi and M. Singh, "Review: in-vitro drug release characterization models," *International Journal of Pharmaceutical Studies and Research*, vol. 2, no. 1, pp. 77–84, 2011.
- [18] P. Costa and J. M. Sousa Lobo, "Modeling and comparison of dissolution profiles," *European Journal of Pharmaceutical Sciences*, vol. 13, no. 2, pp. 123–133, 2001.
- [19] M. Chakraborty, S. Dasgupta, C. Soundrapandian et al., "Methotrexate intercalated ZnAl-layered double hydroxide," *Journal of Solid State Chemistry*, vol. 184, no. 9, pp. 2439–2445, 2011.
- [20] C. R. Rekha and G. Vijayalakshmi, "Biomolecules and nutritional quality of soymilk fermented with probiotic yeast and bacteria," *Applied Biochemistry and Biotechnology*, vol. 151, no. 2-3, pp. 452–463, 2008.
- [21] A. N. Shinde, N. Malpathak, and D. P. Fulzele, "Determination of isoflavone content and antioxidant activity in *Psoralea corylifolia* L. callus cultures," *Food Chemistry*, vol. 118, no. 1, pp. 128–132, 2010.
- [22] E. Zimmermann and R. H. Müller, "Electrolyte- and pH-stabilities of aqueous solid lipid nanoparticle (SLN) dispersions in artificial gastrointestinal media," *European Journal of Pharmaceutics and Biopharmaceutics*, vol. 52, no. 2, pp. 203–210, 2001.
- [23] A. Hentschel, S. Gramdorf, R. H. Müller, and T. Kurz, "β-Carotene-loaded nanostructured lipid carriers," *Journal of Food Science*, vol. 73, no. 2, pp. N1–N6, 2008.
- [24] E. Gonzalez-Mira, M. A. Egea, M. L. Garcia, and E. B. Souto, "Design and ocular tolerance of flurbiprofen loaded ultrasound-engineered NLC," *Colloids and Surfaces B*, vol. 81, no. 2, pp. 412–421, 2010.

- [25] P. Severino, M. H. A. Santana, and E. B. Souto, "Optimizing SLN and NLC by 22 full factorial design: effect of homogenization technique," *Materials Science and Engineering C*, vol. 32, no. 6, pp. 1375–1379, 2012.
- [26] C.-C. Chen, T. Tsai, Z. Huang, and J. Fang, "Effects of lipophilic emulsifiers on the oral administration of lovastatin from nanostructured lipid carriers: physicochemical characterization and pharmacokinetics," *European Journal of Pharmaceutics and Biopharmaceutics*, vol. 74, no. 3, pp. 474–482, 2010.
- [27] T. Li, X. Shi, Y. Du, and Y. Tang, "Quaternized chitosan/alginate nanoparticles for protein delivery," *Journal of Biomedical Materials Research A*, vol. 83, no. 2, pp. 383–390, 2007.
- [28] K. Mladenovska, R. S. Raicki, E. I. Janevik et al., "Colon-specific delivery of 5-aminosalicylic acid from chitosan-Ca-alginate microparticles," *International Journal of Pharmaceutics*, vol. 342, no. 1-2, pp. 124–136, 2007.
- [29] K. Mladenovska, O. Cruaud, P. Richomme et al., "5-ASA loaded chitosan-Ca-alginate microparticles: preparation and physicochemical characterization," *International Journal of Pharmaceutics*, vol. 345, no. 1-2, pp. 59–69, 2007.
- [30] J. R. R. de Souza, J. I. X. de Carvalho, M. T. S. Trevisan, R. C. M. de Paula, N. M. P. S. Ricardo, and J. P. A. Feitosa, "Chitosan-coated pectin beads: characterization and in vitro release of mangiferin," *Food Hydrocolloids*, vol. 23, no. 8, pp. 2278–2286, 2009.
- [31] J.-S. Lee, J. S. Kim, and H. G. Lee, " γ -Oryzanol-loaded calcium pectinate microparticles reinforced with chitosan: optimization and release characteristics," *Colloids and Surfaces B*, vol. 70, no. 2, pp. 213–217, 2009.
- [32] M. Tholstrup Sejersen, T. Salomonsen, R. Ipsen, R. Clark, C. Rolin, and S. Balling Engelsen, "Zeta potential of pectin-stabilised casein aggregates in acidified milk drinks," *International Dairy Journal*, vol. 17, no. 4, pp. 302–307, 2007.
- [33] Q. Luo, J. Zhao, X. Zhang, and W. Pan, "Nanostructured lipid carrier (NLC) coated with Chitosan Oligosaccharides and its potential use in ocular drug delivery system," *International Journal of Pharmaceutics*, vol. 403, no. 1-2, pp. 185–191, 2011.
- [34] P. Sriamornsak, S. Sungthongjeen, and S. Puttipipatkachorn, "Use of pectin as a carrier for intragastric floating drug delivery: carbonate salt contained beads," *Carbohydrate Polymers*, vol. 67, no. 3, pp. 436–445, 2007.
- [35] İ. Gülçin, "Antioxidant activity of caffeic acid (3,4-dihydroxycinnamic acid)," *Toxicology*, vol. 217, no. 2-3, pp. 213–220, 2006.
- [36] H. Pool, D. Quintanar, J. de Dios Figueroa et al., "Antioxidant effects of quercetin and catechin encapsulated into PLGA nanoparticles," *Journal of Nanomaterials*, vol. 2012, Article ID 145380, 12 pages, 2012.
- [37] O. I. Aruoma and S. L. Cuppett, *Antioxidant Methodology: In Vivo and In Vitro Concepts*, AOCS Press, Urbana, Ill, USA, 1997.
- [38] Y.-C. Wang, R.-C. Yu, and C.-C. Chou, "Antioxidative activities of soymilk fermented with lactic acid bacteria and bifidobacteria," *Food Microbiology*, vol. 23, no. 2, pp. 128–135, 2006.
- [39] S. Barnaby, N. Sarker, A. Dowdell, and I. Banerjee, "The spontaneous formation of selenium nanoparticles on gallic acid assemblies and their antioxidant properties," *The Fordham Undergraduate Research Journal*, vol. 1, pp. 41–46, 2011.

Research Article

Restoration of Critical-Sized Defects in the Rabbit Mandible Using Autologous Bone Marrow Stromal Cells Hybridized with Nano- β -tricalcium Phosphate/Collagen Scaffolds

Xuehui Zhang,^{1,2} Mingming Xu,¹ Xinggong Liu,¹ Feng Zhang,³ Yan Wei,¹ Song Meng,¹ Xiaohan Dai,¹ Aizhu Duan,¹ and Xuliang Deng^{1,4}

¹ Department of Geriatric Dentistry, Peking University School and Hospital of Stomatology, Beijing 100081, China

² State Key Laboratory of New Ceramics and Fine Processing, Department of Materials Science and Engineering, Tsinghua University, Beijing 100084, China

³ The Oral Clinic of the 2nd Hospital of Beijing Armed Police Force, Beijing 100037, China

⁴ National Engineering Laboratory for Digital and Material Technology of Stomatology, Beijing 100081, China

Correspondence should be addressed to Xuliang Deng; kqdengxuliang@bjmu.edu.cn

Received 26 July 2013; Accepted 26 September 2013

Academic Editor: Haifeng Chen

Copyright © 2013 Xuehui Zhang et al. This is an open access article distributed under the Creative Commons Attribution License, which permits unrestricted use, distribution, and reproduction in any medium, provided the original work is properly cited.

Nano- β -tricalcium phosphate/collagen (n- β -TCP/Col) is considered with good osteoconductivity. However, the therapeutic effectiveness of n- β -TCP/Col scaffolds in combination with autologous bone marrow stromal cells (BMSCs) remains to be elucidated for the repair of critical-sized bone defects. In this study, we found that n- β -TCP/Col scaffolds exhibited high biocompatibility *in vitro*. The introduction of BMSCs expanded *in vitro* to the scaffolds dramatically enhanced their efficiency to restore critical-sized bone defects, especially during the initial stage after implantation. Collectively, these results suggest that autologous BMSCs in n- β -TCP/Col scaffolds have the potential to be applied in bone tissue engineering.

1. Introduction

In recent years, a critical-sized bone defect has been defined as an intraosseous wound that will not spontaneously heal completely without surgical intervention [1, 2]. Bone autografting is currently considered to be the “gold standard” for clinical treatment. However, it is always associated with irregular rates of resorption, pain, and morbidity of the donor site, and it requires additional surgical procedures [3]. Therefore, alternatives to autologous bone grafting are the subject of intensive research.

Recently, tissue engineering approaches have proven to be very effective in bone regeneration. Successful repair of bone defects has been investigated in many animal species including mice [4], rats [5, 6], rabbits [7], canines [8], and goats [9]. Selection of the most appropriate scaffold for application in bone tissue engineering is a critically important step towards tissue-engineered product [10, 11]. β -Tricalcium phosphate (β -TCP) is a bioactive and biodegradable ceramic

that has been widely used as a scaffold for bone repair because of its excellent biocompatibility, reabsorbability, and osteoconductive properties [12, 13]. However, the use of β -TCP is limited because of its brittleness and low plasticity [14]. Biocompatible polymers, such as collagen (Col), are also regarded as applicable candidates for use in bone regeneration scaffolds. However, there are a number of practical problems for their use alone, including an uncontrollable degradation rate *in vivo* and poor mechanical properties compared with those of natural hard tissues [15, 16].

To overcome the limitations of bioceramics and biopolymers, ceramic/polymer composite materials have been explored for preparation of bone tissue engineering scaffolds [17, 18]. Using a biomimetic strategy, composites based on β -TCP and Col have been developed with a three-dimensional structure to fill bone defects, which show promise because of compositional and structural analogies to natural bone [19–21]. In our previous study [22], we designed and fabricated a novel three-dimensional porous tissue engineering scaffolds

using nanosized β -TCP (n - β -TCP)/Col composite materials. The n - β -TCP particles (about 300 nm) can be distributed homogeneously in the skeleton of a collagen fibril network in which n - β -TCP particles bind tightly to collagen fibrils. These composite scaffolds have been found to repair small bone defects. However, the therapeutic effectiveness of n - β -TCP/Col scaffolds in combination with seed cells remains to be elucidated for the repair of critical-sized bone defects.

Bone marrow stromal cells (BMSCs) are multipotent and have the ability to differentiate into osteoblastic, chondrocytic, and adipocytic lineage cells. BMSCs exhibit advantages over other cell types and have been widely used in bone tissue engineering [23]. However, isolation of bone marrow has some disadvantages in clinical practice, especially to obtain sufficient cell numbers for transplantation into large bone defects. To obtain enough cell numbers, much bone marrow aspiration is needed which would lead to an invasive and painful procedure and increase the risk of morbidity and infection. Expansion of BMSCs *in vitro* is an alternative strategy to gain enough cells for implantation.

The goal of this study was to explore the therapeutic effectiveness of *in vitro* expanded autologous BMSC-loaded n - β -TCP/Col scaffolds for repairing critical-sized bone defects of the rabbit mandible. At 4 and 8 weeks after implantation, gross examination, cone beam computed tomography (CBCT) scanning, and histological analysis were used to assess new bone formation and scaffolds degradation.

2. Materials and Methods

2.1. Fabrication and Characterization of n - β -TCP/Col Scaffolds. β -TCP (~300 nm particle size) was synthesized by calcining an amorphous calcium phosphate precursor [24]. n - β -TCP/Col scaffolds were prepared as reported in our previous study [25]. Briefly, type I collagen (Sigma-Aldrich Co., USA) was dispersed in a diluted hydrochloric acid solution (pH 2) at room temperature. β -TCP was added to the collagen suspension with stirring at a 3:1 (w/w) ratio. After formation of a uniform suspension, the cross-linking reagent glutaraldehyde (Shanghai Pharm Co., China) was added to the mixture. After freezing in liquid nitrogen, the mixture was lyophilized to obtain the porous n - β -TCP/Col composite. After soaking in deionized water for 4 days with daily changes to remove unreacted glutaraldehyde, the porous composite was lyophilized again to form the n - β -TCP/Col composite scaffolds.

The surface morphology and structure of the nanofibers were observed by scanning electron microscopy (SEM, S-4700; Hitachi, Japan). Fourier-transform infrared spectroscopy (FT-IR, 8700; Nicolet, USA) was used to evaluate the chemical structure of the composite scaffolds.

2.2. Isolation, Characterization, and Osteogenic Differentiation of Rabbit BMSCs. All animal experiments were performed in accordance with a protocol approved by the Laboratory Animal Care and Use Committee of Peking University. All reagents were purchased from Sigma-Aldrich Co. (St. Louis, MO) unless otherwise stated. BMSCs were isolated from bone

marrow aspirates of New Zealand white rabbits (12 weeks old, 2.5–3 kg, $n = 12$). Briefly, the bone marrow aspirate was washed three times with Hanks' balanced salt solution, plated onto 100 mm dishes, and cultured in Dulbecco's modified Eagle's medium (DMEM) (Gibco, USA) supplemented with 10% fetal bovine serum (FBS) (HyClone, USA), 100 U/mL penicillin, and 100 mg/mL streptomycin at 37°C with 5% CO₂. After 72 hours, nonadherent cells were removed by changing the medium. To characterize the surface marker expression of BMSCs, passage 3 cells were stained with an anti-rabbit CD34 antibody (1:200; Abcam, Cambridge, MA) for immunohistological analysis (Figure 1(b)). At 80–90% confluence, adherent passage 3 cells were trypsinized, harvested, and subcultured in osteogenic medium. The osteogenic medium consisted of DMEM supplemented with 10% FBS, 50 mg/mL ascorbic acid-2-phosphate, 100 nM dexamethasone, 10 mM β -glycerophosphate, 100 U/mL penicillin, and 100 mg/mL streptomycin. After 1 week of culture, the osteogenic differentiation of BMSCs was confirmed by alkaline phosphatase (ALP) staining.

2.3. Growth and Bioactivity of Rabbit BMSCs in n - β -TCP/Col Scaffolds. The fabricated n - β -TCP/Col scaffolds (10 × 8 × 3 mm³) were sterilized with ethylene oxide and prewetted in osteogenic medium for 24 h. BMSCs that had been cultured in osteogenic medium for 1 week were seeded in the prewetted n - β -TCP/Col scaffolds (2 × 10⁷ cells/scaffold), and then the cell/scaffold constructs were placed in 24-well plates. The cell/scaffold constructs were incubated for 3 hours to allow cell attachment, and then an additional 1 mL of culture medium was added to each well. After 3 days of culture, the constructs were fixed in 2.5% glutaraldehyde and serially dehydrated in an increasing ethanol gradient, air-dried, and sputter coated with gold prior to imaging by SEM at 20 kV.

At 1, 3, and 7 days of culture, cell proliferation was assayed using a CCK-8 kit (Dojindo, Japan) and enzyme-linked immunosorbent assay reader (Bio-Rad, Hercules, CA, USA) at an absorbance wavelength of 450 nm. The ALP activity of the adherent cells was also assessed using an Alkaline Phosphatase Assay Kit (Abcam, Cambridge, MA, USA) according to the manufacturer's instructions.

2.4. Experimental Animal Model. Twelve healthy New Zealand white rabbits were divided into two groups, one group for implantation of n - β -TCP/Col scaffolds alone and the other for n - β -TCP/Col scaffolds combined with autologous BMSCs expanded *in vitro*. The rabbits were anesthetized with pentobarbital sodium and a 3 cm parallel incision was made along the inferior border of the mandible on both sides. The periosteum was then retracted to expose the submaxilla. A critical-sized defect, 10 × 8 × 3 mm³, was made in the Buccal-lingual direction on one side of the mandible of each rabbit. The scaffolds alone or MSC/scaffold constructs were inserted into the defect. The mucoperiosteal flaps were carefully sutured over the defect area using 3-0 absorbable sutures. The rabbits were sacrificed at 4 and 8 weeks after implantation for tissue processing.

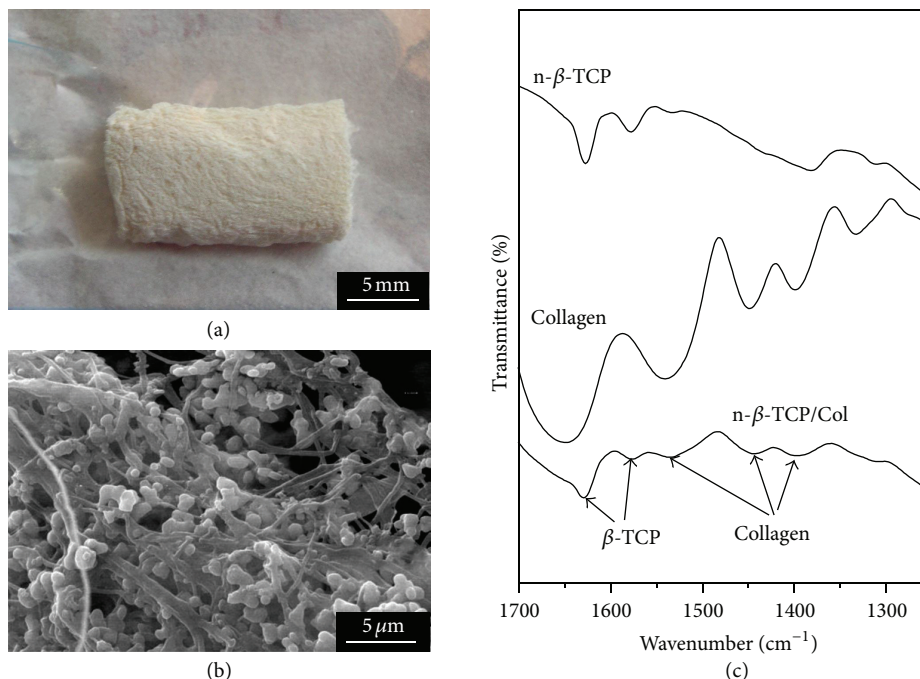


FIGURE 1: Characteristics of the $n\text{-}\beta\text{-TCP/Col}$ scaffolds. (a) Macroscopic image, (b) SEM image, and (c) FT-IR spectra of the $n\text{-}\beta\text{-TCP/Col}$ scaffolds.

2.5. Gross Observation and CBCT Examination. At 4 and 8 weeks after implantation, the scaffolds and surrounding tissues were excised and fixed in 10% neutral buffered formalin. Each mandible defect site was assessed by gross observation, and the morphology of the reconstructed mandibles at 8 weeks after-implantation was assessed by CBCT scanning (J. Morita Mfg. Corp., Kyoto, Japan) at 60 KV and 2.0 mA.

2.6. Histological Evaluation and Histomorphometry. At 4 and 8 weeks after implantation, rabbit mandibles were subjected to tissue processing and sectioning as reported previously [26]. Briefly, the tissue samples were fixed in 10% neutral buffered formalin for 7 days, followed by decalcification and dehydration, and finally embedded in paraffin and sectioned at 5 mm thicknesses. Hematoxylin and eosin (H&E) staining was performed on serial tissue sections, and images were captured under a microscope (CX21; Olympus, Japan). For semi-quantitative evaluation, histomorphometric analyses were performed according to a previously reported method [27] with slight modifications. The bone tissue area and residual scaffold materials area were measured using ImageJ software (National Institutes of Health, Bethesda, MD, USA) in three randomly selected areas ($1 \times 1 \text{ mm}^2$) per histological section. The bone area and residual scaffold materials area were expressed as the percentages of the total tissue area measured in each group.

2.7. Statistical Analysis. Quantitative data are presented as the mean \pm standard deviation. Statistical differences between groups were evaluated by the Student's t -test using SPSS 13.0 (SPSS Science). The critical level of statistical significance was set at $P < 0.05$.

3. Results and Discussion

3.1. Physicochemical Properties of $n\text{-}\beta\text{-TCP/Col}$ Scaffolds. Figure 1 shows the morphology and structure of $n\text{-}\beta\text{-TCP/Col}$ scaffolds. The composite scaffolds were white and opaque with spongy appearance (Figure 1(a)) and interconnected porous structure. $\beta\text{-TCP}$ particles were distributed well and homogeneously in the skeleton network of collagen fibrils (Figure 1(b)). The network structure of collagen fibrils was caused by the acidic environment during fabrication. Collagen fibrils are composed of numerous polypeptide chains with carboxyl groups that interconnect via covalent and hydrogen bonds [28]. In dilute acid solutions, H^+ ions tend to react with these polypeptide chains, leading to the disassembly of the collagen fibrils and subsequent formation of a network structure. The porosity of the composite scaffolds was around 95%. The interconnected porous structure may have beneficial effects on cell proliferation and nutritive transportation for applications in bone tissue engineering [29]. In FT-IR spectra (Figure 1(c)), adsorption bands were clearly detected, which corresponded to $\beta\text{-TCP}$ (PO_4^{3-} : 1627 and 1572 cm^{-1}) and collagen (COO^- : ~ 1541 , 1448 , and 1399 cm^{-1}). These results further confirmed that $n\text{-}\beta\text{-TCP/Col}$ scaffolds with an integrated structure can be formed by acid-treated collagen and nanosized $\beta\text{-TCP}$ particles through chemical bonds.

3.2. Bioactivity of BMSCs in $n\text{-}\beta\text{-TCP/Col}$ Scaffolds In Vitro. In the present study, we isolated and purified rabbit BMSCs based on their ability to form adherent clonogenic cell clusters. The isolated BMSCs formed adherent colonies in which the majority of the cells exhibited fibroblastic spindle shapes

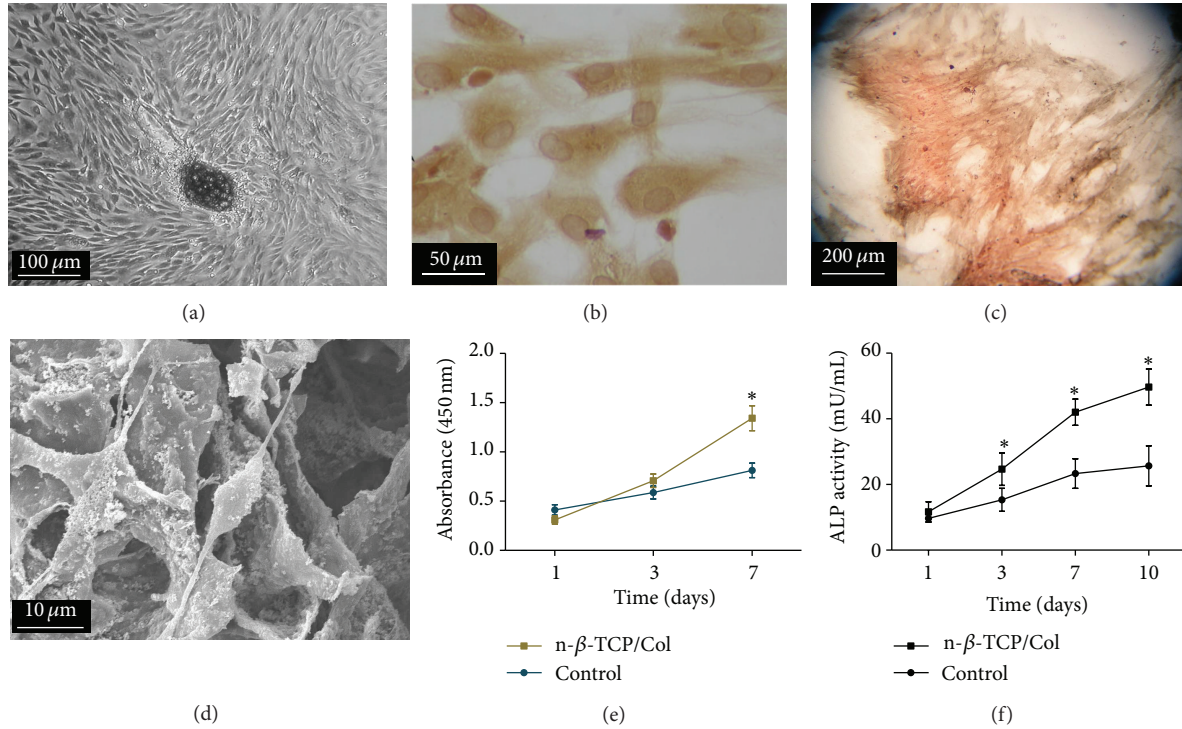


FIGURE 2: Characterization of rabbit BMSCs and *in vitro* bioactivity of BMSCs in $n\text{-}\beta\text{-TCP/Col}$ scaffolds. (a) Micrograph of BMSCs cultured in regular medium for 3 days. (b) CD34 immunohistological staining of BMSCs cultured in regular medium. (c) ALP staining of passage 3 BMSCs cultured in osteogenic medium for 7 days. (d) SEM micrographs of induced BMSCs in the $n\text{-}\beta\text{-TCP/Col}$ scaffolds after 3 days of culture. (e) CCK-8 assay results of the proliferation of BMSCs in $n\text{-}\beta\text{-TCP/Col}$ scaffolds at various time points. (f) Change of ALP activity in BMSCs in direct contact with the $n\text{-}\beta\text{-TCP/Col}$ scaffolds after 10 days of incubation in osteogenic medium (BMSCs cultured on tissue culture plates were used as the control).

(Figure 2(a)). Positive staining for CD34 confirmed that the cells displayed a characteristic of BMSCs (Figure 2(b)). To investigate their osteogenic differentiation potential, the cells were cultured in osteogenic medium. After 7 days of induction, the cells showed extensive positive staining for ALP, thereby exhibiting an osteogenic phenotype (Figure 2(c)). Figure 2(d) shows representative phase-contrast micrographs of BMSCs attached to the scaffolds after 3 days of culture. BMSCs mostly showed a fusiform shape, and they were adhered well to the scaffold surfaces and bridged the micropores with their pseudopodia. These features indicated that the scaffold appeared to have no negative effects on cell morphology and viability. The results of cell proliferation assays are shown in Figure 2(e). At day 3, there was no significant difference in the cell number between BMSCs seeded in $n\text{-}\beta\text{-TCP/Col}$ scaffolds and cells cultured on tissue culture plates (TCPS). At day 7, there were more cells in the $n\text{-}\beta\text{-TCP/Col}$ scaffolds compared with those in TCPS. This higher level of cell proliferation may be attributed to the porous structure of the $n\text{-}\beta\text{-TCP/Col}$ scaffolds, which provides a large surface area for cell spreading [30]. Collectively, these results indicate that the $n\text{-}\beta\text{-TCP/Col}$ scaffolds promote the attachment and proliferation of BMSCs.

Differentiation of BMSCs is a key process for bone regeneration. In our *in vitro* experiments, differentiation of the BMSCs into osteoblastic cells in $n\text{-}\beta\text{-TCP/Col}$ scaffolds was quantitatively measured by ALP activity (Figure 2(f)). ALP

activity is an early marker that identifies osteoblastic cells and is considered as an important factor in bone differentiation and mineralization [31, 32]. After 1 day of osteogenic stimulation, low ALP activity was detected, indicating few BMSCs had differentiated into osteoblastic cells. However, after further stimulation, the level of ALP activity increased substantially ($P < 0.05$). These results indicate that $n\text{-}\beta\text{-TCP/Col}$ scaffolds improve the osteogenic differentiation ability of BMSCs.

3.3. Osteogenesis of BMSCs Hybridized with $n\text{-}\beta\text{-TCP/Col}$ Scaffolds *In Vivo*. To evaluate the osteogenic potential and effects of autologous BMSCs in $n\text{-}\beta\text{-TCP/Col}$ scaffolds *in vivo*, a rabbit mandible defect was selected to assess the performance of the biomaterial [23]. A critical-sized defect model is imperative for the evaluation of biomaterials in bone defect repair [33, 34]. Therefore, we established a critical defect ($10 \times 8 \times 3 \text{ mm}^3$) in the mandible of each rabbit. During the experiment, all rabbits remained in good health and did not show any wound complications.

Figure 3 shows macroscopic images of the implantation. At 4 weeks after implantation, the surface of defects in the only scaffolds group was partially filled with callus bone, while a large proportion of the residual scaffold was observed in the defect site (Figure 3(a1)). In contrast, a larger area was filled with callus bone in defects implanted

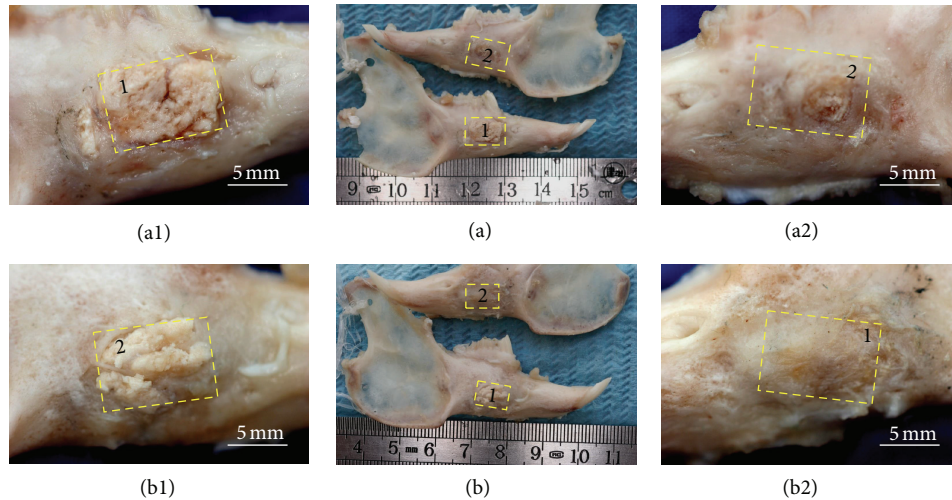


FIGURE 3: Macroscopic images of the implantation sites at 4 weeks (a) and 8 weeks (b). (a1 and b1) $n\text{-}\beta\text{-TCP/Col}$ scaffolds and (a2 and b2) BMSC/scaffold constructs.

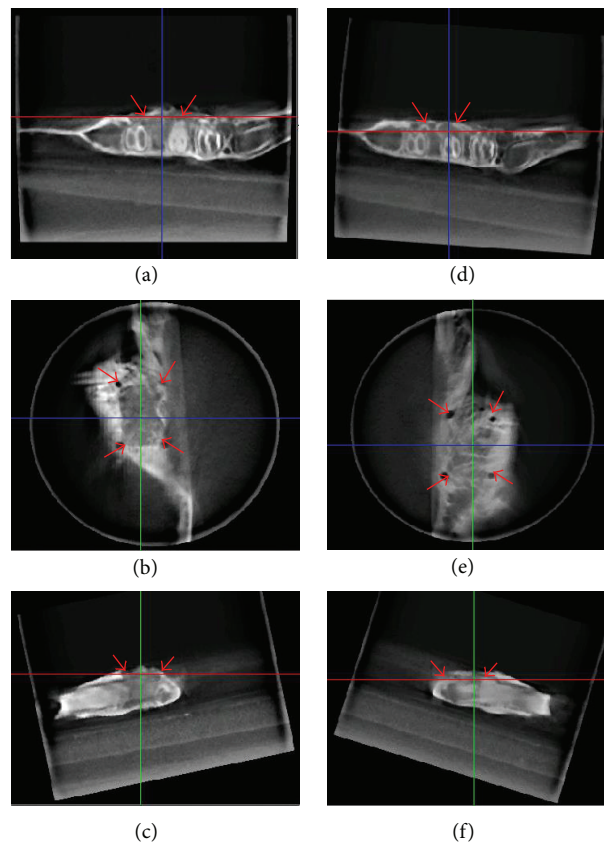


FIGURE 4: CBCT images of rabbit mandible defects with $n\text{-}\beta\text{-TCP/Col}$ scaffolds (a–c) or BMSC/scaffold constructs (d–f) at 8 weeks after implantation. (a, d) Coronal section, (b, e) sagittal section, (c, f) and horizontal section. Red arrows denote the surgical site.

with BMSC/scaffold constructs, and the boundary between scaffolds and host bone was unclear because of active osteogenesis in the implantation area (Figure 3(a2)). At 8 weeks after implantation, the wounds were well healed and there were few differences in the hardness and appearance of newly formed bone and normal osseous tissues in

the BMSC/scaffold construct group (Figure 3(b2)). In contrast, in the only scaffolds group, there was still a proportion of the scaffolds retained in the defects (Figure 3(b1)), which was confirmed by CBCT scanning (Figure 4). These results indicate that BMSC/scaffold constructs provide a better osteogenic outcome than that of pure scaffolds.

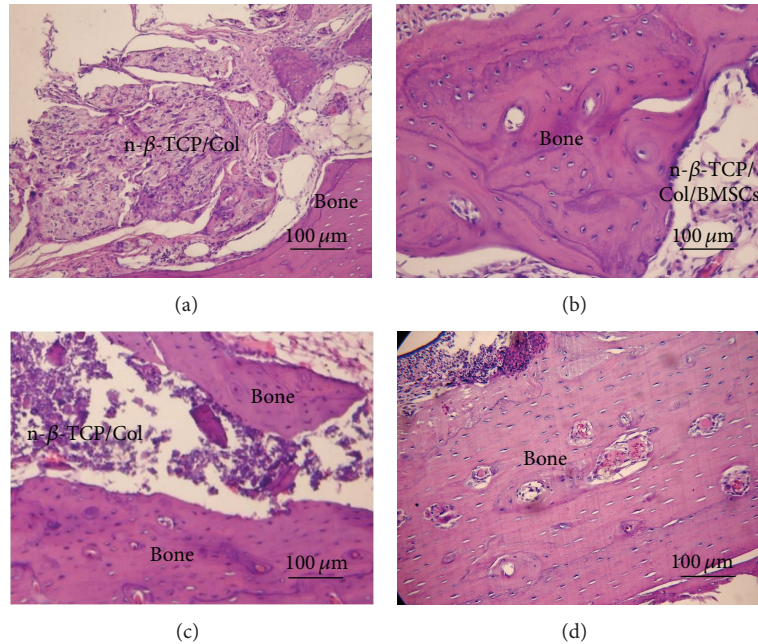


FIGURE 5: Histological images of mandible defects at 4 weeks (a, b) and 8 weeks (c, d) after implantation of $n\text{-}\beta\text{-TCP/Col}$ scaffolds (a, c) and BMSC/scaffold constructs (b, d).

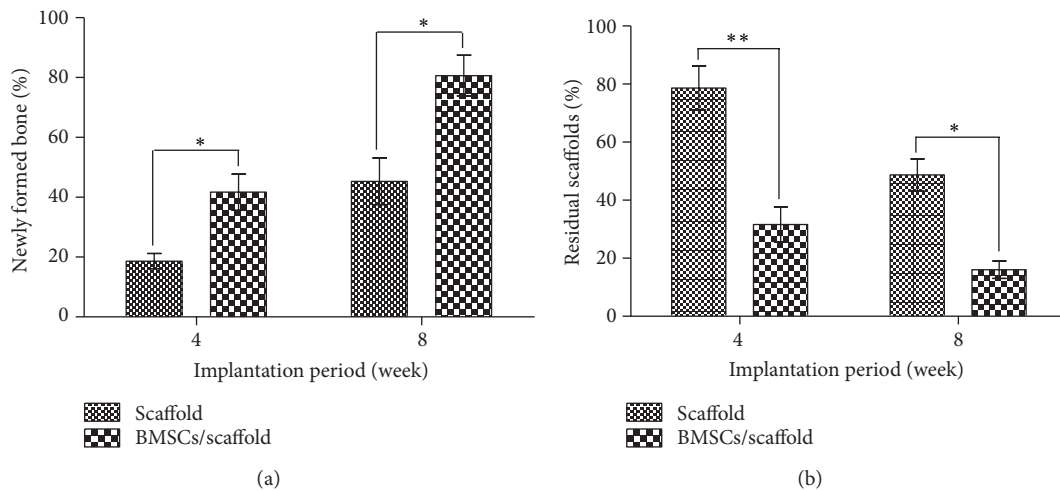


FIGURE 6: Newly formed bone area (a) and residual scaffolds area (b) in rabbit mandible defects at 4 and 8 weeks after implantation.

Figure 5 shows the histological results of mandible defect repair, indicating different trends of bone regeneration and scaffolds degradation from the two groups. In the scaffolds only group, the defect was mainly occupied by an abundance of residual scaffolds with a dense structure at 4 weeks after implantation (Figure 5(a)). In addition, residual scaffolds were present in the defect despite the obvious appearance of newly formed bone at 8 weeks after implantation (Figure 5(c)). In contrast, BMSC/scaffold constructs exhibited not only high biocompatibility but also faster and more efficient osteogenesis in the defect area. At 4 weeks after implantation, a small amount of residual scaffolds with a loose structure was observed in the center of defects that were mostly dominated by newly formed bone (Figure 5(b)).

Moreover, osteoblasts (an indication of bone formation) were observed at the interface between the scaffolds and bone. From these results, seeded BMSCs might differentiate into osteoblast *in vivo* and probably account for the improved bone formation, which is consistent with previous report [23]. At 8 weeks after implantation, there was almost complete restoration of the bone defects with little residual materials (Figure 5(d)). The histological observations were confirmed by quantitative analyses of the percentages of newly formed bone and residual scaffolds (Figure 6).

These results indicate that incorporation of *in vitro* expanded autologous BMSCs into the porous $n\text{-}\beta\text{-TCP/Col}$ scaffolds enhances the efficiency of bone regeneration, especially during the initial period after implantation. Our

findings can be explained by the fact that the interconnected macropores of the $n\text{-}\beta\text{-TCP/Col}$ scaffolds facilitate cell infiltration into the interior of the scaffolds [35]. When culture-expanded autologous BMSCs at a relatively high cell density are preseeded into scaffolds, BMSCs differentiate towards osteoblasts during the early period after implantation, which increases the rate of bone regeneration. In summary, the $n\text{-}\beta\text{-TCP/Col}$ scaffolds hybridized with culture-expanded autologous BMSCs presented not only high biocompatibility but also faster and more effective bone defect restoration.

4. Conclusions

In the present study, we have successfully prepared porous $n\text{-}\beta\text{-TCP/Col}$ composite scaffolds with an interconnected porous structure and $\beta\text{-TCP}$ particles that are homogeneously distributed in the skeleton network of the collagen fibrils. Our results show that $n\text{-}\beta\text{-TCP/Col}$ scaffolds exhibit high biocompatibility *in vitro*. Introduction of autologous BMSCs into the scaffolds dramatically enhances the efficiency of critical-sized bone defects restoration, especially during the initial stage after implantation. Collectively, these results suggest that culture-expanded autologous BMSCs in $n\text{-}\beta\text{-TCP/Col}$ scaffolds have the potential to be applied in bone tissue engineering.

Conflict of Interests

The authors declare that there is no conflict of interests regarding the publication of this paper.

Authors' Contribution

Xuehui Zhang and Mingming Xu equally contributed to this paper.

Acknowledgments

This work was supported by the National Basic Research Program of China (2012CB933900), Beijing Municipal Science and Technology Commission (Z121100005212007), the National Natural Science Foundation of China (81171000), and the National High Technology Research and Development Program of China (2012AA022501). Additionally, the authors also would like to acknowledge the support of the Peking University-Tsinghua University Joint Center for Life Sciences.

References

- [1] J. O. Hollinger and J. C. Kleinschmidt, "The critical size defect as an experimental model to test bone repair materials," *The Journal of Craniofacial Surgery*, vol. 1, no. 1, pp. 60–68, 1990.
- [2] Y. Liu, G. Wu, and K. De Groot, "Biomimetic coatings for bone tissue engineering of critical-sized defects," *Journal of the Royal Society Interface*, vol. 7, supplement 5, pp. S631–S647, 2010.
- [3] T. Liu, G. Wu, D. Wismeijer, Z. Gu, and Y. Liu, "Deproteinized bovine bone functionalized with the slow delivery of BMP-2 for the repair of critical-sized bone defects in sheep," *Bone*, vol. 56, no. 1, pp. 110–118, 2013.
- [4] M. H. Mankani, S. A. Kuznetsov, R. M. Wolfe, G. W. Marshall, and P. G. Robey, "In vivo bone formation by human bone marrow stromal cells: reconstruction of the mouse calvarium and mandible," *Stem Cells*, vol. 24, no. 9, pp. 2140–2149, 2006.
- [5] M. Nishikawa, A. Myoui, H. Ohgushi, M. Ikeuchi, N. Tamai, and H. Yoshikawa, "Bone tissue engineering using novel interconnected porous hydroxyapatite ceramics combined with marrow mesenchymal cells: quantitative and three-dimensional image analysis," *Cell Transplantation*, vol. 13, no. 4, pp. 367–376, 2004.
- [6] M. C. Kruyt, C. Persson, G. Johansson, W. J. A. Dhert, and J. D. De Bruijn, "Towards injectable cell-based tissue-engineered bone: the effect of different calcium phosphate microparticles and pre-culturing," *Tissue Engineering*, vol. 12, no. 2, pp. 309–317, 2006.
- [7] A. Minamide, M. Yoshida, M. Kawakami et al., "The use of cultured bone marrow cells in type I collagen gel and porous hydroxyapatite for posterolateral lumbar spine fusion," *Spine*, vol. 30, no. 10, pp. 1134–1138, 2005.
- [8] J. Yuan, L. Cui, W. J. Zhang, W. Liu, and Y. Cao, "Repair of canine mandibular bone defects with bone marrow stromal cells and porous β -tricalcium phosphate," *Biomaterials*, vol. 28, no. 6, pp. 1005–1013, 2007.
- [9] G. Liu, L. Zhao, W. Zhang, L. Cui, W. Liu, and Y. Cao, "Repair of goat tibial defects with bone marrow stromal cells and β -tricalcium phosphate," *Journal of Materials Science*, vol. 19, no. 6, pp. 2367–2376, 2008.
- [10] D. W. Huttmacher, "Scaffolds in tissue engineering bone and cartilage," *Biomaterials*, vol. 21, no. 24, pp. 2529–2543, 2000.
- [11] A. J. Salgado, O. P. Coutinho, and R. L. Reis, "Bone tissue engineering: state of the art and future trends," *Macromolecular Bioscience*, vol. 4, no. 8, pp. 743–765, 2004.
- [12] K. Kurashina, H. Kurita, Q. Wu, A. Ohtsuka, and H. Kobayashi, "Ectopic osteogenesis with biphasic ceramics of hydroxyapatite and tricalcium phosphate in rabbits," *Biomaterials*, vol. 23, no. 2, pp. 407–412, 2002.
- [13] J. Dong, T. Uemura, Y. Shirasaki, and T. Tateishi, "Promotion of bone formation using highly pure porous β -TCP combined with bone marrow-derived osteoprogenitor cells," *Biomaterials*, vol. 23, no. 23, pp. 4493–4502, 2002.
- [14] K.-Y. Chen, C.-M. Chung, Y.-S. Chen, D.-T. Bau, and C.-H. Yao, "Rat bone marrow stromal cells-seeded porous gelatin/tricalcium phosphate/oligomeric proanthocyanidins composite scaffold for bone repair," *Journal of Tissue Engineering and Regenerative Medicine*, vol. 7, no. 9, pp. 708–719, 2013.
- [15] X. Liu and P. X. Ma, "Polymeric scaffolds for bone tissue engineering," *Annals of Biomedical Engineering*, vol. 32, no. 3, pp. 477–486, 2004.
- [16] S. J. Hollister, "Porous scaffold design for tissue engineering," *Nature Materials*, vol. 4, no. 7, pp. 518–524, 2005.
- [17] G. Wei and P. X. Ma, "Structure and properties of nano-hydroxyapatite/polymer composite scaffolds for bone tissue engineering," *Biomaterials*, vol. 25, no. 19, pp. 4749–4757, 2004.
- [18] H. H. K. Xu and C. G. Simon Jr., "Fast setting calcium phosphate-chitosan scaffold: mechanical properties and biocompatibility," *Biomaterials*, vol. 26, no. 12, pp. 1337–1348, 2005.
- [19] B. M. B. Brkovic, H. S. Prasad, M. D. Rohrer et al., "Beta-tricalcium phosphate/type I collagen cones with or without a barrier membrane in human extraction socket healing: clinical, histologic, histomorphometric, and immunohistochemical

- evaluation,” *Clinical Oral Investigations*, vol. 16, no. 2, pp. 581–590, 2012.
- [20] J. E. Mate-Sanchez de Val, P. Mazon, J. L. Guirado et al., “Comparison of three hydroxyapatite/beta-tricalciumphosphate/collagen ceramic scaffolds: an *in vivo* study,” *Journal of Biomedical Materials Research A*. In press.
- [21] T. Matsuno, T. Nakamura, K.-I. Kuremoto et al., “Development of β -tricalcium phosphate/collagen sponge composite for bone regeneration,” *Dental Materials Journal*, vol. 25, no. 1, pp. 138–144, 2006.
- [22] C. Zou, W. Weng, X. Deng et al., “Preparation and characterization of porous β -tricalcium phosphate/collagen composites with an integrated structure,” *Biomaterials*, vol. 26, no. 26, pp. 5276–5284, 2005.
- [23] H. Wang, Y. Li, Y. Zuo, J. Li, S. Ma, and L. Cheng, “Biocompatibility and osteogenesis of biomimetic nano-hydroxyapatite/polyamide composite scaffolds for bone tissue engineering,” *Biomaterials*, vol. 28, no. 22, pp. 3338–3348, 2007.
- [24] Y. Li, W. Weng, K. Cheng et al., “Preparation of amorphous calcium phosphate in the presence of poly(ethylene glycol),” *Journal of Materials Science Letters*, vol. 22, no. 14, pp. 1015–1016, 2003.
- [25] C. Zou, W. Weng, X. Deng et al., “Preparation and characterization of porous β -tricalcium phosphate/collagen composites with an integrated structure,” *Biomaterials*, vol. 26, no. 26, pp. 5276–5284, 2005.
- [26] X. Zhang, Q. Cai, H. Liu et al., “Osteoconductive effectiveness of bone graft derived from antler cancellous bone: an experimental study in the rabbit mandible defect model,” *International Journal of Oral & Maxillofacial Surgery*, vol. 41, no. 11, pp. 1330–1337, 2012.
- [27] Y. Sawada, A. Hokugo, Y. Yang et al., “A novel hydroxyapatite ceramic bone substitute transformed by ostrich cancellous bone: characterization and evaluations of bone regeneration activity,” *Journal of Biomedical Materials Research B*, vol. 98, no. 2, pp. 217–222, 2011.
- [28] M.J. Beckman, K.J. Shields, and R. F. Diegelmann, “Collagen,” in *Encyclopedia of Biomaterials and Biomedical Engineering*, G. E. Wnek and G. L. Bowlin, Eds., pp. 324–334, Marcel Dekker, New York, NY, USA, 2004.
- [29] S. P. Bruder and B. S. Fox, “Tissue engineering of bone: cell based strategies,” *Clinical Orthopaedics and Related Research*, no. 367, supplement, pp. S68–S83, 1999.
- [30] H.-W. Kim, H.-E. Kim, and V. Salih, “Stimulation of osteoblast responses to biomimetic nanocomposites of gelatin-hydroxyapatite for tissue engineering scaffolds,” *Biomaterials*, vol. 26, no. 25, pp. 5221–5230, 2005.
- [31] R. Marom, I. Shur, R. Solomon, and D. Benayahu, “Characterization of adhesion and differentiation markers of osteogenic marrow stromal cells,” *Journal of Cellular Physiology*, vol. 202, no. 1, pp. 41–48, 2005.
- [32] U. Stucki, J. Schmid, C. F. Hämmerle, and N. P. Lang, “Temporal and local appearance of alkaline phosphatase activity in early stages of guided bone regeneration. A descriptive histochemical study in humans,” *Clinical Oral Implants Research*, vol. 12, no. 2, pp. 121–127, 2001.
- [33] K. Kurashina, H. Kurita, A. Kotani, H. Takeuchi, and M. Hirano, “*In vivo* study of a calcium phosphate cement consisting of α -tricalcium phosphate/dicalcium phosphate dibasic/tetracalcium phosphate monoxide,” *Biomaterials*, vol. 18, no. 2, pp. 147–151, 1997.
- [34] M. Kikuchi, Y. Koyama, T. Yamada et al., “Development of guided bone regeneration membrane composed of β -tricalcium phosphate and poly(L-lactide-co-glycolide-co- ϵ -caprolactone) composites,” *Biomaterials*, vol. 25, no. 28, pp. 5979–5986, 2004.
- [35] H. Guo, J. Su, J. Wei, H. Kong, and C. Liu, “Biocompatibility and osteogenicity of degradable Ca-deficient hydroxyapatite scaffolds from calcium phosphate cement for bone tissue engineering,” *Acta Biomaterialia*, vol. 5, no. 1, pp. 268–278, 2009.

Research Article

Polymeric Nanosuspensions for Enhanced Dissolution of Water Insoluble Drugs

Roya Yadollahi,¹ Krasimir Vasilev,^{1,2} Clive A. Prestidge,³ and Spomenka Simovic³

¹ Mawson Institute, University of South Australia, Mawson Lakes, SA 5095, Australia

² School of Engineering, University of South Australia, Mawson Lakes, SA 5095, Australia

³ Ian Wark Research Institute, University of South Australia, Mawson Lakes, Adelaide, SA 5095, Australia

Correspondence should be addressed to Spomenka Simovic; spomenka.simovic@unisa.edu.au

Received 2 August 2013; Accepted 1 September 2013

Academic Editor: Haifeng Chen

Copyright © 2013 Roya Yadollahi et al. This is an open access article distributed under the Creative Commons Attribution License, which permits unrestricted use, distribution, and reproduction in any medium, provided the original work is properly cited.

The aim of the present research is to formulate and evaluate polymeric nanosuspensions containing three model water insoluble drugs, nifedipine (NIF), carbamazepine (CBZ), and ibuprofen (IBU) with various physicochemical properties. The nanosuspensions were prepared from hydroxypropyl methylcellulose (HPMC) and polyvinylpyrrolidone (PVP) by a cosolvent technique with polyethylene glycol (PEG-300) and water as the cosolvents. Physicochemical and morphological characteristics of the nanosuspensions (particle size, polydispersity index, and crystallinity) have been correlated with the drug release behaviour. The effects of polymer, drug ratio on the physical, morphological, and dissolution characteristics of the drugs are reported. Drug release is significantly enhanced from the nanosuspensions; for example, the maximum NIF, IBU, and CBZ concentrations after 8-hour dissolution are increased approximately 37, 2, and 1.2 times, respectively, in comparison with the pure powdered drugs. Based on this solubilization enhancement performance, the nanosuspensions have potential for increasing the orally dosed bioavailability of NIF, IBU, and CBZ.

1. Introduction

More than 40% of new chemical entities (NCE) are water insoluble compounds which currently make up 1/3 of the United States Pharmacopeia recognised drugs [1, 2]. Water insoluble compounds (BCS Class II) have poor aqueous solubility and imperfect dissolution, which causes their low bioavailability [3]. Generation of drug nanosuspensions presents one solution to delivery of water insoluble drugs. Nanosuspensions have been defined as drug carriers with particle size range within 10–1000 nm [4]. Therefore, formulating new dosage forms to achieve adequate bioavailability has become a serious and challenging scientific, industrial, and medical issue. Water insoluble drugs are typically formulated with the help of various excipients whose aim is to improve drug dissolution rate and storage stability. Interaction of reactive functional groups of excipients with the drug molecules increases active surface area and consequently dissolution rate [5]. The use of excipients in formulations of insoluble drugs has proven ability to increase

drug dissolution rate, but limitations such as toxicity of some surfactant compounds and limited drug loading have been identified [6]. According to the Noyes-Whitney equation, smaller particle size with higher surface area in contact with biological media leads to an enhanced drug dissolution rate [7, 8]. Hence, scaling down convention drug powders to nanoparticles enhances drug solubility and bioavailability. Nanosuspensions can be prepared by different methods such as high pressure homogenization and media milling. However these techniques have drawbacks such as contamination of final products, broad particle size distributions, and the need for high energy input [9, 10]. The co-solvent technique has been extensively used to prepare *in situ* nanosuspensions [11–17] and has numerous advantages over evaporation or heating-cooling techniques, such as being fast and easy to perform and suitable for thermolabile compounds.

The aim of this work is to explore solid-state and dissolution characteristics of polymeric nanosuspensions prepared by a co-solvent technique. Water insoluble drugs nifedipine (NIF), carbamazepine (CBZ), and ibuprofen (IBU) with

different physiochemical properties (Table 1) were selected and used in realistic extended release doses. Commonly used pharmaceutical polymers hydroxypropyl methylcellulose (HPMC) and polyvinylpyrrolidone (PVP) were used as stabilisers/crystal growth inhibitors [18–21]. In addition to crystal inhibition, the HPMC polymer acts as a hydrophilic matrix agent which forms a strong viscous gel in contact with aqueous media, facilitating extended drug release [22]. The influence of polymer:drug ratio on nanoparticle formation, drug stabilization, and dissolution characteristics were explored. Drug crystallinity and polymorphic forms in nanosuspension polymeric matrices consisting of different polymers ratio were investigated using differential scanning calorimetry (DSC). The molecular structure and specifications of model drugs (nifedipine, carbamazepine, and ibuprofen) and excipients (mannitol, PEG-300, HPMC, and PVP) which were used in this study are presented in Table 1.

2. Materials and Method

2.1. Materials. High-purity (Milli-Q) water was used throughout the study ($\text{pH} = 6.5 \pm 0.5$). PEG-300 (Sigma Aldrich, Australia) was used as the co-solvent. Hydroxypropyl methylcellulose (HPMC) containing 28–30% methoxyl and 7–12% hydroxypropyl content, polyvinylpyrrolidone (PVP), and mannitol: $\geq 98\%$ (Sigma-Aldrich) were used as received. Model drugs (NIF: $\geq 98\%$ TLC, CBZ: $\geq 98\%$ TLC, IBU: $\geq 98\%$ GC) and phosphate buffer ($\text{pH} = 7.4$) were also purchased from Sigma-Aldrich.

2.2. Preparation of Nanosuspensions. Nanosuspensions of model drugs were prepared by the co-solvent technique [30]. This technique includes mixing of two different phases. The first phase (organic phase) is PEG-300 with dissolved model drugs (NIF: 30 mg, CBZ: 400 mg, IBU: 400 mg dissolved in 5 gr of PEG-300). The second phase (aqueous phase) where the model drugs are almost insoluble contains dissolved polymers (HPMC & PVP) (Table 2). The two phases were sonicated for 2 hours. Upon subsequent addition of mannitol (10% w/v), the system was additionally sonicated for 2 hours.

2.3. Freeze Drying/Lyophilization and Redispersibility of Nanosuspensions. Nanosuspension formulations were lyophilized using mannitol as cryoprotectant. The freeze drying (Alpha 1-2 LDplus) was performed at a temperature of -70°C and vacuum 0.09 mbar for 72 hours. The redispersibility of lyophilized samples was investigated by manual shaking of 5 mg in glass vial with 20 mL PBS ($\text{pH} = 7.4$). Formation of aggregates or precipitates was monitored visually.

2.4. Particle Size Analysis. Size and polydispersity index (the width of particle size distribution) of nanosuspensions were measured with dynamic light scattering (Zetasizer Nano ZS, Malvern Instruments, Ltd.). Refractive index values of PBS: $\text{pH} = 7.4$ (1.33) as the continuous phase and HPMC/PVP polymers with refractive index value of 1.45 were used in the

size measurements. Nanosuspensions were diluted 1:100 in PBS ($\text{pH} = 7.4$) and measured in the specified cuvettes at $23 \pm 0.5^\circ\text{C}$ in triplicate.

2.5. Differential Scanning Calorimetry (DSC). Differential scanning calorimetric (DSC) analysis was carried out using TA Instruments model 2920. Samples (5–10 mg) were heated under nitrogen atmosphere on an aluminium pan at a rate of $10^\circ\text{C}/\text{min}$ over the temperature range of 25 and 300°C . An empty pan of the same type was utilized as the reference. DSC thermograms were obtained by using TA universal analysis software. Calibrations of temperature and heat flow were performed with indium.

2.6. In Vitro Release Study. *In vitro* release of model drugs from nanosuspensions was studied for 8 hours using Vankel USP apparatus type 2 (paddle method) at the rotation speed of 50 rpm and 900 mL of phosphate buffer ($\text{pH} = 7.4$) as a dissolution medium. The dissolution test was thermo-regulated at $37 \pm 0.5^\circ\text{C}$. Sample aliquots of 4 mL were withdrawn from the receptor chamber at determined time intervals (0.5, 1, 2, 3, 4, 5, 6, 7, and 8 hours) and replaced with fresh buffer medium. The aliquots were then filtered through a Millipore membrane filter ($0.45 \mu\text{m}$). The concentrations of NIF, IBU, and CBZ in the samples were analysed spectrophotometrically at a wavelength of 234, 263, and 283 nm, respectively.

2.7. Kinetics of Drug Release. In order to investigate the drug release mechanism, *in vitro* release data were fitted by the following equations [31].

(a) Consider zero-order release:

$$Q = Q_0 + K_0 t, \quad (1)$$

where Q is the amount of drug dissolved at particular time, t , Q_0 is the initial amount of drug in solution at $t = 0$, and K_0 is the zero-order release constant.

(b) Consider first-Order release:

$$\ln Q = \ln Q_0 + K_1 t, \quad (2)$$

where K_1 is the first order release constant.

(c) Consider Hixson-Crowell cube root release:

$$Q^{1/3} = Q_0^{1/3} - K_c t, \quad (3)$$

where K_c is the cube root law release constant.

TABLE 1: Characteristics of model water insoluble drugs (NIF, CBZ, and IBU) and excipients (HPMC, PVP, PEG-300, and mannitol) used in this study.

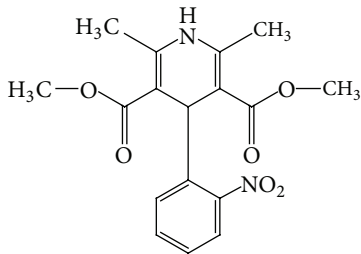
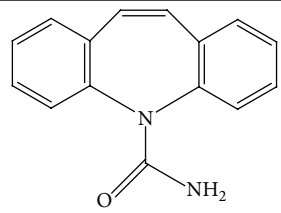
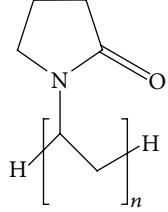
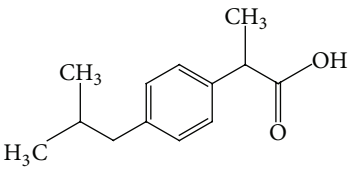
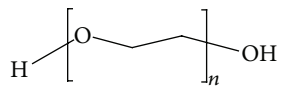
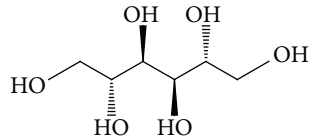
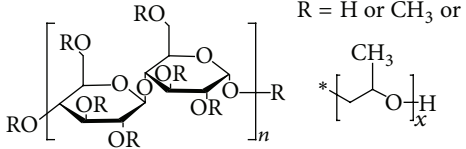
Name and characteristics	Structure
<p><i>Nifedipine</i> Dimethyl 2,6-dimethyl-4-(2-nitrophenyl)-1,4-dihydropyridine-3,5-dicarboxylate Appearance: a yellow crystalline powder Molecular weight: 346.3 Solubility: practically insoluble in water, sparingly in dehydrated alcohol, freely in acetone Indication: calcium channel blocker [23] Log P: 2.2 [24] Solubility in PBS (pH 7): 0.0056 g/L [25]</p>	
<p><i>Carbamazepine</i> 5H-dibenzo[b,f]azepine-5-carboxamide Appearance: a white crystalline powder Molecular weight: 236.3 Solubility: practically insoluble in water, soluble in alcohol and acetone Indication: anticonvulsant and mood-stabilizing [23] Log P: 2.67 [26]</p>	
<p><i>PVP</i> Molecular weight: 29000 Specifications: improving the wettability, dissolution rate, and crystal inhibitor [20, 21, 27]</p>	
<p><i>Ibuprofen</i> (RS)-2-(4-(2-methylpropyl)phenyl)propanoic acid Appearance: a white to off-white crystalline powder Molecular weight: 206.3 Solubility: practically insoluble in water, very soluble in alcohol and acetone, Chloroform, methyl alcohol, slightly soluble in ethyl acetate. Indication: anti-inflammatory [23] Log P: 3.6 [28] Solubility in PBS (pH 7.4): 25.16 mcg/mL [29]</p>	
<p><i>PEG-300</i> Monomer: ethylene oxide Molecular weight: 285–315 Application: cosolvent</p>	
<p><i>Mannitol</i> (2R,3R,4R,5R)-hexan-1,2,3,4,5,6-hexol Application: converting the drug nanosuspensions to a stable solid form and easy redispersibility</p>	
<p><i>HPMC</i> Molecular weight: 86000 Specifications: improving the wettability, dissolution rate, and crystal inhibitor [18, 19, 27]</p>	 <p>R = H or CH₃ or</p>

TABLE 2: Amount of polymers used in nanosuspension formulations.

Drug	Sample label	Organic phase PEG-300 (wt%)	Aqueous phase HPMC/PVP (ratio 1:1) (wt%)
NIF	A ₁	43.36	4.32
	A ₂	31.16	31.2
	A ₃	23.77	47.54
	A ₄	16.11	64.44
CBZ	A ₁	42.01	4.2
	A ₂	30.48	30.5
	A ₃	23.36	46.72
	A ₄	15.92	63.68
IBU	A ₁	42.01	4.2
	A ₂	30.48	30.5
	A ₃	23.36	46.72
	A ₄	15.92	63.68

3. Results and Discussion

3.1. Lyophilization and Redispersibility of Nanoparticles. To remove water from the nanoparticle system, freeze drying, also known as lyophilization, was employed. The basic principle of freeze drying is to remove water from a frozen sample by sublimation and desorption under vacuum [32, 33]. However, the process generates various stresses which destabilise nanoparticles. In order to protect the particles from freezing and desiccation stresses, cryoprotectants or lyoprotectants are incorporated into the formulation before freeze drying. Freeze drying is generally carried out below the T_c temperature. T_c can be defined as collapse temperature in which the particles cannot maintain their microscopic structure. Hence, nanoparticles have the chance to immobilize within the glassy matrix of the cryoprotectants [34].

Lyophilization helps in converting a nanosuspension formulation, that is, liquid dispersion into a solid form which can be reconstituted prior to use. Nanosuspension formulations were lyophilized using mannitol as cryoprotectant at a constant concentration level (10% w/v). Mannitol acts as a carrier which prevents nanoparticle aggregation during the freeze drying process. Figure 1 shows the nanosuspension samples with and without mannitol. Freeze dried nanosuspensions without mannitol appeared as off-white fluffy and sheet-like materials and large aggregates were also observed. Nanosuspensions with mannitol formed a powder easily redispersible in PBS after manual shaking.

3.2. Particle Size and Size Distribution. The effect of the polymer : drug ratio on the size of the nanoparticles was studied using four different batches A₁, A₂, A₃, and A₄. The mean particle size for all different drug formulations (NIF, CBZ, and IBU) varied in the range from 426.4 nm to 995.4 nm. The mean PDI values for all formulations varied in the range of 0.4 to 0.687. It is inferred from the results that the polymer and drug type have significant effect on the particle size. This

could be explained by the interaction of PVP with HPMC in aqueous media. The interaction between the methoxy and hydroxypropoxy groups of HPMC with carbonyl group of PVP creates a hydrogen bonding layer which covers the drug particles [35]. Hence hydrogen bonding prevents or retards crystal growth which results in smaller particle size. The other possible reason could be due to a specific drug-polymer interaction which forms compacted structure at higher polymer concentrations. Figure 2(a) shows that the particle size decreases with increasing the amount of polymers. The particle size of CBZ and IBU in nanosuspension formulations did not show any significant indication regarding the polymer ratio (Figures 2(b) and 2(c)) due to no significant drug-polymer interaction to form a compacted structure.

3.3. In Vitro Drug Dissolution Studies. Several formulations (as shown in Table 2) were prepared to evaluate the effect of the polymer : drug ratio on the drug dissolution profiles. The percentage release of pure drugs and drugs in polymer matrix as a function of time is presented in Figure 3 for the NIF (a), IBU (b), and CBZ (c). It can be seen that solubility of model drugs from the polymer matrix in PBS (PH = 7.4) at $37^\circ\text{C} \pm 0.5^\circ\text{C}$ is higher than that of pure drugs. The data shows that the dissolution of NIF and IBU in the highest concentration of polymer matrix increased approximately 37 and 2 times, respectively, in comparison with the pure drug. Figure 3(c) shows that in the case of CBZ there was only a moderate increase in dissolution (1.2 times) at the highest concentration of polymers used. The general trend is that the extent of dissolution increases with increasing polymers content (Figure 3). Figure 4 illustrates that incorporation of polymers in the formulations has direct influence on the drug release profile compared to pure drug. Possible reasons for increased dissolution of drug nanosuspensions are (a) smaller drug particles in nanosuspension formulation compared to pure drugs, (b) interaction of HPMC and PVP as crystal growth inhibitor of drugs particles, (c) adsorption of drugs on the carriers which leads to increased surface area [36] and (d) methoxy and hydroxypropoxy groups of HPMC with carbonyl group of PVP form a hydrogen bonding with the molecules of drugs, that is, molecular complex formation, which results in improvement of dissolution of model drugs. In addition, the other advantage of using HPMC in the formulation is formation a gel around the particles which forms a barrier against diffusion of the dissolved drugs into dissolution medium and hence controls the release [22].

3.4. Kinetics of Drug Release. The *in vitro* dissolution data were fitted by various kinetic models; the release constants and regression coefficients (R^2) are shown in Table 3. Among the models tested, for the first 2 hours, the drug release profiles for NIF batch A₄ were best fitted by zero-order kinetics based on the regression coefficient (R^2) of 0.9858. Release of the constant amount of drug in specific time points characterises zero order kinetics. The zero-order process indicates that the drug release mechanism is not dependent on the drug concentration [37, 38]. The Hixson-Crowell model which plots the cube root of cumulative percentage of

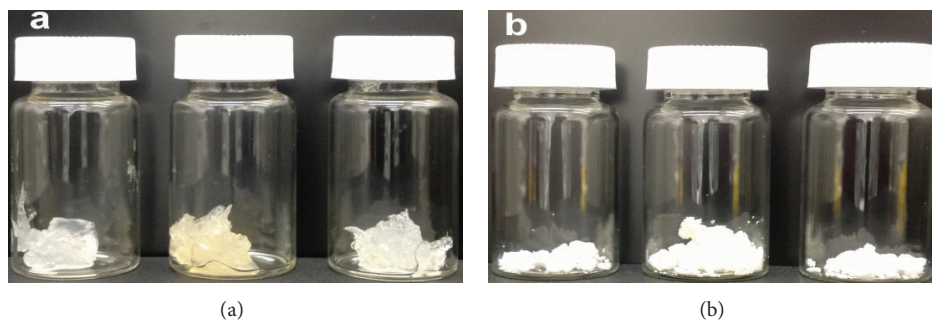


FIGURE 1: Physical state of drugs nanosuspensions without mannitol (a) and with mannitol (b).

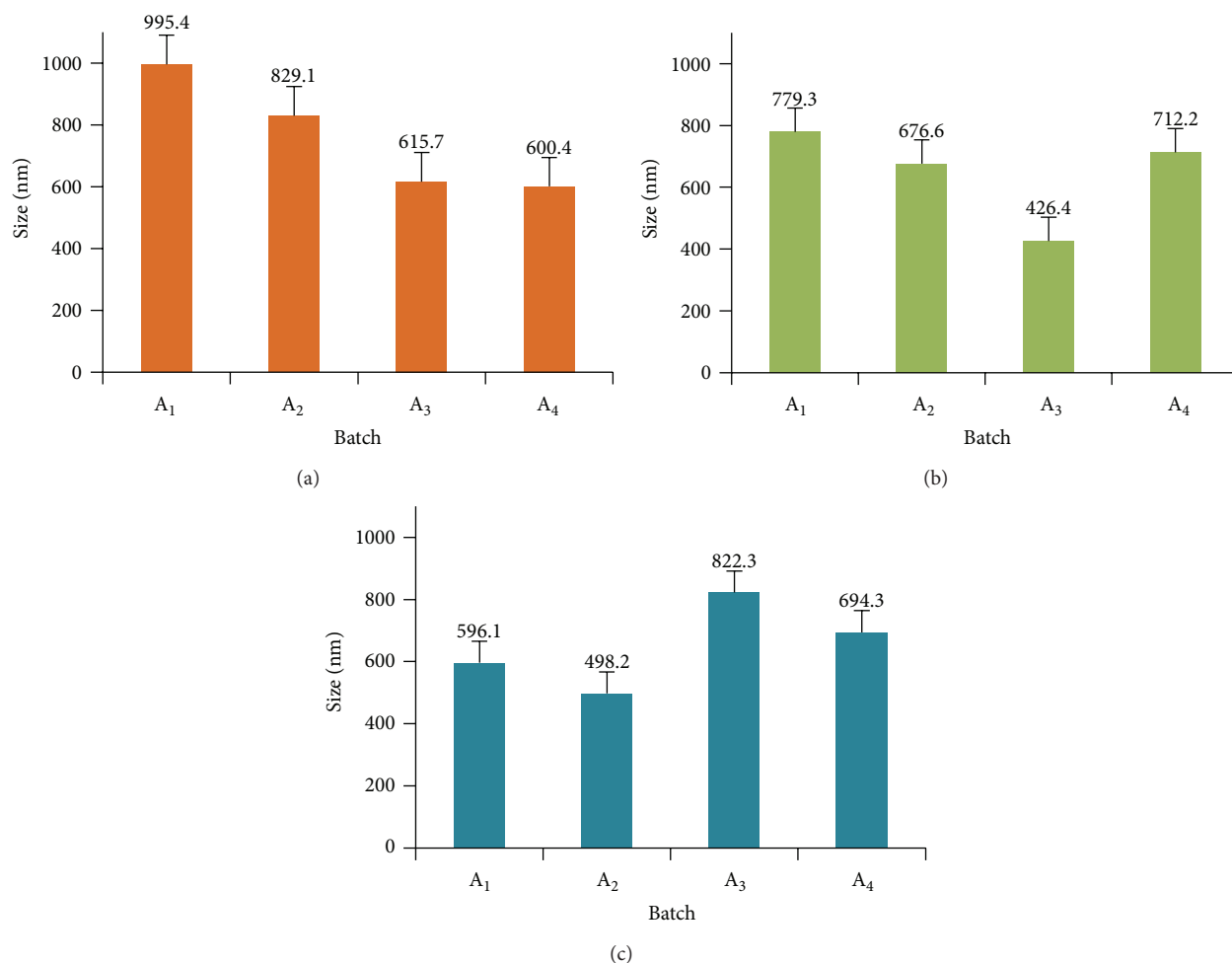


FIGURE 2: Comparison between size and polymer ratio: NIF (a), CBZ (b), and IBU (c) ($n = 3$).

drug release versus the time showed an excellent fit for the batch A₄ of IBU (R^2 : 0.9984). The Hixson-Crowell kinetics describes drug release from systems where there is a change in surface area and diameter of particles [39, 40]. For different CBZ nanosuspensions, no strong indication of fitting was observed. R^2 value for batches A₂, A₃, and A₄ of CBZ was between 0.6836 and 0.8082.

3.5. Differential Scanning Calorimetry (DSC) Studies. Figure 5 shows the DSC curves for pure drugs (NIF, CBZ, and IBU) and drug nanosuspensions with different polymer content. Pure nifedipine, carbamazepine, and ibuprofen exhibit a sharp melting endotherm peaks at 174.76°C, 192.65°C, and 74.77°C, respectively, and corresponding to their melting points and crystalline nature [23]. Figure 5

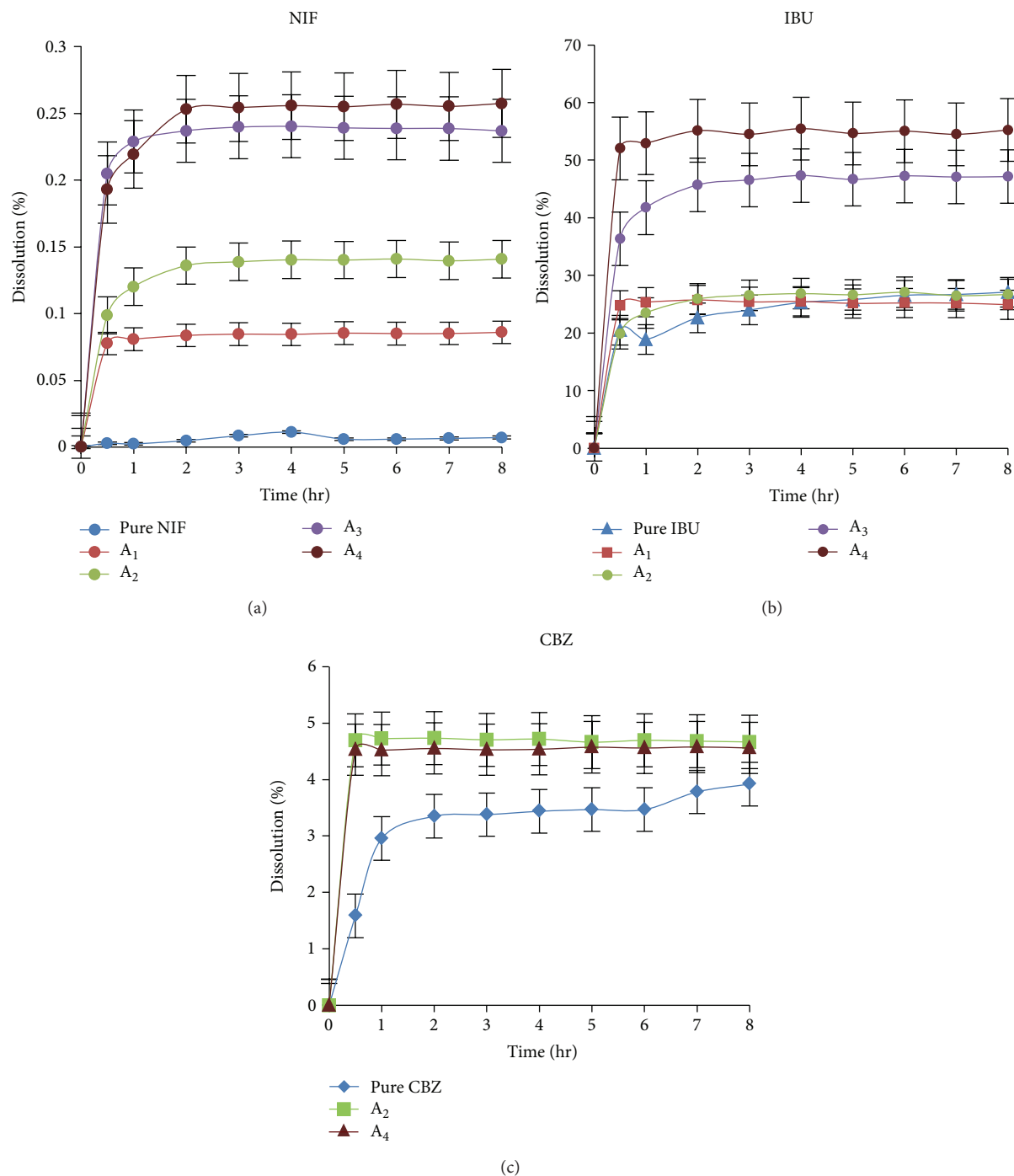


FIGURE 3: *In vitro* release of NIF (a), IBU (b), and CBZ (c) nanosuspensions in phosphate buffer PH = 7.4 at $37^{\circ}\text{C} \pm 0.5^{\circ}\text{C}$ ($n = 3$).

shows that formulations with higher concentration of polymers display lower enthalpy and melting temperature. The reason for such behaviour is polymers-drug interaction which prevents drug particles from rearranging within the polymer network. Figure 5 shows that the drug-free sample (carrier) prepared by the same method (co-solvent method) exhibited two broad melting endotherm peaks at 87.74°C and 159.74°C . The endotherm peaks indicate the partial crystallinity of the carrier. The endotherms peaks of NIF,

CBZ, and IBU nanosuspension formulations are presented in the Table 4. No endotherm peaks corresponding to the melting points of pure crystalline nifedipine, carbamazepine, or ibuprofen were observed. Similar behaviour has been reported for the triamterene in Gelucire 44/14 and PEG [41], cinnarizine in Gelucire 53/10 [42], and paracetamol in PEG 4000 [43]. Hence, the DSC results suggest that drugs progressively dissolved in the polymer matrix upon heating during the DSC measurements. Craig [44] has

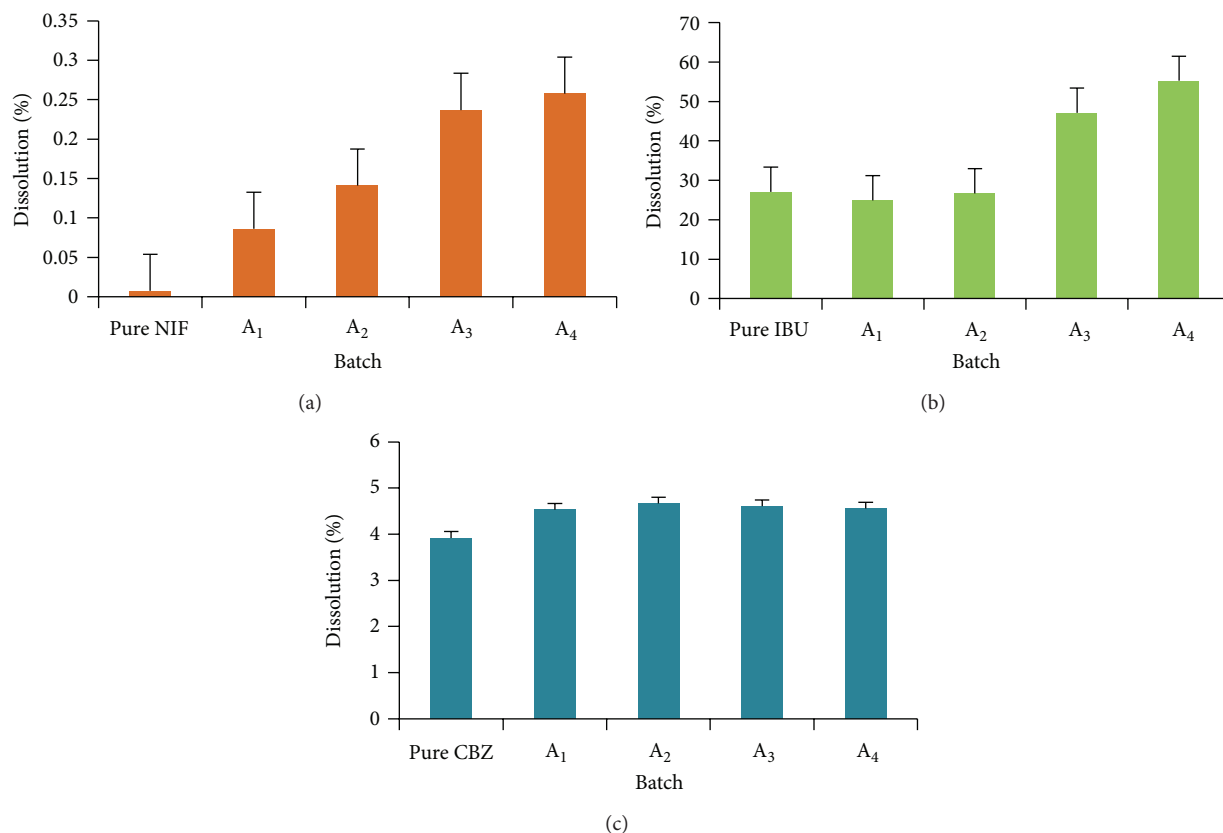


FIGURE 4: Comparison of the dissolution for NIF (a), IBU (b), and CBZ (c) in form of pure drug and nanosuspensions ($n = 3$).

TABLE 3: Kinetic release rate constants and correlation coefficients of various kinetic models (first 2 hours).

Drug	Sample label	Zero order		First order		Hixson-Crowell	
		K_0	R^2	K_1	R^2	K_2	R^2
NIF	A ₁	0.0038	0.9500	0.0471	0.9453	0.0068	0.9469
	A ₂	0.0235	0.9260	0.2001	0.9015	0.0325	0.9099
	A ₃	0.0195	0.7963	0.0881	0.7847	0.0177	0.7885
	A ₄	0.0392	0.9858	0.1754	0.9751	0.0353	0.9790
CBZ	A ₁	0.0045	0.0262	0.0010	0.0263	0.0005	0.0262
	A ₂	0.0214	0.8082	0.0045	0.8076	0.0025	0.8078
	A ₃	0.0064	0.7631	0.0014	0.7630	0.0008	0.7630
	A ₄	0.0171	0.6843	0.0038	0.6836	0.0020	0.6838
IBU	A ₁	0.5817	0.9195	0.0230	0.9167	0.0220	0.9176
	A ₂	3.7847	0.9115	0.0230	0.9167	0.1531	0.8975
	A ₃	5.9004	0.9240	0.1435	0.9065	0.1614	0.9125
	A ₄	2.0760	0.9978	0.0387	0.9982	0.0475	0.9984

previously suggested that the drug may be dissolved in the molten polymer, such as PEG, over a wide range of temperatures. The characteristic DSC peak of the carrier matrix without endothermic peaks due to drug melting indicates that the drugs were dissolved in the molten carrier during the measurements. The DSC and dissolution data indicate that in the presence of polymers, the drugs were

subsequently transformed into their amorphous or molecular forms.

4. Conclusion

The potential of NIF, CBZ, and IBU nanosuspensions for increasing the dissolution rate and extent was demonstrated.

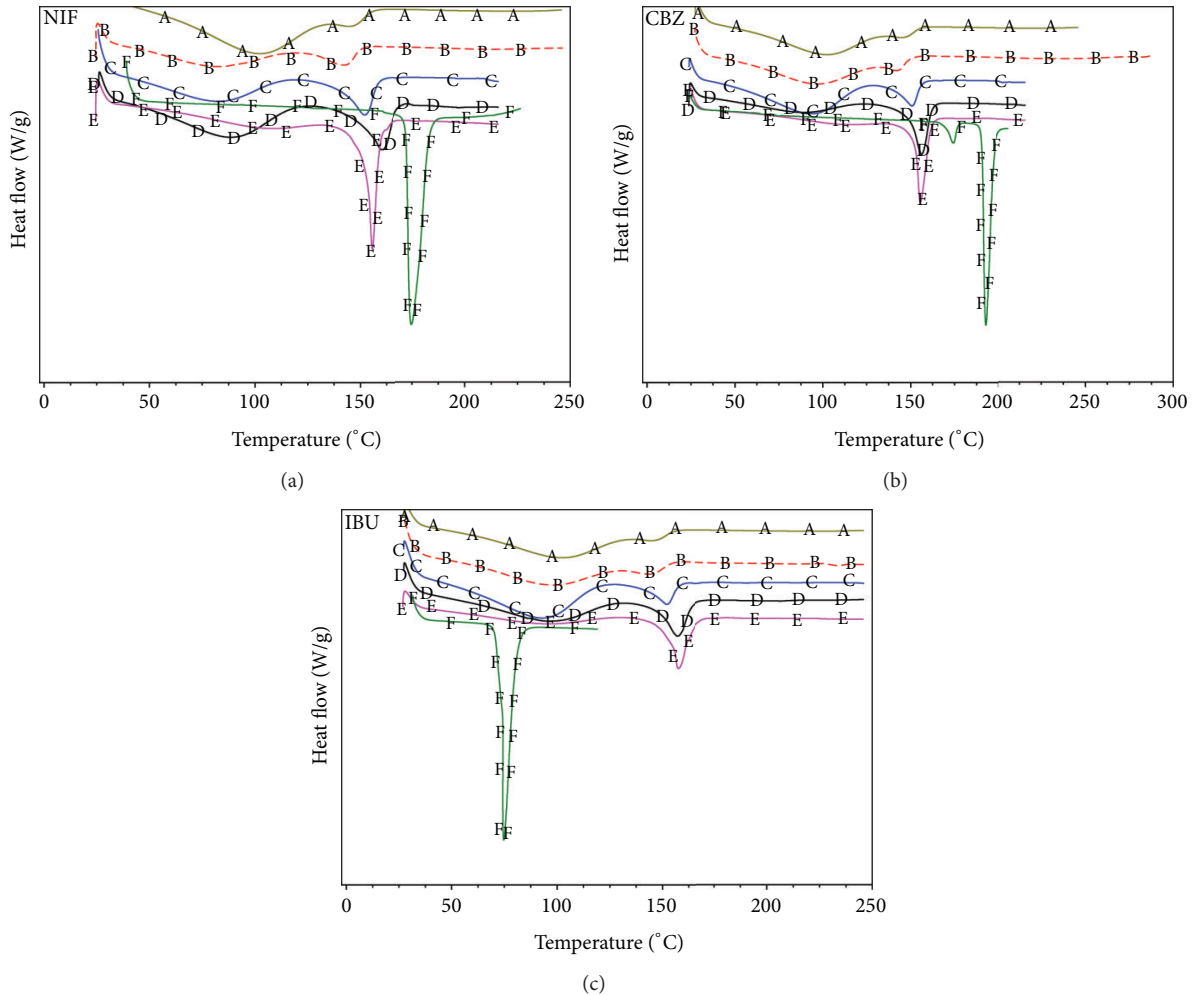


FIGURE 5: DSC thermograms of NIF, CBZ, and IBU: pure drug (F), nanosuspension formulations: batch A₁ (E), batch A₂ (D), batch A₃ (C), batch A₄ (B), and carrier (A) (the spectra are offset in vertical direction for clarification).

TABLE 4: Heat flow and endothermic peaks of drug formulations obtained from DSC measurements.

Drug	Sample label	Heat flow (W/g)	Endotherm peaks (°C)
NIF	A ₁	-2.435	155.69
	A ₂	-1.049 and -1.216	88.93 and 160.46
	A ₃	-0.8706 and -1.053	83.45 and 152.11
	A ₄	-0.804 and -0.7874	82.97 and 142.82
CBZ	A ₁	-2.473	155.69
	A ₂	-0.867 and -1.765	89.41 and 156.17
	A ₃	-1.298 and -1.125	93.70 and 150.68
	A ₄	-1.152 and -0.8744	97.56 and 143.05
IBU	A ₁	-1.69	157.60
	A ₂	-1.082 and -1.404	96.80 and 157.36
	A ₃	-1.318 and -1.024	93.22 and 152.35
	A ₄	-1.115 and -0.8825	98.47 and 145.20

Nanosuspensions were prepared by the cosolvent technique which is a simple method without the need for any complicated instruments. Due to formation of nanosuspensions,

the dissolution rates of drugs were increased in comparison with the pure drugs. The results also showed that extent of dissolution of the drugs from polymer matrix was affected by changing the drug: polymer (HPMC & PVP) ratio and the highest dissolution of NIF (0.26%), CBZ (4.56%), and IBU (55.24%) were observed at the highest concentrations of polymers (batch A₄). The results of DSC studies demonstrated that amorphous fractions of model drugs NIF, CBZ, and IBU increase upon increasing polymer level in the nanosuspension formulations. The results confirmed that the co-solvent technique can be used to prepare drug nanosuspensions using HPMC and PVP as carriers as a means of increasing the dissolution rates.

References

- [1] X. Pu, J. Sun, M. Li, and Z. He, "Formulation of nanosuspensions as a new approach for the delivery of poorly soluble drugs," *Current Nanoscience*, vol. 5, no. 4, pp. 417–427, 2009.
- [2] H. Chen, C. Khemtong, X. Yang, X. Chang, and J. Gao, "Nanonization strategies for poorly water-soluble drugs," *Drug Discovery Today*, vol. 16, no. 7-8, pp. 354–360, 2011.

- [3] Y. Kawabata, K. Wada, M. Nakatani, S. Yamada, and S. Onoue, "Formulation design for poorly water-soluble drugs based on biopharmaceutics classification system: basic approaches and practical applications," *International Journal of Pharmaceutics*, vol. 420, no. 1, pp. 1–10, 2011.
- [4] R. H. Muller, R. Becker, B. Kruss, and K. Peters, "Pharmaceutical nanosuspensions for medicament administration as systems with increased saturation solubility and rate of solution," US Patent 5858410, 1999, <http://www.google.com.au/patents/US5858410>.
- [5] G. Pifferi and P. Restani, "The safety of pharmaceutical excipients," *Farmaco*, vol. 58, no. 8, pp. 541–550, 2003.
- [6] G. C. S. Rao, M. S. Kumar, N. Mathivanan, and M. E. B. Rao, "Nanosuspensions as the most promising approach in nanoparticulate drug delivery systems," *Pharmazie*, vol. 59, no. 1, pp. 5–9, 2004.
- [7] V. B. Patravale, A. A. Date, and R. M. Kulkarni, "Nanosuspensions: a promising drug delivery strategy," *Journal of Pharmacy and Pharmacology*, vol. 56, no. 7, pp. 827–840, 2004.
- [8] R. O. Williams III, A. B. Watts, and D. A. Miller, *Formulating Poorly Water Soluble Drugs*, Springer, New York, NY, USA, 2012.
- [9] V. Kharb, M. Bhatia, H. Dureja, and D. Kaushik, "Nanoparticle technology for the delivery of poorly water-soluble drugs," *Pharmaceutical Technology*, vol. 30, no. 2, pp. 82–92, 2006.
- [10] C. M. Keck and R. H. Müller, "Drug nanocrystals of poorly soluble drugs produced by high pressure homogenisation," *European Journal of Pharmaceutics and Biopharmaceutics*, vol. 62, no. 1, pp. 3–16, 2006.
- [11] K. Moser, K. Kriwet, Y. N. Kalia, and R. H. Guy, "Stabilization of supersaturated solutions of a lipophilic drug for dermal delivery," *International Journal of Pharmaceutics*, vol. 224, no. 1–2, pp. 169–176, 2001.
- [12] S. L. Raghavan, A. Trividic, A. F. Davis, and J. Hadgraft, "Crystallization of hydrocortisone acetate: influence of polymers," *International Journal of Pharmaceutics*, vol. 212, no. 2, pp. 213–221, 2001.
- [13] S. L. Raghavan, K. Schuessel, A. Davis, and J. Hadgraft, "Formation and stabilisation of triclosan colloidal suspensions using supersaturated systems," *International Journal of Pharmaceutics*, vol. 261, no. 1–2, pp. 153–158, 2003.
- [14] R. G. Strickley, "Solubilizing excipients in oral and injectable formulations," *Pharmaceutical Research*, vol. 21, no. 2, pp. 201–230, 2004.
- [15] U. Kumprakob, J. Kawakami, and I. Adachi, "Permeation enhancement of ketoprofen using a supersaturated system with antinucleant polymers," *Biological and Pharmaceutical Bulletin*, vol. 28, no. 9, pp. 1684–1688, 2005.
- [16] M. C. Lamas, L. Villaggi, I. Nocito et al., "Development of parenteral formulations and evaluation of the biological activity of the trypanocide drug benznidazole," *International Journal of Pharmaceutics*, vol. 307, no. 2, pp. 239–243, 2006.
- [17] N. Leveque, S. L. Raghavan, M. E. Lane, and J. Hadgraft, "Use of a molecular form technique for the penetration of supersaturated solutions of salicylic acid across silicone membranes and human skin in vitro," *International Journal of Pharmaceutics*, vol. 318, no. 1–2, pp. 49–54, 2006.
- [18] M. Iervolino, B. Cappello, S. L. Raghavan, and J. Hadgraft, "Penetration enhancement of ibuprofen from supersaturated solutions through human skin," *International Journal of Pharmaceutics*, vol. 212, no. 1, pp. 131–141, 2001.
- [19] M. Iervolino, S. L. Raghavan, and J. Hadgraft, "Membrane penetration enhancement of ibuprofen using supersaturation," *International Journal of Pharmaceutics*, vol. 198, no. 2, pp. 229–238, 2000.
- [20] R. Nair, S. Gonen, and S. W. Hoag, "Influence of polyethylene glycol and povidone on the polymorphic transformation and solubility of carbamazepine," *International Journal of Pharmaceutics*, vol. 240, no. 1–2, pp. 11–22, 2002.
- [21] H. Sekikawa, M. Nakano, and T. Arita, "Inhibitory effect of polyvinylpyrrolidone on the crystallization of drugs," *Chemical and Pharmaceutical Bulletin*, vol. 26, no. 1, pp. 118–126, 1978.
- [22] E. Karavas, E. Georgarakis, and D. Bikiaris, "Application of PVP/HPMC miscible blends with enhanced mucoadhesive properties for adjusting drug release in predictable pulsatile chronotherapeutics," *European Journal of Pharmaceutics and Biopharmaceutics*, vol. 64, no. 1, pp. 115–126, 2006.
- [23] S. C. Sweetman, *Martindale: The Complete Drug Reference*, Pharmaceutical Press, 2007.
- [24] C. Jamaty, B. Bailey, A. Larocque, E. Notebaert, K. Sanogo, and J. M. Chauny, "Lipid emulsions in the treatment of acute poisoning: a systematic review of human and animal studies," *Clinical Toxicology*, vol. 48, no. 1, pp. 1–27, 2010.
- [25] S. L. Ali and K. Florey, *Analytical Profiles of Drug Substances*, Academic Press, San Diego, Calif, USA, 1989.
- [26] A. F. El-Kattan, C. S. Asbill, N. Kim, and B. B. Michniak, "The effects of terpene enhancers on the percutaneous permeation of drugs with different lipophilicities," *International Journal of Pharmaceutics*, vol. 215, no. 1–2, pp. 229–240, 2001.
- [27] C. Leuner and J. Dressman, "Improving drug solubility for oral delivery using solid dispersions," *European Journal of Pharmaceutics and Biopharmaceutics*, vol. 50, no. 1, pp. 47–60, 2000.
- [28] P. K. Lakshmi, M. K. Kumar, A. Sridharan, and S. Bhaskaran, "Formulation and evaluation of ibuprofen topical gel: a novel approach for penetration enhancement," *International Journal of Applied Pharmaceutics*, vol. 3, no. 3, pp. 25–30, 2011.
- [29] A. Nayak and A. Jain, "In vitro and in vivo study of poly(ethylene glycol) conjugated ibuprofen to extend the duration of action," *Scientia Pharmaceutica*, vol. 79, no. 2, pp. 359–373, 2011.
- [30] A. F. Davis and J. Hadgraft, "Effect of supersaturation on membrane transport: I. Hydrocortisone acetate," *International Journal of Pharmaceutics*, vol. 76, no. 1–2, pp. 1–8, 1991.
- [31] P. Costa and J. M. S. Lobo, "Modeling and comparison of dissolution profiles," *European Journal of Pharmaceutical Sciences*, vol. 13, no. 2, pp. 123–133, 2001.
- [32] N. A. Williams and G. P. Polli, "The lyophilization of pharmaceuticals: a literature review," *Journal of Parenteral Science and Technology*, vol. 38, no. 2, pp. 48–60, 1984.
- [33] M. J. Pikal, S. Shah, M. L. Roy, and R. Putman, "The secondary drying stage of freeze drying: drying kinetics as a function of temperature and chamber pressure," *International Journal of Pharmaceutics*, vol. 60, no. 3, pp. 203–207, 1990.
- [34] X. Tang and M. J. Pikal, "Design of freeze-drying processes for pharmaceuticals: practical advice," *Pharmaceutical Research*, vol. 21, no. 2, pp. 191–200, 2004.
- [35] N. Nyamweya and S. W. Hoag, "Assessment of polymer-polymer interactions in blends of HPMC and film forming polymers by modulated temperature differential scanning calorimetry," *Pharmaceutical Research*, vol. 17, no. 5, pp. 625–631, 2000.

- [36] Y. Javadzadeh, B. Jafari-Navimipour, and A. Nokhodchi, "Liquisolid technique for dissolution rate enhancement of a high dose water-insoluble drug (carbamazepine)," *International Journal of Pharmaceutics*, vol. 341, no. 1-2, pp. 26–34, 2007.
- [37] T. Chatzaeioannou, *Quantitative Calculations in Pharmaceutical Practice and Research*, VCH Publishers, New York, NY, USA, 1993.
- [38] M. H. Shoaib, J. Tazeen, H. A. Merchant, and R. I. Yousuf, "Evaluation of drug release kinetics from ibuprofen matrix tablets using HPMC," *Pakistan Journal of Pharmaceutical Sciences*, vol. 19, no. 2, pp. 119–124, 2006.
- [39] S. Dash, P. N. Murthy, L. Nath, and P. Chowdhury, "Kinetic modeling on drug release from controlled drug delivery systems," *Acta Poloniae Pharmaceutica*, vol. 67, no. 3, pp. 217–223, 2010.
- [40] A. Hixson and J. Crowell, "Dependence of reaction velocity upon surface and agitation," *Industrial and Engineering Chemistry*, vol. 23, no. 8, pp. 923–931, 1931.
- [41] S. K. Dordunoo, J. L. Ford, and M. H. Rubinstein, "Preformulation studies on solid dispersions containing triamterene or temazepam in polyethylene glycols or gelucire 44/14 for liquid filling of hard gelatin capsules," *Drug Development and Industrial Pharmacy*, vol. 17, no. 12, pp. 1685–1713, 1991.
- [42] J. M. Ginés, M. D. Veiga, M. J. Arias, and A. M. Rabasco, "Elaboration and thermal study of interactions between cinnarizine and gelucire 53/10 physical mixtures and solid dispersions," *International Journal of Pharmaceutics*, vol. 126, no. 1-2, pp. 287–291, 1995.
- [43] G. R. Lloyd, D. Q. M. Craig, and A. Smith, "An investigation into the melting behavior of binary mixes and solid dispersions of paracetamol and PEG 4000," *Journal of Pharmaceutical Sciences*, vol. 86, no. 9, pp. 991–996, 1997.
- [44] D. Q. M. Craig, "Polyethylene glycols and drug release," *Drug Development and Industrial Pharmacy*, vol. 16, no. 17, pp. 2501–2526, 1990.

Research Article

Fabrication of Conductive Polypyrrole Nanofibers by Electrospinning

Yiqun Cong, Shize Liu, and Haifeng Chen

Department of Biomedical Engineering, College of Engineering, Peking University, Beijing 100871, China

Correspondence should be addressed to Haifeng Chen; haifeng.chen@pku.edu.cn

Received 5 July 2013; Accepted 3 September 2013

Academic Editor: Krasimir Vasilev

Copyright © 2013 Yiqun Cong et al. This is an open access article distributed under the Creative Commons Attribution License, which permits unrestricted use, distribution, and reproduction in any medium, provided the original work is properly cited.

Electrospinning is employed to prepare conductive polypyrrole nanofibers with uniform morphology and good mechanical strength. Soluble PPy was synthesized with NaDEHS as dopant and then applied to electrospinning with or without PEO as carrier. The PEO contents had great influence on the morphology and conductivity of the electrospun material. The results of these experiments will allow us to have a better understanding of PPy electrospun nanofibers and will permit the design of effective electrodes in the BMIs fields.

1. Introduction

Electrospinning is a broadly applied technology used to fabricate nanofibers from a wide range of materials including both natural and synthetic polymers [1]. A high voltage electrostatic field is used to induce the ejection of a liquid jet which stretches into continuous fibers in the submicron range [2]. The electrospun material exhibits unique features such as uniform ultrafine fibers, high surface-to-volume ratio, tunable porous structures, and controllable composition, making it capable to achieve the desired result from its prosperities and functionality. These qualities allow the materials to be successfully applied in various fields such as biosensor [3], tissue engineering scaffold [4], drug delivery [5], wound dressing [6], and protective clothing [7].

Polypyrrole (PPy) is one of the most widely investigated conductive polymers due to its easy synthesis, high conductivity, good environmental stability, and biocompatibility [2]. In the past decades, it has been applied in biosensors [8], electrodes [9], and especially nerve tissue engineering scaffolds [10]. For instance, George et al. [11] found that the PPy film could support the growth of nerve system. Either of these applications would prefer to have a high surface area for a given mass or volume, which would provide a large interface in sensing, to enhance the ions transportation for electrode or to promote cell growth as the scaffold. This could be realized using electrospinning to generate PPy nanofibers

with porous structure. It is possible to coat the electrospun PPy nanofibers on materials like electrodes prior to inserting them in the brain which can help relieve some damage done to the tissues as well as provide better results due to the more positive interaction between the coated electrodes and the cells. This will be helpful to the development of brain-machine interfaces (BMIs) biomedical devices.

In the present work, we have developed a way to electrospinning PPy solution with carrier into ultrafine fibers. Using scanning electron microscopy (SEM), Fourier transform-infrared spectroscopy (FTIR), XPS, and four-probe method, the morphology, chemical composition, and conductivity of the nanofibers were examined. The results of these experiments will allow us to have a better understanding of PPy electrospun nanofibers and will permit the design of effective electrodes in the BMIs fields.

2. Experimental

2.1. Synthesis of Soluble PPy [12]. Soluble PPy was synthesized at 0°C by 0.06 mol NaDEHS (Sigma-Aldrich) dissolved in 180 mL distilled water as the dopant and 0.12 mol Pyrrole (Sinopharm) added. 0.018 mol APS (Xilong Chemical) dissolved in 20 mL distilled water solely as the oxidant was slowly added into the NaDEHS solution with vigorous string. The polymerization was carried out for 24 h at 0°C and

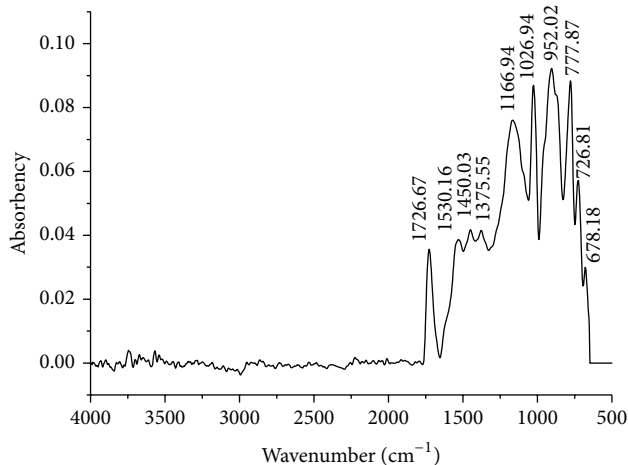


FIGURE 1: FT-IR Spectrum of NaDEHS doped PPy.

terminated by pouring the solution into methanol. The PPy powder was collected by filtering and was dried at 60°C for 24 h.

FT-IR (Magna-IR 750, Nicole) and XPS (Axis Ultra, Kratos) were employed to demonstrate the PPy powder.

2.2. Electrospinning of PPy Fibers. PPy and PEO were dissolved in CHCl_3 with the concentration 8 wt% and 4 wt%, respectively. PEO and PPy solutions were then mixed with the ratios of 1:10, 1:8, 1:6, 1:4, and 1:2. The 8 wt% PPy and PEO/PPy blends were prepared for electrospinning.

Electrospinning was carried out with a 10 kV voltage and 0.8 mL/h flow rate. A ground screen covered by aluminum sheet was placed 10 cm from the tip of the syringe. The nonwoven fibers were collected and characterized by SEM (Quanta 200F, FEI).

2.3. Conductivity Characterization. The conductivity of each sample is measured using the four-probe method. Afterwards, the 1:10 ratio PEO/PPy nanofibers was kept in the 30°C, 40°C, 50°C, 60°C, and 70°C atmosphere orderly, and the conductivity at each temperature was recorded.

3. Results

3.1. Synthesis of Soluble PPy. The formation of PPy and the doping of NaDEHS are confirmed with FT-IR spectroscopy in the range of 4000–650 cm^{-1} as shown in Figure 1. The peak at 905.0 is associated to the out-of-plane vibration of =C-H; the wide peak at 1166.9 cm^{-1} is associated with the N-C stretching; and the peaks at 1373.55 cm^{-1} and 1026.94 cm^{-1} are corresponding to the =C-H plan vibration, while the peak at 1726.67 cm^{-1} corresponds to the C=O vibration in NaDEHS.

The XPS analysis is shown in Figure 2 while the quantitative element analysis is in Table 1. The N element is from PPy, while the presence of S and Na confirmed the doping of NaDEHS.

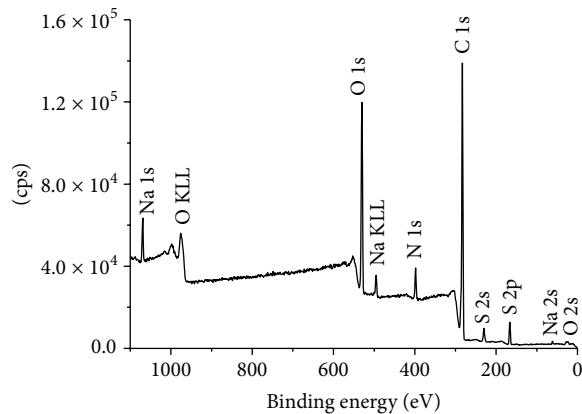


FIGURE 2: XPS analysis of NaDEHS doped PPy.

TABLE 1: Quantitative element analysis of NaDEHS doped PPy.

Name	Position	Area	% Conc.
Na 1s	1071.65	2592.8	0.28
S 2p	168.00	6989.5	1.89
N 1s	399.95	16082.2	6.10
O 1s	531.80	67833.9	15.73
C 1s	284.80	116790.6	76.00

3.2. Morphology of PPy Nanofibers. Figure 3 presents the SEM images of electrospun PEO/PPy nanofibers with different ratios. PPy nanofibers are nonuniform with droplets, and the material is fragile. When PEO is added, cylindrical fibers are formed. As the ratio of PEO increases, there are less droplets and broken ends. The diameter statistics of fibers of PEO/PPy nanofibers are shown in Figure 4. The fibers are thinner, and the diameters are more uniform with more PEO component due to the change of solution viscosity and surface tension.

3.3. Conductivity. There is a linear relationship between the conductivity of these nanofibers and the content of PEO as shown in Figure 5 ($R^2 = 0.9571$). As the content of PEO varies, the conductivity increased by one-order of magnitude ranged from $1.44 \times 10^{-3} \text{ S}\cdot\text{cm}^{-1}$ to $2.45 \times 10^{-4} \text{ S}\cdot\text{cm}^{-1}$.

By increasing the temperature, we found that the conductivity of the 1:10 ratio PEO/PPy nanofibers rises following the power function $\sigma = A \exp(B/T)$ ($R^2 = 0.9939$), which is a typical property of semiconductor.

4. Discussion

These significant characteristic peaks of PPy in the FT-IR spectrum demonstrate the formation of PPy, while the C=O liberation peak at 1726.67 cm^{-1} in FT-IR spectrum and the S and Na elements in XPS characterization illustrate that the NaDEHS has been successfully doped into PPy. In the quantitative element analysis, the ratio of N and S is about 3.2:1, suggesting that in the polymer chain the mole ratio of Py unit and NaDEHS is around 3. As the pure PPy

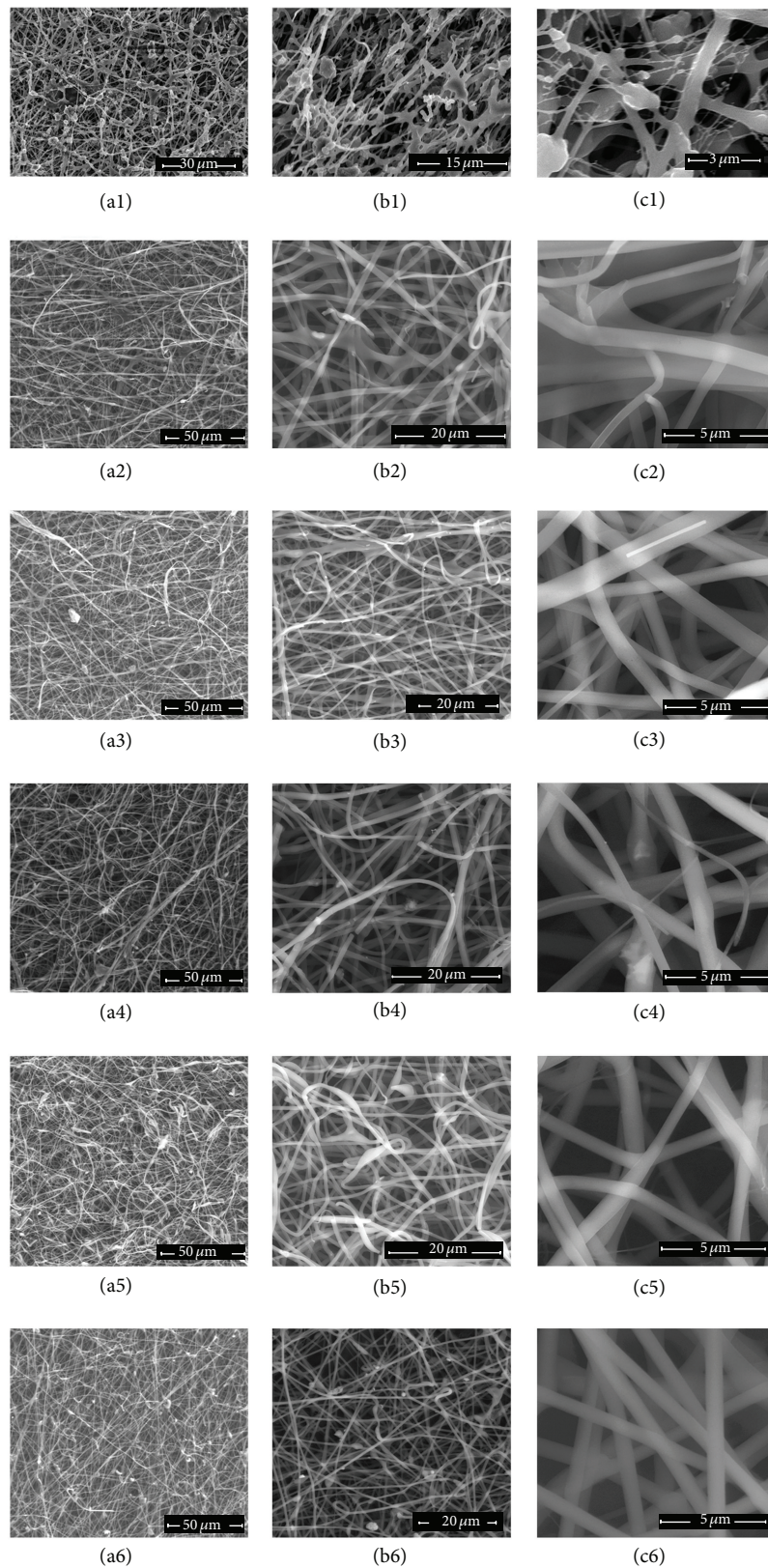


FIGURE 3: SEM micrographs of PEO/PPy electrospun fibers. (a1),(b1),(c1) PPy nanofibers without PEO; (a2),(b2),(c2) 1:10 PEO/PPy fibers; (a3),(b3),(c3) 1:8 PEO/PPy fibers; (a4),(b4),(c4) 1:6 PEO/PPy fibers; (a5),(b5),(c5) 1:4 PEO/PPy fibers; (a6),(b6),(c6) 1:2 PEO/PPy fibers.

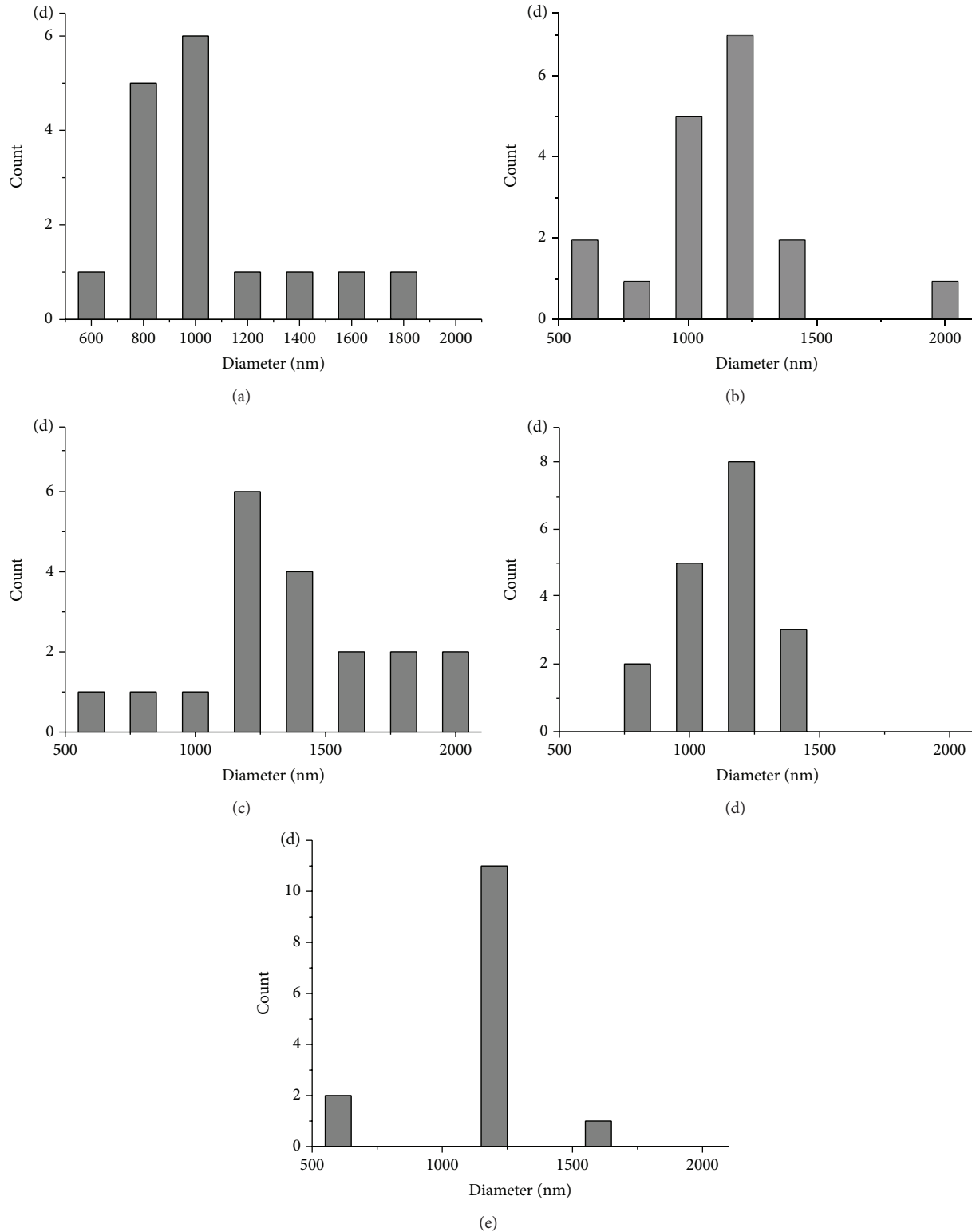


FIGURE 4: Statistics of PEO/PPy fiber diameter. (a) 1:10 PEO/PPy fibers; (b) 1:8 PEO/PPy fibers; (c) 1:6 PEO/PPy fibers; (d) 1:4 PEO/PPy fibers; (e) 1:2 PEO/PPy fibers.

powder is insoluble in most solvent due to the strong internal interactions within and between the chains; the doping of NaDEHS result in the solubility in CHCl_3 .

The doped PPY solution cannot be preceded into smooth fibers, and the electrospun web is fragile. To enhance the

electrospinning process, PEO is added as carrier, and the resulted fibers are much more smooth and ultrafine.

The droplets and broken ends in the fibers are because of inadequate viscosity, which could be increased by adding PEO into PPY solution. So the fibers become longer and more

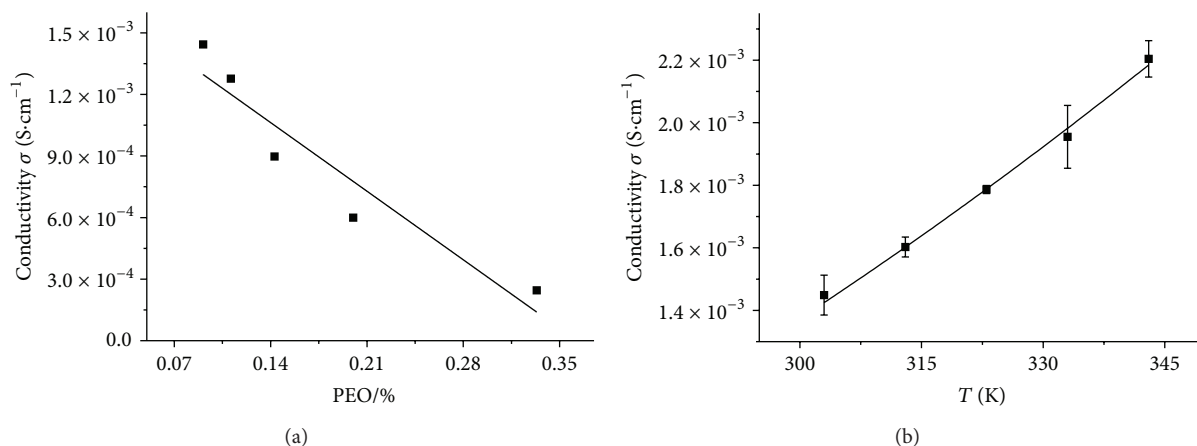


FIGURE 5: Electrical conductivity of PEO/PPy nanofibers as a function of PEO content and 1:10 PEO/PPy nanofibers as function of temperature. (a) Electrical conductivity of PEO/PPy nanofibers as a function of PEO content; (b) electrical conductivity of 1:10 PEO/PPy nanofibers as function of temperature.

uniform as the ratio of PEO and PPy rise. As in the 1:2 PEO/PPy electrospun materials, the long nanofibers exhibit a cylindrical morphology and are randomly distributed in a uniform and dense way. Since PEO is a flexible material, the mechanical strength of PEO/PPy nanofibers is improved.

The size of the fibers could also be affected by the ratio of PEO and PPy. As the viscosity increases, the surface tension, which the dividing of the jets has to overcome, also increases. So the splitting ability of the jets declines and results in thicker fibers. Without the splitting, the diameters of the fibers exhibit narrower distribution.

Although the electrospinning process is promoted, the conductivity of the material will reduce and exhibit a linear relation with the contents of PEO. Pure PPy is semiconductor because of the delocalized π bond, while the presence of PEO molecular leads to the fold and twist of the conjugated chain, which would limit the delocalization of electrons. Also, the conductive PPy content will become discontinuous because of PEO, which finally reduce the conductivity.

For semiconductor, as the temperature rises, more electrons are activated and transit into conduction band. Meanwhile, the migration rate will also grow with the temperature, resulting in the better conductivity of the material. In the study of the 1:10 PEO/PPy electrospun material, the conductivity grows with temperature following the power function, demonstrating that after adding PEO, the PPy remains to be semiconductor.

5. Conclusion

In summary, the soluble PPy is synthesized by doping NaDEHS. The conductive nanofibers web could be fabricated by electrospun PEO/PPy composite. Increase in the content of PEO will enhance the electrospinning process and the mechanical strength of the fiber web but meanwhile reduce the conductivity. Also, the conductivity will increase

as temperature rises following a power function like most semiconductors. This work shows the potential of applying electrospun PPy nanofibers to the BMIs fields.

Acknowledgment

The work is supported by the Ministry of Science and Technology of China (Grants 2012CB933903).

References

- [1] N. Bhardwaj and S. C. Kundu, "Electrospinning: a fascinating fiber fabrication technique," *Biotechnology Advances*, vol. 28, no. 3, pp. 325–347, 2010.
- [2] T. S. Kang, S. W. Lee, J. Joo, and J. Y. Lee, "Electrically conducting polypyrrole fibers spun by electrospinning," *Synthetic Metals*, vol. 153, no. 1–3, pp. 61–64, 2005.
- [3] Y. Liu, H. Teng, H. Hou, and T. You, "Nonenzymatic glucose sensor based on renewable electrospun Ni nanoparticle-loaded carbon nanofiber paste electrode," *Biosensors and Bioelectronics*, vol. 24, no. 11, pp. 3329–3334, 2009.
- [4] S. Agarwal, J. H. Wendorff, and A. Greiner, "Use of electrospinning technique for biomedical applications," *Polymer*, vol. 49, no. 26, pp. 5603–5621, 2008.
- [5] Z. M. Huang, C. L. He, A. Z. Yang et al., "Encapsulating drugs in biodegradable ultrafine fibers through co-axial electrospinning," *Journal of Biomedical Materials Research Part A*, vol. 77, no. 1, pp. 169–179, 2006.
- [6] J. Jia, Y. Y. Duan, S. H. Wang, S. F. Zhang, and Z. Y. Wang, "Preparation and characterization of antibacterial silver-containing nanofibers for wound dressing applications," *Journal of US-China Medical Science*, vol. 4, pp. 52–54, 2007.
- [7] S. Ramakrishna, K. Fujihara, W. E. Teo, T. Yong, Z. Ma, and R. Ramaseshan, "Electrospun nanofibers: solving global issues," *Materials Today*, vol. 9, no. 3, pp. 40–50, 2006.
- [8] N. K. Guimard, N. Gomez, and C. E. Schmidt, "Conducting polymers in biomedical engineering," *Progress in Polymer Science*, vol. 32, no. 8–9, pp. 876–921, 2007.

- [9] B. Veeraraghavan, J. Paul, B. Haran, and B. Popov, "Study of polypyrrole graphite composite as anode material for secondary lithium-ion batteries," *Journal of Power Sources*, vol. 109, no. 2, pp. 377–387, 2002.
- [10] J. Y. Lee, C. A. Bashur, A. S. Goldstein, and C. E. Schmidt, "Polypyrrole-coated electrospun PLGA nanofibers for neural tissue applications," *Biomaterials*, vol. 30, no. 26, pp. 4325–4335, 2009.
- [11] P. M. George, A. W. Lyckman, D. A. Lavan et al., "Fabrication and biocompatibility of polypyrrole implants suitable for neural prosthetics," *Biomaterials*, vol. 26, no. 17, pp. 3511–3519, 2005.
- [12] K. S. Jang, S. S. Han, J. S. Suh, and E. J. Oh, "Synthesis and characterization of alcohol soluble polypyrrole," *Synthetic Metals*, vol. 119, no. 1–3, pp. 107–108, 2001.

Research Article

Microfluidic Device for Controllable Chemical Release via Field-Actuated Membrane Incorporating Nanoparticles

Xiang Wang,¹ Shunbo Li,² Limu Wang,¹ Xin Yi,¹ Yu Sanna Hui,¹
Jianhua Qin,³ and Weijia Wen^{1,2}

¹ Nanoscience and Nanotechnology Program, Hong Kong University of Science and Technology, Clear Water Bay, Kowloon, Hong Kong

² Department of Physics and KAUST-HKUST Joint Micro/Nanofluidic Laboratory, Hong Kong University of Science and Technology, Clear Water Bay, Kowloon, Hong Kong

³ Dalian Institute of Chemical Physics, Chinese Academy of Science, 457 Zhongshan Road, Dalian, China

Correspondence should be addressed to Weijia Wen; phwen@ust.hk

Received 2 July 2013; Accepted 25 August 2013

Academic Editor: Krasimir Vasilev

Copyright © 2013 Xiang Wang et al. This is an open access article distributed under the Creative Commons Attribution License, which permits unrestricted use, distribution, and reproduction in any medium, provided the original work is properly cited.

We report a robust magnetic-membrane-based microfluidic platform for controllable chemical release. The magnetic membrane was prepared by mixing polydimethylsiloxane (PDMS) and carbonyl-iron nanoparticles together to obtain a flexible thin film. With combined, simultaneous regulation of magnetic stimulus and mechanical pumping, the desired chemical release rate can easily be realized. For example, the dose release experimental data was well fitted by a mathematical sigmoidal model, exhibiting a typical dose-response relationship, which shows promise in providing significant guidance for on-demand drug delivery. To test the platform's feasibility, our microfluidic device was employed in an experiment involving *Escherichia coli* culture under controlled antibiotic ciprofloxacin exposure, and the expected outcomes were successfully obtained. Our experimental results indicate that such a microfluidic device, with high accuracy and easy manipulation properties, can legitimately be characterized as active chemical release system.

1. Introduction

Controllable release describes materials or devices that can control the release time or the release rate of chemicals or both. This technique has provided broad usefulness in different fields such as foods, cosmetics, pesticides, and agricultural industries [1, 2], while the most important application is active drug release [3]. It is well known that how and when a drug is delivered can have a significant effect on its potency. Traditional drug-release systems are characterized by immediate and uncontrolled drug-delivery kinetics, such system is usually referred to as passive drug release. Under such circumstance, it is possible that a given drug concentration dangerously approaches its toxic threshold to subsequently fall below the level with effective potency. From the viewpoint of the pharmacotherapy optimization, drug release should be controlled in accordance with the potent purpose and the pharmacological properties of active substances. This

purpose has given great impetus to the concept known as active drug release, which first arose in the 1960s. Typically, controlled or active release is used to achieve sustained or pulsatile drug release. The rationale is to maintain drug concentration in the target receptors at a desired value as long as necessary [4]. What is actively controlled, in other words, is the drug-release rate and duration [5]. Compared with conventional dosage protocols, controlled drug release systems offer numerous advantages such as enhanced efficacy and reduced toxicity [6].

In recent years, many of the thrusts into the field have spurred the rapid development of advanced drug-release systems and made numerous new discoveries. One popular approach involves incorporation of drug molecules into the matrix of microscopic polymer spheres or capsules [7, 8]. Most are fabricated with polymers having particular physical or chemical characteristics, such as good biodegradability, biocompatibility or sensitive responses to PH value

[9–11], temperature [12], light intensity [13, 14], external electric [15] or magnetic field [16], glucose [17], and others. Additionally, recent achievements in microtechnologies have been applied in designing drug-release microdevices, for example, microneedles and implantable microchips [18–20], which possess inherent advantages such as hand-held portability, sample saving, and implantable properties. The aforementioned controlled drug-release systems, moreover, can circumvent problems that are commonly encountered in traditional drug-release methods. However, some of these systems fail to achieve any desired complex release profile or involve complicated design and fabrication. To address these problems, we here introduce a novel prototypical microfluidic controlled-chemical-release platform based on a magnetic-field-actuated composite membrane which incorporates carbonyl-iron nanoparticles for actuation by magnetic field. Compared with existing release systems, our platform possesses such remarkable advantages as simple fabrication, easy manipulation, and high accuracy. And we demonstrate the microfluidic chip's feasibility for the realization of customizable release profiles as well as its general applicability in the drug release for biological system.

2. Experiments, Results, and Analyses

2.1. Materials. Polydimethylsiloxane (PDMS) was used in the fabrication of both the microfluidic chip and magnetic composite membrane due to its good flexibility, biocompatibility, and transparency, among other merits. The magnetic membrane used as the drug-delivery component, consists of carbonyl-iron (CI) nanoparticles mixed with PDMS, so-called CI-PDMS [21]. Due to its high magnetization and good mechanical elasticity, the CI-PDMS magnetic membrane shows good vibration characteristics under an external alternative magnetic field [21]. Ciprofloxacin and GFP recombinant *E. coli* bacteria in L-Broth standard growth medium, one liter of which contains 10 g tryptone, 5 g yeast extract, 10 g sodium chloride, and 2 mL ampicillin solution (100 mg/mL), were employed in the biological experimentation.

2.2. Microfluidic Chip Fabrication. Figure 1(a) schematizes the three-dimensional microfluidic chip fabrication procedure. It can be seen in the upper-left area of the figure, premixed PDMS gel (Sylgard 184 Silicone Elastomer, Dow Corning Corporation; weight ratio of prepolymer: cross-linker = 10:1) was mixed with CI nanoparticles and degassed, after which it was spun-coated on a Teflon-treated glass wafer so as to form thin layers of CI-PDMS. After solidification in an oven (65°C, 2 hours), a CI-PDMS membrane of about 100 μm in thickness was fabricated to the desired size using the laser-cutting technique. The CI-PDMS composite properties can be found in our previous report [21]. The chamber layers were patterned directly onto a cured PDMS sheet by laser cutting, as shown in the upper-right area of Figure 1(a). The aforementioned layers were bounded together by means of oxygen plasma bonding. The same steps were repeated for the fabrication of the diffusion PDMS membrane and the lower chamber layers. The microfluidic chip shown in the

lower inset of the figure consists of two individual chambers separated by a diffusion membrane, while at the bottom of the chip, a CI-PDMS magnetic membrane is located. It should be pointed out that other hydrophilic polymer films (e.g., MEMBRA-CEL MC18 X 100 CLR, Viskase Companies, USA) also can be used as the diffusion membrane and that the bonding methodology is similar to that for PDMS thin film. Figures 1(b)–1(c) show the top and bottom views, respectively, of a well-made microfluidic chip including five reservoirs, each one with diameter of 1000 μm and depth of 0.1 cm.

2.3. Working Mechanism of Microfluidic Chip. The experimental setup shown in Figure 2 was used to test the release characteristics of the microfluidic chip. In the upper chamber, water was injected to the full; sodium chloride (NaCl) solution of 0.5 mol/L was pumped to the bottom chamber with flow rate 0.04 mL/h. Two platinum electrodes, mounted in the upper chamber and connected to a digital multimeter (Agilent 34411A), were used to determine the solution's conductance variation when the NaCl diffused from the lower chamber to the upper one through the diffusion membrane. An electromagnet positioned directly beneath the CI-PDMS membrane of the microchip served to actuate membrane vibration via push-pull movement when acted on by an alternative current within the 60–110 Hz frequency range, while two syringe pumps controlled the flow status of two fluids to the two chambers. LabVIEW software was utilized for device control and data collection.

2.4. Determination of Chemical-Release Profiles. Figure 3(a) presents the NaCl ion concentration's variation profiles resulting from the changes of electrical conductance in the upper chamber when the solution diffused from the lower chamber through the membrane. Based on the proportional relationship between conductance and ion concentration, the vertical axis is normalized to the original conductance and represents ion concentration. These profiles can be realized under different working conditions of the electromagnet and syringe pump 2 (in the current experiment, syringe pump 1 was used only for water filling and usually was kept in the OFF state). The ON/OFF signals for both the electromagnet and syringe pump 2 are illustrated in Figure 3(b). For example, when syringe pump 2 was ON and the electromagnet was OFF over the entire working duration, the solution diffused naturally through the membrane without any actuated function, the corresponding variation of the NaCl ion concentration delivery route in the upper chamber is drawn as curve 2. It can be seen that the magnetic field applied to the magnetic membrane obviously strengthens the diffusion effect caused by membrane vibration. NaCl diffused very rapidly initially and then slowly approached the saturation value. Other routes could also be obtained by varying the ON/OFF states of electromagnet and syringe pump 2. The demonstrated curves are plotted in Figure 3(a) and the corresponding actuated signals are shown in Figure 3(b).

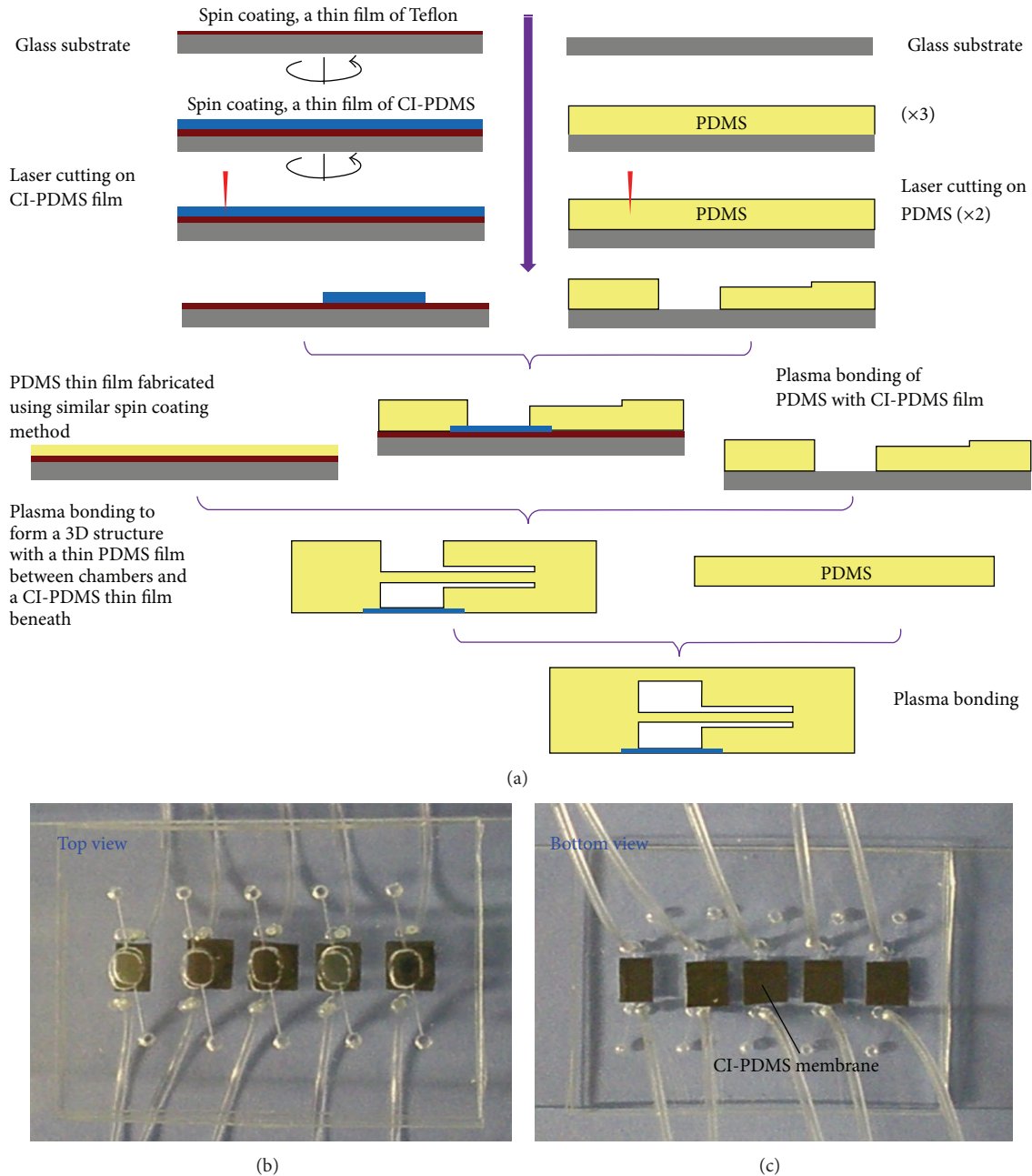


FIGURE 1: The preparation of drug delivery microfluidic chip and real pictures: (a) schematical fabrication process; (b) top view of this chip; (c) bottom view of this chip.

Sigmoidal fitting to the experimental data was carried out with the following Boltzmann equation of software OriginPro-8:

$$y = \frac{A_1 - A_2}{1 + e^{-(x-x_0)/dx}} + A_2, \quad (1)$$

where y represents the ion concentration measured in the upper chamber, A_1 and A_2 are the initial and final values of the ion concentration, respectively, x_0 is the inflection point at which y shows the most significant change, and dx relates

to the slope of the tangent line at x_0 . These parameters are clearly illustrated in the upper-right inset of Figure 3(a).

Since the ion concentration was normalized to 1 as the maximum, A_1 and A_2 in (1) can be fixed to 0 and 1, respectively. Thus, (1) can be rewritten as

$$y = \frac{1}{1 + e^{-(x-x_0)/dx}}. \quad (2)$$

From (2), we can simply obtain $y'(x_0) = 1/4dx$ and $y''(x_0) = 0$.

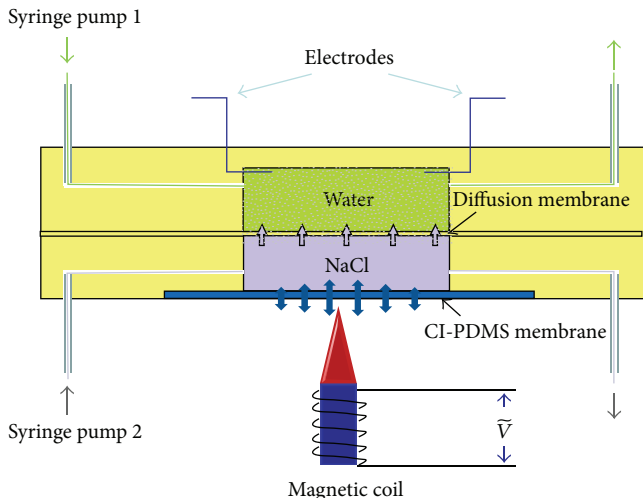


FIGURE 2: Cross-section view of the microfluidic device.

The first-order derivative of (2) at x_0 is inversely proportional to the parameter dx , the smaller value of which signifies the larger ion concentration changes per unit time. The inflection point x_0 marks the time at which the growth rate of the solution's diffusion effect of solution shifts from acceleration to deceleration. Therefore, the second-order derivative at x_0 equals zero.

Interpreting the parameters in their biological meanings is helpful in understanding the corresponding drug-release characteristics. From a pharmacological standpoint, the x_0 value can be used to differentiate drug administration rates, acceleration or deceleration, the steepness factor dx representing a most significant response per unit change in administered dose. Accordingly, these parameters can be utilized as indicators in evaluating the potency and efficacy of administered drugs. If assigning any arbitrary values to x_0 and dx , we can, based on the solution diffusion results, purposely construct a new delivery route by proper, simultaneous manipulation of the respective magnetic field and pumping signals. In this way, active drug release can be achieved.

Figure 3(a) clearly shows good agreement between the fitting results from above mathematical model and the experimental data. Table 1 indicates that the values for x_0 and dx differ from each other for different curves, which result from the combined regulation of the magnetic field and mechanical pumping. From the fitted value, we note that dx and x_0 for curve 1 are much smaller than those for curve 2.

Biological Experimentation for Dose-Response Assessment. The sigmoid-shaped curve in Figure 3(a) represents a typical dose-response relationship, which is the most fundamental and pervasive concept in toxicology [22]. Studying dose-response model is crucial to determine the "safe" and "hazardous" levels and dosages of drugs to which organisms are exposed. It is known that dose-responses can be elucidated in cell culture preparations wherein there is a discrete and controlled pharmacologic environment. Additionally,

TABLE 1: Fitting parameters for curves 1–5 in Figure 3(a).

Parameter	Curve				
	1	2	3	4	5
x_0	28.85	67.84	140.55	194.07	246.1
dx	16.45	43.42	54.7	27.24	16.98

a comparison of dose-response curves among drugs can identify both the therapeutic and the toxic effects of the potential drugs. Thus, given the above experimental results, we deduced that if we substituted, in a biological experiment, ciprofloxacin solution and growth medium (L-Broth) for sodium chloride and water, respectively, similar dose-response consequences could be observed. Ciprofloxacin is a synthetic chemotherapeutic antibiotic of the fluoroquinolone drug class [23, 24], while *E. coli* is a gram-negative rod-shaped bacterium commonly found in the lower intestine of warm-blooded organisms (endotherms). Pharmacologically, ciprofloxacin can inhibit the reproduction and genetic material repairment of GFP recombinant *E. coli* bacteria.

In order to verify our hypothesis and characterize the established drug-delivery platform for realistic application, ciprofloxacin was pumped into the lower chamber and GFP recombinant *E. coli* bacteria with L-Broth standard growth medium in the upper compartment. One liter of this medium contains 10 g tryptone, 5 g yeast extract, 10 g sodium chloride, and 2 mL ampicillin solution (100 mg/mL). Similar to the microfluidic chip shown in Figure 2, the chip used in the present experiment consisted of five pairs of reservoirs labeled C1, C2, C3, C4, and C5, respectively. The drug-delivery routes of ciprofloxacin for C1–C5 were consistent with curves 1–5 described in Figure 3(a), but the experiment was carried out for 120 min. During the experiment, fluorescent images of *E. coli* in the chip reservoirs were taken by a Canon camera (EOS 5D, Mark II) equipped with a macro lens.

We extracted the average light intensity from each optical image using Adobe Photoshop software, and the results are illustrated in Figure 4, where it is evident that in chamber C5, the *E. coli* grew and multiplied very well. The intensity of fluorescence doubled every 20 min during the first one and a half hours, since initially less drug amount was diffused to the cell chamber. Thereafter, the growth rate decreased somewhat. The reason lies in the limitation of L-Broth growth medium; that is, it becomes deficient after one-hour cell culture; consequently, the drug effect increased more rapidly. With regard to chamber C1, at first the ciprofloxacin concentration reached a high level, prevented cells from reproduction, and in that way maintained the cell concentration at a relatively low level during the 2-hour experiment. As for chamber C4, at the very outset the ciprofloxacin concentration was low enough not to cause much effect, and so the cells grew very well. However, after one hour, more and more drug diffused from the lower chamber through the diffusion membrane to the upper one. This highly concentrated ciprofloxacin successfully inhibited cell reproduction and genetic material repairment. As a result, the cells in chamber C4 multiplied little during the last 20 min of the experiment. From this

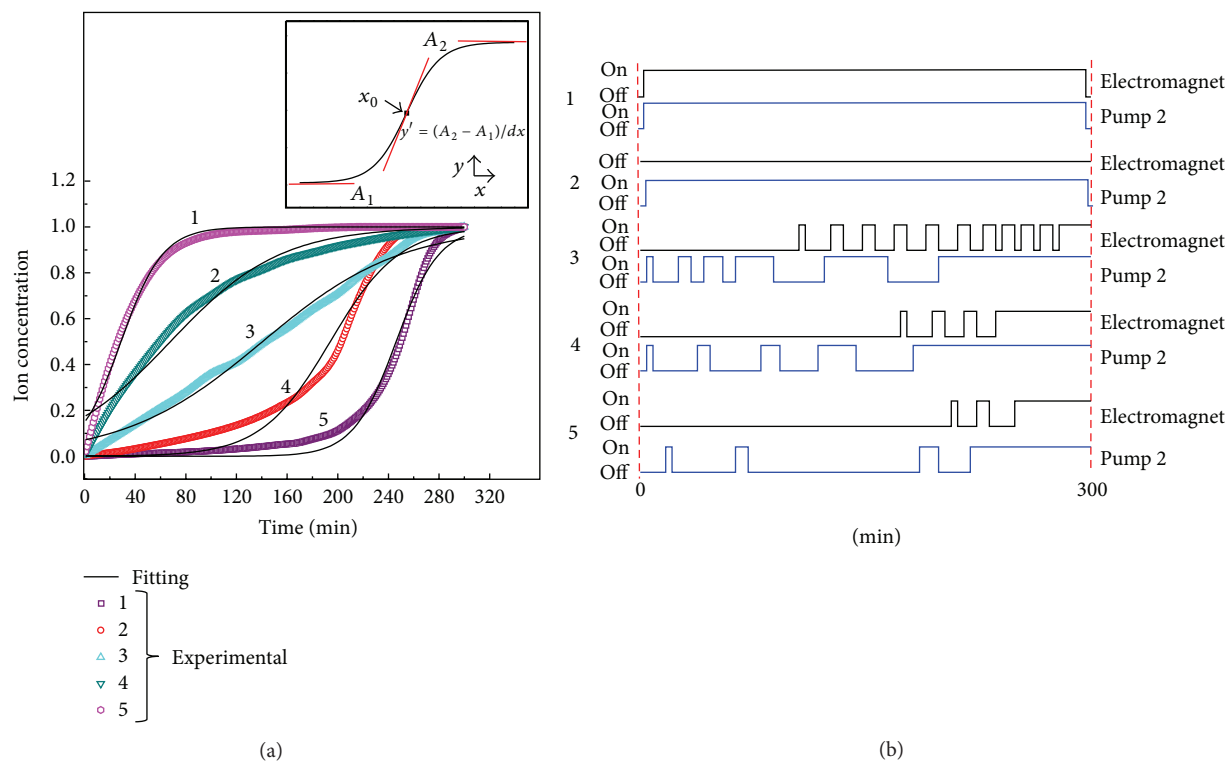


FIGURE 3: Normalized NaCl solution diffusion profiles. Each curve corresponds to the combined regulation from electromagnetic and syringe pump. The square-wave signal shows the working situation of electromagnet and syringe pump, respectively.

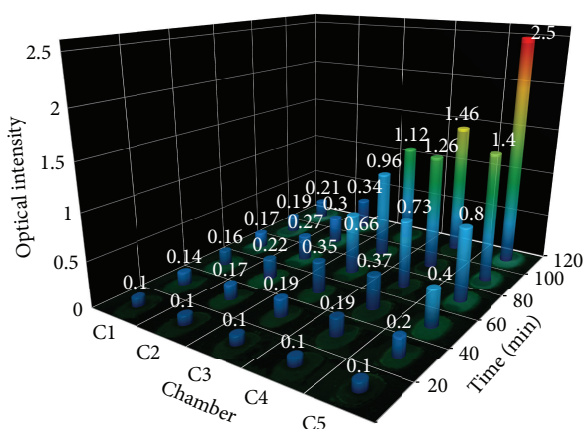


FIGURE 4: Antibacterial property of loaded fluoroquinolone ciprofloxacin in *E. coli*. The drug delivery routes of ciprofloxacin to *E. coli* chambers C1–C5 correspond to curves 1–5 shown in Figure 3(a), respectively. The column bars indicate the fluorescent intensity in each chamber which reflects the rough number of bacterial inside.

experiment on the antimicrobial effect, we can conclude that *E. coli* is capable of enhancing its drug resistance when ciprofloxacin increases slowly at the initial stage, even though the final dose is the same. These results agree very well with the normalized diffusion profiles in Figure 3(a). That is to say,

the drug-delivery profiles indicate that treatment doses and duration times can be modulated for the desired task.

3. Conclusions

By utilizing magnetic nanoparticles, we successfully demonstrated a microdevice for chemical release. This kind of device has numerous potential advantages, such as being simple to fabricate and operate, high precision in chemical release, and low cost. The present research explicated the formulaic dose-response drug-release property based on the magnetically actuated membrane. The active functionality of a microfluidic device, all of its processing digitized via actuated signals, was demonstrated in an investigation of the antibacterial property of loaded fluoroquinolone Ciprofloxacin in *E. coli*. The results clearly indicated the device's potential to control dosage at a satisfactory level, thereby illustrating the promise of such a controlled drug-release method. Specifically, by changing the size of the drug reservoir, the amount of medication can be accurately controlled; hence, a variety of drugs, especially sensitive or highly potent drugs, potentially can be delivered in a safe manner using the microdevice.

Acknowledgments

This paper is based on work partially supported by Award no. SA-C0040/UK-C0016, made by King Abdullah University of Science and Technology (KAUST), Saudi Arabia, Hong Kong

RGC Grants HKUST 603608, 604710, and N_HKUST601/11, respectively.

References

- [1] L. Brannon-Peppas, "Novel vaginal drug release applications," *Advanced Drug Delivery Reviews*, vol. 11, no. 1-2, pp. 169–177, 1993.
- [2] R. Levy, M. A. Nichols, and T. W. Miller, "Encapsulated systems for controlled release and pest management," *ACS Symposium Series*, vol. 520, pp. 202–212, 1993.
- [3] R. Langer, "Drug delivery and targeting," *Nature*, vol. 392, no. 6679, pp. 5–10, 1998.
- [4] R. Langer, R. Siegel, and L. Brown, "Controlled release systems: some recent advances," *Proceedings of the ACS Division of Polymeric Material*, vol. 51, pp. 115–118, 1984.
- [5] P. Gruber, M. A. Longer, and J. R. Robinson, "Some biological issues in oral, controlled drug delivery," *Advanced Drug Delivery Reviews*, vol. 1, pp. 1–18, 1987.
- [6] M. N. V. Ravi Kumar, *Handbook of Particulate Drug Delivery*, vol. 2, American Scientific Publishers, 2008.
- [7] P. L. Madan, "Microencapsulation II. Interfacial reactions," *Drug Development and Industrial Pharmacy*, vol. 4, pp. 289–304, 1978.
- [8] E. Mathiowitz, D. Kline, and R. Langer, "Morphology of polyanhydride microsphere delivery systems," *Scanning Microscopy*, vol. 4, no. 2, pp. 329–340, 1990.
- [9] A. Yu, Y. Wang, E. Barlow, and F. Caruso, "Mesoporous silica particles as templates for preparing enzyme-loaded biocompatible microcapsules," *Advanced Materials*, vol. 17, pp. 1737–1741, 2005.
- [10] D. G. Shchukln, E. A. Ustinovich, G. B. Sukhorukov, H. Möhwal, and D. V. Sviridov, "Metallized polyelectrolyte microcapsules," *Advanced Materials*, vol. 17, no. 4, pp. 468–472, 2005.
- [11] T. Narita, T. Yamamoto, D. Suzuki, and T. Dobashi, "Dynamics of the volume phase transition of a hydrogel membrane of a microcapsule," *Langmuir*, vol. 19, no. 10, pp. 4051–4054, 2003.
- [12] T. Kidchob, S. Kimura, and Y. Imanishi, "Thermoresponsive release from poly(Glu(OMe))-block-poly(Sar) microcapsules with surface-grafting of poly(N-isopropylacrylamide)," *Journal of Controlled Release*, vol. 50, no. 1–3, pp. 205–214, 1998.
- [13] A. S. Angelatos, B. Radt, and F. Caruso, "Light-responsive polyelectrolyte/gold nanoparticle microcapsules," *Journal of Physical Chemistry B*, vol. 109, no. 7, pp. 3071–3076, 2005.
- [14] X. Yuan, K. Fischer, and W. Schärtl, "Photocleavable microcapsules built from photoreactive nanospheres," *Langmuir*, vol. 21, pp. 9374–9380, 2005.
- [15] D. G. Shchukin, K. Köhler, and H. Möhwal, "Microcontainers with electrochemically reversible permeability," *Journal of the American Chemical Society*, vol. 128, pp. 4560–4561, 2006.
- [16] X. Gong, S. Peng, W. Wen, P. Sheng, and W. Li, "Design and fabrication of magnetically functionalized core/shell microspheres for smart drug delivery," *Advanced Functional Materials*, vol. 19, no. 2, pp. 292–297, 2009.
- [17] B. G. De Geest, A. M. Jonas, J. Demeester, and S. C. De Smedt, "Glucose-responsive polyelectrolyte capsules," *Langmuir*, vol. 22, no. 11, pp. 5070–5074, 2006.
- [18] H. J. G. E. Gardeniers, R. Luttge, E. J. W. Berenschot et al., "Silicon micromachined hollow microneedles for transdermal liquid transport," *Journal of Microelectromechanical Systems*, vol. 12, no. 6, pp. 855–862, 2003.
- [19] J.-H. Park, M. G. Allen, and M. R. Prausnitz, "Biodegradable polymer microneedles: fabrication, mechanics and transdermal drug delivery," *Journal of Controlled Release*, vol. 104, no. 1, pp. 51–66, 2005.
- [20] M. Shikida, T. Hasada, and K. Sato, "Fabrication of a hollow needle structure by dicing, wet etching and metal deposition," *Journal of Micromechanics and Microengineering*, vol. 16, no. 10, pp. 2230–2239, 2006.
- [21] J. Li, M. Zhang, L. Wang, W. Li, P. Sheng, and W. Wen, "Design and fabrication of microfluidic mixer from carbonyl iron-PDMS composite membrane," *Microfluidics and Nanofluidics*, vol. 10, no. 4, pp. 919–925, 2011.
- [22] L. J. Cassarett and J. Doull, *Toxicology: The Basic Science of Poisons*, Macmillan, 1975.
- [23] J. M. Nelson, T. M. Chiller, J. H. Powers, and F. J. Angulo, "Fluoroquinolone-resistant *Campylobacter* species and the withdrawal of fluoroquinolones from use in poultry: a public health success story," *Clinical Infectious Diseases*, vol. 44, no. 7, pp. 977–980, 2007.
- [24] S. Kawahara, "Chemotherapeutic agents under study," *Japanese Journal of Clinical Medicine*, vol. 56, no. 12, pp. 3096–3099, 1998.

Research Article

***In Vitro* Evaluation of Cytotoxicity of Colloidal Amorphous Silica Nanoparticles Designed for Drug Delivery on Human Cell Lines**

**Venugopal Balakrishnan,¹ Hajarul Azwana Ab Wab,²
Khairunisak Abdul Razak,^{1,2} and Shaharum Shamsuddin^{1,3}**

¹ *NanoBiotechnology Research and Innovation (NanoBRI), Institute for Research in Molecular Medicine, Universiti Sains Malaysia, 11800 Georgetown, Penang, Malaysia*

² *School of Materials and Mineral Resources Engineering, Universiti Sains Malaysia, 14300 Nibong Tebal, Penang, Malaysia*

³ *School of Health Sciences, USM Health Campus, 16150 Kubang Kerian, Kelantan, Malaysia*

Correspondence should be addressed to Shaharum Shamsuddin; shaharum@kb.usm.my

Received 13 July 2013; Revised 13 August 2013; Accepted 15 August 2013

Academic Editor: Haifeng Chen

Copyright © 2013 Venugopal Balakrishnan et al. This is an open access article distributed under the Creative Commons Attribution License, which permits unrestricted use, distribution, and reproduction in any medium, provided the original work is properly cited.

Silica nanoparticles are being developed and tested vigorously in drug delivery systems to treat various diseases. There are many advantages of using silica nanoparticles as a nanodelivery system because they are relatively inexpensive to produce, chemically inert, thermally stable and can be tailored to contain porous structures for drug encapsulation and to be hydrophilic for higher solubility in the human body. Despite these tremendous benefits, one of the pivotal requirements of these drug delivery systems is to be biocompatible with the human body. In this study, the cytotoxicity of colloidal amorphous silica nanoparticles synthesized using the micelle formation method has been tested against normal human foreskin fibroblast cell line (Hs27) as well as selected human bone carcinoma (U-2 OS), human breast cancer (MCF-7), and human cervical carcinoma (HeLa) and (Ca Ski) cell lines to determine the IC₅₀ values. Two different sizes of silica nanoparticles, 20 nm and 40 nm, were used to study the relationship between their size and the level of toxicity exerted on the different cells being tested. The cytotoxicity results indicated that 20 nm and 40 nm silica nanoparticles significantly reduce cell viability in a dose- and cell-type-dependent manner in the normal and cancerous cells tested.

1. Introduction

Nanomedicine is the application of nanotechnology or nanomaterials in the healthcare field. Nanomedicine as an evolution of the modern medicine has provided a different paradigm in the way the modern medical practitioners can approach or treat various illness or disorders. Nanomedicine has offered various tools to lift the limitations that have existed in the conventional medicine, hence ensuring higher success in the treatment and diagnosis of disease. One of the tools of nanomedicine being widely applied is nanodelivery systems to carry drugs into the human body [1, 2]. There are various benefits of employing nanodelivery systems for drug delivery purposes. For instance, by reducing the size of the drugs into nanosized formulations, the drug dissolution rate can be increased, thereby improving the drug absorption

and bioavailability in the body. Apart from that, drugs can be delivered at the desired site of action in the human body, thereby improving the therapeutic index of the drugs by increasing their efficiency and reducing their toxicity. For example, chemotherapeutic drugs administered at high dosages in the human body to destroy tumor cells can inadvertently destroy the surrounding healthy tissues or cells as well, thereby eliciting unwanted ill effects. Another major advantage of employing nanoparticle to deliver drugs is to provide protection for easily degraded or short half-life drugs, such as small peptides and nucleic acids to prolong the pharmacological effects.

Nanomaterials, engineered or synthesized for the purpose of delivering the drugs, are the major component of the drug delivery system which may ensure its success or failure. Nanomaterials used in nanodelivery systems can exist in

various forms and types. Nanoparticles are a subset of nanomaterials which can be tailored for specific usage depending on the material and method of synthesis. Silica nanoparticle is a type of nanoparticle that is being developed and tested vigorously in drug delivery systems to treat various diseases [3–6]. There are many advantages of using silica nanoparticles as a nanodelivery system because they are relatively inexpensive to produce, chemically inert, and thermally stable. Apart from that, depending on the methods used to produce the silica nanoparticles, it can be tailored to contain porous structures for drug encapsulation and to be hydrophilic for higher solubility and stability in the human body.

Despite these tremendous benefits, one of the pivotal requirements of these drug delivery systems is to be biocompatible with the human body. Hence the nanoparticles used as a drug delivery system must be preferably nontoxic and must not elicit the body's natural immune responses at the doses administered. In other words, the nanoparticles should be considerably inert and any form of toxicity elicited at the intended target site, tissues, or cells should be solely due to the action of the drug molecules alone. This is important because if the nanoparticles exhibit high levels of toxicity, it will damage or kill healthy cells along with the diseased cells, and, by eliciting the body's natural immune responses, the nanoparticles will be effectively cleared by the macrophages in the circulation system before reaching the intended target. Therefore, preliminary studies must be conducted on the biocompatibility or cytotoxic potential of the nanoparticles on human tissues or cells as a basic prerequisite before it can be deemed to be utilized as a drug delivery system.

The cytotoxic potential of the nanoparticles can be mainly attributed to its physicochemical properties such as its size, shape, chemical purity, surface chemistry, and colloidal stability [7]. Much research has been done to relate the physicochemical properties of nanoparticles to their cytotoxicity. Because each type of nanoparticles has its own distinct physicochemical features, the toxic effects exerted on the cells may also vary. Some of the toxic effects are irreversible and permanent, leading to cell deaths and some are reversible; after the exposures to nanoparticles are removed, the cells may begin to proliferate normally. The mechanism of action that leads to the cells deaths may also be different. The toxic effect of the nanoparticles can be measured using *in vitro* cell-based assays [8].

In this study, the cytotoxicity of colloidal amorphous silica nanoparticles synthesized using the micelle formation method has been tested against normal human foreskin fibroblast cell line (Hs27) as well as selected human bone carcinoma (U-2 OS), human breast cancer (MCF-7), and human cervical carcinoma (HeLa) and (Ca Ski) cell lines to determine the IC₅₀ values. Different sizes of silica nanoparticles were used to study the relationship between its size and the level of toxicity exerted on the different cells being tested.

2. Materials and Methods

2.1. Materials for Colloidal Silica Nanoparticles Synthesis. Vinyltrimethoxysilane (98%) and Tween 80 were purchased

from Sigma Aldrich. 2-Butanol, ammonia 35%, and dialysis tubing (12–14 KDa) were obtained from Fisher Scientific.

2.2. Synthesis and Characterization of Colloidal Silica Nanoparticles. Silica nanocolloids spheres were prepared by micelle formation approach, where Tween 80 anionic surfactant was introduced in the presence of water (solvent) and butanol (cosolvent), and ammonium was added to adjust the pH. Typical preparation involved rapid mixing of reagents under vigorous stirring at room temperature of 24°C. The mixture was then transferred into a preheated reactor. After an hour, vinyltrimethoxysilane (Si precursor) was added. The effect of Si precursor amount, butanol amount, and reaction temperature on the formation and size distribution of silica was studied. The mixture usually began to turn to a turbid white in about 5–15 min, as silica nanoparticles were formed. The mixture was left overnight with a continuous stirring rate of 320 rpm. The silica nanocolloids produced were then subjected to dialysis process for 4–5 days using dialysis tubing 12–14 KDa to remove the surfactant.

To investigate the relationship between the physicochemical properties and toxicities, characterization of the silica nanoparticles was performed using transmission electron microscopy (TEM), X-ray diffractometer (XRD), dynamic light-scattering (DLS) methods, and NIR-UV-Vis spectrophotometer, which provided information on the nanoparticles morphology, crystallinity, size distribution, and concentrations, respectively.

To investigate the morphology and size distribution of the silica nanoparticles, a drop of the particle suspension in the test medium was dried on a carbon-coated 200 mesh copper grid and imaged with a transmission electron microscope (Model FEI CM12 version 3.2 image analysis systems 120 kV). The images from TEM were analyzed using ImageJ software whereby 100 particles were measured. For X-ray diffraction (XRD) analysis, the samples were dried in an oven at 120°C overnight. XRD analysis was performed using CuK α radiation from 5–90° (Bruker AXS D8) to determine the crystallinity of silica nanoparticles. The images were analyzed with EVA software. Particles size distribution was evaluated using Zetasizer (Model ZEN 3600, Nanoseries, Malvern Instruments). The concentration of silica nanoparticles was measured by using UV-Visible near infrared spectrophotometer (UV-Vis 3600, Shimadzu), with absorbance value taken at peak of 233 nm.

2.3. Human Normal and Cancer Cell Lines and Reagents. U-2 OS (HTB-96) human osteosarcoma, MCF-7 (HTB-22) human breast adenocarcinoma, HeLa (CCL-2) human cervical cancer, Ca Ski (CRL-1550) human cervical cancer, and Hs27 (CRL 1634) human foreskin fibroblast cell lines were all obtained from the American Type Culture Collection (ATCC), USA. The growth media: McCoy's 5a medium, Dulbecco's Modified Eagle Medium (DMEM), DMEM/F12 medium, RPMI 1640 medium, fetal bovine Serum (FBS), penicillin-streptomycin, and trypsin were obtained from Invitrogen, USA. The phosphate buffer solution (PBS) tablets were obtained from AMRESCO, USA. The cell proliferation reagent (WST-1) was obtained from Roche, USA.

2.3.1. Cell Culture. MCF-7, HeLa, and Hs27 cells were maintained in DMEM. U-2 OS cells were maintained in McCoy's 5a medium. Ca Ski cells were maintained in RPMI 1640 medium. The cells were cultured in the appropriate medium, supplemented with 5–10% fetal bovine serum and 1% penicillin-streptomycin, using 25 cm² flasks in a 37°C incubator with 5% CO₂ in humidified incubator.

2.3.2. Cell Subculture. To subculture the cells, the cells were divided and the culture medium was replaced with fresh medium as follows. First, the old medium was removed, and then the cells were rinsed briefly with PBS to wash the cells. One to two mL of trypsin was then added, and the flask was incubated at 37°C and 5% CO₂ for 5 minutes. After the cells had detached from the lower part of the flask, 20 mL of medium was added to the flask and the culture was divided in to two parts. One part was then transferred to a new flask.

2.4. Cell Proliferation Assay. The cells were grown until they were confluent. Then, the cells were trypsinised and the number of viable cells was counted with a hemocytometer to prepare a cell suspension. Two hundred microlitres of suspension containing 1×10^4 cells was seeded in each well of a 96-well microtiter plate (BD, USA) and incubated overnight at 37°C with 5% CO₂. In the following day, the medium was replaced and the cells were treated with silica nanoparticles with varying concentrations and maintained at 37°C with 5% CO₂ for 24–72 hours. After the incubation period, the old medium was discarded from the wells and rinsed with PBS before adding fresh culture medium with a final volume of 100 μL per well. Then, 10 μL of WST-1, cell proliferation reagent, was added to each well. The microtiter plate was then incubated again for 2 hours at 37°C with 5% CO₂. After the incubation period, the cell viability was measured using an ELISA reader (Multiskan Spectrum) at 450 nm.

2.5. Statistical Analysis. The experiment was carried out in three replicates. Microsoft Excel templates were used for the collection of raw data and transformation of the data to the proper format for GraphPad Prism 5.0 software. Prism was used to calculate the concentrations associated with 50% viability (IC50 values) with 95% confidence limits using a Hill function nonlinear regression analysis.

3. Results and Discussion

3.1. Synthesis and Characterization of Silica Nanoparticles. In this study, we synthesized colloidal amorphous silica nanoparticles of two different sizes for drug delivery purposes using the micelle formation method. Primarily, silica can be present in two forms, crystalline and amorphous. We selected amorphous form of silica because it has higher solubility in water as opposed to crystalline form of silica which has very low water solubility [9]. The solubility of amorphous silica in water at body pH is normally around 130–150 ppm (μg/mL) [10]. Apart from that, amorphous silica can dissolve into body fluid as silicic acid and is then removed through urine [11, 12]. The micelle formation method was used to

synthesize the silica nanoparticles because it produces more homogenous particle size distribution and can directly entrap drug molecules inside micelles structure before forming silica nanoparticles. Schematic diagram in Figure 1 illustrates the formations of silica nanoparticles using micelle formation approach. Silica nanoparticles form due to hydrolysis, alcohol condensation, and water condensation. Hydrolysis occurs when Si precursor, organosilanes reacts with water and 2-butanol in the aqueous solvent and forms siloxane bridge (1). Hydrolysis process is enhanced with the addition of ammonia by producing more hydroxyl ions (OH⁻) to react with organosilanes. For alcohol and water condensations, silanols react with each other to form crosslinking between Si–O–Si chains until all Si precursors reacted (equations (2) and, see (3) [13, 14]):

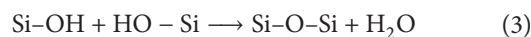
hydrolysis:



alcohol condensation:



water condensation:



Both kinds of silica nanoparticles were observed to be spherical in shape under TEM as shown in Figure 2, with average size of $20 \text{ nm} \pm 3.5 \text{ nm}$ and $40 \text{ nm} \pm 4.6 \text{ nm}$, analyzed using Image J software whereby 100 particles were measured. The X-ray diffraction patterns of the silica nanoparticles are shown in Figure 3. XRD diffractogram shows that a broad peak is present at $2\theta = 10\text{--}30^\circ$ for both the silica nanoparticles, verifying it to be of amorphous structure. Particle size distributions for the 20 nm and 40 nm silica nanoparticles are shown in Figures 4(a) and 4(b), respectively. The Z-average hydrodynamic diameter and polydispersity index of the silica nanoparticles were measured by dynamic light-scattering techniques to determine the particle size distributions. The Z-average value and polydispersity index (PdI) value for 20 nm silica nanoparticles are 47.80 nm and 0.099, respectively. The Z-average value and polydispersity index (PdI) value for 40 nm silica nanoparticles are 64.45 nm and 0.097, respectively. The Z-average value for both the silica nanoparticles is larger compared to the primary diameter as determined by TEM. This is because the Z-average is a hydrodynamic parameter and is usually affected by surface charge of the particles as the samples were measured in its colloidal form whereas TEM measurements of the samples were taken in dry conditions. The graphs in Figures 4(a) and 4(b) which exhibit narrow particle size distributions about an average value and a polydispersity index value of <0.100 for both the silica nanoparticles indicate that the particles are monodispersed. Monodisperse suspensions of nanoparticles contain particles of nearly the same size and are better suited for studying size-dependent toxic effects as opposed to using polydispersed suspensions of nanoparticles which may mask size effects. The concentration of silica nanoparticles was measured in absorbance (OD) taken at

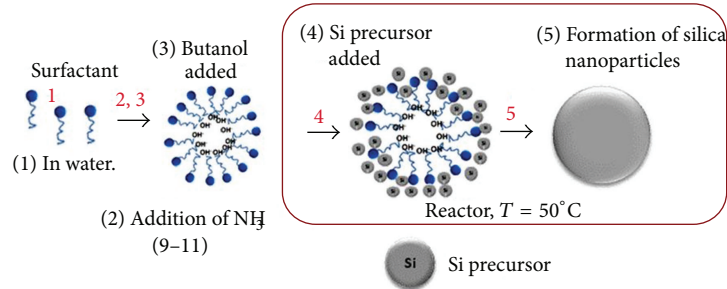


FIGURE 1: Formation of silica nanoparticles using micelle formation method.

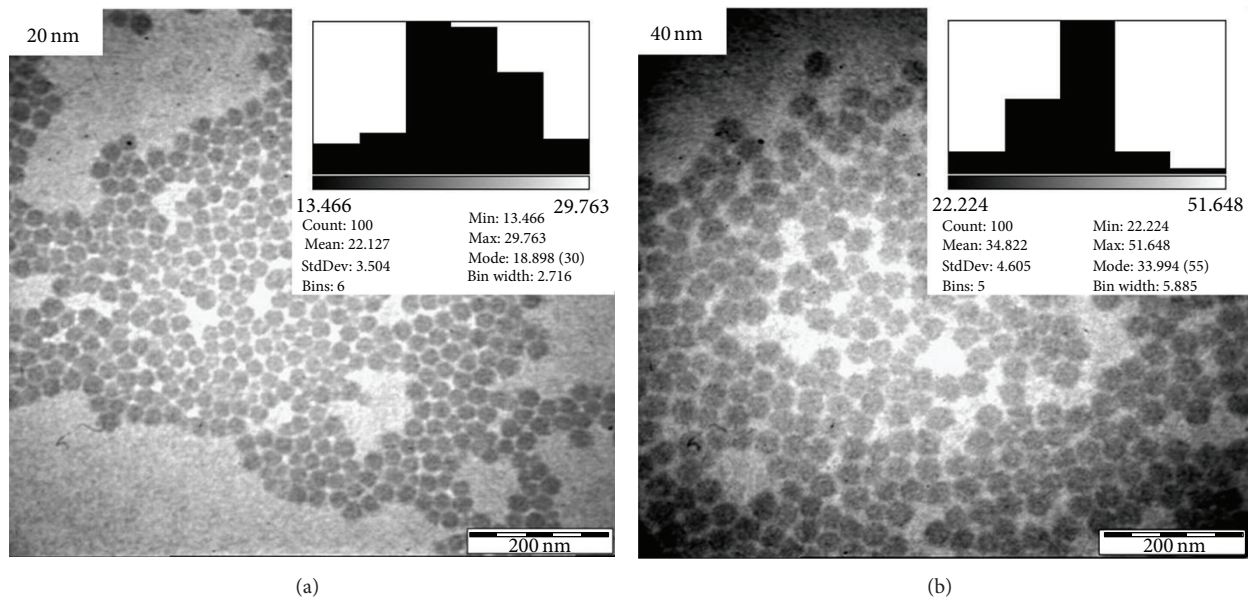


FIGURE 2: TEM images and histograms of particle size distribution from TEM analysis.

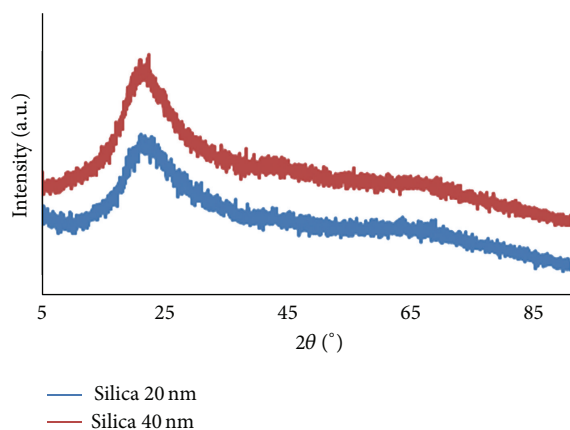


FIGURE 3: XRD patterns of colloidal amorphous silica nanoparticles.

a peak value of 233 nm by using UV-Visible near infrared spectrophotometer. The optical properties of silica nanoparticles are caused by surface defects related to large surface to volume ratio [15]. These structural defects are classified

into paramagnetic and nonparamagnetic defects, which can be characterized by optical absorption in a broad range of wavelengths: near-infrared, visible, and ultraviolet (UV) [16]. A single absorption band was observed at 233 nm (~ 5 eV) during photometric scanning of both the silica nanoparticles in the UV range as shown in Figure 5. This optical absorption band at 5 eV is one of the oldest known nonparamagnetic defects in amorphous silica and also known as the “ B_2 band.” This band is attributed to occur due to some form of oxygen deficiency in the silica network [17, 18]. Therefore, we were able to validate that the optical absorption exhibited at 233 nm was due to silica nanoparticles, hence rationalizing our method of measuring the concentration of colloidal silica nanoparticles in this manner. The absorbance values at peak 233 nm for 20 nm and 40 nm silica nanoparticles are tabulated in Table 2. From Figure 6, it can be seen that the intensity of the peak for 40 nm silica nanoparticles is slightly higher than 20 nm silica nanoparticles suggesting that bigger particles have higher UV absorption. Similar findings were reported by Rahman and coworkers who carried out experiments on size-dependent physicochemical and optical properties of silica nanoparticles. They have observed that

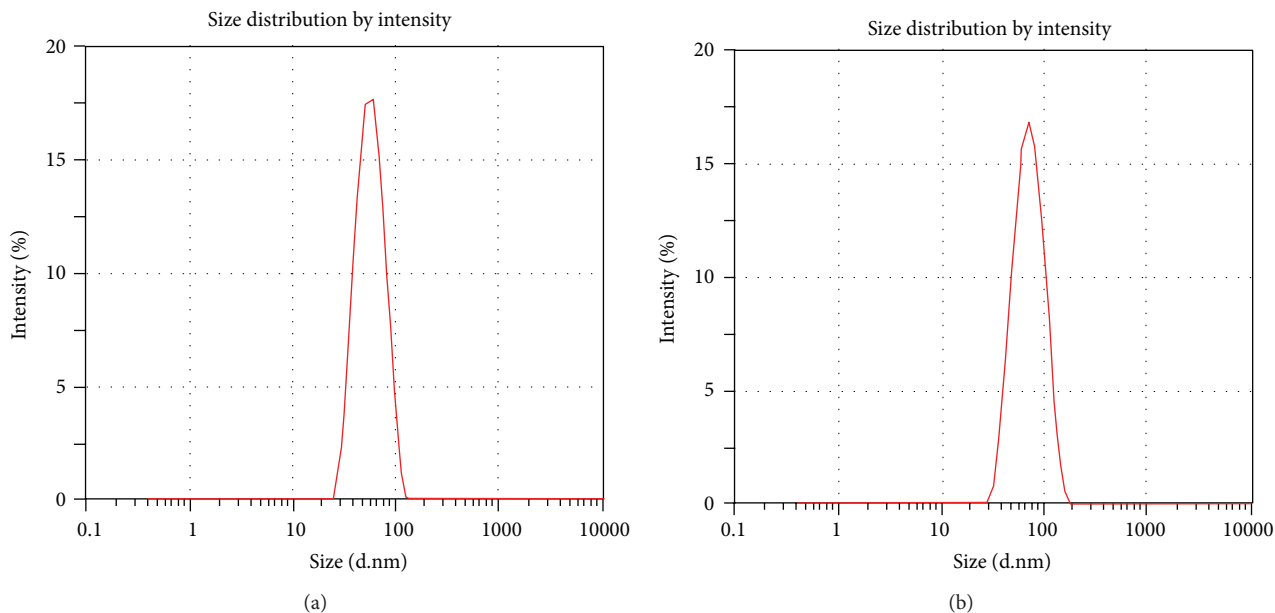


FIGURE 4: Particle size distribution of (a) 20 nm silica nanoparticles and (b) 40 nm silica nanoparticles.

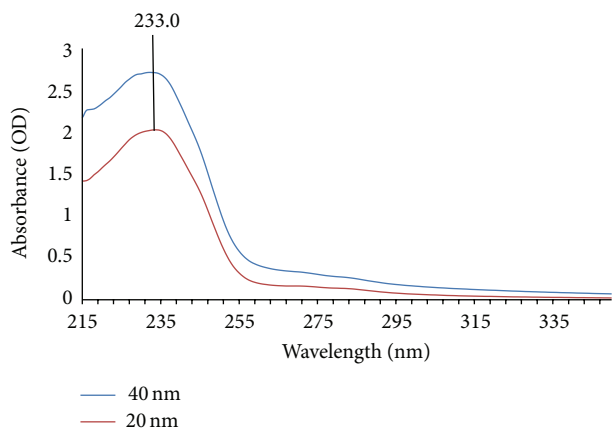


FIGURE 5: Optical absorption of 20 nm and 40 nm silica nanoparticles in UV range.

the intensity of the peak slightly decreases as the sizes of silica particles decrease and attributed their findings to the intense interparticle interactions at smaller particle size, that is, aggregation phenomena which could decrease the exposure of the E centers present at the silica surface to the UV light source [19].

3.2. Acute Cytotoxicity. To study the cytotoxic effect of the 20 nm and 40 nm colloidal amorphous silica nanoparticles against the selected normal and cancerous human cell lines, WST-1 assay was used to measure the amount of cell viability. The cell lines used for this study are Hs27, U-2 OS, MCF-7, HeLa, and Ca Ski. All the cell lines were exposed to the silica nanoparticles for a period of 24 h to measure the acute

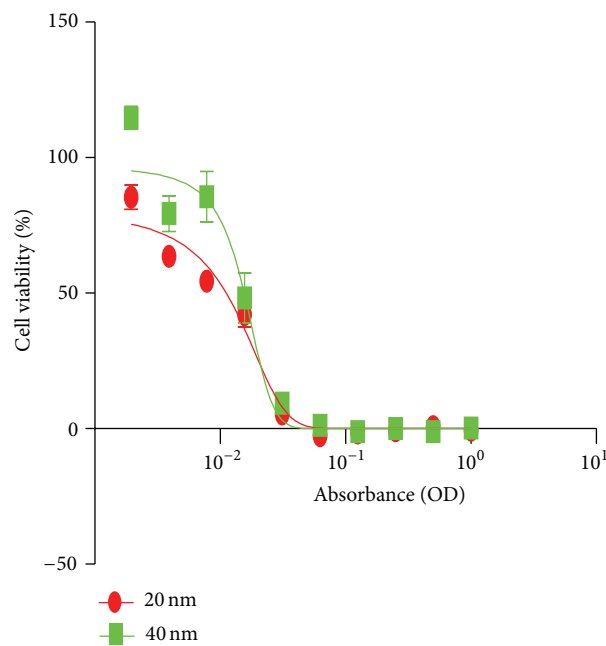


FIGURE 6: Cell viability assay for silica nanoparticles on U-2 OS cell line. The cell line was treated with 20 nm and 40 nm silica nanoparticles for 24 h with IC_{50} of 0.011 OD and 0.015 OD, respectively.

cytotoxicity. Since the particles were produced in colloidal form, the concentration of the silica nanoparticles were measured in absorbance (OD) taken at a peak value of 233 nm. Subsequently we have used the absorbance (OD) as a unit of particle mass concentration to perform the cytotoxicity testing with concentrations ranging from 1 to 0.002 OD. The results for the IC_{50} are also presented in absorbance (OD).

TABLE 1: List of IC₅₀ based on the size of nanoparticles and the cells tested.

Cell lines	Size of nanoparticles (nm)	IC ₅₀ (absorbance OD)
U-2 OS	20	0.01118
	40	0.01555
MCF-7	20	0.05408
	40	0.07288
Hs27	20	0.01967
	40	0.01438
HeLa	20	0.09516
	40	0.08063
Ca Ski	20	0.03821
	40	0.02447

TABLE 2: Absorbance values (OD) of 20 nm and 40 nm silica nanoparticles.

Blank silica NPs colloids (nm)	Absorbance value at peak 233 nm (OD)	Absorbance value at peak 233 × dilution factor 100 (OD)
20	2.028	202.8
40	2.713	271.3

In our effort to correlate the effect of size of the silica nanoparticles to its cytotoxic potential, we have tried to standardize and control all the other physicochemical parameters that may exist between the different-sized nanoparticles used in this experiment as discussed in the characterization of nanoparticles section. To minimize variability in production process the same batch of synthesized silica nanoparticles was used to perform the cytotoxicity assays. Preliminary steps were taken to evaluate the suitability of using WST-1-based assay in this study by measuring the interference of silica nanoparticles on WST-1 reagents and its reaction products for all the cell lines at the similar concentrations of silica nanoparticles used for the cytotoxicity assay before proceeding with the experiment. Also, appropriate blanks and controls were included when performing cytotoxicity assays. Hence, any interference that may exist during cytotoxicity testing attributable to factors other than size of the nanoparticles can be safely ruled out.

The acute cytotoxicity of the silica nanoparticles is presented as a percentage of the cell viability versus concentration in Figures 6 to 10. The IC₅₀ values were calculated from the graphs to determine the concentration of the silica nanoparticles needed to inhibit 50% of the cells from proliferating. Table 1 presents the IC₅₀ values of the silica nanoparticles. In this study, the silica nanoparticles have been proven to inhibit the proliferation of both the normal and cancer cell lines that were tested in a dose-dependent manner. This is evident: as the concentration of silica nanoparticles increases, the percentage viability of the cells decreases for all the cell lines tested as shown in Figures 6 to 10. Thus, our results are in general agreement with previously reported studies on the dose-dependent cytotoxicity of amorphous silica nanoparticles [20, 21]. The results also reveal differences

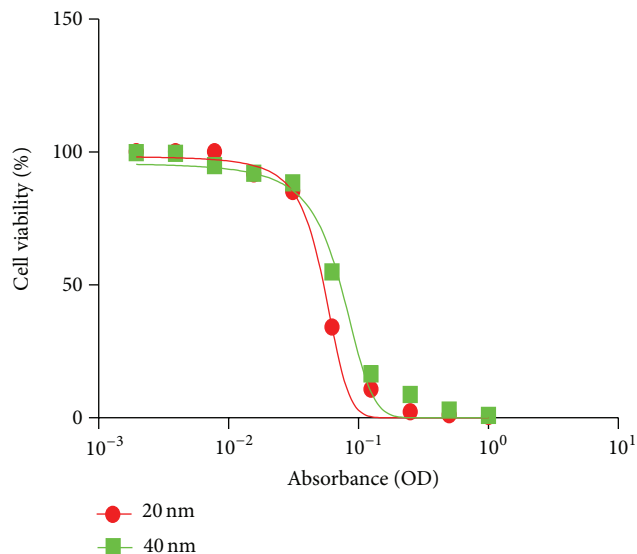


FIGURE 7: Cell viability assay for silica nanoparticles on MCF-7 cell line. The cell line was treated with 20 nm and 40 nm silica nanoparticles for 24 h with IC₅₀ of 0.054 OD and 0.072 OD, respectively.

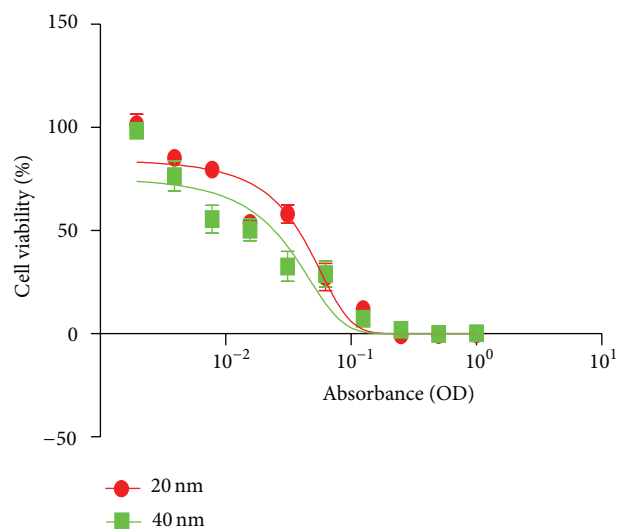


FIGURE 8: Cell viability assay for silica nanoparticles on Ca Ski cell line. The cell line was treated with 20 nm and 40 nm silica nanoparticles for 24 h with IC₅₀ of 0.038 OD and 0.024 OD, respectively.

in the responses among the five cell lines tested. Based on the results obtained, 20 nm nanoparticles were shown to be more toxic compared to 40 nm sized nanoparticles in U-2 OS and MCF-7 cell lines as shown in Figures 6 and 7, respectively. However, in both the human cervical cancer cell lines tested, Ca Ski and HeLa, as well as on Hs27 cell line, 40 nm nanoparticles were shown to be more toxic compared to 20 nm sized nanoparticles as shown in Figures 8, 9 and 10, respectively.

Thus, our data indicate that the size of silica nanoparticles does not relate to its cytotoxicity in a straightforward manner. In fact studies based on the size-dependent cytotoxicity of amorphous silica nanoparticles have produced contradictory

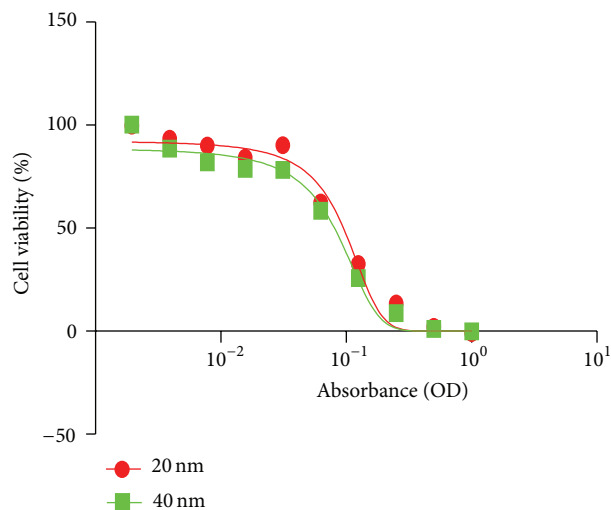


FIGURE 9: Cell viability assay for silica nanoparticles on HeLa cell line. The cell line was treated with 20 nm and 40 nm silica nanoparticles for 24 h with IC_{50} of 0.095 OD and 0.081 OD, respectively.

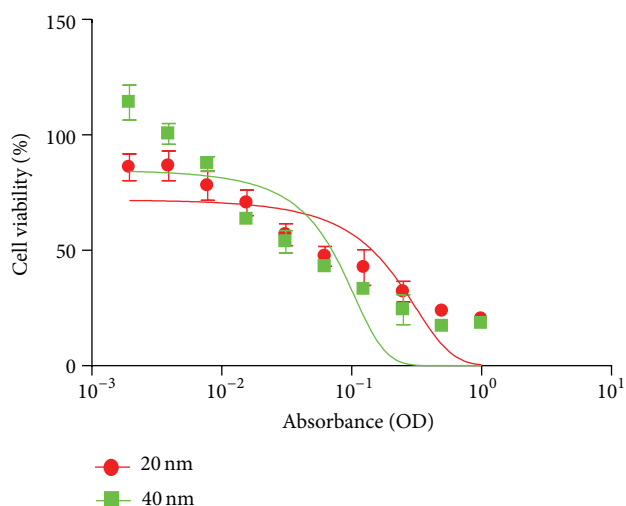


FIGURE 10: Cell viability assay for silica nanoparticles on Hs27 cell line. The cell line was treated with 20 nm and 40 nm silica nanoparticles for 24 h with IC_{50} of 0.019 OD and 0.014 OD, respectively.

results. For example, several independent researchers have found that smaller-sized silica nanoparticles induced severe cellular damage in lung cancer cells, myocardial cells, and human endothelial cells [20–22]. This was attributed to the fact that smaller nanoparticles have larger ratio of surface area to weight, leading to more contact with the cells to induce damage [23–25]. This may explain our current findings of higher toxicity induced by 20 nm particles on MCF-7 and U-2 OS cell lines. On the other hand, some researchers have found that bigger-sized silica nanoparticles may exert higher toxicity against the cells tested. For instance, Lu and coworkers have reported that 20 nm silica nanoparticles are more cytotoxic than 7 nm particles on human hepatoma cells [26]. One possible explanation could be the protein corona

formation on the surface of silica nanoparticles that may alter the cytotoxic potential of the nanoparticles. It has been established by numerous *in vitro* studies that various nanoparticles are able to adsorb serum proteins from tissue culture media, which affected the toxicity of the nanoparticles [27, 28]. Tenzer and coworkers have reported particle-size-dependent binding of several proteins involved in blood coagulation [29]. They studied the long-lived blood plasma-derived corona on monodispersed amorphous silica nanoparticles differing in size and observed that the type of nanoparticle corona formation is significant even if the size of the particles only differs in 10 nm. Therefore it is possible that the type of protein corona formed on the 40 nm silica nanoparticles is significantly different from the one formed on 20 nm silica nanoparticles, thus rendering it to be more cytotoxic to Ca Ski, HeLa, and Hs27 cell lines. Since our results do not support size-dependent toxicity on the cell lines tested, the only other probable reason we could infer is that toxicity of silica nanoparticles is cell type dependent. Plausible explanation for this can be made on the basis that as different cell types have different physiological function, their interaction with nanoparticles can also differ considerably. These results are in line with those of Yu and coworkers, who demonstrated that the ability of silica nanoparticles to inhibit cell proliferation of macrophages and lung carcinoma cells was cell type dependent [30]. Similar findings were reported by Kroll and coworkers who performed cytotoxicity screening of 23 engineered nanomaterials using a test matrix of ten cell lines and three different assays [31]. Their findings have suggested that even when assessing nanomaterials toxicity to cells originating from the same organ, the outcome highly depends on the cell type used and attributed the occurrence to sensitivity of cell lines.

4. Conclusion

The aim of this study was to assess the cytotoxic responses of five different human cell lines exposed to two different-sized monodispersed amorphous silica nanoparticles. In conclusion, we have demonstrated that 20 nm and 40 nm silica nanoparticles significantly reduce cell viability in a dose- and cell type-dependent manner in the normal and cancerous cells tested. Therefore, more research is necessary to investigate the underlying mechanisms of the cytotoxic effects of silica nanoparticles before they can be used in drug delivery and controlled release applications.

Acknowledgments

The authors appreciate technical support from the Electron Microscopy Facility, School of Biology, Universiti Sains Malaysia. This work was supported by Research University Grant (RU: 1001/Pbahan/814080).

References

- [1] B. Mishra, B. B. Patel, and S. Tiwari, “Colloidal nanocarriers: a review on formulation technology, types and applications

- toward targeted drug delivery," *Nanomedicine: Nanotechnology, Biology, and Medicine*, vol. 6, no. 1, pp. 9–24, 2010.
- [2] N. A. Ocheke, P. O. Olorunfemi, and N. C. Ngwuluka, "Nanotechnology and drug delivery part 2: nanostructures for drug delivery," *Tropical Journal of Pharmaceutical Research*, vol. 8, no. 3, pp. 275–287, 2009.
 - [3] D. J. Bharali, I. Klejbor, E. K. Stachowiak et al., "Organically modified silica nanoparticles: a nonviral vector for in vivo gene delivery and expression in the brain," *Proceedings of the National Academy of Sciences of the United States of America*, vol. 102, no. 32, pp. 11539–11544, 2005.
 - [4] J. Lu, M. L. Liong, J. I. Zink, and F. Tamanoi, "Mesoporous silica nanoparticles as a delivery system for hydrophobic anticancer drugs," *Small*, vol. 3, no. 8, pp. 1341–1346, 2007.
 - [5] T. Y. Ohulchanskyy, I. Roy, L. N. Goswami et al., "Organically modified silica nanoparticles with covalently incorporated photosensitizer for photodynamic therapy of cancer," *Nano Letters*, vol. 7, no. 9, pp. 2835–2842, 2007.
 - [6] I. I. Slowing, J. L. Vivero-Escoto, C. W. Wu, and V. S. Y. Lin, "Mesoporous silica nanoparticles as controlled release drug delivery and gene transfection carriers," *Advanced Drug Delivery Reviews*, vol. 60, no. 11, pp. 1278–1288, 2008.
 - [7] P. Rivera-Gil, D. Jimenez de Aberasturi, V. Wulf et al., "The challenge to relate the physicochemical properties of colloidal nanoparticles to their cytotoxicity," *Accounts of Chemical Research*, vol. 46, no. 3, pp. 743–749, 2012.
 - [8] J. M. Hillegass, A. Shukla, S. A. Lathrop, M. B. MacPherson, N. K. Fukagawa, and B. T. Mossman, "Assessing nanotoxicity in cells in vitro," *Wiley Interdisciplinary Reviews: Nanomedicine and Nanobiotechnology*, vol. 2, no. 3, pp. 219–231, 2010.
 - [9] R. K. Iler, *The Chemistry of Silica: Solubility, Polymerization, Colloid and Surface Properties, and Biochemistry*, John Wiley & Sons, New York, NY, USA, 1979.
 - [10] R. Viitala, S. Areva, M. Jokinen, and M. Koskinen, "About interactions between sol-gel derived silica, titania and living organisms," in *Sol-Gel Methods for Materials Processing*, P. Innocenzi, Y. Zub, and V. Kessler, Eds., vol. 15, pp. 251–268, 2008.
 - [11] J. F. Popplewell, S. J. King, J. P. Day et al., "Kinetics of uptake and elimination of silicic acid by a human subject: a novel application of ^{32}Si and accelerator mass spectrometry," *Journal of Inorganic Biochemistry*, vol. 69, no. 3, pp. 177–180, 1998.
 - [12] W. Lai, P. Ducheyne, and J. Garino, "Removal pathway of silicon released from bioactive glass granules in vivo," *Bioceramics*, vol. 11, 1998.
 - [13] F. J. Arriagada and K. Osseo-Asare, "Synthesis of nanosize silica in a nonionic water-in-oil microemulsion: effects of the water/surfactant molar ratio and ammonia concentration," *Journal of Colloid and Interface Science*, vol. 211, no. 2, pp. 210–220, 1999.
 - [14] R. Chen, H. Qu, A. Agrawal, S. Guo, and P. Ducheyne, "Controlled release of small molecules from silica xerogel with limited nanoporosity," *Journal of Materials Science: Materials in Medicine*, vol. 24, no. 1, pp. 137–146, 2013.
 - [15] A. Anedda, C. M. Carbonaro, F. Clemente, R. Corpino, and P. C. Ricci, "Low temperature investigation of the blue emission in mesoporous silica," *Materials Science and Engineering C*, vol. 25, no. 5–8, pp. 631–634, 2005.
 - [16] M. Jafarzadeh, I. A. Rahman, and C. S. Sipaut, "Optical properties of amorphous organo-modified silica nanoparticles produced via co-condensation method," *Ceramics International*, vol. 36, no. 1, pp. 333–338, 2010.
 - [17] L. N. Skuja, A. N. Streletsky, and A. B. Pakovich, "A new intrinsic defect in amorphous SiO_2 : twofold coordinated silicon," *Solid State Communications*, vol. 50, no. 12, pp. 1069–1072, 1984.
 - [18] R. Tohmon, H. Mizuno, Y. Ohki, K. Sasagane, K. Nagasawa, and Y. Hama, "Correlation of the 5.0- and 7.6-eV absorption bands in SiO_2 with oxygen vacancy," *Physical Review B*, vol. 39, no. 2, pp. 1337–1345, 1989.
 - [19] I. A. Rahman, P. Vejayakumaran, C. S. Sipaut, J. Ismail, and C. K. Chee, "Size-dependent physicochemical and optical properties of silica nanoparticles," *Materials Chemistry and Physics*, vol. 114, no. 1, pp. 328–332, 2009.
 - [20] W. Lin, Y. W. Huang, X. D. Zhou, and Y. Ma, "In vitro toxicity of silica nanoparticles in human lung cancer cells," *Toxicology and Applied Pharmacology*, vol. 217, no. 3, pp. 252–259, 2006.
 - [21] Y. Y. Ye, J. W. Liu, M. C. Chen, L. J. Sun, and M. B. Lan, "In vitro toxicity of silica nanoparticles in myocardial cells," *Environmental Toxicology and Pharmacology*, vol. 29, no. 2, pp. 131–137, 2010.
 - [22] D. Napierska, L. C. J. Thomassen, V. Rabolli et al., "Size-dependent cytotoxicity of monodisperse silica nanoparticles in human endothelial cells," *Small*, vol. 5, no. 7, pp. 846–853, 2009.
 - [23] A. Nel, T. Xia, L. Mädler, and N. Li, "Toxic potential of materials at the nanolevel," *Science*, vol. 311, no. 5761, pp. 622–627, 2006.
 - [24] H. M. Kipen and D. L. Laskin, "Smaller is not always better: nanotechnology yields nanotoxicology," *The American Journal of Physiology—Lung Cellular and Molecular Physiology*, vol. 289, no. 5, pp. L696–L697, 2005.
 - [25] G. Oberdörster, E. Oberdörster, and J. Oberdörster, "Nanotoxicology: an emerging discipline evolving from studies of ultra-fine particles," *Environmental Health Perspectives*, vol. 113, no. 7, pp. 823–839, 2005.
 - [26] X. Lu, J. Qian, H. Zhou et al., "In vitro cytotoxicity and induction of apoptosis by silica nanoparticles in human HepG2 hepatoma cells," *International Journal of Nanomedicine*, vol. 6, pp. 1889–1901, 2011.
 - [27] T. Cedervall, I. Lynch, M. Foy et al., "Detailed identification of plasma proteins adsorbed on copolymer nanoparticles," *Angewandte Chemie—International Edition*, vol. 46, no. 30, pp. 5754–5756, 2007.
 - [28] E. G. Barrett, C. Johnston, G. Oberdörster, and J. N. Finkelstein, "Silica binds serum proteins resulting in a shift of the dose-response for silica-induced chemokine expression in an alveolar type II cell line," *Toxicology and Applied Pharmacology*, vol. 161, no. 2, pp. 111–122, 1999.
 - [29] S. Tenzer, D. Docter, S. Rosfa et al., "Nanoparticle size is a critical physicochemical determinant of the human blood plasma corona: a comprehensive quantitative proteomic analysis," *ACS Nano*, vol. 5, no. 9, pp. 7155–7167, 2011.
 - [30] T. Yu, A. Malugin, and H. Ghandehari, "Impact of silica nanoparticle design on cellular toxicity and hemolytic activity," *ACS Nano*, vol. 5, no. 7, pp. 5717–5728, 2011.
 - [31] A. Kroll, C. Dierker, C. Rommel et al., "Cytotoxicity screening of 23 engineered nanomaterials using a test matrix of ten cell lines and three different assays," *Particle and Fibre Toxicology*, vol. 8, article 9, 2011.

Research Article

Effects of Polymeric Additives on the Crystallization and Release Behavior of Amorphous Ibuprofen

Su Yang Lee,¹ Guiduk Yu,² and Il Won Kim¹

¹ Department of Chemical Engineering, Soongsil University, Seoul 156-743, Republic of Korea

² School of Chemical and Biological Engineering, Seoul National University, Seoul 151-744, Republic of Korea

Correspondence should be addressed to Il Won Kim; iwkim@ssu.ac.kr

Received 28 April 2013; Accepted 30 June 2013

Academic Editor: Krasimir Vasilev

Copyright © 2013 Su Yang Lee et al. This is an open access article distributed under the Creative Commons Attribution License, which permits unrestricted use, distribution, and reproduction in any medium, provided the original work is properly cited.

Some polymeric additives were studied to understand their effects on the amorphous phase of ibuprofen (IBU), used as a poorly water soluble pharmaceutical model compound. The amorphous IBU in bulk, as well as in nanopores (diameter ~24 nm) of anodic aluminum oxide, was examined with the addition of poly(acrylic acid), poly(*N*-vinyl pyrrolidone), or poly(4-vinylphenol). Results of bulk crystallization showed that they were effective in limiting the crystal growth, while the nucleation of the crystalline phase in contact with water was nearly instantaneous in all cases. Poly(*N*-vinyl pyrrolidone), the most effective additive, was in specific interaction with IBU, as revealed by IR spectroscopy. The addition of the polymers was combined with the nanoscopic confinement to further stabilize the amorphous phase. Still, the IBU with addition of polymeric additives showed sustained release behavior. The current study suggested that the inhibition of the crystal nucleation was probably the most important factor to stabilize the amorphous phase and fully harness its high solubility.

1. Introduction

Enhancing the bioavailability of active pharmaceutical ingredients (APIs) is becoming increasingly important because of the mounting problem of their sparing solubility. The solubility problem has escalated in the recently developed APIs, as it occurs in about 60% of them [1]. To overcome this problem, the enhancement of bioavailability is realized by the increase of the dissolution rate. In the dissolution rate, the importance of the surface area (A) and solubility (C_s) is well recognized, for example, from the Noyes-Whitney equation: (dissolution rate) = $k_d A(C_s - C_b)$, where k_d is the rate constant and C_b is the bulk concentration [2–4].

The increase of the surface area has been investigated through nanoformulation. Nanocrystals of the poorly soluble APIs as well as polymeric nanoparticles containing the APIs have been extensively studied in the recent years [5, 6]. Also, the increase of the solubility has been explored by changing the intermolecular interactions of the APIs. Amorphous phases, cocrystals, and polymorphs are some of the representative examples [7–9].

We have previously reported the formation of an amorphous API through the confinement within nanoporous

anodic aluminum oxide (AAO) using ibuprofen (IBU) as a model API [10]. In the case of IBU, the kinetically stabilized amorphous phase rapidly changed into a crystalline form during the release experiment, as was similarly observed in the amorphous IBU stabilized within polymer matrices (IBU/polymer = ca. 20 : 80) [11, 12]. These results suggested that the stability of the amorphous phase in contact with water would be the key component to successfully utilize the high solubility of the amorphous phase [13]. In addition, the crystallization of IBU is implicated in the possibly damaging effects on the stomach membrane [12]. In the present study, some polymeric additives (IBU/polymer = 90 : 10) were tested in their ability to stabilize the amorphous phase in bulk, as well as in nanopores (diameter ~24 nm) of anodic aluminum oxide.

2. Materials and Methods

2.1. Fabrication of AAO with Nanopores. AAOs with nanopores were prepared from the Al foil (99.999%, Goodfellow; thickness 0.5 mm) through the two-step anodization technique [10, 14, 15]. Before anodization, Al was electropolished

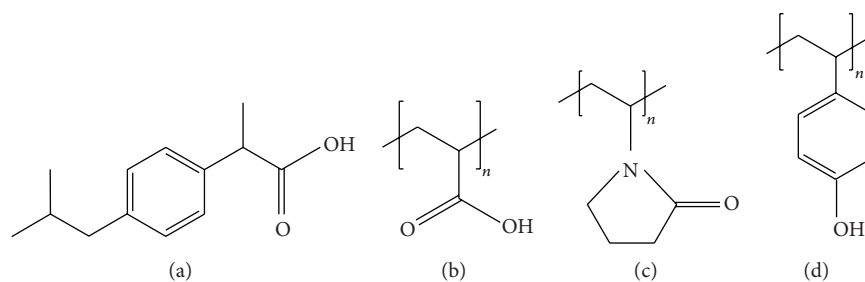


FIGURE 1: Chemical structures of (a) ibuprofen (IBU), (b) poly(acrylic acid) (PAA), (c) poly(*N*-vinyl pyrrolidone) (PVP), and (d) poly(4-vinyl phenol) (PVPh).

in a perchloric acid/ethanol (1:4 by volume) solution for 10 min (4°C, 20 V) to reduce surface roughness. Perchloric acid (60%) was purchased from Sigma-Aldrich (ACS grade), and ethanol was from Daejung Chemicals and Metals (extra pure grade; Siheung, Korea).

First anodization was performed in 0.3 M sulfuric acid (aq) for 12 h (4°C, 25 V). Then, the anodized alumina layers on both sides of Al were removed in chromic acid (aq) (18 g CrO₃ and 40.4 mL phosphoric acid in 1 L water) for 3 h (65°C), after which well-ordered dimples were made on Al surfaces. Second anodization on the dimpled Al was conducted in 0.3 M sulfuric acid (aq) for 24 h (4°C, 25 V) to obtain AAO with nanopores. The one side of the AAO substrate was masked with a teflon tape, and the alumina on the other side was removed in 5 wt% NaOH (aq). This was followed by the removal of the remaining Al in cupric acid (aq) (17 g CuCl₂ in 500 mL HCl (aq) and 500 mL water) to finally obtain AAO substrates with nanopores. The average diameter of the nanopores was calculated by measuring about 240 pores from SEM micrographs (JSM-6701F, JEOL). Sulfuric acid (95–98%) and phosphoric acid (>85%) were purchased from Sigma-Aldrich (ACS grade). Sodium hydroxide, hydrochloric acid (35–37%), and copper(II) chloride were obtained from Daejung Chemicals and Metals (extra pure grade; Siheung, Korea). Chromium trioxide (99.5%) was from Acros.

2.2. Solidification of IBU/Polymers in AAO and Their Release Behavior. Ibuprofen (IBU, purity > 98%) was purchased from Sigma. Poly(acrylic acid) (PAA, M_w 1,800 g/mol) and poly(*N*-vinyl pyrrolidone) (PVP, M_w 10,000 g/mol) were from Sigma-Aldrich. Poly(4-vinyl phenol) (PVPh, M_w 10,000 g/mol) was obtained from Polysciences, Inc. (Warrington, PA). Structures of the polymers are shown in Figure 1.

IBU and each polymer (9:1 by weight) were well mixed for 30 min using a ball mill (MM200, Retsch; frequency 5 Hz, two stainless steel balls of diameter 9 mm). The mixed powder (ca. 1 mg) was then placed on the AAO substrate, and it was melted at 130–165°C using a temperature controlled hot plate (HS180, Misung Scientific Co., Seoul, Korea). The melt filled the nanopores by the capillary force assisted by a slight mechanical force (pushed through a polyimide (DuPont) film). The external surfaces of AAO substrates were carefully cleaned using cotton swabs for any residual material; the absence of which was microscopically confirmed afterwards.

The amount of material filled in the AAO was measured by weight (CP225D, Sartorius). Then, the infused AAO substrates were placed in the cells of differential scanning calorimeter (DSC: 821e, Mettler-Toledo) and precalibrated using indium for enthalpy and temperature. Thermal treatment in DSC was performed by cyclic heating and cooling (2 times) from 25°C to 130–150°C (heating and cooling rates at 10 and 20°C/min, resp.). Also, the same experiment was performed on neat IBU.

After the thermal treatment in DSC, the AAO samples were immediately used for the release test at room temperature (20–24°C). Each sample was immersed in deionized water (2 mL in a quartz UV cell, pH~6), and the IBU release was monitored by measuring the UV absorbance at 214 nm using a UV/Vis spectrophotometer (Agilent 8453, Agilent). The wavelength was selected for the maximum UV absorbance for IBU, and the IBU concentration was calculated from the absorbance using a preconstructed calibration curve. The UV cell was covered with a paraffin film to prevent any water evaporation during the measurements. Deionized water (resistivity > 18.2 MΩ-cm) was obtained from a Direct-Q (Millipore). The release experiments were independently repeated three times.

2.3. Optical Microscopy and Fourier Transform Infrared Spectroscopy. The effect of polymers on the crystallization of IBU was studied using optical microscopy (OM: BX51, Olympus). Ball-milled samples of IBU and IBU/polymers (3–5 mg) were placed on glass slides and shielded with cover glass. They were melted at 140–165°C for 10 min using a hot stage (FP90, Mettler-Toledo). The melt was withdrawn from the hot stage, and its glass cover was removed. It was naturally cooled to form amorphous solid during this process. Then, a drop (30 μL) of deionized water was placed at the center, and the cover glass was restored. OM images were taken after 1, 2, and 3 min of water contact in the transmission mode under cross-polarization and with a 530-nm retardation plate (U-TP530, Olympus).

Fourier transform infrared spectroscopy (FTIR: Cary 660, Agilent Technologies) was also used in the transmission mode (400–4000 cm⁻¹) to analyze any structural change with addition of polymers. Ball-milled and melt/cooled samples of IBU and IBU/polymers were ground with KBr (>99%, Sigma-Aldrich) to prepare the IR specimen.

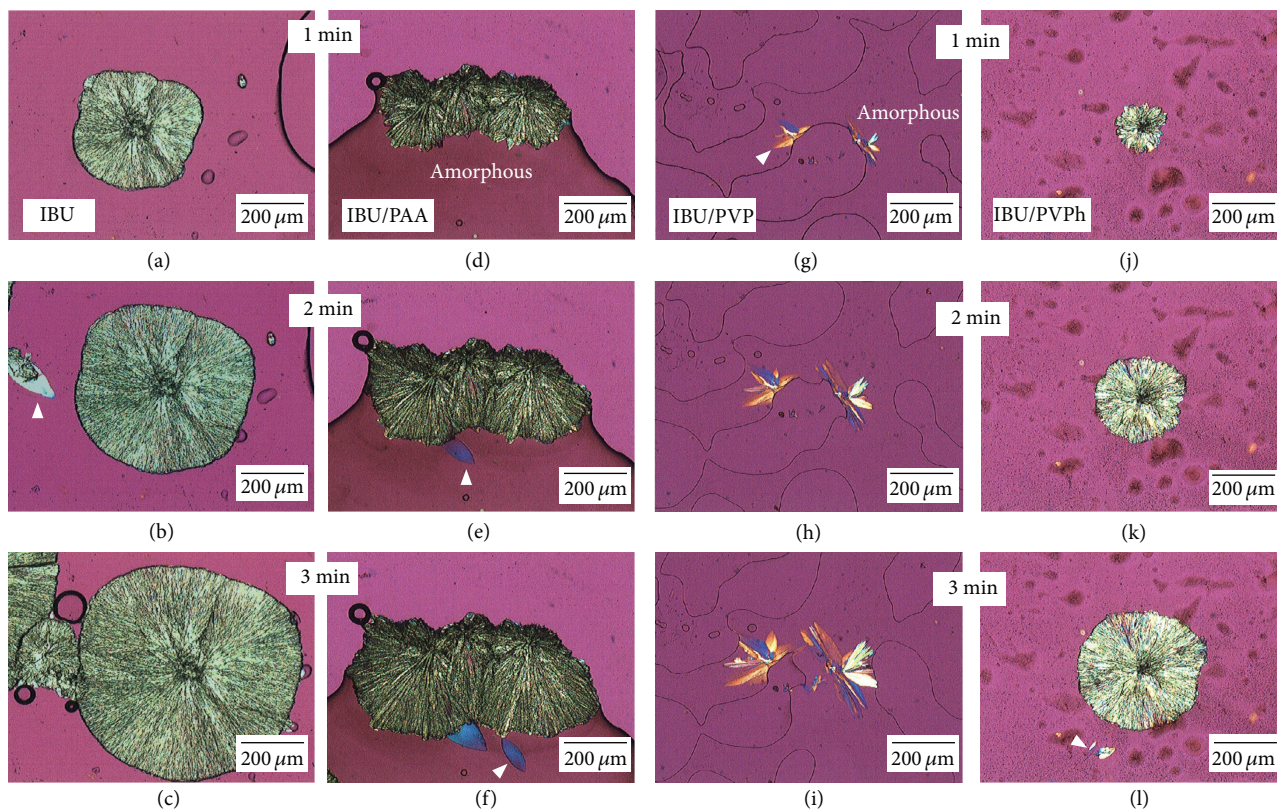


FIGURE 2: OM micrographs showing crystal growth from the amorphous IBU (a)–(c), IBU/PAA (d)–(f), IBU/PVP (g)–(i), and IBU/PVPh (j)–(l).

3. Results and Discussion

3.1. Effects of Polymeric Additives on IBU Crystallization.

When IBU or IBU/polymer (9:1) mixtures were melted and solidified on glass slides, clear solid films were obtained. These did not show birefringence under cross-polarization, which indicated the formation of amorphous phases. When the amorphous phases were exposed to water, regions of birefringence showed up nearly instantaneously. Figure 2 shows the temporal evolution of the amorphous-to-crystalline transformation for IBU ((a)–(c)), IBU/PAA ((d)–(f)), IBU/PVP ((g)–(i)), and IBU/PVPh ((j)–(l)). The initial form of the crystalline phase was oval shaped, as indicated by white arrowheads at the various places of Figure 2. Then, the crystalline phase became disk shaped probably through the assembled formation of the ovals sharing the center of the disk as their common corner. Also, the peripheries of the disk-shaped crystalline phase grew outward with time.

The nucleation of the crystalline phase seemed not very much suppressed by the addition of polymers in this bulk experiments. In all cases, the crystalline phase could be found within 1 min of water contact (Figure 2). By contrast, the growth of the crystals was significantly affected by the presence of polymers. The growth rate was in the following order: IBU ($73.9 \pm 4.2 \mu\text{m}/\text{min}$) > IBU/PVPh ($59.4 \pm 5.4 \mu\text{m}/\text{min}$) \approx IBU/PAA ($57.2 \pm 7.5 \mu\text{m}/\text{min}$) > IBU/PVP ($41.7 \pm 7.6 \mu\text{m}/\text{min}$). The crystal growth was measured from the increased distance of the crystal edge from the center of

the disks or assemblies, and the directions were chosen to avoid possible external hindrance such as void and adjacent crystalline phases. PVP was most effective in reducing the growth speed of the crystalline phase. Also, its effect was unique in that the crystalline formation of the spherulitic shape was least complete.

IR spectra were examined to probe possibly strong intermolecular interactions between IBU and polymers. Spectra of IBU with and without polymeric additives were shown in Figure 3(a), and those of neat polymers were displayed in Figure 3(b). Overall, there are only subtle changes from which the intermolecular interactions could be inferred. The peaks related to IBU, the main component (90 wt%), remained the same. The interpretation on the intermolecular interaction was from the peaks related to polymers, the minor component (10 wt%). First, the C=O stretching peak of PAA (1710 cm^{-1}) overlapped too much with that of IBU (1721 cm^{-1}). However, the lack of significant shoulder formation, which could occur from the downshift of the PAA peak [16], suggested insignificant intermolecular interactions between IBU and PAA. Second, the C=O stretching peak (marked with asterisks) of PVP (1664 cm^{-1}) showed significant red shift (1640 cm^{-1}), which suggested strong interaction, probably hydrogen bonding with the OH group of IBU. Similar shifts were previously observed for PVP, when intimate interactions were established [17–19]. Finally, the broad OH stretching peaks of PVPh were at about 3380 (peak) and

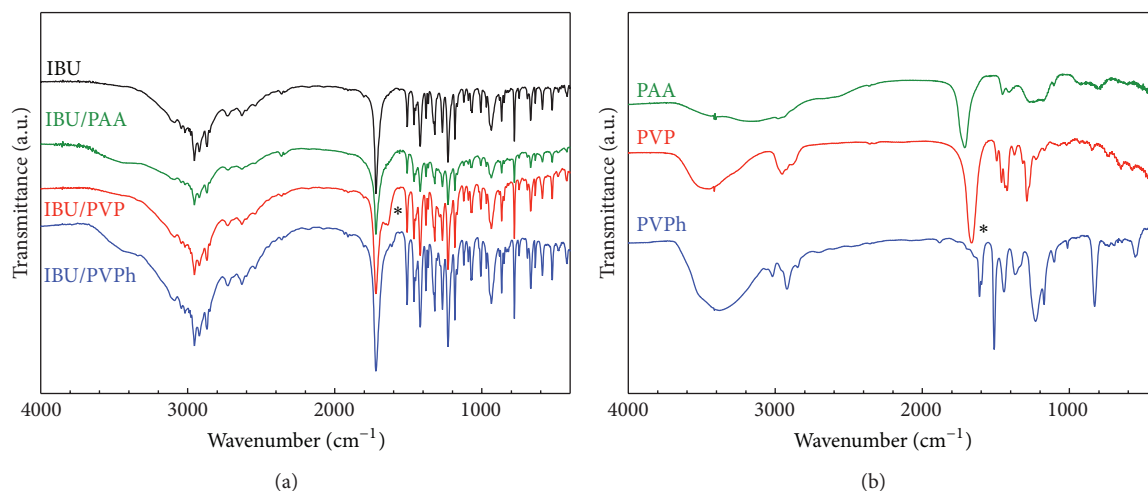


FIGURE 3: IR spectra of (a) IBU with and without polymeric additives and (b) neat polymers.

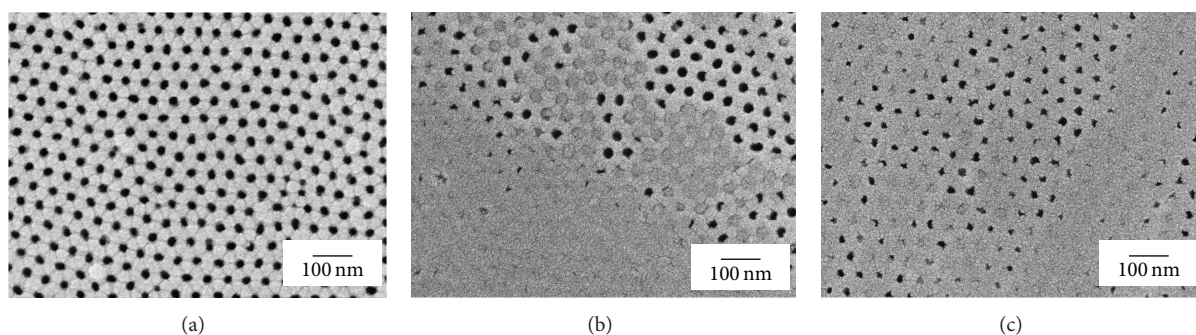


FIGURE 4: SEM micrographs of nanoporous AAO: (a) before IBU filling, (b) after IBU filling and surface cleaning, and (c) after thermal treatment in DSC.

3522 (shoulder) cm^{-1} : the former for the hydrogen-bonded groups and the latter for the free groups [20, 21]. The overlap with peaks of IBU made it difficult to accurately assess the possible changes of the PVPh peaks, but the general shapes and positions of the PVPh peaks appeared not significantly altered. Overall, the IR experiments showed that PVP interacted more strongly with IBU than PAA and PVPh did at this level of concentration. (Further increase of the polymer concentration was not pursued because of the practicalities of drug formulation.) Note that the strong interaction of PVP is in good agreement with the OM observation of bulk crystallization, where the crystalline phase with PVP seemed less mature than with other polymers, and its growth rate was most significantly reduced (Figures 2(g)–2(i)).

3.2. IBU in the Nanoporous AAO Substrates. The pore diameter of the AAO substrates utilized in the present study was 24 ± 2 nm, of which representative image was shown in Figure 4(a). The two-step anodization technique, as described in the experimental section, successfully formed the nanopores. The conditions to generate this particular pore diameter were chosen based on the results of the previous study, where pore diameter less than or equal to 55 nm was necessary to form and stabilize amorphous IBU during solidification [10].

Amount of IBU (and polymer when present) infused in the AAO pores was 0.62–1.34 mg, which corresponded to the 51–88% filling. The percentage was calculated as previously reported [10]: $(\text{Filled}\%) = \{(\text{Measured mass of infused materials})/(\text{Maximum possible mass of infused materials})\} \times 100$, where $(\text{Maximum possible mass of infused materials}) = \{(\text{Measured mass of AAO})/(\text{Density of AAO})\} \times \{\text{porosity}/(1 - \text{porosity})\} \times (\text{Density of infused materials})$. Densities of IBU and AAO were taken as 1.06 and 3.1 g/cm^3 , respectively [22, 23]. When PVP, PVPh, or PAA was present as an additive, their density of 1.25, 1.16, or 1.22 g/cm^3 was considered for the calculations [24–26]. Representative image of AAO filled with IBU was shown in Figure 4(b).

After IBU/polymer infusion in AAO, the thermal behavior of the infused material was observed during resolidification using DSC. No melting was observed, which indicated successful formation of amorphous phase (Figure 5). This result was as expected because our previous study showed the kinetic stabilization of the amorphous phase when the spatial confinement was less than or equal to 55 nm [10]. Note that the IBU not in subject of such confinement showed melting behavior at ca. $74\text{--}76^\circ\text{C}$ [10]. Representative image of AAO filled with IBU, after the thermal treatment, was shown in Figure 4(c).

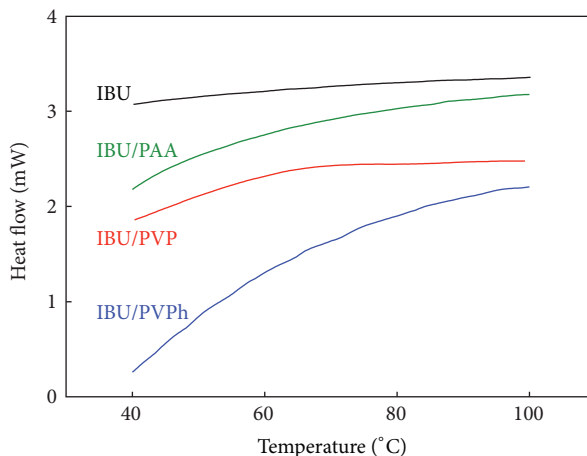


FIGURE 5: DSC thermograms showing the thermal behavior of IBU in nanoporous AAO. No melting was observed, indicating amorphous formation under spatial confinement.

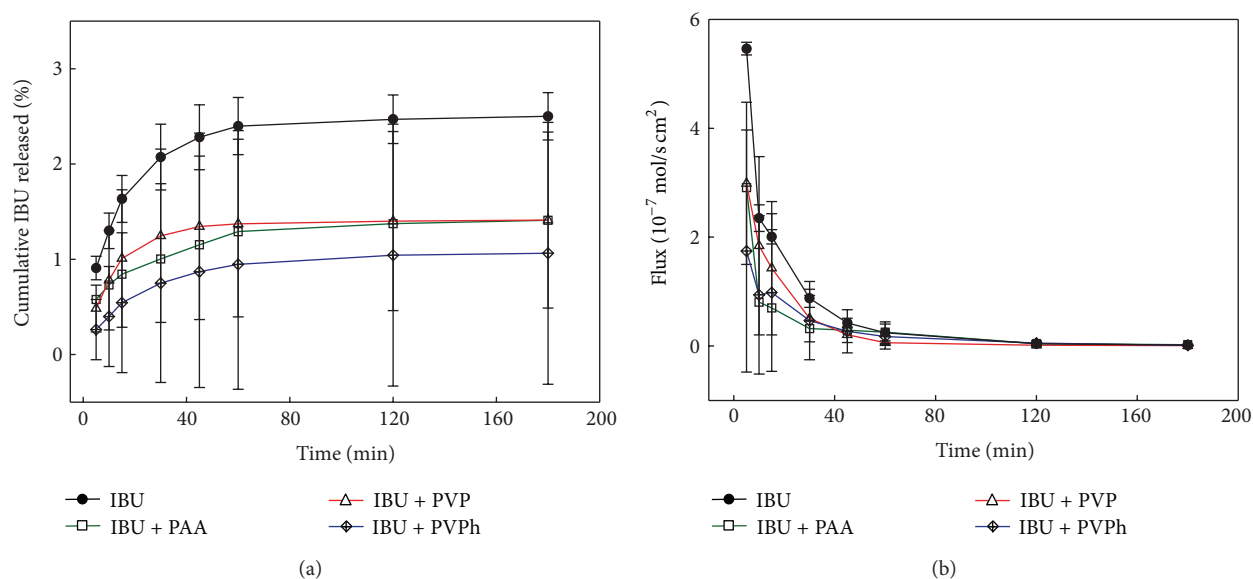


FIGURE 6: Release behavior of IBU from AAO substrates. (a) Cumulative release percentage and (b) flux were shown along with the release time.

Release behavior of IBU from AAO was summarized in Figure 6. In all cases, the cumulative release (Figure 6(a)) increased slowly with time, probably due to the low solubility of IBU (e.g., 1.54×10^{-3} mol/L at 25°C and pH 6.1 for crystalline IBU) [10, 27]. The IBU concentration after 180 min was less than 10^{-4} mol/L in all cases; it was much smaller than the equilibrium concentration indicating that the current results were from the early stage of the IBU dissolution. The addition of polymeric additives decreased the cumulative release. Also, it generally increased the variation among the repeated release experiments, suggesting that the variation increase was probably due to the inhomogeneous distribution of polymer molecules. In spite of the variation, all repeats showed the same release trends. The IBU flux (Figure 6(b)) also showed the similar trends. The flux decreased dramatically as a function of time in all cases, and it was diminished

with addition of polymers. Note that the UV absorption of the polymers at the wavelength used to monitor IBU release (214 nm) was determined negligible as follows. First, the aqueous solutions of PVP, PAA, and PVPh had maximum absorbance at 195, 195, and 190 nm, respectively. Second, assuming that the release of IBU and polymer was proportional to the composition, the corresponding polymer solutions were prepared, and their UV absorbance was measured at 214 nm. The UV absorption of the polymers was at the most two hundredth of the total absorbance observed for the IBU release.

The reason of the decreased flux with time was already reported in our previous study [10]. The initially high flux (0 to 5 min) was because of the large solubility of amorphous IBU, and the decrease with time was due to the crystallization of IBU in contact with water [10]. The water contact was

known to start the crystallization of the amorphous IBU almost instantaneously [11, 28], and this was also confirmed in our bulk crystallization (Figure 2), where the initiation of the crystallization was found in less than 1 min.

The basis of the decreased flux with polymer addition could be found from two different sources. First, the polymer molecules associated with IBU appeared to act as diffusion barriers, as previously observed with other APIs [29]. In particular, PVPh with the most hydrophobic characteristics showed the most pronouncedly diminished release behavior. Second, the addition of polymer did not stabilize the amorphous IBU enough to increase its release rate. In the bulk crystallization study (Figure 2), the polymers decreased the growth rate of the crystals. However, they did not significantly hinder the nucleation of the crystalline phase. Since IBU was confined in the pores of 24 nm diameter, nucleation followed by growth in nanoscale might be enough to form a crystalline “cap” that essentially stopped the unobstructed release from any remaining amorphous phase [11].

4. Conclusions

In summary, the AAO substrates were employed to generate amorphous IBU with polymeric additives by confining them within the nanopores (diameter, 24 nm). The amorphous IBU had tendency to rapidly crystallize upon water contact, which was the origin of the temporal decrease of the IBU release flux [10, 11, 28]. The polymeric additives, which retarded the crystal growth, were less effective in inhibiting the nucleation of the crystalline phase. In addition, the IBU with polymeric additives showed the sustained release behavior, probably because of the polymer molecules acting as the diffusion barriers. Since the temporal decrease of the flux was insignificantly affected by the polymers, the present study suggests that the inhibition of the crystal nucleation is the key aspect of stabilizing the amorphous IBU in the nanoscopic confinement, which is essential to make full use of its high solubility (ca. 6 times higher than that of the bulk crystalline phase) [10].

Conflict of Interests

The authors declare that they have no conflict of interests.

Acknowledgments

This research was supported by the Basic Science Research Program through the National Research Foundation of Korea (NRF) funded by the Ministry of Education, Science, and Technology (Grant no. 2010-0005045).

References

- [1] J.-U. A. H. Junghanns and R. H. Müller, “Nanocrystal technology, drug delivery and clinical applications,” *International Journal of Nanomedicine*, vol. 3, no. 3, pp. 295–309, 2008.
- [2] A. A. Noyes and W. R. Whitney, “The rate of solution of solid substances in their own solutions,” *The Journal of the American Chemical Society*, vol. 19, no. 12, pp. 930–934, 1897.
- [3] A. Dokoumetzidis and P. Macheras, “A century of dissolution research: from noyes and whitney to the biopharmaceutics classification system,” *International Journal of Pharmaceutics*, vol. 321, no. 1–2, pp. 1–11, 2006.
- [4] T. Yang, C. Kim, J. Jho, and I. W. Kim, “Regulating fluoride uptake by calcium phosphate minerals with polymeric additives,” *Colloids and Surfaces A*, vol. 401, pp. 126–136, 2012.
- [5] R. Shegokar and R. H. Müller, “Nanocrystals: industrially feasible multifunctional formulation technology for poorly soluble actives,” *International Journal of Pharmaceutics*, vol. 399, no. 1–2, pp. 129–139, 2010.
- [6] A. Kumari, S. K. Yadav, and S. C. Yadav, “Biodegradable polymeric nanoparticles based drug delivery systems,” *Colloids and Surfaces B*, vol. 75, no. 1, pp. 1–18, 2010.
- [7] B. C. Hancock and M. Parks, “What is the true solubility advantage for amorphous pharmaceuticals?” *Pharmaceutical Research*, vol. 17, no. 4, pp. 397–404, 2000.
- [8] N. J. Babu and A. Nangia, “Solubility advantage of amorphous drugs and pharmaceutical cocrystals,” *Crystal Growth and Design*, vol. 11, no. 7, pp. 2662–2679, 2011.
- [9] B. Rodríguez-Spong, C. P. Price, A. Jayasankar, A. J. Matzger, and N. Rodríguez-Hornedo, “General principles of pharmaceutical solid polymorphism: a supramolecular perspective,” *Advanced Drug Delivery Reviews*, vol. 56, no. 3, pp. 241–274, 2004.
- [10] S. Lee, G. Yu, K. Shin, and I. W. Kim, “Estimating the solubility of amorphous ibuprofen using nanoporous anodic aluminum oxide as a solidification template,” *Journal of Nanoscience and Nanotechnology*, vol. 13, no. 3, pp. 2348–2353, 2013.
- [11] S. G. Kazarian and K. L. Andrew Chan, “Chemical photography of drug release,” *Macromolecules*, vol. 36, no. 26, pp. 9866–9872, 2003.
- [12] D. Velasco, C. B. Danoux, J. A. Redondo et al., “PH-sensitive polymer hydrogels derived from morpholine to prevent the crystallization of ibuprofen,” *Journal of Controlled Release*, vol. 149, no. 2, pp. 140–145, 2011.
- [13] P. J. Marsac, T. Li, and L. S. Taylor, “Estimation of drug-polymer miscibility and solubility in amorphous solid dispersions using experimentally determined interaction parameters,” *Pharmaceutical Research*, vol. 26, no. 1, pp. 139–151, 2009.
- [14] H. Masuda, H. Yamada, M. Satoh, H. Asoh, M. Nakao, and T. Tamamura, “Highly ordered nanochannel-array architecture in anodic alumina,” *Applied Physics Letters*, vol. 71, no. 19, pp. 2770–2772, 1997.
- [15] A. P. Li, F. Müller, A. Bimer, K. Nielsch, and U. Gösele, “Hexagonal pore arrays with a 50–420 nm interpore distance formed by self-organization in anodic alumina,” *Journal of Applied Physics*, vol. 84, no. 11, pp. 6023–6026, 1998.
- [16] Y. Gotoh, R. Igarashi, Y. Ohkoshi, M. Nagura, K. Akamatsu, and S. Deki, “Preparation and structure of copper nanoparticle/poly(acrylic acid) composite films,” *Journal of Materials Chemistry*, vol. 10, no. 11, pp. 2548–2552, 2000.
- [17] S. G. Kazarian and G. G. Martirosyan, “Spectroscopy of polymer/drug formulations processed with supercritical fluids: in situ ATR-IR and Raman study of impregnation of ibuprofen into PVP,” *International Journal of Pharmaceutics*, vol. 232, no. 1–2, pp. 81–90, 2002.
- [18] W. Xu, H. Chen, H. Li, and M. Wang, “Fabrication of carbon black/crosslinked poly(vinyl pyrrolidone) core-shell nanoparticles stable in water,” *Colloids and Surfaces A*, vol. 266, no. 1–3, pp. 68–72, 2005.

- [19] G. G. Couto, J. J. Klein, W. H. Schreiner, D. H. Mosca, A. J. A. de Oliveira, and A. J. G. Zarbin, "Nickel nanoparticles obtained by a modified polyol process: synthesis, characterization, and magnetic properties," *Journal of Colloid and Interface Science*, vol. 311, no. 2, pp. 461–468, 2007.
- [20] P. Xing, L. Dong, Z. Feng, and H. Feng, "Miscibility and specific interactions in poly(β -hydroxybutyrate-co- β -hydroxyvalerate) and poly(p-vinylphenol) blends," *European Polymer Journal*, vol. 34, no. 8, pp. 1207–1211, 1998.
- [21] S. W. Kuo, "Effect of copolymer compositions on the miscibility behavior and specific interactions of poly(styrene-co-vinyl phenol)/poly(vinyl phenyl ketone) blends," *Polymer*, vol. 49, no. 20, pp. 4420–4426, 2008.
- [22] I. Tanis and K. Karatasos, "Association of a weakly acidic anti-inflammatory drug (ibuprofen) with a poly(amidoamine) dendrimer as studied by molecular dynamics Simulations," *Journal of Physical Chemistry B*, vol. 113, no. 31, pp. 10984–10993, 2009.
- [23] R. Lizárraga, E. Holmström, S. C. Parker, and C. Arrouvel, "Structural characterization of amorphous alumina and its polymorphs from first-principles XPS and NMR calculations," *Physical Review B*, vol. 83, Article ID 094201, 9 pages, 2011.
- [24] J. H. Ko, "Poly(N-vinyl pyrrolidone)," in *Polymer Data Handbook*, J. E. Mark, Ed., pp. 962–964, Oxford University Press, New York, NY, USA, 1999.
- [25] N. Hernandez-Montero, E. Meaurio, K. Elmiloudi, and J. R. Sarasua, "Novel miscible blends of poly(p-dioxanone) with poly(vinyl phenol)," *European Polymer Journal*, vol. 48, pp. 1455–1465, 2012.
- [26] R. A. Orwoll and Y. S. Chong, "Poly(acrylic acid)," in *Polymer Data Handbook*, J. E. Mark, Ed., pp. 252–253, Oxford University Press, New York, NY, USA, 1999.
- [27] X. Qiu, E. Donath, and H. Möhwald, "Permeability of ibuprofen in various polyelectrolyte multilayers," *Macromolecular Materials and Engineering*, vol. 286, no. 10, pp. 591–597, 2001.
- [28] D.-J. Lee, S. Lee, and I. W. Kim, "Effects of humidity and surfaces on the melt crystallization of ibuprofen," *International Journal of Molecular Sciences*, vol. 13, no. 8, pp. 10296–10304, 2012.
- [29] M. K. Lee, H. Lee, I. W. Kim, and J. Lee, "Novel polymorphic form of adefovir dipivoxil derived from polymer-directed crystallization," *Pharmazie*, vol. 66, no. 10, pp. 766–770, 2011.